DEM hydromechanical modeling of fault reactivation

Alexandra Tsopela

Communauté UNIVERSITÉ Grenoble Alpes

THÈSE

Pour obtenir le grade de

DOCTEUR DE LA COMMUNAUTÉ UNIVERSITÉ GRENOBLE ALPES

Spécialité : 2MGE : Matériaux, Mécanique, Génie civil, Electrochimie

Arrêté ministériel : 25 mai 2016

Présentée par

Alexandra TSOPELA

Thèse dirigée par **Frédéric-victor DONZE**, Professeur, UGA
et codirigée par **YVES GUGLIELMI**

préparée au sein du **Laboratoire Laboratoire Sols, Solides, Structures et Risques**
dans **l'École Doctorale I-MEP2 - Ingénierie - Matériaux, Mécanique, Environnement, Energétique, Procédés, Production**

Modélisation hydromécanique de la réactivation de faille par la méthode des éléments discrets

DEM hydromechanical modeling of fault reactivation

Thèse soutenue publiquement le **25 juin 2018**,
devant le jury composé de :

Monsieur FREDERIC DONZE
PROFESSEUR, UNIVERSITE GRENOBLE ALPES, Directeur de thèse
Monsieur FLORIAN AMANN
PROFESSEUR, UNIVERSITE RWTH AACHEN - ALLEMAGNE, Rapporteur
Monsieur JEAN SULEM
PROFESSEUR, ENPC PARIS, Rapporteur
Monsieur LUC SCHOLTES
MAITRE DE CONFERENCES, UNIVERSITE DE LORRAINE, Examinateur
Monsieur BERTRAND MAILLOT
PROFESSEUR, UNIVERSITE DE CERGY-PONTOISE, Président
Monsieur YVES GUGLIELMI
PROFESSEUR, UNIVERSITE AIX-MARSEILLE, Co-directeur de thèse

To my grandmother

Abstract

Faults in the Earth crust are localized zones of deformation which can drive fluids over long distances. Estimating the permeability of fault zones and their hydro-mechanical properties is crucial in a wide range of fields of research and industrial applications. In the petroleum industry, and more specifically in exploration and production applications, the seal integrity of faults in low permeability formations (e.g. shale) needs to be evaluated for the detection of hydrocarbon traps. There already exist approaches able to sufficiently estimate the "side-sealing" capacity of a fault based on the clay or shale content of the layers (e.g. Shale Gouge Ratio). Nevertheless, the conditions under which the fault acts as a drain along its structure are still not properly constrained. In this context, the response of the fault is directly controlled by a number of factors that can be better approached from a geomechanics point of view. These factors include the stress field, the fluid pressure, the orientation of the fault-related structures and the material properties. Meso-scale field injection experiments were carried out inside a fault zone located in the Tournemire massif at the South of France during which the fluid pressure, the deformation, the seismicity and the flow rate were monitored. Based on the Tournemire experiments and field observations, a numerical study was performed exploring the evolution of the permeability and how it is related to the fault hydro-mechanical reactivation and potentially to the induced seismicity. Fault-related structures such as subsidiary faults or fractures that were targeted during the experiments together with the surrounding intact rock, were modeled using the Discrete Element method. Modeling of the experimental tests and the analysis of generic models used to perform parametric studies highlighted the primary role of the in-situ stress conditions. The combined effect of stress and orientation of the fault structures determine in the first place the nature of the reactivation according to the critically stressed fault concept reported in the literature. For given stress conditions and structural features, it was shown that depending on the fluid pressure level, the fault offers three different ranges of permeability: i) permeability that is equivalent to the formation's permeability, ii) 2 to 4 orders of magnitude higher and iii) more than 4 orders of magnitude higher. While for the two extreme cases the fault is characterized as hydro-mechanically inactive or active, the second case is mostly controlled by fluid channeling mechanisms promoted by heterogeneities at the scale of a single fracture or at the scale of the fracture network. Changes in the hydraulic properties are in some cases detected by the seismicity triggered during the injection under the assumption that the seismicity is the direct effect of fluid propagation, fluid pressure increase and effective stress drop. However, the mechanisms behind the injection induced seismicity are still poorly understood. Using experimental results from the Tournemire site, the role of the hydraulic diffusivity of the fault-related structures was explored on the recorded seismicity in the framework of a hydro-mechanical analysis. The results suggest that the induced microseismicity was possibly related to stress perturbations caused by a significant aseismic deformation rather than fluid propagation through hydraulically connected structures.

Keywords : Fault zone; Fault permeability; Fluid pressurization; Hydro-mechanical reactivation; Field injection; Discrete Element Method

Résumé

Les failles dans la croûte superieure sont des zones de déformation localisées capables de conduire des fluides sur de longues distances. L'estimation de la perméabilité des zones de failles et de leurs propriétés hydro-mécaniques est cruciale dans nombreux domaines de recherche et applications industrielles. Dans l'industrie pétrolière, et plus particulièrement dans les applications d'exploration et de production, l'intégrité de l'étanchéité des failles doit être évaluée pour la détection des pièges à hydrocarbures. Il existe déjà des approches permettant d'estimer la capacité de scellement latéral d'une faille à partir de la teneur en argile des couches (par exemple le Shale Gouge Ratio). Pourtant, les conditions dans lesquelles la faille se comporte comme un conduit le long de sa structure ne sont pas encore suffisamment contraintes. Dans ce contexte, la géomécanique peut apporter un éclairage complémentaire sur les paramètres qui contrôlent le comportement hydrodynamique de la faille. Ces paramètres comprennent le champ de contraintes, la pression du fluide, l'orientation des structures de la zone de faille et les propriétés des matériaux. Des expériences d'injection à une échelle décamétrique ont été réalisées dans une zone de faille située dans le site expérimental de Tournemire, dans le sud de la France, au cours desquelles la pression et le débit du fluide, la déformation du massif, la sismicité ont été suivis. Sur la base des observations issues de ces expériences, une étude numérique a été réalisée pour explorer l'évolution de la perméabilité et établir le lien avec la réponse hydromécanique de la faille ainsi que la sismicité induite. Les comportements des failles secondaires, les fractures de la zone endommagée ainsi que la roche encaissante ont été modélisés numériquement en utilisant la méthode des éléments discrets La modélisation des essais expérimentaux et l'analyse des modèles génériques utilisés pour les études paramétriques ont mis en évidence le rôle majeur des conditions de contrainte in situ. L'effet combiné de la contrainte et de l'orientation des structures de la faille détermine en premier lieu la nature de la réactivation selon le concept de l'état de contrainte critique de la faille décrit dans la littérature. Pour des conditions de contrainte et des éléments structuraux donnés, il a été démontré que selon le niveau de pression du fluide, la faille offre trois gammes différentes de perméabilité : i) perméabilité équivalente à la perméabilité de la formation, ii) 2 à 4 ordres de grandeur plus élevés et iii) plus de 4 ordres de grandeur plus élevés. Alors que pour les deux cas extrêmes, la faille est caractérisée comme étant hydro-mécaniquement active ou inactive, le second cas est principalement contrôlé par des mécanismes de chenalisation du fluide favorisés par des hétérogénéités aussi bien à l'échelle d'une seule fracture ou qu'à l'échelle du réseau de fractures. Les changements dans les propriétés hydrauliques sont dans certains cas détectés par la sismicité induite lors de l'injection en supposant que la sismicité est l'effet direct de la propagation du fluide, de l'augmentation de la pression du fluide et de la chute de la contrainte effective. Néanmoins, les mécanismes à l'origine de la sismicité induite par injection sont encore peu connus. A partir des résultats expérimentaux du site de Tournemire, le rôle de la diffusivité hydraulique des structures de la faille a été exploré sur la sismicité observée dans le cadre d'une analyse hydro-mécanique. Les résultats indiquent que la microsismicité induite était probablement liée à des perturbations de contrainte résultantes d'une déformation asismique importante plutôt que de la propagation de fluides à travers des structures hydrauliquement connectées.

Mots clés : Zone de faille; Perméabilité de faille; Pressurisation du fluide; Réactivation hydro-mécanique; Injection du fluide; Méthode des éléments discrets

Acknowledgements

First of all, I would like to thank my supervisor, Frédéric Donzé, for all his support and motivation during the 4.5 years that I have had the chance to know him. Thank you for your enthusiastic spirit especially in times that I truly needed it. Finally, thank you for the unforgettable "mountaineering" moments where I had the chance to hike and canyon with one of the best!

Furthermore, I would like to express my gratitude to my co-supervisor, Yves Guglielmi, for all the long, helpful and constructive skype meetings and all the fruitful discussions during my stays in the USA. Even though they were short, the outcome was always exciting.

Apart from my two supervisors, I want to thank all the people involved in the Fluids & Faults project from whom I have learned a lot during my PhD. Special thanks go to Claude Gout for his warm welcomes in Pau and Pierre Henry for his useful comments regarding all aspects of this work.

Moreover, I would like to express my gratitude to the reviewers of my thesis: Florian Amman and Jean Sulem, for accepting and for taking the time to review my manuscript and provide constructive and helpful advice. In addition, I would like to thank the rest of the committee members: Bertrand Maillot and Luc Scholtès, for their comments and stimulating discussion during the defense.

Obviously, I owe a huge thanks to all the people with whom I have shared some of the most memorable moments of my life in Grenoble. Thank you Timos, Olga and Christina, for turning my stressful moments into laughs. Eleni and Bratislav, thank you for being there from the beginning until the end of my Grenoble experience with breaks, "terrasse" moments and jazzy magical nights. Eleni, thank you for always "contaminating" me with your positivity and optimism and for all the wonderful late night risky adventures that I will never forget. Fabio, thank you for all the GOAT moments we have spent together and for your endless support.

Finally, I would like to thank Giannis for going through all the good and the bad with me, and last but not least my family, my mom and dad, my aunts, Semi and Olga and my sisters, Aliki and Marina for always reminding me how much they believe in me. Thank you for everything!

Contents

Introduction

Faults in the Earth crust are the result of tectonic processes in the Earth crust. They are recognized by the relative movement occurring on the two sides of the fault that have slided. Apart from the part of the faults that is exposed to the surface, fault structures are characterized by a high degree of uncertainty regarding their structural, hydraulic and mechanical characteristics. In a large number of applications the evaluation of the fault's properties and hydro-mechanical thresholds is necessary in order to evaluate the in-situ conditions and predict the fault's behavior in the long or short term. Having said that, the faults have been long known to control a wide range of processes in the Earth crust related to fluid migration and deformation. In the industry, faults are mainly linked to the energy industry domain affecting the exploration and production in the petroleum industry, the disposal of radioactive waste in deep geological formations, the unconventional hydrocarbon extraction as well as the geothermal energy extraction. Another domain that has raised significant research efforts is the deep geological sequestration of CO_2 in order to reduce gas emissions. The majority of the above applications involve perturbation of the in-situ conditions due to the increase of the fluid pressure and they require fundamental understanding of hydro-mechanical couplings occurring in the rock mass and more importantly on the macro-scale heterogeneities that are recognized to control the response of the rock mass.

In the exploration and production field the need to predict and characterize the response of a fault in a sedimentary basin environment is of crucial importance for estimating seals and traps of hydrocarbons. The processes occurring in a petroleum basin system involve the generation of hydrocarbons in the source rock, their expulsion and migration through the reservoir rock, and their accumulation in traps. The basic objective of exploration in the petroleum industry is the detection of potential traps along the hydrocarbon migration path, the most common among which are either the stratigraphic or the structural traps. Stratigraphic traps are formed due to changes in the rock type from a high porosity reservoir rock usually sandstones or carbonates, to a low porosity and permeability seal rock like shale or evaporites. Structural traps concern geological structural elements such as anticlines and faults that result from the deformation of the strata and whose geometry allows the accumulation of hydrocarbons. Typical examples of structural traps are shown in Figure 1.

While the role of faults in the processes of a basin is primary, it was not until the 1910s that it was recognized and accounted for as major traps [Sorkhabi & Tsuji, 2005]. Faults can act as traps based on the juxtaposition across the fault where a reservoir rock meets a seal rock due to the relative movement of the involved strata, based on the fault structure and fault geometry or finally based on the fault rock properties and characteristics providing a seal to hydrocarbons migration.

However, faults are complex features actively affecting the migration and accumulation of hydrocarbons at different stages. It has been recognized that faults can act both as barriers and conduits for fluids

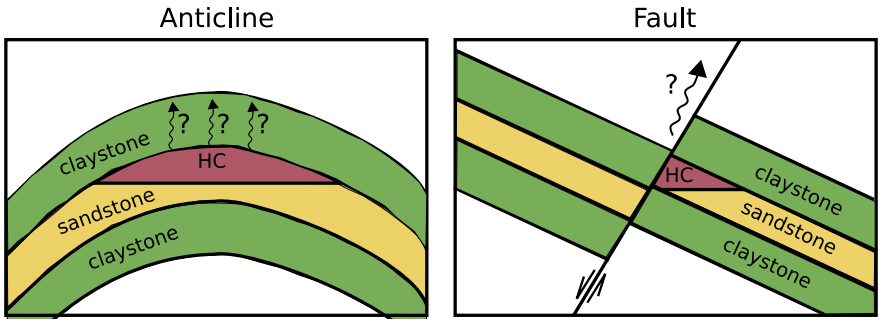

Figure 1: Examples of structural traps and the associated questions related to caprock or fault seal integrity.

depending on a variety of factors that are in most cases difficult if not impossible to determine. It is often accepted that faults can provide a barrier across their structure but can act as conduit along their structure under favorable conditions (e.g. Caine et al. [1996]). In exploration and production, in order to evaluate the seal integrity, which implies the stability of the structures in the seal, it is important to have information on the stress and pressure conditions, the fault history, the architecture and the fault hydro-mechanical properties. Based on data that are usually recovered and treated in the context of exploration and production, two questions arise that link the geology, the fluid pressure, the stress conditions and the permeability:

- For a given stress condition and geological context, at what overpressure will the permeability of the fault increase?
- In defined geological settings and for a given overpressure, which mechanical conditions will cause significant permeability increase?

Focusing on the above questions, the "Fluids and Faults" project, sponsored by TOTAL S.A, was carried out with the main objective of defining a permeability-stress-fluid pressure relationship. Such relationship provides useful information regarding fault seal integrity in exploration, production and CO_2 storage in terms of predicting the hydrocarbon column height and estimating the likelihood of trap leakage. The project included the performance of a series of mesoscale field experiments at the Tournemire Underground Research Laboratory, laboratory experiments and numerical modeling. Focusing on the mesoscale experiments and the subsequent numerical modeling, the main objectives involved the monitoring of fluid migration in a low permeability medium through a dense instrumentation network that allowed the monitoring of deformation, flow rate, fluid pressure, microseismicity and electrical phenomena. The numerical modeling task deals with the interpretation of the tests results, the understanding of the associated mechanisms during structure reactivation and testing of the permeability-stress-fluid pressure relationship observed during the experiments.

The present thesis is focused on the numerical modeling of the field tests. Based on the experimental observations, an effort is made towards determining the conditions that favor fault hydro-mechanical reactivation. More specifically, the points that are addressed in this study are the following:

- Under which stress conditions fault related structures are reactivated?
- What are the fluid pressure thresholds leading to reactivation and permeability enhancement?

- What are the geometrical (e.g. orientation, fracture interaction) or material properties (e.g. stiffness, friction, dilation) favoring the reactivation?
- Does the mechanical and hydraulic reactivation along a fault coincide?

The research community is now focusing on the points stated above in order to assess the fault sealing properties and the potential of fault leakage in industrial applications. Moreover, the rising concern of the increasing rate of seismicity related to anthropogenic activities is leading the research efforts towards better understanding the role of fluid and the complex coupled hydro-mechanical phenomena taking place in fault environments under fluid pressurization conditions. The risk associated to the presence of faults and their response to fluid pressurization (seismicity, leakage) needs to be estimated and can dramatically affect the course and life of a project. Therefore, depending on the context, answers to these points can provide insight to different mechanisms favoring permeability enhancement but also to the complex fluid pressure diffusion and/or stress perturbation processes commonly responsible for fluid induced seismicity.

Concentrating on the importance of discrete structures such as subsidiary faults or fractures that tend to focus fluid flow and deformation, the Discrete Element Method is used where the hydro-mechanical coupling effects occur along these heterogeneities. In the present document, different modeling studies are presented based on the field tests conditions in an effort to approach the points reported earlier. An overview of the state of the art is first given (Chapter 1). The fault zone concept is described especially in shale environments and the evolution of the permeability is discussed from a geomechanical point of view where the state of stress, fluid pressure and strength criteria are considered as key parameters determining the conductivity of these structures and especially the fracture controlled permeability. In addition, the relations between the hydro-mechanical reactivation, the permeability enhancement and the induced seismicity are also discussed.

Chapter 2 contains the necessary information regarding the in-situ experiments performed at the Tournemire Underground Research Laboratory. Two specific field injection tests are described in more detail as they are used as a basis for further numerical modeling. The software used for the numerical analysis is also described in Chapter 2 as well as the modeling protocol used for the majority of the simulations.

In Chapter 3 an attempt is made towards evaluating the effect of fracture connectivity, interaction and orientation based on the field injection test performed in the damage zone of the Tournemire fault zone. The interaction of natural fractures is first investigated and their contribution to the hydro-mechanical response of the system based on the field measurements. A generic model is then presented along with a sensitivity study in order to better understand the dominant mechanisms of fractures interaction and the key parameters, such as stress state and properties under fluid pressurization conditions.

Chapter 4 deals with the consideration of the fault plane heterogeneities in the hydro-mechanical analysis and their potential impact on the flow propagation regime, mechanical response and induced seismicity. A model is presented where mechanical heterogeneities are introduced along a fault plane representing contact areas, cementation patches or rock bridges. The localization of the flow and rupture along distinct channels is then discussed along with its relation to the hydraulic properties of the fault. Using a specific case study, the concept of the subcritical permeability increase is investigated according to which the fault mechanical and hydraulic reactivation do not coincide.

In Chapter 5 building on seismicity observations of the in-situ injection test in the Tournemire host rock few meters away from the fault zone, the processes behind the induced seismicity are discussed in the

light of a hydro-mechanical analysis. Accounting for the location of the seismic events recorded in-situ, different configurations are tested with the purpose of investigating whether the induced seismicity that migrated to the fault zone is a result of pressure diffusion along hydraulically connected structures or of stress transfer effects associated to aseismic deformation.

In the last chapter (Chapter 5), the main findings of this thesis are summarized and the questions that remain to be answered are discussed along with suggestions regarding future work that would complete and enhance the presented results.

Chapter 1

State of the art

1.1 Rupture and reactivation of pre-existing discontinuities

From a geomechanical point of view, at the laboratory scale, the term failure corresponds to a process in which the rock physically deteriorates and its ability to support a load decreases [Jaeger et al., 2009]. Depending on the confining pressure, the response of the rock at failure can be considered as ductile or brittle. Focusing on the brittle failure and considering intermediate values of confining pressure, failure generally occurs along a defined inclined plane of fracture characterized by shearing displacement along its surface [Jaeger et al., 2009]. However, depending on the rock type and the micro-scale processes involved, it has been shown that the localization at the laboratory scale might occur in a variety of forms such as concentration or coalescence of cracks, a gouge zone of finely comminuted material [Bésuelle & Rudnicki, 2004]. In low porosity rocks the micro-crack growth and coalescence, which are influenced by grain boundaries and the different strengths and crystallographic properties of the constituent minerals, is a dominant mechanism while in high porosity rocks, pore collapse and indentation of hard grains can be important [Bésuelle & Rudnicki, 2004]. The necessary conditions for failure to occur are usually described from the three principal stress components (σ_1, σ_2, σ_3). In an effort to describe failure in terms of the stress state, the Mohr-Coulomb failure criterion appears as a practical and widely used tool for rock mechanics applications. According to the Mohr-Coulomb criterion, failure should occur along a plane that forms an angle β with the direction of the maximum principal stress (σ_1) due to a shear stress τ acting on the plane. The resistance to this sliding is expressed as the sum of the normal stress σ_n acting on the plane multiplied by the coefficient of internal friction $\mu = tan\phi$ and the constant c called cohesion which represents the cohesive force of the material. The criterion is mathematically expressed as:

$$\tau = c + \sigma_n tan\phi \tag{1.1}$$

The graphical representation of the Mohr-Coulomb criterion is shown in Figure 1.1.

Even though the criterion presents a very practical approach to characterize failure, it should be noted that according to the above, the intermediate principal stress has no effect on failure.

In the presence of fluid pressure, the Terzaghi effective stress concept is introduced, according to which

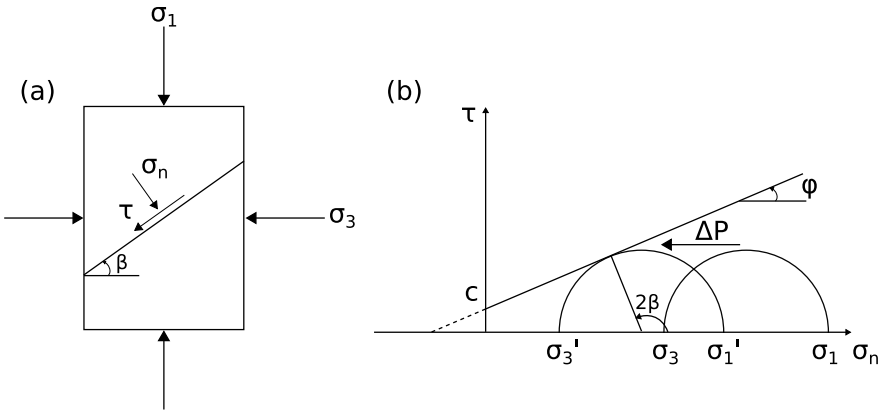

Figure 1.1: (a) Normal and shear stresses resolved on the plane of rupture; (b) Mohr diagram of shear stress (τ) versus normal stress (σ_n) showing how the increasing fluid pressure (ΔP) moves the Mohr circle towards the failure envelope.

the failure of the rock is controlled by the effective stress tensor equal to:

$$\sigma'_{ij} = \sigma_{ij} - \delta_{ij} P \tag{1.2}$$

where σ'_{ij} is the effective stress tensor, σ_{ij} is the total stress tensor, δ_{ij} is the Kronecker delta and P is the fluid pressure.

In the Mohr-Coulomb criterion, the effective stresses are accounted for by shifting the Mohr circle to the left of the (effective) normal stress axis (Figure 1.1), thus approaching the failure envelope.

It can be understood that on larger scales, rock masses are strongly heterogeneous and contain discontinuities that in most cases control the hydro-mechanical response of the rock mass. These planes of weakness are mostly cracks, fractures or faults. In the presence of such structures, frictional sliding can occur along their surfaces leading to their reactivation mainly due to shear stress or fluid pressure increase (Figure 1.1).

In the 2D consideration of the problem (σ_1-σ_3 plane), the condition for sliding to occur along a plane of weakness whose unit normal vector forms an angle β with the direction of the maximum principal stress, σ_1 is described by Equation 1.1 where the normal traction component σ_n and the shear component τ are given by the following equations:

$$\sigma_n = \frac{(\sigma_1 + \sigma_3)}{2} + \frac{(\sigma_1 - \sigma_3)}{2} cos2\beta \tag{1.3}$$

$$\tau = -\frac{(\sigma_1 - \sigma_3)}{2} sin2\beta \tag{1.4}$$

The angle β is expressed in terms of the friction angle ϕ through the following relationship:

$$2\beta = \frac{\pi}{2} + \phi \tag{1.5}$$

It should be noted that the cohesion term and the friction angle in Equation 1.1 depends on the surface characteristics of the fracture as these may be open or characterized by contact areas or be filled with different minerals.

The same effective stress concept described above applies to the case of sliding along preexisting planes

of weakness meaning that for conductive fractures, a fluid pressure increase will yield to a decrease of the effective normal stress acting on the plane. It is therefore possible to predict for a given plane orientation the normal and shear stress acting on its surface and to predict under which conditions the plane will slide or not. The strength of the rock mass is mainly controlled by the frictional strength of the discontinuities of different scales and more specifically, discontinuities that are critically oriented with respect to the stress field.

The relationship between the mechanical reactivation and especially the sliding of a fracture or fault surface with the hydraulic transmissivity has been studied extensively revealing a strong hydro-mechanical coupling effect. The usual mechanism under which a fracture is able to become conductive given a shear displacement is associated to the dilation of the fracture. When a fracture is experiencing shear deformation, dilation is associated to a normal to the fracture plane displacement due to the surface morphology. In the presence of asperities, dilation arises because the asperities of one fracture surface must by necessity ride up in order to move past those of the other surface [Jaeger et al., 2009]. In the context of fracture fluid flow, the property indicating the conductivity of the fracture is its hydraulic aperture. Therefore, sliding of a fracture will result to some extent to the increase of the hydraulic aperture and consequently to the increase of the hydraulic transmissivity.

1.2 Fault zones

Accordingly to the concept of failure and rupture described in the previous section, considering larger scales, fault systems are the best example of failure and localization offering highly complex structures at various scales. Faults in the Earth crust are well known to control a wide range of crustal processes by significantly influencing the crust's mechanical and fluid flow properties [Faulkner et al., 2010]. Faults initiate as a result of extensional and compressional forces mainly caused by plate tectonics [Hantschel & Kauerauf, 2009]. They are distinguished in several categories regarding the relative movement of the opposite compartments of a fault. The main fault types are the normal, the reverse, the strike slip and the mixed mode fault. The fault type is a result of the stress conditions as shown in Figure 1.2.

It is undoubtedly accepted that fault zones are characterized by spatial variability in terms of structure and consequently in terms of properties. Numerous studies have proven that fault zones are composed by different components, the fault core where the majority of the strain is localized and the damage zone surrounding the fault core that is related to the growth of the fault zone (Faulkner et al. [2010] and references therein). The damage zone acts as the transition zone between the fault core and the host rock. This conceptual fault zone model can be seen in Figure 1.3.

The variability of the fault's hydro-mechanical properties is also evolving over geological time and has been evidenced to evolve for periods of time corresponding to certain industrial activities.

Different factors determine the internal structure of a fault zone which are related to the depth of the formation, the protolith, the tectonic environment, the displacement magnitude and the fluid flow [Faulkner et al., 2010].

Therefore, three aspects should inevitably be considered in the analysis of the response of a fault zone, the fault zone structure, the mechanics and the fluid flow properties. The interdependence of these three factors is indisputable and their coupled effect needs to be accounted for when analyzing the response of a

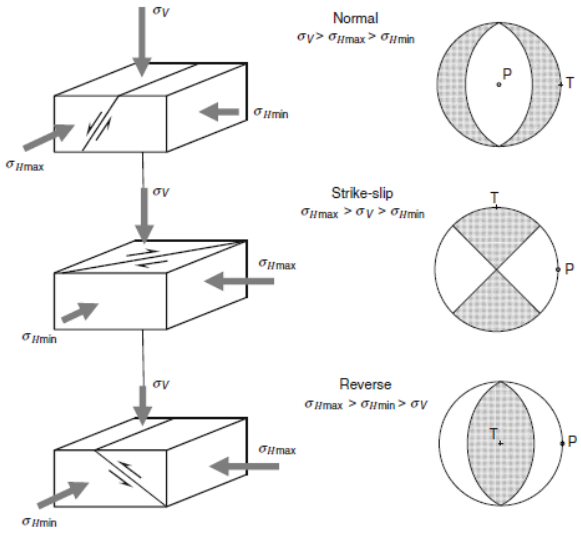

Figure 1.2: Anderson's classification scheme of stress in the Earth's crust (left) and corresponding faulting regimes (right). The focal mechanisms with the P and T axes are shown in the lower-hemisphere equal-area projection [Vavryčuk, 2014]).

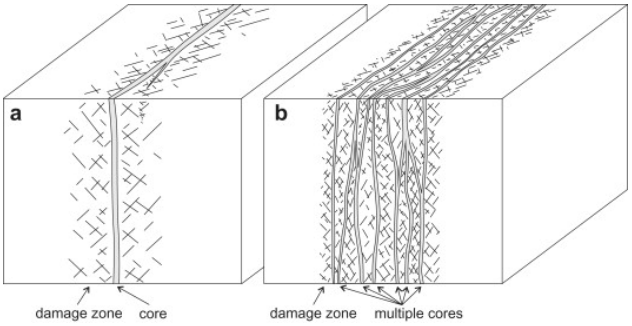

Figure 1.3: Typical representation of fault zone structures with a single (a) or multiple fault cores (b) (after Faulkner et al. [2010].

fault system (see Figure 1.4). Fluid pressures induce changes expressed in fluid-rock interaction processes as well as effective stress variations. On the other hand, deformation can induce changes on fluid pressure distribution.

As discussed in the Introduction, the crucial role of the presence of faults is a key point in a number of applications. In sedimentary basins, faults dramatically influence the hydrocarbon migration, accumulation and leakage [Faulkner et al., 2010]. In such contexts, it is of great importance to evaluate the fluid properties of the fault both spatially and temporally. Based on the aforementioned, it is impossible to define fault zones as conductive or sealing systems. Fault zones can potentially act as barriers, conduits or mixed conduit/barrier systems [Caine et al., 1996]. Based on the fault structure model (Figure 1.3), permeability models of fault zones usually includes a low permeable fault core preventing fluid flow across the fault and a more permeable damage zone facilitating flow along the fault as illustrated in Figure 1.5. The fault core that is known to consist of gouge, cataclasite or ultracataclasite or a combination of these usually acts as a flow barrier while the permeability in the damage zone that consists of fractures at differ-

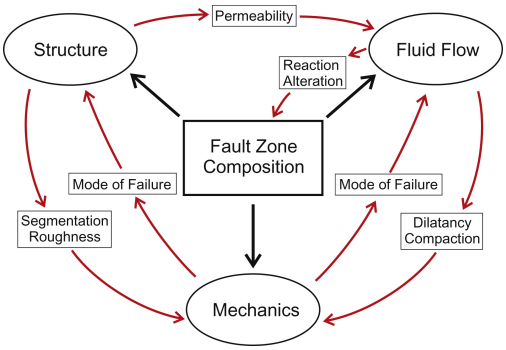

Figure 1.4: Flow diagram showing inter-relationships among the three main topics of structure, mechanics and fluid flow. Mode of failure refers to whether or not seismic slip occurs [Faulkner et al., 2010].

ent scales and subsidiary faults is expected to be fracture controlled with the hydraulic aperture of these structures being an important factor. The aperture of fractures and subsidiary faults is mainly controlled by their orientation with respect to the current stress field and their infill material.

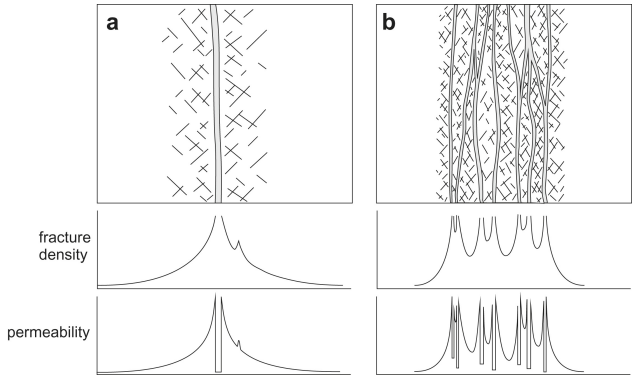

Figure 1.5: Some physical properties of fault zones related to their structure (damage zone and fault core). (a) Single fault core and (b) multiple fault core, which illustrates the resulting complexity in characterizing the resultant properties [Faulkner et al., 2010].

1.3 Fault zones in shale formations

Focusing on the behavior of fault systems in shale formations, there are several aspects pointing out their particularity in clay-rich environments such as shale. Shale is one of the most ubiquitous sedimentary rock types in the earth crust together with sandstone and limestone. It is the most abundant out of the three types and estimates of the proportion of shale in the sedimentary rock column range from 50-70% while sandstone is thought to account for 20-30%, and the remaining small part of the column, is limestone [Jonas, 1977]. Shales are generally recognized as fine-grained, indurated sedimentary rocks with finely laminated structure related to the orientation of micaceous clay mineral constituents [Jonas, 1977]. Illite, kaolinite, montmorillonite or smectite and chlorite are common clay minerals within the clay size range with illite being the most abundant one. Quartz, feldspars or calcite can also be found in sedimentary rocks classified as shales. Keeping this in mind, a number of physical properties of shales are expected to

depend on the behavior and amount of the clay minerals. The role of clay minerals is crucial in a number of applications due to their complex properties. They are believed to play a key role when considering nuclear waste disposal in low permeability media, frictional sliding along weak faults or fluid flow regime and migration processes in complex basin systems. In the oil and gas industry, recognizing and characterizing clay minerals can provide useful information related to basin tectonic evolution, depositional environments, thermal history and maturation, history of organic matter in the source rock, hydrocarbon generation, migration and accumulation process, diagenetic history and reservoir quality prediction [Jiang, 2012]. The presence or not of specific clay minerals at different depths as a result of diagenesis and mineral alterations has been found to influence the hydro-mechanical properties of shales. Clay minerals and organic matters usually co-exist in sedimentary rocks as organic-rich muds not only contain particulate organic matter dispersed within them but they also have organic molecules adsorbed to the surfaces which can potentially converted into petroleum hydrocarbons [Jonas, 1977].

Therefore, in a sedimentary basin system, shales can be identified as source rocks, they can form caprocks to conventional traps due to their extremely low permeability or finally they can be found as reservoir rocks (unconventional tight gas reservoirs). As caprocks, even though shales are considered as seals trapping hydrocarbons in the reservoirs below, the seal integrity can be questioned by overpressure formation or the presence of preexisting fractures or fault zones. Even if the matrix permeability is very low, localized fluid pathways can influence dramatically the bulk permeability of the system and dominate the fluid flow regime. Caprocks and faults seal capacities and their potential impact on the fluid migration can be characterized on the basis of geochemical or geomechanical formulations [Jones & Hillis, 2003; Mildren et al., 2004]. If dissolution, mineralization or diffusion processes may play a long term role on the seal capacity of shale rocks, the stress environment related to the possible over-pressurization of the fluid can dramatically increase the permeability in a short time scale [Finkbeiner et al., 2001]. Quantifying the contribution of the in-situ stress state to permeability changes, while considering the fluid pressure, implies that there is a minimum knowledge available on hydro-mechanical properties of the geological structures, which includes the characterization of the present inherited fracture sets or the presence of faults. The type of mechanical instabilities that may be responsible of these fluid leakages in caprock formation can be listed as follow [Shukla et al., 2010]:

- Shear or open failure of the intact but generally stratified caprock,
- Reactivation of inherited fracture or joint sets present within the caprock layer,
- Reactivation of fault zones present inside or crossing the caprock.

Focusing on the last point, when referring to the fault sealing capacity, it is vital to make the difference between the permeability across and along the fault. As mentioned in the Introduction, the sealing capacity of a fault in the sense of supporting a pressure difference between its two sides results from a reservoir/non-reservoir juxtaposition or from the development of fault rock characterized by high entry pressure [Yielding et al., 1997]. This concept concerns the permeability across the fault assuming that there is no fluid leakage along the fault.

In the reservoir/reservoir juxtaposition case, for a fault to act as a side seal, the developed fault rock has to be rich in phyllosilicates (clay or shale) that are entrained into the fault zone either by shale or clay smearing or abrasional mixing (Faulkner et al. [2010] and references therein). Depending on the dominant mechanism, different approaches exist aiming at estimating the composition of the fault zone. Clay or

shale smearing depends on a number of factors that include the thickness of the source rock layer, the distance from the source layer, and the fault throw [Yielding et al., 1997]. The approaches that predict the continuity or not of the fault smear are the Clay Smear Potential [Weber et al., 1978] and the Shale Smear Factor [Lindsay et al., 1993]. For abrasional mixing mechanism, the Shale Gouge Ratio introduced by Yielding et al. [1997] represents the percentage of clay or shale that might be entrained in the fault zone by taking into account the percentage of clay or shale in the slipped interval.

While the proposed methods concern the prediction of fault leakage across the fault, the present work is focused on the permeability variation along the fault. For a reservoir/non reservoir juxtaposition, if leakage occurs, it is expected to occur mainly along the fault. This usually requires the reactivation of the fault that is evaluated within a geomechanics framework. Keeping in mind the main objective of this work which is the investigation of the conditions under which a fault can be reactivated, leading to a permeability increase and leakage along the fault zone, the following sections mostly cope with the geometrical, stress and fluid pressure conditions and how these control the permeability of a fault or fracture along its structure. Based on the above, the role of the stress environment and of the fluid pressure on the fault permeability is discussed pointing out the need in considering the effect of each parameter separately and in combination.

It should be clarified at this point that in the course of this document, when referring to a fault or a fracture, the author is referring to distinct structures within the fault zone that tend to concentrate deformation and fluid flow and are susceptible of increasing the permeability along the fault zone. Such structures are secondary faults or large scale fractures present in the damage zones, or distinct persistent planes as for example the boundary between the fault core and the damage zone.

1.3.1 Stress and shear-dependent permeability

Shale permeability being very low and capillary entry pressures becoming very high, faults present efficient preferential pathways for the fluids to migrate [Finkbeiner et al., 2001]. The co-existence of low permeable host rock and high permeable structures such as faults or fractures complicates flow analyses which must consider a range of permeability values for argillaceous units depending on the porosity and fracture density [Neuzil, 1994].

The dependency of the permeability of fault rocks and gouges on the effective confining stress has been extensively studied in order to derive relationships correlating the permeability and porosity with depth. In an effort to characterize the fluid flow and mechanical properties of gouge materials Morrow et al. [1984] performed experiments on clay-rich and non-clay gouges measuring the permeability at different confining pressures and at different shear displacements under a given confining pressure. The permeability and porosity reduction that a formation undergoes when subjected to increasing confining pressure is the result of different mechanisms such as micro-crack closure, particle rearrangement and crushing [David et al., 1994]. The results of Morrow et al. [1984] suggest that with the presence of fine-grained gouges and expandable minerals such as montmorillonite, the permeability appears to be very low at the order of $10^{-22}m^2$ at 200 MPa of confining pressure. During shearing of the samples, the low permeability gouges showed little decrease in the permeability mostly at the beginning as a result of compaction at the onset of shearing. The strength curves under drained conditions at 200 MPa confining pressure revealed that the samples without clay supported higher frictional stress compared to any clay sample.

More recent results on permeability measurements of sandstone and silty-shale samples from holes drilled through the Chelungpu fault, Taiwan, point out the importance of the rock type in determining

the permeability of the wall rocks around the fault [Dong et al., 2010]. They showed that the permeability of the silt-shale tested is more sensitive to the changes in the effective confining pressure than that of the sandstone (Figure 1.6) with the permeability of the shales ranging from 10^{-20} to 10^{-15} m^2 for a range of effective confining pressures of 3 to 120 MPa.

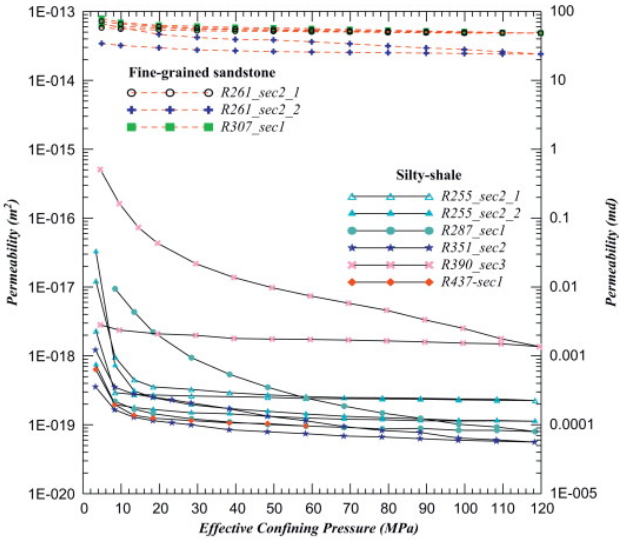

Figure 1.6: Stress dependent permeability of the sandstone and silty-shale, for sandstone (red dashed lines)and silty-shale (solid black lines) [Dong et al., 2010].

While the permeability evolution of sandstone is controlled by the movement of the grains during compaction, the permeability evolution of shale resembles the behavior of low porosity crystalline rocks. In this case, the permeability is more stress-sensitive with micro-crack closure being the dominant mechanism of permeability reduction [Kwon et al., 2004]. Dong et al. [2010] compared their results with the power law stress-permeability relationship proposed by Shi & Wang [1986] and the exponential relationship proposed by David et al. [1994]. The power law stress-permeability (Equation 1.6) and the exponential relationship (Equation 1.7) are expressed as follows:

$$K = K_o(P_e/P_o)^p \tag{1.6}$$

$$K = K_o exp[-\gamma(P_e - P_o)] \tag{1.7}$$

where K is the permeability under the effective confining pressure P_e, K_o represents the permeability under atmospheric pressure P_o and p and γ are material constants. Dong et al. [2010] reported that the results are better fitted using the power law relationship although they pointed out the difficulties in extrapolating the permeability to larger confining pressures.

Considering the other component of a fault zone, the characterization of the damage zone is important in a wide range of applications as the structures involved can provide a potential flow network. It is generally accepted that in low porosity rocks the permeability of the fault damage zone is fracture dominated [Screaton et al., 1995; Balsamo et al., 2010] hence strongly conditioning the permeability of the fault system. Damage zones in fault systems are characterized by fractures at different scales from grain-scale

microfractures to discrete macrofractures and subsidiary faults [Faulkner et al., 2010]. Depending on the type of rock and on the porosity, the damaged zone can offer different characteristics.

In terms of fracture-controlled permeability one has to account for complex hydro-mechanical mechanisms occurring upon the reactivation of even a single fracture. Experimental and numerical studies have pointed out the effect of stress on the transmissivity of a single fracture or a fracture network. From a mechanical point of view, the apertures of fractures can change due to normal stress-induced closures or openings and due to shear stress-induced dilations. Dilation is related to the progressive mismatch of rough surfaces during fault slip, that modifies the flow conducting aperture [Barton et al., 1985; Gentier et al., 2000; Olsson & Barton, 2001].

Fluid flow through fractures decreases with increasing normal stress. Smaller fracture apertures are the result of the progressive fracture closure and the increase in the fracture contact area. Consequently, the connectivity of the fluid flow paths decreases and the flow tortuosity increases [Tsang, 1984].

Under laboratory conditions and considering a single fracture, Gutierrez et al. [2000] studied the permeability of a de-mineralized fracture and its variation by focusing on the consequence of a mechanical closure on the permeability. The permeability of the fracture decreased with increasing effective normal stress without however reaching complete closure (Figure 1.7) as the permeability was found eight orders of magnitude higher than the permeability of the intact shale. It is generally accepted that an apparently "closed" fracture whose surfaces are in contact can still conduct the fluid because of the roughness of the fracture surface providing fluid channels. Shearing of the fracture at constant normal stress was accompanied by positive or negative dilation depending on the applied effective normal stress. At low normal stress levels, when positive dilation was observed, the permeability was enhanced by one order of magnitude. The permeability increase is attributed to the opening of the fracture as the fracture surfaces ride on top of the fracture asperities. In the case of negative dilation, the permeability was decreased by six orders of magnitude due to failure of the asperities and local gouging.

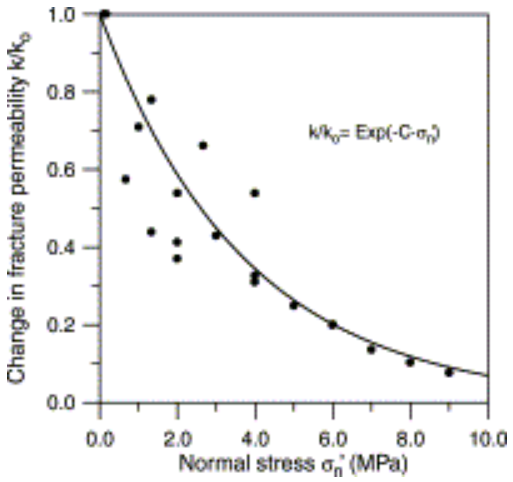

Figure 1.7: Fracture permeability as function of effective normal stress for both loading and unloading [Gutierrez et al., 2000].

Moreover, enhancement of fluid flow anisotropy during active shearing has been reported in experimental studies [Gentier et al., 1997; Auradou et al., 2006; Matsuki et al., 2010; Cuss et al., 2011]. Cuss et al. [2011] performed shear tests on initially smooth and planar fracture in Opalinus clay and investigated the

changes in fracture transmissivity during active shear at a constant normal load and single strain rate. Based on their experiments, they conclude that the fracture transmissivity is also conditioned by the deformation under shear loading where complex patterns may appear. Flow was not uniformly radial even if the fracture was initially smooth and planar and it occurred predominantly along the direction of shear. Dilation was not found to be the dominant mechanism as usually observed or hypothesized. Instead opening flow paths were localized and did not result to bulk dilatancy. However, as mentioned above, in in-situ conditions, the bulk permeability of a fractured rock mass depends not only on the complex evolution of the permeability of a single fracture but also on the distribution, size, connectivity and orientation of preexisting fractures. The bulk permeability of the damage zones can be considered as the equivalent permeability of fracture networks which is in turn determined by the connectivity of the fractures, their orientation with respect to the ambient stress field and their hydraulic aperture distribution. The interest in understanding such natural systems originates from the necessity to characterize coupled properties in fractured rocks. The connectivity of the fractures in the damage zones which is considered as a necessary condition for fluid propagation can be expressed in terms of the percolation threshold. The percolation threshold is defined as the density of fractures above which the connectivity of fractures is sufficient to permit flow through at least a portion of the network, from one side of a domain to the other [Berkowitz, 2002]. However, even if the condition of fracture connectivity is satisfied, there are other factors that will define the preferential fluid flow paths as imposed by the orientation of the fractures and their hydromechanical properties. Numerical studies have focused on the stress-dependent equivalent permeability of a fracture network [Zhang & Sanderson, 1996; Min et al., 2004]. Min et al. [2004] performed numerical experiments on 2D fracture networks underlining the importance of the orientation of the fractures with respect to the stress field. Due to the difference in local stresses acting along and across the fractures, Min et al. [2004] concluded that permeability enhancement, localization and clustering of the fluid flow is the result of shear-induced dilation along critically oriented fractures under increasing differential stresses (Figure 1.8). Taking into account the fluid anisotropy that occurs at the fracture scale as well as at the network scale, Dreuzy et al. [2012] proposed a flow model incorporating the combined effect of fracture scale heterogeneity and network topology on the equivalent permeability of a fractured medium. Their results show that there is a significant coupling between the heterogeneities at the fracture scale and the heterogeneities at the network scale.

1.3.2 Fluid pressure-dependent permeability

The influence of the fluid pressure on the mechanical stability of faults in sedimentary basins has been long known [Hubbert & Rubey, 1959; Sibson, 1990; Byerlee, 1990]. It has been shown that these heterogeneous structures, generally considered as fluid barriers can however, modify the hydraulic properties under certain stress and pressure conditions [Wiprut & Zoback, 2000; Hooker et al., 2011]. Pore pressure is defined as the measurable pressure value in the pore fluid and it is mainly caused by the overburden weight, but fluid flow together with compaction can decrease the overburden induced pressure and the resulting pore pressure is usually smaller than the lithostatic pressure [Hantschel & Kauerauf, 2009]. Even under ideal conditions of compaction, the pore pressure does not reduce to zero and is equal to the weight of the overlaying water column. This is called the hydrostatic pressure and it is generally defined as the part of the pore pressure that does not contribute to water flow. Several processes such as overburden load together with mechanical under–compaction, cementation and fluid expansion processes (e.g. gas

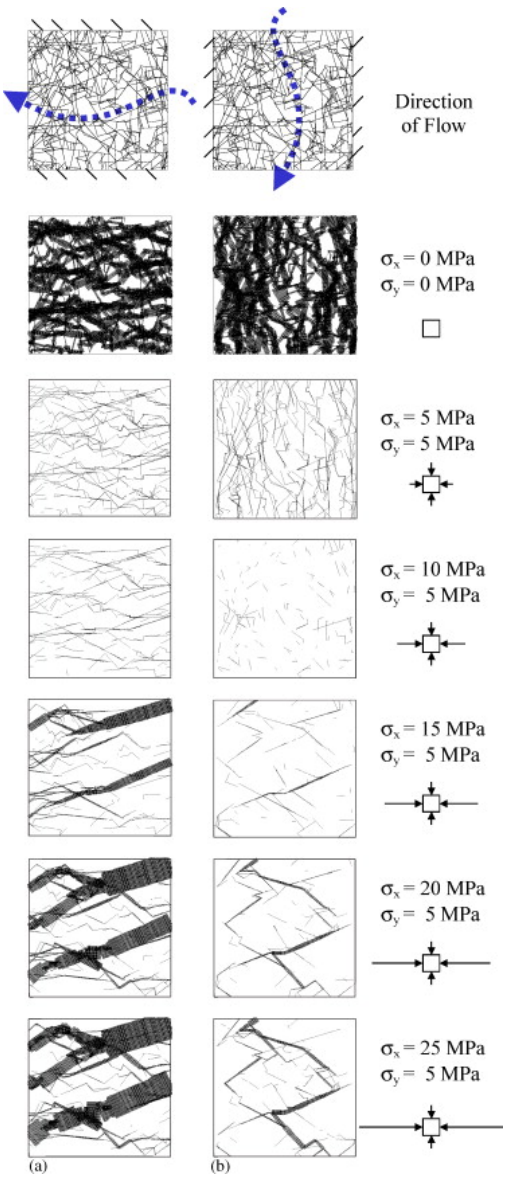

Figure 1.8: Fluid pathways during stress applications with the direction of hydraulic pressure gradient (a) from right to left, (b) from top to bottom. Thickness of the line represents the magnitude of flow rates [Min et al., 2004].

generation) cause overpressure build up which directly controls water flow. Given the pore pressure value at a specific depth, the difference between this value and the lithostatic pressure (overburden) is equal to the effective stress while the difference between this value and the hydrostatic pressure is the overpressure.

Common in sedimentary basins, the fluid pressure increases with depth approaching sometimes the lithostatic pressure for the reasons stated above. In such systems faults have been known to control the distribution of the fluid pressure. In the case of a fault cutting across a suprahydrostatic gradient, fault rupture may open a permeability barrier and allow episodic fluid discharge and a local reversion towards a hydrostatic fluid pressure gradient.

In the seismogenic upper crust, the shear resistance and stability of fault surfaces is expressed by

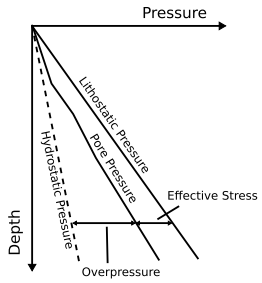

Figure 1.9: Schematic view of a pore pressure profile vs depth, bounded between the hydrostatic and the lithostatic pressure.

Equation 1.1 in terms of effective stress (see Equation 1.2). It can be understood that fault instability may result from an increase of the shear stress (τ) due to elastic strain accumulation, from a decrease in the normal stress (σ_n) or from an increase in the fluid pressure (P_f) leading to a reduction of the effective normal stress (σ'_n). Faults that are favorably oriented for reactivation are the ones that remain close to the Andersonian trends depending on the ambient stress field. For unfavorably oriented fault surfaces, reactivation would originate from very elevated fluid pressure values approaching the minimum total stress value and resulting in a mode I reactivation.

As it has been already mentioned, given the complex structure of faults, they can behave either as a permeable conduits for fluid flow or as impermeable barriers or as a combination of both. This has led to the consideration of the "fault-valve" model [Sibson et al., 1988; Sibson, 1990, 1992] according to which the fault although impermeable can act as a conduit under specific conditions mainly controlled by the fluid pressure. The conditions favoring the fault-valve behavior are related to the ambient stress state, the fluid pressure and the orientation of the fault. The fault-valve activity depends on the ability of faults to behave as impermeable seals in the interseismic period, but to form highly permeable pathways for fluid flow immediately post-failure as a consequence of the inherent roughness of natural rupture surfaces (dilation mechanism). The fault-valve cycle therefore includes pressure build-up, frictional reactivation of critically oriented shear surfaces, permeability increase and subsequent sealing of the reactivated surfaces and decrease in the permeability until the pressure builds up again. Fluid pressure fluctuations during faulting are evidenced by the presence of vein systems within fault zones [Cox, 1995; Lefèvre et al., 2016] that provide information about the temporal evolution of the fluid flow properties and of the deformation mechanisms at different stages of faulting. A necessary condition for fault-valve behavior to occur is that the fault cut across a vertical fluid pressure gradient that exceeds the hydrostatic gradient. Development of such gradients requires the existence of localized or regionally extensive low permeability barriers such as laterally extensive sequences of shales in sedimentary basins.

Figure 1.10 describes the fault-valve model. Given an accumulation of fluid pressure at a specific point of the fault, the failure condition is met and fault reactivation occurs (X-Y). This opens a permeable path for upwards fluid flow from the overpressured zone until the entire hydraulic gradient reverts to hydrostatic or the fault reseals.

Barton et al. [1995] and Barton et al. [1997] introduced the concept of critically stressed faults according to which, critically stressed faults in the upper crust are hydraulically conductive, hence maintaining high crustal permeability [Townend & Zoback, 2000] whereas not critically stressed faults are not hydraulically conductive. This is illustrated in Figure 1.11 where the failure envelopes are taken for friction coefficients,

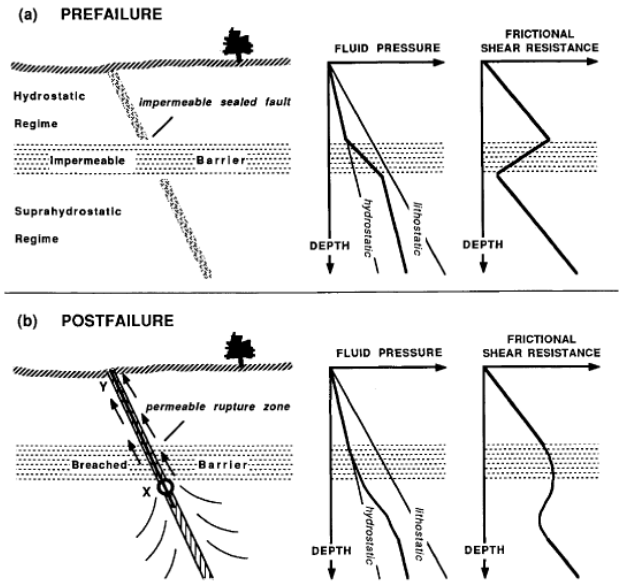

Figure 1.10: Potential for fault-valve behavior (a) Impermeable barrier separating hydrostatic and suprahydrostatic fluid pressure regimes. (b) Breaching of barrier by fault rupture X-Y, leading to an upwards discharge of fluids [Sibson, 1990].

μ equal to 0.6 and 1 according to experimental observations by Byerlee [1978]. It is therefore assumed that the condition for a fault or fracture to be conductive is that the fracture or fault is critically stressed. This raises a question whether the criticality of such structures is a sufficient condition for predicting their permeability variation. However, the interactions between the hydraulic and the mechanical aspects of a fracture reactivation are far more complex.

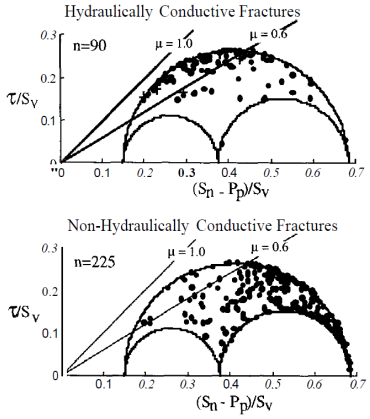

Figure 1.11: Normalized shear stress versus effective normal stress for (a) hydraulically conductive and (b) non-hydraulically conductive fractures, based on precision temperature logs (after Barton et al. [1997]).

Similar to this model, Finkbeiner et al. [2001] proposed the dynamic capacity model based on the knowledge of in-situ stress data and pore pressure measurements, suggesting two dynamic mechanisms responsible for petroleum migration in sedimentary basins by enhanced fracture permeability. These mechanisms are hydraulic fracturing and flow along active shear fractures.

In the context of alternating sand/shale layers sequence, a necessary condition for these mechanisms to occur is for the pore pressure in the sand to be higher than in the overlying shale. Depending on the value of the pore pressure at the top of the sand reservoir, fault shear activation or hydraulic fracturing can occur. More specifically, according to what was discussed in Section 1.1, if the pore pressure is equal to the critical pore pressure for Coulomb failure to occur, then fault activation is occurring allowing the migration of the fluids through slip-induced fracture dilation. If the pore pressure is equal to the minimum principal stress then the dominant migration mechanism is hydraulic fracturing. Figure 1.12 summarizes the possible migration scenarios.

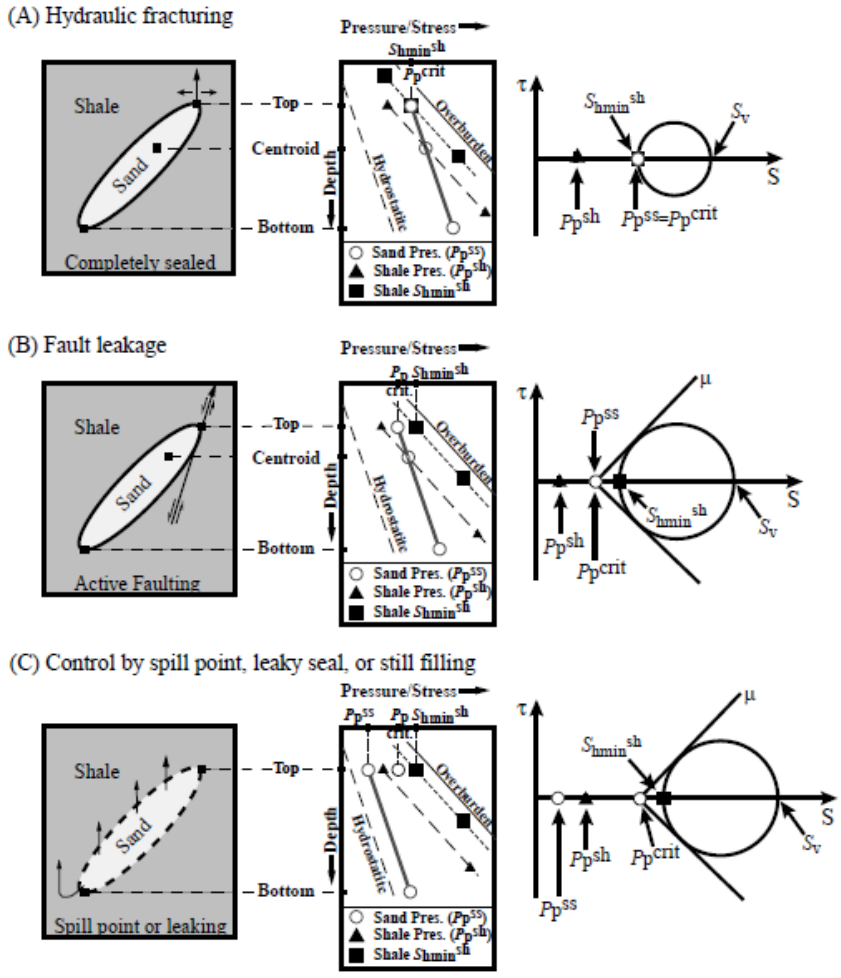

Figure 1.12: The dynamic capacity model (after Finkbeiner et al. [2001]).

The first two cases present a state of dynamic equilibrium in which the pore pressure in the sand has reached a maximum possible value called by the authors the dynamic capacity of the reservoir. Beyond this critical pore pressure, failure occurs, allowing fluids to escape. In the third migration scenario (Figure 1.12C), the reservoir is thought to be in a relatively static state not involving any dynamic failure mechanisms. Finkbeiner et al. [2001] propose that for this third case the sand could still be filling, it could be leaking, or the column height could be spill-point controlled.

The dynamic capacity model has been applied to the controversial case of the severely over-pressured

reservoirs in the South Eugene Island 330 field, Gulf of Mexico [Cooper et al., 1999]. The South Eugene Island (SEI) Block 330 field is located in the Gulf of Mexico under a water depth of 65-85 m, 270 km southwest of New Orleans. This field was chosen as a case study by the GBRN project (Global Basin Research Network), to better understand the hydrocarbon migration mechanism up-fault from deep geo-pressured reservoirs with the possibility to identify these pathways. The specific site was particularly chosen due to the abundant evidence of long-distance vertical migration over a very short period of time (0.5 My approximately). The field was discovered in 1971 and put in production in 1972 and 258 wells (exploration and production) had been drilled in 1988, which provided a consequent sources of information. The field consists in 25 sandy fluvio-deltaic Pleistocene levels compartmentalized by faults. The reservoirs overly 600 m of shales themselves covering geo-pressured turbidites and the prograding deposits are in transition zone and the coastal levels hydrostatic. Production at the oil field, deep in the Gulf of Mexico off the coast of Louisiana, was supposed to decline rapidly but after a while it produced again [Cooper et al., 1999]. The source of additional oil was analyzed as migrating through faults from deeper and older formations below.

Based on the aforementioned, Finkbeiner et al. [2001] proposed that this fluid migration could be related to a hydraulic fracturing processes, i.e. the fluid pressure reaches the minimum in-situ stress value as well as shear fracture reactivation, i.e., when the fluid pressure reaches a value which correspond to the critical effective stress. This model suggests a direct relationship between an irreversible mechanical behavior of the fault to its substantial variation of permeability. Several authors consider also that this migration of the fluid is possible because the fault system in block 330 is considered as active [Holland et al., 1990] and fluid migration would only occur along the fault itself from deep accumulations. A possible cycle that involves fluid pressure buildup, tectonic slip, fluid transport, and ultimately, draining of the fault could take place [Losh et al., 2002], reminiscing the fault-valve behavior described above. However, there is no strong evidence of frequent tectonic slips along the fault and since clayed rocks are present, these ones should be aseismic [Losh & Haney, 2006].

Revil & Cathles [2002] have proposed a fluid transport mechanism based on the propagation of pressure solitary waves first introduced by Rice [1992]. They support that the fluids have transiently channeled along the fault plane through the propagation of solitary waves presenting an efficient mechanism for rapid fluid transfer through the sedimentary column. Based on this mechanism, permeability depends only on the effective pressure without considering the significance of shear stress or strain. These solitary waves are assumed to be accompanied by dilatancy of the fault plane and a significant permeability increase through the formation of a highly permeable conduit of 600 mD approximately in the fault zone. It indicates the existence of faults acting both as boundaries between pressured compartments and as vertical fluid migration conduits. This has been reported from direct pressure measurements that a fault system in the SEI block 330 acts as a lateral permeability barrier supporting 5-10 MPa of pore fluid overpressure between the two compartments observed on both sides [Hart et al., 1995]. This transport mechanism implies that the fast propagation of solitary waves does not interact significantly with the surrounding compartments.

In a different context, observations show that fluids are channeled through low angle decollement zones and thrust faults in accreationary complexes. Hydrogeologic tests at the Oregon accretionary prism revealed some information regarding fluid flow along a hydrogeologically active thrust fault [Screaton et al., 1995]. Screaton et al. [1995] suggested that the observed increase in transmissivity is better explained by the dilation of the fractures of the fault zone. In the decollement zone at the Barbados accretionary

wedge, the measured bulk permeability at specific locations appeared to be fluid pressure-dependent and increase significantly for fluid pressures well below the lithostatic pressure [Fisher & Zwart, 1997]. Results from a two-well test performed at the same decollement zone indicate higher permeabilities at lower in-situ pressures which appear to be sufficient to focus fluid expulsion along the decollement zone [Screaton et al., 2000]. The mechanism of solitary waves propagation has been also used to describe the fluid transport along the decollement zone of the Barbados accretionary prism [Henry, 2000]. More specifically, Henry [2000] stated that at certain locations, the pressures measured in-situ were not sufficient to promote sliding along the decollement zone except if the friction of the zone is supposed to be very low. Therefore, it is possible that sliding occurs mostly during transient increases in pore pressure. Bourlange & Henry [2007] revisited the mechanical significance of the pressure surges for the Nankai wedge site and their influence on the seismic/aseismic response and decollement propagation.

Considering either of the models, a question rises regarding the mechanical significance of the mechanisms proposed by Finkbeiner et al. [2001] and Revil & Cathles [2002] regarding the South Eugene Island field or the hypothesized episodic fluid flow within the accretionary prisms. The question focuses on the fact that the mechanical and hydraulic thresholds along the fault zone might not coincide. This implies that a sub-critical significant permeability increase could be envisaged that will not be accompanied by an instability along the fault. The fault responses observed in the South Eugene Island field as well as on the accretionary wedge decollements could be the consequence of a subcritical permeability increase. Recent field studies suggest that sub-critical mechanical criterion may explain why the permeability of a fault zone can reach the milli-Darcy range when increasing the fluid pressure, while the mechanical response exhibit a reversible behavior or has not reached the critical Coulomb stress. For example, in the Mont Terri clay-rich fault zone experimental results suggest that it is possible that fault leakage could occur before or without reactivation [Guglielmi et al., 2016]. In addition, in-situ field injections in different compartments of a fault zone in the Tournemire massif show a significant reversible part of the deformation measured simultaneously to the fault reactivation and permeability increase [Guglielmi et al., 2015b].

1.3.3 Fracture interaction upon fluid pressurization

To evaluate the effect of fluid pressurization on the reactivation and permeability evolution of natural structures, efforts of the scientific community have focused on the properties and the hydro-mechanical response of fracture networks and preexisting discontinuities due to the increasing exploitation of tight shale gas. In unconventional hydrocarbon exploitation, hydraulic fracturing is a technique aiming at the permeability enhancement of tight reservoir formations where fluid is injected at a pressure whose value is close to the minimum horizontal stress in order to create new fractures that will serve as pathways facilitating the hydrocarbons' extraction. Studying the hydraulic fracture-natural fracture interaction can give valuable insight into the interaction mechanisms and the combined effect of the stress field, the fluid pressure and the natural discontinuity's orientation.

Due to the presence of natural discontinuities in shale (e.g. Gale et al. [2014]), an increase in the fluid pressure related to the growth of a hydraulic fracture can affect the reservoir stimulation results by promoting reactivation and interaction mechanisms that might as well lead to the enhancement of the productivity [Riahi & Damjanac, 2013]. Indeed, the interpretation of field microseismic events occurring during hydraulic fracturing [Van Der Baan et al., 2013; Zhao et al., 2009; Rutledge & Phillips, 2003] show that such events are in their majority generated by shear failure along natural fracture planes [Nagel et al., 2013].

Based on laboratory tests [Warpinski et al., 1987; Zhou et al., 2008; Fu et al., 2016], three types of interactions between a fluid – driven fracture and a natural fracture are reported. Depending on a number of parameters, the hydraulic fracture can cross the natural fracture or it can be stopped by the natural fracture either by dilation and hydraulic activation or by shear slip along the natural fracture. The natural discontinuity could be a pre-existing natural fracture of a reservoir, a natural fracture in the damaged zone of a fault system or planes of weakness such as bedding planes or interfaces separating media of different mechanical and physical properties.

Microseismic imaging of hydraulic fractures is a useful tool to assess hydraulic fracture geometry, i.e. its height, length, orientation [Maxwell et al., 2011] as well as, especially in the case of shales, the interactions between hydraulic fractures and natural ones [Warpinski et al., 2012]. However, induced microseismicity is not enough to image the stimulation volume since pore pressure perturbations may promote both seismic and/or aseismic motions [Cornet, 2016] with the induced slip not necessarily being the source of instability [Khazaei et al., 2016].

A number of theoretical studies [Liu et al., 2015; Chuprakov et al., 2014; Gu et al., 2012] and numerical approaches have focused on the problem of the interaction between a fluid induced fracture and preexisting discontinuities [Yaghoubi & Zoback, 2012; Grasselli et al., 2015; Damjanac & Cundall, 2016; Daneshy, 2016; Khoei et al., 2016; Papachristos, 2017]. Regarding the response of a natural fracture under the effect of a hydraulic fracture growth, different mechanisms can occur depending mainly on the stress field, the orientation of the natural fracture with respect to the maximum stress and the material properties. Under certain conditions, the reactivation of a natural discontinuity can be accompanied by a significant permeability enhancement or can be purely mechanical with the fracture exhibiting shear deformation without any slip-induced dilation. Hydraulic loading of a natural discontinuity is complex especially in the vicinity of a hydraulic fracture propagation due to effective stress redistribution and pressure increase. In the case of a fluid driven fracture, the intersected fracture is under the influence of the effective stress field variation before fluid eventually invades the intersected fracture [Yew & Weng, 2014]. According to Nagel et al. [2013], the coupled behavior of a natural fracture under two distinct stress effects needs to be accounted for. The first effect consists in the increase of the total stresses due to the propagation of the hydraulic fracture which tends to eliminate possible shear deformation of the natural fracture. The second effect concerns the decrease of the effective normal stress due to the fluid pressure rise within the natural fracture, favoring shear displacement. In addition, fluid pressure can also change as a result of stress transfer mechanisms when changes in the applied stresses occur [Preisig et al., 2015]. Stress/strain transfer effects have been reported through mesoscale field experiments on well-characterized sites where the deformation of low permeable, rigid, low dip angle structures is controlled by the opening by a few microns of the surrounding highly permeable sub-faults [Guglielmi et al., 2008].

The hydraulic fracturing context appears as a suitable problem in order to study the combined effect of fractures interaction, orientation, stress and fluid pressure on the reactivation of a natural discontinuity. According to the above, further numerical modeling is needed in order to better capture and understand aseismic deformation and the associated permeability change and explore whether a mechanical activation of a discontinuity implies its permeability change and vice versa.

1.4 Induced seismicity and hydro-mechanical response

Similarly to what was discussed in section 1.3.3, fluid pressurization is considered to play a key role in a number of applications including seismicity related problems. Recently, a number of studies have focused on the induced seismicity related to anthropogenic activities. Such activities concern impoundment of reservoirs, surface and underground mining withdrawal of fluids and gas from the subsurface and injection of fluids into underground formations [Ellsworth, 2013]. Regarding the applications where fluid is injected into a targeted formation, the most common among these are the hydraulic fracturing technique, the waste water disposal associated with stimulation and production, the injection of water to develop an enhanced geothermal system and the geological carbon storage. During fluid injection, it is understood that pore pressure perturbations are occurring within the targeted part of the formation.

With the recent increase of the seismic activity within the Central and Eastern United States, it has been observed that a number of these earthquakes have occurred in areas where specific types of nearby industrial activities raise the possibility that these events were induced by human activity [Ellsworth, 2013]. For most of the earthquakes recorded, several authors have proposed that the mechanism associated with the induced seismicity consists in the reactivation of nearby critically oriented structures such as faults [Ellsworth, 2013; van der Elst et al., 2013; Davies et al., 2013; Keranen et al., 2014; McGarr et al., 2015] due to the increase in the fluid pressure especially during waste water disposal. Based on the Coulomb criterion and on the Terzaghi effective stress formulation (Equations 1.1 and 1.2), a fluid pressure increase along a critically oriented fault with respect to the ambient stress field will result in a decrease in the effective stress and the sliding of the fault surfaces.

Hydro-mechanical fault reactivation is a well recognized consequence of anthropogenic fluid injections. However the probability of an earthquake of significant magnitude ($M \geq 3$) to occur depends on a number of factors including the operational parameters such as the injected volume [McGarr, 2014], the injection pressure and the reservoir conditions. These conditions are related to the pore pressure, the stress field, the presence of pre-existing faults, their orientation and the hydrogeologic regime. Due to the obvious difficulties in constraining the reservoir conditions mentioned, the exact mechanisms responsible for the induced earthquakes are difficult to identify. As mentioned in section 1.3.2, an increase in fluid pressure can induce seismic or aseismic deformations and the observed induced seismicity is not necessarily accompanied by a permeability enhancement of the structure. It is therefore necessary to keep in mind the possibility that a decoupling might occur between the mechanical and the hydraulic response of the discontinuities.

Assuming that the reactivation mechanism and the potential induced seismicity are at a certain extent the result of the increase of the fluid pressure [Nur & Booker, 1972; Zoback & Harjes, 1997], Shapiro et al. [2002] proposed an approach where the spatio-temporal characteristics of the pressure diffusion induced microseismicity are used to characterize hydrocarbon and geothermal reservoirs. They suggested that the spatio-temporal distribution of the microseismicity is controlled by the hydraulic diffusivity of rocks as well as by the distribution and the degree of rock criticality defined as the minimum pore pressure required at a given location to trigger a seismic event [Shapiro et al., 2005]. Examples of rock criticality are critically stressed structures such as faults and fractures close to the injection area.

According to Shapiro et al. [2002], the microseismic events can be characterized on the basis of Biot's equations (1962) at the low frequency range describing the linear relaxation of pore pressure perturbations. In other words, it is assumed that the front of the propagating microseismicity follows a diffusion law as

expressed in the following equation:

$$r_t = \sqrt{4\pi D t} \tag{1.8}$$

where r_t is the distance from the injection point, t is the time from the injection start and D is the scalar hydraulic diffusivity. Hence, if the hydraulic diffusivity value is correctly selected, Equation 1.8 represents the "triggering front" that should correspond to the upper bound of the events' cloud in the plot of their spatio-temporal distribution [Shapiro et al., 2002]. The triggering front concept applied to two case studies is shown in Figure 1.13.

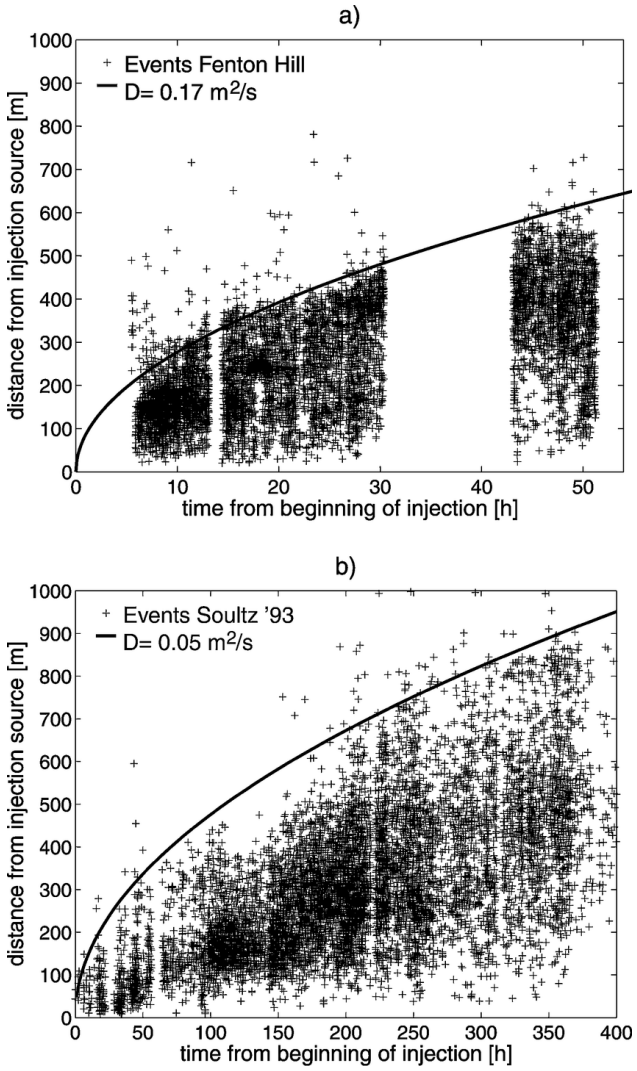

Figure 1.13: Distances of events from the injection source versus their occurrence time for a) the Fenton Hill experiment, 1983 and b) the Soultz-sous-Forets experiment, 1993 [Shapiro et al., 2002].

Microseismicity thus appears as a useful tool for estimating fluid transport properties of reservoirs [Shapiro et al., 2002], but its interpretation in terms of fault diffusivity variations is often delicate [Cornet et al., 1997; Rutledge & Phillips, 2003; Zhao et al., 2009; Van Der Baan et al., 2013]. This is because the signals during fast fault deformations due to fluid flow are not simple, measurements of deformations

being difficult to achieve in fault zones and the source of the seismic waves being complex.

Fluid injection analogue into critically stressed laboratory samples have shown that the injected fluid front and the AE activity can closely correspond, suggesting that the fracture induced damage is associated to the fluid flow for some types of rock [Stanchits et al., 2011; David et al., 2015]. Fault rupture involves such fracture mechanics processes as natural faults display a surface roughness, and must break through sections of rock where they interlock [Lockner, 1993; Lockner & Byerlee, 1993]. Surface roughness induces variations in faults frictional strength that can trigger potentially seismic stick-slip motions [Brace & Byerlee, 1966]. Such frictional slip may also enhance fluid flow anisotropy and alter the fault hydraulic properties through associated dilation or compaction as discussed in section 1.3.1.

Recent in situ fault activation experiments highlighted that fluid injections trigger highly dilatant slip inducing quick and several orders of magnitude increases in fault hydraulic diffusivity associated to magnitude $\sim$-3.5 earthquakes in average [Guglielmi et al., 2015a; De Barros et al., 2016; Duboeuf et al., 2017]. These experiments show a strong aseismic fault strain component in and around the injection point and a complex seismic behavior characterized by diffusion-type pattern of earthquakes coexisting with cluster of events related to stress relaxation effects around localized or "channeled" fluid pressurized zones [Rivet et al., 2016]. At the decameter scale of these experiments, the dispersion in the focal mechanisms solutions highlight that channeling is related to the heterogeneity of the fault zones.

These observations point out the need to properly consider the heterogeneous nature of the fault zones in order to assess and establish links between the hydro-mechanical properties of fault zones and induced seismicity.

1.5 Fault hydro-mechanical modeling

Modeling of the hydro-mechanical fault reactivation can provide information and insight into the reactivation mechanisms and the seismic activity and permeability changes associated with fluid migration or underground fluid injections. Depending on the size of the problem, the scale of observation and the objective of the numerical study, there are different approaches and methods that appear more or less appropriate. While a number of codes exist in the field of rock mechanics for different applications (Rutqvist [2011] and references therein), this section focuses on the studies and existing models regarding fault hydro-mechanical response associated with fault reactivation and fluid propagation. Efforts of the scientific community have focused on the induced seismicity, the leakage potential and seal integrity related to faults in the context of different applications and at different scales.

1.5.1 Mesoscale field injection tests modeling

Field injection tests have proven to be very useful for characterizing the hydro-mechanical properties of fractured rock masses or fault zones. Such insitu tests are usually performed at a medium scale between the laboratory and the reservoir scale and they serve as a bridge between the two scales [Amann et al., 2018]. Hydro-mechanical modeling is a necessary tool in order to interpret the experimental results and better understand the mechanisms associated to the observed response.

A number of studies have focused on the numerical modeling of the field hydro-mechanical experiment at the Coaraze Laboratory Site located in the French Southern Alps aiming at the interpretation of the field data and observations deduced from different loading protocols. The tested site consists of a natural

reservoir ($30\times30\times15$ m) of fractured limestone characterized by highly permeable and well connected fractures (sub-faults and bedding planes) and drained by a spring. Different numerical approaches in two or three dimensions were used and compared for modeling the response of the natural reservoir under different loading protocols.

Modeling of the field tests using a discontinuum approach allowed for simulating fluid flow and deformation coupled processes of discrete fractures embedded in an impervious medium and provided useful information regarding the significant interaction and connectivity mechanisms during the increase and decrease of the pore pressure within a fractured rock mass. On the other hand, using a continuum modeling approach aimed at investigating the effects of leakage into the rock matrix [Cappa et al., 2006].

Cappa et al. [2005] presented the hydro-mechanical modeling of the experiment associated with the longer term pressurization of the studied area. The 2D distinct element code UDEC [Cundall, 1980; Cundall & Hart, 1985] was used and the response of the discontinuities in the model was considered elastic according to a nonlinear relation between the effective normal stress and normal displacement. The rock matrix was considered elastic and impervious. The results showed that there is a strong interaction between the highly permeable and less rigid faults and the low permeability, stiffer bedding planes pointing out the importance of an explicit representation of the discontinuities in the model.

Comparing the different numerical approaches, Cappa et al. [2006] performed a numerical study for simulating a series of pulse tests in a targeted fracture by analyzing the normal displacement-versus-pressure results of the test. The finite element code ROCMAS was used where a few fractures embedded in a permeable rock matrix can be discretized with discontinuity model elements embedded in solid model elements. The results were then compared to the results obtained using the 2D distinct element code UDEC and the 3D code 3DEC [Cundall, 1988; Hart et al., 1988]. Both the rock matrix and the discontinuities were considered linearly elastic. Based on their results, it was concluded that the 3D analysis is more appropriate in order to reproduce the radial flow behavior observed near the well bore. Since both approaches appeared equally suitable for the same set of input data, it was shown that leakage in the rock matrix and poro-elastic effects were not important during the pulse tests. The results in [Cappa et al., 2006] also show that the decreasing pressure path of the test is influenced by mechanical processes within a larger portion of the surrounding rock that need to be accounted for when calibrating the hydro-mechanical properties of the tested fracture.

As an extension of the previous studies, Cappa et al. [2008] explored the influence of the governing flow laws in the analysis of the field data from the pulse tests in terms of pressure-versus-time. Their approach included a hydraulic model used to estimate the flow parameters by either considering a parallel plate flow model (as in the previous studies) or a channeling model as it was experimentally evidenced that flow was channeled within the fracture. A hydro-mechanical model was then used to account for the deformation effect and the presence of contact areas on the hydro-mechanical response. The numerical study from Cappa et al. [2008] showed that channeling is one of the dominant parameters of fluid flow within a fracture. Comparing the hydraulic and the hydro-mechanical simulations results demonstrated that the fracture permeability and storativity are affected by the fracture displacements which are in turn influenced by the amount of contact areas along the plane.

Finally, in an effort to link the pore pressure, strain and seismic data, Guglielmi et al. [2008] used the 3DEC code for modeling the elasto-plastic Coulomb response of the discontinuities and showed that the observed seismicity was the result of shear slip along inherited optimally oriented planes which was initiated by poro-elastic strain transfer from the elastically deformed subfaults.

Field hydro-mechanical tests measuring insitu permeability evolution coupled to fault movement at rupture provide useful insight into the coupled processes associated with fault reactivation within different parts of a fault zone. Recent representative examples are the field injection tests at the underground research laboratories of Mont Terri, Switzerland [Guglielmi et al., 2016; Jeanne et al., 2017a], Tournemire, France [Guglielmi et al., 2015b; De Barros et al., 2016] and Low Noise Underground Laboratory (LSBB), France [Guglielmi et al., 2015a; Duboeuf et al., 2017]. Modeling of the experimental observations of such tests aims at their interpretation by estimating the state of stress, the main reactivated structures according to the slip direction measured and by investigating the main coupling mechanisms associated with the permeability evolution of the fault during rupture.

The Tournemire site consists of the experimental context related to the modeling of the work that follows and is described in details in the next chapter (Chapter 2).

1.5.2 Generic studies at the kilometer scale

At the kilometer scale, a number of publications focus on faults response when subjected to a fluid pressure increase in the context of CO_2 sequestration. More specifically, considerable effort has been put in the modeling of induced seismicity and leakage potential along faults during deep underground injection of CO_2 in order to reduce greenhouse gas emissions to the atmosphere. Targeting sedimentary basins, CO_2 is injected into a permeable sequence, e.g. sandstone that is bounded by a top and bottom impermeable layer, the caprock which usually consists of shale. As it has been already mentioned, the presence of faults in such environments is critical considering the risk associated with fault activation or the leakage potential along the fault that could eventually lead to a contamination of upper aquifers.

Due to the size of the problem that considers the response of reservoirs and associated large discontinuities, hydro-mechanical modeling of such systems has been reported using the continuum modeling approach. The fault zone in these studies, that are in their majority generic, has been represented as an interface, as a multi-zone medium or as a combination of both.

Cappa & Rutqvist [2011b] investigated the interaction between mechanical deformation and fluid flow using the TOUGH-FLAC simulator which is based on linking the TOUGH2 finite volume code for simulating multiphase fluid flow [Pruess et al., 2011] with the FLAC3D finite difference code developed by Itasca [Itasca Consulting Group, 2011] used for solving geomechanical stress-strain equations [Rutqvist et al., 2002; Rutqvist, 2011]. This modeling approach consists of two well-established codes that are sequentially coupled at the course of the simulation. In their study, under fluid pressurization conditions, they compared the response of the fault represented as a zero-thickness interface or as finite-thickness solid elements, with isotropic or anisotropic elasto-plastic constitutive model. Cappa & Rutqvist [2011b] showed that when permeability does not vary as a a function of the deformation, the different mechanical approaches provide similar results. For a finite-thickness elements fault representation, mechanically induced changes were taken into account which can promote the propagation of the rupture zone and enhance leakage in the overlying caprock.

In order to estimate the maximum earthquake magnitude during CO_2 injection Cappa & Rutqvist [2011a] extended their previous study [Cappa & Rutqvist, 2011b] by considering frictional weakening during plasticity. More specifically, Cappa & Rutqvist [2011a] considered a slip-weakening friction model in order to simulate the possibility of seismic slip and to study the distribution and magnitude of fault slip. In the fault weakening behavior, the static friction coefficient of the fault falls to a lower residual value over a critical plastic strain. The parametric study performed by Cappa & Rutqvist [2011a] suggests

that fault slip and rupture width are more sensitive to the horizontal-to-vertical stress ratio and less to the initial fault permeability. Nevertheless, it was shown that for a low permeability of the fault, the initiation of slip is accelerated as the pressure buildup sufficient for failure is reached faster than in a high permeability fault.

While the above studies concern major faults characterized by a large shear offset, Mazzoldi et al. [2012] focuses on estimating the seismic activity and leakage potential of minor faults, possibly not detectable by geological or geophysical surveys. The results of their simulations showed that for different fault permeability and stress ratios, minor faults can act as flow barriers facilitating pressure buildup but without major seismic events.

Based on what was discussed in the previous sections, the properties of natural faults can significantly vary along and across the fault affecting the overall mechanical and hydraulic response. In an effort to take into account these heterogeneities, a number of studies focus on the implementation and significance of the variation and contrast of properties inside the numerical model.

Cappa [2009] proposed a fully coupled thermo-hydro-mechanical model of fluid flow in a vertical fault zone using the finite-difference method. In order to investigate the effect of heterogeneous hydro-mechanical characteristics on fluid transfer and slip processes in and around the fault zone, different fault models were compared by also taking into consideration strain-dependent permeability and porosity. For a heterogeneous fault zone, Cappa [2009] used a representation where in terms of hydraulic properties, the lower permeability and lower Young's modulus fault core is surrounded by higher permeability and higher Young's modulus damage zones. In addition, the host rock is more permeable than the fault core and less permeable than the damage zone and it is characterized by a higher Young's modulus. Cappa [2009] concluded that integrating the fault zone's heterogeneities affects overpressure, stress transfer and mechanical strength changes. In the case of properties contrast within the fault zone, the pressurized zone is concentrated mainly along the fault affecting a larger area as the result of the high permeability damage zones.

As an extension of the study in [Cappa, 2009], Cappa [2011] performed 2D hydro-mechanical simulations in order to examine how the degree of material properties contrast in terms of permeability and rigidity between the fault zone components can influence fault rupture during pressurization. The materials composing the fault zone in the model respond according to an elasto-plastic constitutive model without slip weakening. Inside the fault core which is surrounded by the damage zone, the principal slip zone is represented by an interface with a Coulomb friction law. The damage zone consists of multiple, parallel layers with different hydro-mechanical properties reflecting the heterogeneity of fracture density. The permeability and porosity of the different components is assumed to vary as a function of the volumetric strain. For different hydro-mechanical properties on each side of the fault core, the results from Cappa [2011] suggest that plastic deformation is preferentially localized in the damage zone representing the more permeable and less rigid side of the fault zone due to the reduction of the effective normal stress. Such asymmetric off-fault plastic strain promotes larger slip along the principal slip zone underlying the bimaterial effect associated with the permeability and rigidity contrast.

Accounting for the properties contrast along the fault zone, Jeanne et al. [2014] compared the fault reactivation and fluid propagation of a mature and of an immature fault. According to in-situ observations and measurements made along a seismically active fault zone several kilometers in length and along a minor fault zone a few hundred meters in length, Jeanne et al. [2014] incorporated in a modeling study using TOUGH-FLAC the effects of fault maturity on the fault damage zone heterogeneity. In the immature

fault zone model, the hydro-mechanical properties (permeability and Young's modulus) and size of the damage zone varied depending on the properties of the host rock in the layer while in the mature fault zone model it was assumed that the fault deformation was sufficient to create damage zone connectivity and to eliminate any hydro-mechanical heterogeneity linked to the initial properties of the host rock. Their numerical study shows that while an immature fault zone will favor rupture due to fast focused pressurization in the most permeable and deformable layers, leakage is unlikely to occur because of the heterogeneities along the damage zone. On the other hand, inside a mature fault zone no rupture occurs as the fault is sufficiently permeable but leakage is expected as the fluid can propagate for larger distances.

Seyedi et al. [2015] proposed a coupled pressure-permeability model based on homogenization method by focusing on the permeability of the damage zones. Using the two-scale model, at the fault zone scale, the damage zones are modeled as porous media with statistically distributed fractures and at the site scale, the equivalent fault model consists of a fault core surrounded by equivalent damage zones. Mechanically, the fault core behaves according to an elastic-perfectly plastic constitutive law based on the Drucker-Prager failure criterion. According to the accepted permeability model of the a fault zone mentioned in section 1.2, the permeability assigned to the fault core is lower than the permeability of the damage zones. For the numerical simulations, the `Code_Aster` developed by EDF was used coupled with the TOUGH2 multiphase fluid flow code. The results show that their modeling approach appears reliable for estimating the sustainable injection pressure in order to avoid fault leakage and reactivation.

Based on the modeling studies there are several factors that are considered as key parameters when considering the induced seismicity and leakage potential associated to the reactivation of a fault zone. These parameters include the fault orientation, the ambient stress field and the rock properties [Rutqvist et al., 2016].

1.5.3 Faults in basin scale modeling

At larger scales than the ones described in the previous sections (section 1.5.2 and 1.5.1), the evolution of fault permeability is a crucial parameter for basin modeling while being complicated to properly address. Basin modeling is of great importance for the petroleum industry in exploration and production applications that focus on the evolution of sedimentary basins for targeting oil and gas traps.

Sedimentary basins can be characterized by a thickness of approximately 1 to 15 km and extend laterally over distances of up to 1500 km [Person et al., 1996]. Modeling of the evolution of a sedimentary basin presents some particularities as the simulations span over million of years and very large deformations occur. Therefore, taking into account the spatial and temporal dimensions of the problem, faults represent an important yet complicating factor in representing basin hydrodynamics (Person et al. [1996] and references therein). The representation of faults in a basin scale model is very challenging due to the size of faults that are usually much smaller than the gridcells of the model [Hantschel & Kauerauf, 2009]. While the orientation and location of faults can be introduced as lines (2D) or planes (3D) by boundary elements along cell faces, the hydro-mechanical properties of the fault need to be assigned over a fault volume [Hantschel & Kauerauf, 2009]. In order to properly represent the fault volume, the introduction of locally refined elements around the faults is recommended which nonetheless could also bear a number of difficulties.

The questions that still need to be answered focus on the degree of the fault zone complexity that needs to be taken into account in basin modeling and on the evolution of the permeability as a result of coupled hydro-mechanical processes involving stress, fluid pressure and hydro-mechanical properties.

Chapter 2

Experimental context and methodology

The experimental context of this study is presented in this chapter. The geology of the site where the injection tests were performed is briefly described along with the structural characteristics of the targeted fault zone. Experimental results of the field experiments that were modeled are also presented with special attention paid to the data used for the modeling. Finally, the numerical tool used for the hydromechanical simulations is introduced together with some elements of the general methodology followed in the numerical approach of the problem.

2.1 Tournemire experimental site

The in situ field injection experiments were performed at the Tournemire underground research laboratory (URL) which is located in an old railway tunnel excavated in 1885 and now operated by the French Institute of Radioprotection and Nuclear Safety (IRSN). The main goals of the insitu injection experiments were the determination of the Tournemire fault zone's hydromechanical properties and the understanding of the role of stress, fluid pressure on deformation (slip) on the permeability evolution of the fault zone.

These injection tests were part of the "Fluids and Faults" project which was undertaken in order to constrain and better understand the relationships relating permeability, pressure, stress and strain of fault zones in shale for application to basin and reservoir modeling [Henry et al., 2016]. The project included (i) In situ injection tests performed in Tournemire IRSN underground laboratory (ii) Laboratory experiments on core samples from Tournemire shale at ENS Paris, Université Cergy-Pontoise and (iii) Seismic monitoring of the injection tests lead by Géoazur (UNS) and iv) Numerical modeling of the results obtained from the field injection tests.

2.1.1 Site description and shale properties

Geology and fault structure

The Tournemire URL is located in a Mesozoic marine basin on the southern border of the French Massif Central and at the western limit of the Causse du Larzac. The argillaceous formation where the URL is nested (Figure 2.1) is 250 m thick and corresponds to sub-horizontal consolidated argillaceous and marly layer of Toarcian and Domerian age [Matray et al., 2007]. The argillites and marls are in the form of thin interstratified layers of argillaceous minerals giving the rock mass a naturally anisotropic texture [Rejeb

& Cabrera, 2006]. The experimental station in Tournemire offers ideal conditions for research purposes regarding the storage of radioactive waste in deep geological repositories due to the low permeability and swelling properties of Tournemire shale.

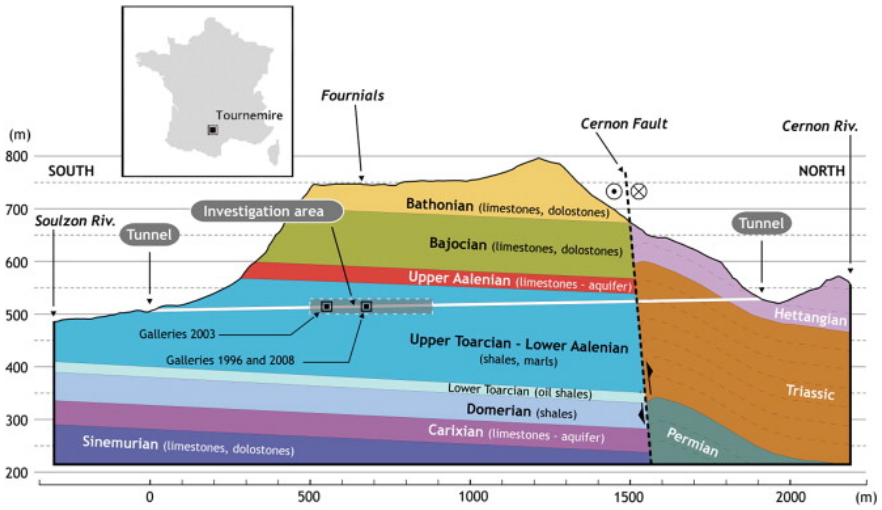

Figure 2.1: Geological cross-section of the Tournemire Underground Research Laboratory showing the location of the investigation area (after Bailly et al. [2014]).

The Tournemire massif is traversed by a kilometric extension fault, the Cernon fault, roughly oriented West-East, and by two faults of hectometric extension, the principal and secondary fault, oriented N170°-180°E (Figure 2.2left). It is the secondary fault cutting through the IRSN tunnel that was studied and instrumented during the insitu field tests. It consists of a strike-slip fault with a reverse component.

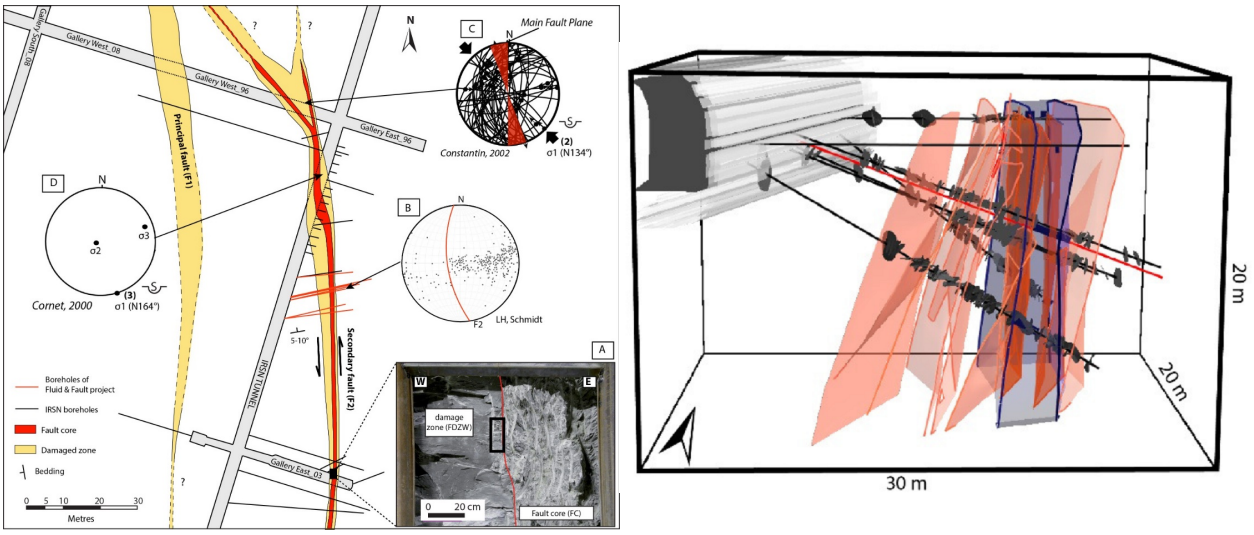

Figure 2.2: Left: IRSN URL structural map showing faults F1 and F2 (after Lefèvre et al. [2016]), right: 3D view of the secondary fault architecture (after Lefèvre [2016]).

A conceptual model proposed by [Lefèvre, 2016] considers that the fault zone contains two domains

of deformation, a damage zone and a fault core separated by the main fault planes (Figure 2.2right). The orientation of the main fault planes that bound the fault core is approximately N150-180°, 60°-80°W. Three main fracture families were distinguished inside the fault zone. The first family consists of structures oriented N150-180°/30-60°W. Fractures of this orientation were found in both the West damage zones (hanging wall) and the East damage zone (foot wall) and estimated to be smaller than 1 m and filled with calcite cement. Subvertical secondary faults are also present in the West damage zone, striking N160-200° (Family 2) extending over several meters showing little or no calcification. Family 3 contains planes with a subhorizontal to 20°N dip that are partially calcified. The hanging wall damage zone is much thicker than the foot wall damage zone, 4.5 m and 1.75 m respectively. The fault core is 2.5 m thick on average and is mainly composed of fault breccia and partially cemented with intact clasts [Lefèvre, 2016].

The present day in situ stress regime was determined through a series of leak-off tests [Cornet, 2000]. The state of stress was estimated as a strike-slip regime with the maximum stress σ_1 being horizontal, oriented N162° $\pm$ 15°E and equal to 4 ± 2 MPa. The intermediate stress σ_2 is equal to 3.8 ± 0.4 MPa and it is the vertical component with a plunge 83-82° and azimuth N072°. σ_3 is the minimum horizontal stress equal to 2.1 ± 1 MPa with a plunge 7-8° and azimuth N072° (see Figure 2.2left).

Tournemire shale

The mineralogical composition of the Tournemire shale consists of 40 to 50% of phyllosilicates mainly smectite, illite, kaolinite, chlorite and mica, 10 to 20% of quartz, 10 to 30% of calcite and 4 to 8% of feldspars [Tremosa et al., 2012].

The shale is characterized by a low porosity, from 8 to 12%, corresponding to a water content of 3.5 to 5% weight at saturation and a hydraulic conductivity of 10^{-14} to 10^{-15} m/s (10^{-21} to 10^{-22} m^2) measured on core samples in the laboratory [Boisson et al., 2001].

Tournemire shales show anisotropic elastic and strength properties. The elastic properties are summarized in Table 2.1 [Rejeb & Cabrera, 2006]. The elastic response of Tournemire shales could be approximated by a transversely isotropic material with a plane of isotropy that corresponds to the bedding plane. The elastic properties are then defined for the directions normal and parallel to the bedding plane.

Young's modulus parallel to bedding	E_1	27.68 GPa
Young's modulus normal to bedding	E_2	9.27 GPa
Poisson ratio parallel to bedding	ν_1	0.17
Poisson ratio normal to bedding	ν_2	0.2
Shear modulus	G_{12}	3.94 GPa

Table 2.1: Elastic properties of the Tournemire shale [Rejeb & Cabrera, 2006].

Strength anisotropy of Tournemire shale was also observed in recent laboratory experiments [Bonnelye et al., 2017]. The bedding orientation is strongly influencing the peak stress with the orientation of 45° with respect to the maximum stress being the weakest and 90° the strongest.

2.1.2 In-situ injection tests-Results

The experiment zone was densely instrumented through the boreholes from the URL gallery as shown in Figure 2.3. The injection experiments and the installation of sensors (hydromechanical, seismic and

electric) for near field monitoring required drilling several boreholes across the fault zone which is approximately 8.5 m thick. The injection experiments were performed in a 30 m long and 0.146 m diameter borehole (INJ borehole in Figure 2.3) drilled from the Tournemire tunnel and inclined at 21°E to intersect the fault perpendicularly.

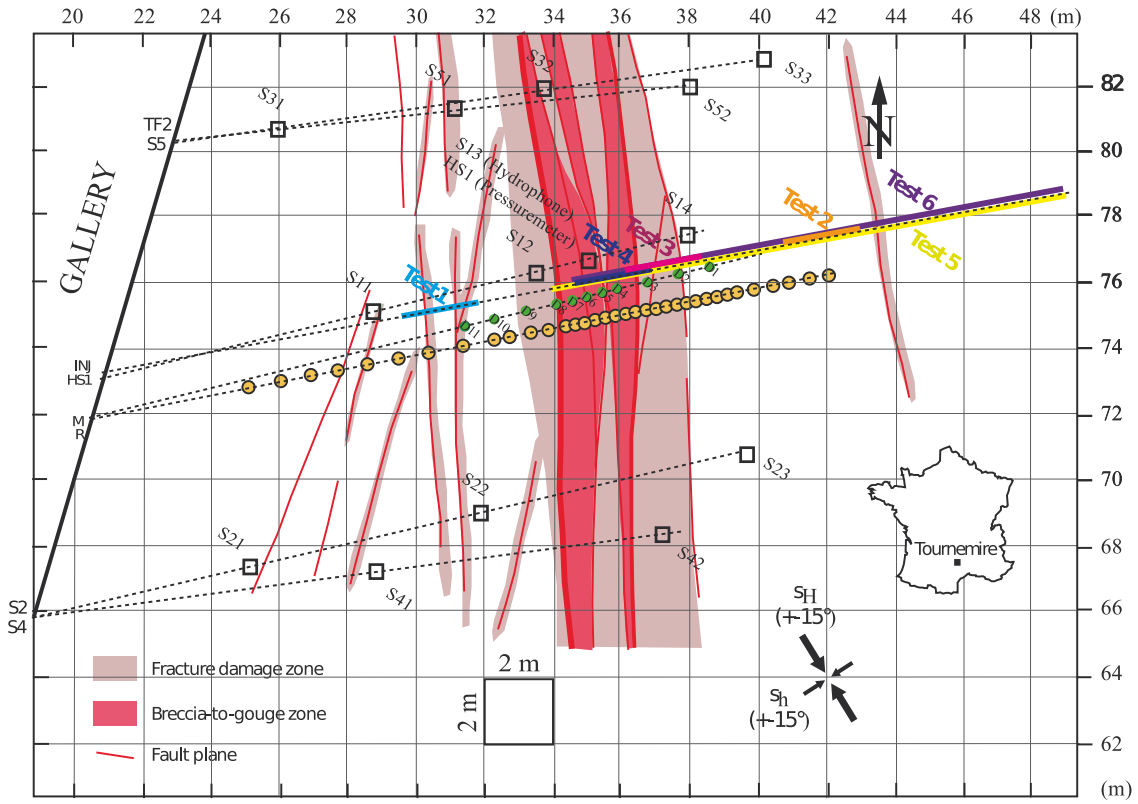

Figure 2.3: Horizontal map view of the instrumented experimental site. The locations of the different tests are shown along the injection borehole with different colors. The orange dots correspond to strain sensors, the green dots to resistivity sensors and squares correspond to accelerometric sensors (modified from De Barros et al. [2016]).

Six hydromechanical tests were performed in total whose locations can be seen in Figure 2.3. Test 1 is performed in the West Damage Zone, Test 2 in the host rock a few meters away from the fault zone, Test 3 is performed in the East Damage Zone and partly in the fault core, Test 4 in the fault core. Tests 5 and 6 were single packer tests and lasted several days. Tests 1-4 were performed using the mHPP probe according to the step-rate injection method for fracture in situ properties (SIMFIP) [Guglielmi et al., 2013]. A 2.4 m injection chamber is isolated by the dual packer system of the probe (Figure 2.4a). The three-dimensional deformation of the targeted fault/fracture intersecting the borehole is captured by an extensometer centered along the axis connecting the two packers (Figure 2.4b). Two steel rings are anchored to the borehole wall on each side of the fracture and they are connected by six deformable steel tubes with varying oblique orientations [Guglielmi et al., 2015b]. The three-dimensional deformation measuring system is able to measure the displacements of the borehole on each side of the tested fracture with an accuracy of 10^{-6} m. Fluid pressure sensors independently monitor pressure variations in the test interval as well as above and below the straddle packer with an accuracy of 0.001 MPa (Figure 2.4a).

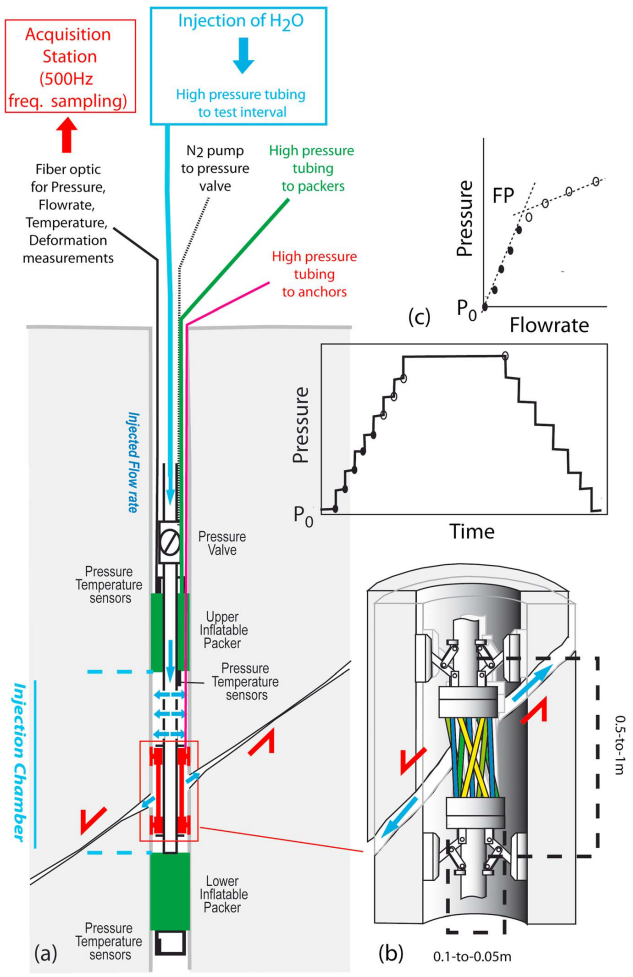

Figure 2.4: (a) SIMFIP test equipment setup. (b) Schematic view of the three-dimensional deformation unit. Tubes are differently colored to show that they display different deformations when there is a relative movement of the rings anchored to the borehole wall across the activated fracture. (c) Typical Step-Rate Test protocol [Guglielmi et al., 2015b].

The step-rate injection protocol was applied to tests 1, 3 and 4 (Figure 2.4c). According to the step-rate injection protocol water is injected at a low pressure for a fixed duration. The injection pressure is incremented and held constant, typically for the same duration. After reaching a threshold pressure, called the Fracture Opening Pressure (FOP), for which a large increase in the flow rate is observed at constant pressure, a longer duration constant pressure step is performed at a pressure above this threshold. Then successive step-down experiments follow until the pressure returns to its initial value.

Test 2 was performed as an Extended Leak Off Test in the host rock (orange interval in Figure 2.3), a method used to estimate the minimum principal stress [Rutqvist et al., 2000; Raaen et al., 2006; Lin et al., 2008]. According to the XLOT protocol, water is pumped in the formation resulting in an increase of the pressure. Different pressure thresholds and information can be obtained from the pressure-versus-time curve. The XLOT protocol together with the pressure thresholds are shown in Figure 2.5.

The leak-off pressure (LOP) is reached when the relationship between pressure increase and volume of fluid pumped becomes nonlinear indicating that the fluid begins to diffuse into the formation at a more

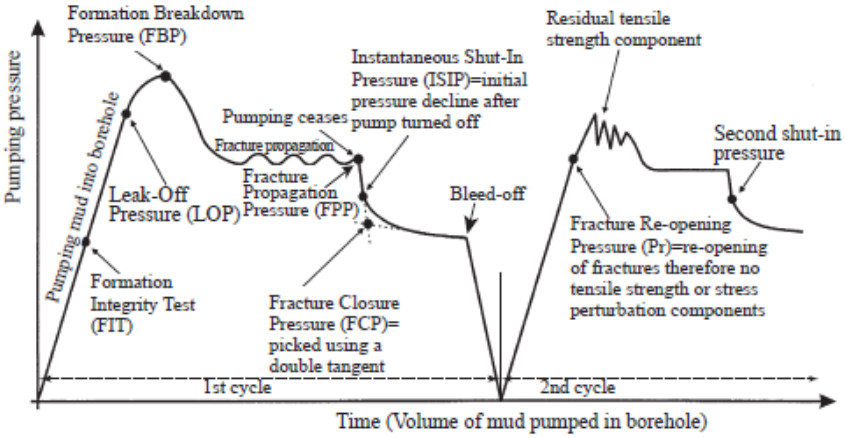

Figure 2.5: Idealized relationship between pumping pressure and time or volume of injected fluid during an XLOT (Lin et al. [2008] and reference therein).

rapid rate. The Formation Breakdown Pressure (FBP) is then reached for which a new fracture is created in the walls of the borehole. This value represents the peak value in the pressure curve. As pumping continues, the pressure stabilizes at a value called the Fracture Propagation Pressure (FPP) where the newly created fractures propagates away from the borehole. Once the pumping ceases, the Instant Shut-In Pressure (ISIP) is recovered as the point where the steep pressure decreases after shut-in deviates from a straight line. Finally, the created fracture closes at the Fracture Closure Pressure (FCP), determined as the intersection point of the two tangents as shown in Figure 2.5. The FCP is assumed to represent the minimum principal stress because the stress in the formation and fluid pressure remaining in the fracture have reached a state of mechanical equilibrium [Lin et al., 2008].

In the present work, the modeling of the tests 1 and 2 is presented in order to explore different concepts and mechanisms involved in the reactivation of a fault zone, keeping in mind the interplay of different factors. The field injection tests of interest are described in the following sections.

Injection test in the West Damage Zone (Test 1)

In Test 1 the reactivated structure was distinguished and it was possible to associate part of the measurements to the hydromechanical response of this particular structure. The geology of Test 1 interval in the West damage zone (blue interval in Figure 2.3) is shown in Figure 2.6. It should be noted that even though an important number of fractures were intersected by the test interval, only the ones that were not completely sealed with calcite are shown as the ones that are more favorable to conduct flow.

An open secondary fault oriented N0-to-170, 75-to-80°W can be distinguished as the black plane between the displacement anchors. The fractures intersected by the borehole interval are mainly located at the eastern compartment of the secondary fault and they display three principal orientations [Guglielmi et al., 2015b]:

- N110-to-140, 50°N-to-S,
- N160, 20-to-40°W,

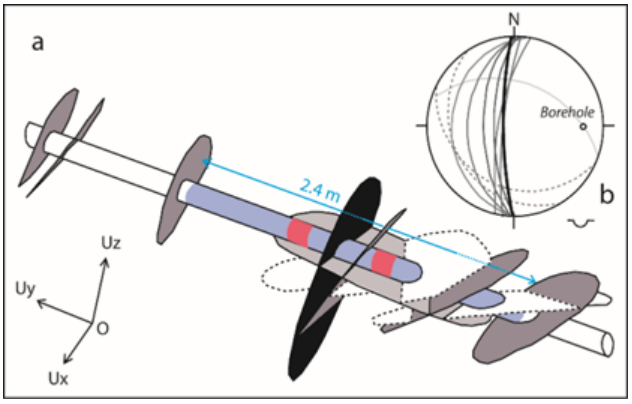

Figure 2.6: Structures distribution along the injection borehole. Injection interval is shown in blue, red intervals correspond to the location of the SIMFIP probe displacement sensor anchors (after Guglielmi et al. [2015b]).

- N0-to-20, 40-to-80°W-to-E.

The fracture families were partially or fully sealed with calcite. The fault main plane is characterized by a polished but striated rough surface that cuts all the other fractures. The injection pressure was progressively increased in a step-wise manner while monitoring the deformation across the fault. The increasing and decreasing pressure steps lasted approximately 60 seconds each. Once the fracture opening pressure was reached, a longer step of 200 seconds was performed at a pressure higher than the FOP. The temporal evolution of the fluid pressure, the flow rate and the displacements (U_x,U_y,U_z) is shown in Figure 2.7 (for more details see Guglielmi et al. [2015b]).

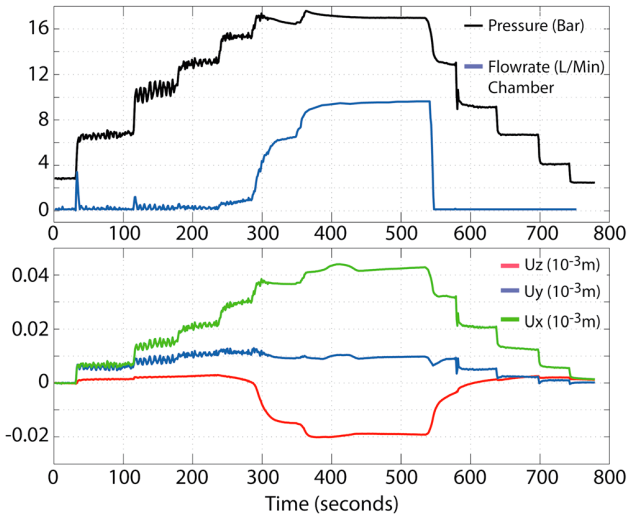

Figure 2.7: Variations of pressure- and flow rate -versus-time (upper graphs), and fault (Ux, Uy, Uz) hanging wall displacement-versus-time (lower graphs) [Guglielmi et al., 2015b].

The flow rate and pressure evolution during the step-rate test (Figure 2.7top) show that before 237 seconds of increasing fluid pressure, there was no flow rate induced by diffusion in the formation. At 237 seconds and for a pressure equal to 1.5 MPa, a large non-linear flow rate increase was observed that

later reached a quasi-constant value (450-537 seconds) before the pressure was gradually decreased. The pressure at which the flow rate exhibited a substantial increase is defined as the Fault Opening Pressure for this test. At the onset of pressure decrease from 1.7 to 1.4 MPa, the flow rate falls abruptly to zero without any further flow injected in the fault for the rest of the injection test.

The mechanical response of the test showed that the induced displacements are characterized by a shear component much larger than the normal component (Figure 2.7bottom). The direction of the displacement components is shown in Figure2.6. The movement of the fault is associated to a left-lateral strike-slip which is in agreement with the direction of the principal stresses as measured by [Cornet, 2000]. The high increase in the flow rate was associated to a predominant normal slip (negative U_z variation) and a small contraction along the borehole axis (negative U_y variation). With the decreasing fluid pressure, the displacements appeared to return to their initial values by the end of the injection. It was observed that there is a high increase in the hydraulic conductivity associated with slip activation and not dilatancy and normal opening of the fault. According to Guglielmi et al. [2015b] it is possible that off-fault hydromechanical processes take place such as opening/closing of localized conduits controlled by the slip along the fault. Moreover, further observations indicated that the water flow was channeled because fluid flow from the injection borehole appeared asymmetric as geophysical anomalies [Rivet et al., 2016], leaking through boreholes and tunnel Excavation Damage Zone, dozen of meters away from the injection point, and some micro-seismicity occurred South of the injection borehole [De Barros et al., 2016].

Modeling of the injection test using a single smooth parallel plate fracture model [Guglielmi et al., 2015b] showed good match for the increasing pressure path of the test but failed to reproduce the reversibility of the displacements and the sudden fall to zero of the flow rate during the pressure decreasing steps. Therefore, further modeling is necessary in order to examine whether fracture interaction and poro-elastic effects can affect the decreasing part of the observed response as described in Chapter 3.

Injection test in the Host Rock (Test 2)

Test 2 was performed in the host rock a few meters away from the fault zone inducing the largest number of seismic events compared to the rest of the injection tests. Although an intact rock zone was targeted by the test, the interval was characterized by two bedding planes N113-to-166 dipping 0-to-10°S and by five fractures N160-to-175 dipping 40-to-65°W. Figure 2.8 shows the geology of the tested interval with the fractures that are not sealed with calcite and thus more favorable to conduct flow. The position of the two displacement anchors is shown in gray and it can be observed that none of the fractures is located between the sensors.

As mentioned above, the injection test 2 followed an extended leak-off test protocol. Six consequent pressure cycles were performed by manual pump as shown in Figure 2.9. During the first cycle (black cycle in Figure 2.9), there appeared to be a first peak of the pressure around 2.5 MPa and a second one at 4.4 MPa. It is possible that the first one corresponded to a first rupture under a stress field around the borehole that is assumed to be disturbed due to the presence of the packers. The peak at 4.4 MPa around $t = 0.74$ hours was more likely to represent the pressure at which the formation broke down (FBP) or a fracture was reactivated in normal or shear mode. For the cycles that followed, this maximum pressure was not reached again but a pressure of 4 MPa indicated for each cycle the pressure at which the newly created or reactivated fracture was propagating (FPP). Below this pressure, there was no water injection in the interval. The last cycle was the longest one maintaining a pressure equal to the FPP for

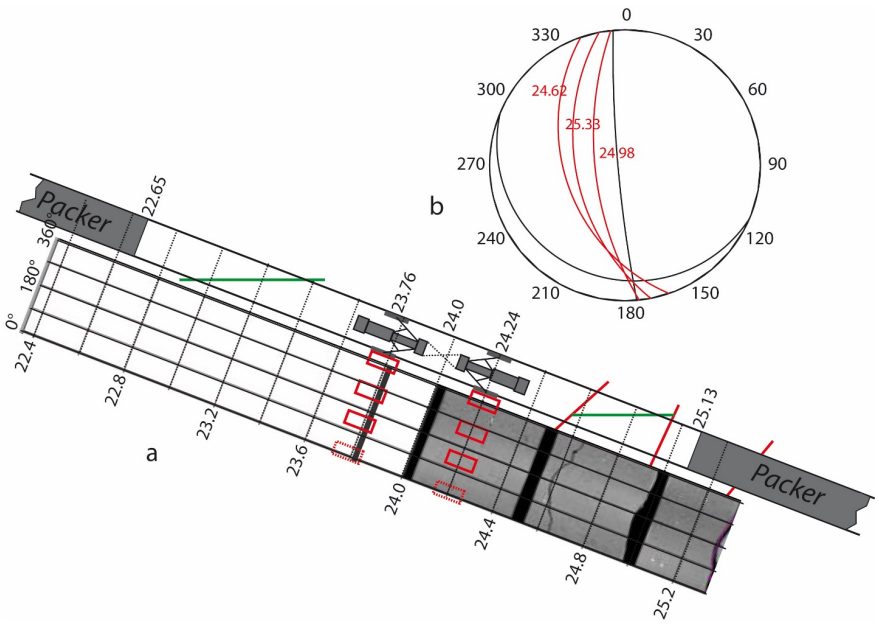

Figure 2.8: Geology of the Test 2 interval in the host rock. Two fractures (red) and two bedding planes (green) are shown as more favorable to conduct flow. The isolating packers and the displacement sensor anchors are also shown.

1000 seconds approximately (magenta cycle in Figure 2.9). This last cycle was long enough to capture a fracture propagation at a pressure of 4 MPa and it corresponded to the highest injected volume. Seismic activity was also recorded during the last cycle.

Interestingly, the maximum pressure attained is equal to 4.4 MPa, a value much higher than the one deduced from Test 1 described above for which the FOP was found equal to 1.5 MPa. This pronounced difference could imply a stress variation across the fault zone from one compartment to the other.

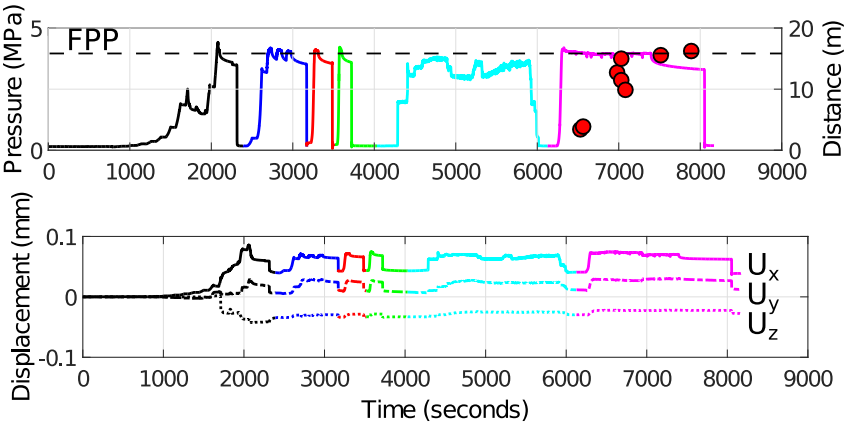

Figure 2.9: Test 2 results. Top: variation of pressure-versus-time, Fracture Propagation Pressure (FPP) and event distance from the injection test-versus-time (modified from De Barros et al. [2016]). Bottom: variation of probe displacements-versus-time.

In terms of displacement, keeping in mind that x axis is pointing to the South, y axis to the East

and z axis Upwards (see also Figure 2.4), the measured movement is mainly towards South-East following the same shape for each cycle apart from the first failure where a deformation towards North-West was measured. The highest irreversible displacement was also observed during this first cycle. For the analyses that follow in the next chapters, the last cycle is considered as the period when the fracture is propagating away from the borehole stress perturbation zone under the "natural" stress state, providing a lot of information on the strength of the reactivated fractures and on the interval's state of stress. The measured movement during the last cycle was associated with the movement of the pre-existing fracture N161°/42°W (red fracture closer to the anchors in Figure 2.8) under a rotated stress tensor and higher in terms of magnitude with respect to the estimated stress state of Test 1 as explained in Chapter 5. More specifically, the deduced stress field was:

- $\sigma_1 = 4.9 \pm 2$ MPa, N188°,
- $\sigma_2 = 4.1 \pm 0.4$ MPa, N72°,
- $\sigma_3 = 3.9 \pm 1$ MPa, N98°.

Interestingly, there were observations evidencing that structures within the fault zone were reactivated during Test 2. Observations from the near field monitoring boreholes showed that the fluid reached fractures in the East damage zone. In addition recorded seismicity during the last cycle (Figure 2.9) and mainly for a fluid pressure above the FPP (4.0 MPa) showed that the events were located 3.5 to 10 m away from the injection close to the fault zone represented by the magenta color layer in Figure 2.10 [De Barros et al., 2016]. The injection chamber for Test 2 is represented as a point (pentagram) in the Figure 2.10 for simplicity and it is taken as the center of the injection interval. Both observations imply a resulting pressurized zone of 10 m towards the fault zone that could be also supported by a flow channeling regime also observed in Test 1.

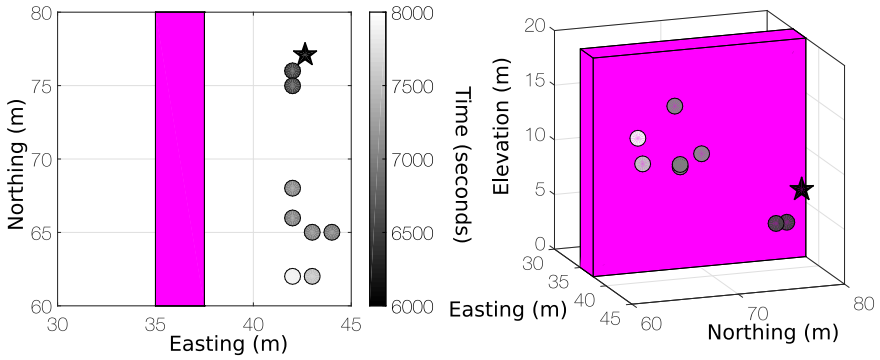

Figure 2.10: Left: map view, right: view from the East of the location of the microseismic events for Test 2 results. The occurrence time of the results is also shown. The position of the center of the injection interval is represented by a star (modified from De Barros et al. [2016]).

The magnitudes of the events were calculated smaller than -3.7 and correspond to a slip of 1 μm and a radius of the slipping zone equal to 0.3 m. Based on their analysis, De Barros et al. [2016] proposed that Family 1 fractures (N150-180, 30-60°W) present in the damage zone could be responsible for the recorded seismicity. Nevertheless, in Chapter 5 we investigate the possibility of the reactivation of another fault

plane, as a number of the events appear to be aligned with the main direction of the fault zone and could correspond to slip along the boundary between the East damage zone and the intact rock a few meters away from the injection chamber.

2.2 Numerical approach

2.2.1 Discrete Element Modeling

Based on the mesoscale field experiments, coupled hydromechanical calculations were performed in this work using the Discrete Element Method (DEM) and more specifically the 3DEC software [Cundall, 1988; Hart et al., 1988; Itasca Consulting Group, 2013]. 3DEC is based on the Discrete Element Method (DEM) that refers to two basic features: the finite displacements and rotations of discrete bodies, including complete detachment and the automatic recognition of new contacts as the calculation progresses. 3DEC stands for 3Dimension Distinct Element Code. The Distinct Element Method refers to a particular discrete-element scheme that uses deformable contacts and an explicit, time-domain solution of the original equations of motion [Cundall & Strack, 1979].

The discontinuous medium (fractured rock mass) is modeled as a 3D assemblage of discrete blocks whereas the discontinuities (contacts) are treated as distinct boundary interactions between blocks. A block can either be rigid or deformable depending on the needs and purpose of the analysis. For the simulation of the deformable blocks' behavior, the blocks are subdivided into finite-difference tetrahedral zones where the mechanical changes are calculated (stress/strain). Four gridpoints (nodes) are associated with each zone. They are characterized by x, y, z coordinates and vector quantities such as velocities or forces are stored within the gridpoints. Blocks of different size are created by defining the coordinates in the x, y and z axis. By introducing the cutting plane, meaning the joint, the 3DEC model geometry will be finally formed with the initial block cut into smaller blocks (see Figure 2.11).

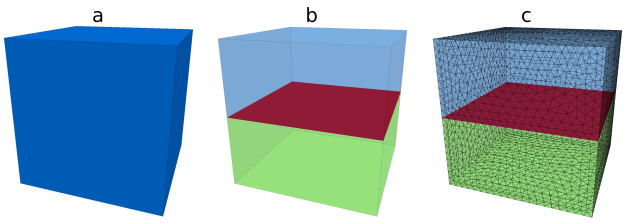

Figure 2.11: (a) Rigid block, (b) two rigid blocks created by the insertion of a horizontal joint, (c) two deformable blocks after the generation of the mesh.

Contact representation and detection

In order to perform an analysis in 3DEC, the model must first recognize the existence of contacts or interfaces between the discrete bodies that comprise the system. Firstly, neighboring blocks must be identified. This is done by dividing the domain containing the blocks into rectangular 3D cells. Each block is then mapped into the cell or cells that its "envelope space" occupies defined as the smallest 3D box with sides parallel to the coordinate axes that contain the block. Once the mapping has taken place for all blocks, the neighbors to a given block can be easily identified based on the entries of other blocks

in the occupied by the block cells. During the simulation and as a block moves, it is remapped and tested for contact with new neighbors. Based on the accumulated movement of the block and if this is more or less than a defined tolerance, remapping and contact testing are reactivated or not. In addition, the same tolerance is used to decide whether a contact is created or deleted based on the separation gap between two blocks. Contact detection logic must supply the contact type if the blocks are touching (for assigning the appropriate physical law), the maximum gap (for a pair to be tested if the blocks are not touching), and the unit normal vector that will define the plane along which sliding will occur. The "common plane" logic is used in 3DEC that supplies the above mentioned and speeds up the process. According to the common-plane logic, a plane is determined that bisects the space between two blocks and tests each block separately for contact with the common plane. The algorithm to position the Common-Plane is based on the calculation of the distance between the centroid of two blocks tested for contacts, and of the unit normal to the plane.

In terms of the contact type, a face-to-face contact physically corresponds to a joint and requires the definition of an area of contact where force-displacement laws can be applied to simulate the mechanical response of the interface. For each common-plane found corresponding to a pair of blocks touching, one regular data element is allocated for the contact. The block face in contact with the common-plane is automatically discretized into sub-contacts. The sub-contacts correspond to internal surface nodes that are contained in the triangular faces of the tetrahedral zones at the block face. For face-to-face contacts, an area corresponds to each sub-contact where joint constitutive relations can be applied. Same conditions apply for the other side of the interface.

Mechanical calculations for motion and interaction

3DEC is based on a dynamic (time-domain) algorithm that solves the equations of motion of the block system by an explicit finite difference method. At each timestep the law of motion and the constitutive equations are applied. The new block positions and the contact-displacement increments (or velocities) are obtained through the integration of the law of motion. Using the sub-contact force-displacement law, the new sub-contact forces are calculated that will be applied to the blocks in the next timestep.

The relative velocity across a sub-contact is obtained from the velocity associated with the sub-contact V_i^V and the velocity of the corresponding point on the opposing face V_i^F. For deformable blocks V_i^F can be calculated by linear interpolation of the velocities of the three vertices of the face using a weighting factor. For a sub-contact with the unit normal n_i pointing from block A to block B, if the vertex belongs to block A then the relative velocity of the sub-contact is calculated as:

$$V_i = V_i^V - V_i^F \tag{2.1}$$

If the vertex belongs to block B, then:

$$V_i = V_i^F - V_i^V \tag{2.2}$$

The increment in the relative displacement at the sub-contact is:

$$\Delta U_i = V_i \Delta t \tag{2.3}$$

that is resolved into normal and shear components along the common plane:

$$\Delta U^n = \Delta U_i n_i \tag{2.4}$$

$$\Delta U_i^s = \Delta U_i - \Delta U_j n_i n_j \tag{2.5}$$

The elastic force increments are then calculated based on the displacement increments:

$$\Delta F_n = -K_n \Delta U_n A_c \tag{2.6}$$

$$\Delta F_i^s = -K_s \Delta U_i^s A_c \tag{2.7}$$

where A_c is the area of the sub-contact taken as to $1/3$ or $1/2$ of the areas of the triangular faces containing the sub-contact depending on the contact type. The total normal force and shear force vector are updated for the sub-contacts according to the following equations and adapted to the contact constitutive relations:

$$F^n := F^n + \Delta F^n \tag{2.8}$$

$$F_i^s := F_i^s + \Delta F_i^s \tag{2.9}$$

Finally, the action of the block A on block B is represented by the sub-contact force vector which is added to the corresponding gridpoints:

$$F_i = -(F^n n_i + F_i^s) \tag{2.10}$$

After describing the scheme for block interaction, the equations of motion for each gridpoint of a deformable block are formulated as:

$$\ddot{u}_i = \frac{\int_s \sigma_{ij} n_j ds + F_i}{m} + g_i \tag{2.11}$$

where s is the surface enclosing the mass, m, lumped at the gridpoint, n_j is the unit normal to s and g_i is the gravitational acceleration. F_i is the resultant of all external forces applied to the gridpont, taken as the sum of the external applied loads, the result from the sub-contact forces (only for gridpoints along the block boundary) and the contribution of the internal stresses in the zones adjacent to the gridpoint. Adding the contributions from body forces due to gravity, a net nodal force vector $\sum F_i$ is calculated at each gridpoint which will be zero if the body is at equilibrium. Otherwise, the node will be accelerated according to the finite difference form of Newton's second law of motion:

$$\dot{u}_i^{t+\frac{\Delta t}{2}} = \dot{u}_i^{t-\frac{\Delta t}{2}} + \sum F_i^{(t)} \frac{\Delta t}{m} \tag{2.12}$$

where the superscripts denote the time at which the corresponding variable is evaluated. During each timestep, strains and rotations are related to nodal displacements following:

$$\dot{\epsilon}_{ij} = \frac{1}{2}(\dot{u}_{i,j} + \dot{u}_{i,j}) \tag{2.13}$$

$$\dot{\theta}_{ij} = \frac{1}{2}(\dot{u}_{i,j} - \dot{u}_{i,j}) \tag{2.14}$$

Therefore after each timestep, the strain state of each zone is known and the stress is defined by the stress-strain relation in order to proceed to the next timestep.

In order to perform a static analysis, which is the case in the study that follows, the equations of motion are damped to reach a force equilibrium state as quickly as possible under the applied initial and boundary conditions. Damping is velocity-proportional meaning that the magnitude of the damping force is proportional to the velocity of the blocks. The mechanical damping used by default in 3DEC among other options, is the adaptive global damping that adjusts the damping constant automatically. Viscous damping forces are used, but the viscosity constant is continuously adjusted in such a way that the power absorbed by damping is a constant proportion of the rate of change of kinetic energy in the system.

Constitutive models

The constitutive models selected for the present work are the generalized Coulomb friction law for the discontinuities and the elastic or transversely isotropic material for the response of the intact rock.

As far as the intact rock material behavior is concerned, two constitutive models implemented in 3DEC were used, the elastic isotropic model and the transversely isotropic elastic model. For the elastic model, the material exhibits a linear stress-strain behavior with no hysteresis on unloading. According to the linear and reversible Hooke's law:

$$\Delta\sigma_{ij} = 2G\Delta\epsilon_{ij} + \alpha_2\Delta\epsilon_{kk}\delta_{ij} \tag{2.15}$$

where

$$\alpha_2 = K - \frac{2}{3}G \tag{2.16}$$

and G is the shear modulus, K is the bulk modulus, δ_{ij} is the Kronecker delta and ϵ_{kk} is the Einstein summation:

$$\epsilon_{kk} = \epsilon_{11} + \epsilon_{22} + \epsilon_{33} \tag{2.17}$$

The new stress values for the zones are then obtained:

$$\sigma_{ij}^{N} = \sigma_{ij} + \Delta\sigma_{ij} \tag{2.18}$$

The transversely isotropic elastic model takes into account a plane of isotropy inside the material. This is quite representative of the shale material due to the strong presence of the parallel bedding which is assumed to be the plane of isotropy. If the local axis 3 is the axis of rotational symmetry, normal to the plane of isotropy (plane 1-2), the following apply:

$E = E_1 = E_2$

$E' = E_3$

$\nu = \nu_{12}$

$\nu' = \nu_{13} = \nu_{23}$

$G = G_{12}$

$G' = G_{13} = G_{23}$ where E is the Young's modulus in the plane of isotropy and E' is the Young's modulus

in the direction normal to the plane of isotropy, ν is the Poisson's ratio characterizing lateral contraction in the plane of isotropy when tension is applied in this plane, $\nu'$is the Poisson's ratio characterizing lateral contraction in the plane of isotropy when tension is applied in the direction normal to it, G is the shear modulus for the plane of isotropy and G' the shear modulus for any plane normal to the plane of isotropy.

Explicitly representing the bedding planes in the models was usually not considered. After some modeling efforts, it had been observed that the reactivation of the bedding planes was most of the times impossible due to the ambient stress field and the presence of more favorably oriented fractures. The bedding planes in the Tournemire shale are therefore accounted for by including a transversely isotropic intact material characterized by different elastic properties in the directions parallel and normal to the bedding.

The fractures or faults modeled in this work follow the generalized Coulomb friction law. In the elastic range, the response is governed by the following equations:

$$\Delta F^n = -K_n \Delta U^n A_c \tag{2.19}$$

$$\Delta F^s = -K_s \Delta U^s A_c \tag{2.20}$$

where K_n and K_s are the normal and shear stiffness respectively (in Pa/m), ΔU^n and ΔU^s are the normal and shear displacement increments, ΔF^n and ΔF^s are the normal and shear force increments and A_c is the contact area.

In the plastic range, the maximum tensile normal force is given as:

$$T_{max} = TA_c \tag{2.21}$$

where T is the tensile strength of the fracture. The maximum shear force is defined by:

$$F^s_{max} = cA_c + F^n tan\phi \tag{2.22}$$

where c is the cohesion and ϕ is the friction angle. As soon as the sub-contact fails, the tensile strength and the cohesion are set to zero simulating a "displacement-weakening" joint. As soon as the fracture slips the dilation is activated according to the following equation:

$$\Delta U^n(dil) = \Delta tan\psi \tag{2.23}$$

where ψ is the dilation angle.

Summarizing, the material properties that need to be defined for the mechanical response of the intact rock and the discontinuities, are:

- the density and the elastic parameters of the intact rock matrix,
- the elastic parameters (normal and shear stiffness) and the strength parameters (friction, cohesion, tensile strength, dilation angle) of the discontinuities.

Hydromechanical analysis in 3DEC

3DEC offers the possibility of performing hydromechanical calculations due to the demands in modeling coupled hydro-mechanical processes of a fractured rock mass. However, in the software version used in this work, the fluid flow in the rock mass only considers the flow through the fractures by neglecting the flow within the intact rock blocks. This assumption is based on the fact that the flow rate and permeability of the fractures is in most cases several orders of magnitude higher than the intact rock's permeability. Hence, the fractures are represented as joint surfaces separating the impermeable blocks.

For the fluid flow calculations, the flow model is generated automatically as a function of the solid model. The flow model implemented in 3DEC consists of the following basic geometric elements (Figure 2.12):

- Flow plane: planar polygon corresponding to a face-to-face contact between two solid blocks. Consequently the "mechanical" contact is automatically a flow plane.
- Flow plane zone: a triangular discretization element of the flow plane.
- Flow plane vertex: vertex of a flow plane zone that generally corresponds to a sub-contact between solid blocks.
- Flow knot: it is the same as a flow plane vertex except along the flow plane intersects, in which case one flow knot corresponds to two or more co-locational flow plane vertices from the intersecting flow planes. The flow knot stores the fluid pressures.
- Flow pipe: connection between one or more flow planes.

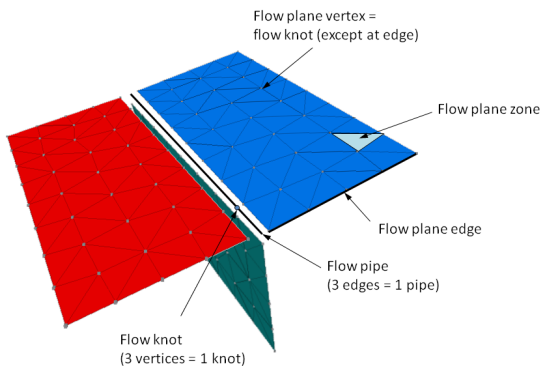

Figure 2.12: Flow structures for the intersection of three flow planes (after Itasca Consulting Group [2013]).

The flow rate per unit width of the plane is calculated according to the form of the cubic law proposed by [Witherspoon et al., 1980] assuming a parallel plate model:

$$q = -\frac{u_h^3 \rho g}{12\mu} \nabla h = -k_h \nabla h \tag{2.24}$$

where u_h is the equivalent hydraulic aperture of the idealized fracture (m), k_h is the hydraulic conductivity of the fracture (m/s), ∇h is the hydraulic gradient, ρ is the fluid density (kg/m^3), g is the gravitational acceleration (m/s^2) and μ is the fluid dynamic viscosity ($Pa \times s$).

Both the flow rate and the transmissivity are calculated in the triangular geometrical flow plane zones used for the discretization of the flow plane by taking into account the aperture and pressure values of the corresponding flow plane vertices (or flow knots). Even if the transmissivity is calculated along a given zone, its value is recovered at a single flow plane vertex with the contribution of each connected zone accumulated on each vertex. This value represents a geometrical weighted average of the transmissivity values of the zones surrounding the specific vertex. Therefore, once the conductivity matrix, k, is calculated, the transmissivity matrix is then expressed as:

$$T = k \nabla x \tag{2.25}$$

where

$$k = \frac{u_h^3}{12\nu} \tag{2.26}$$

and ∇x is a geometrical gradient accounting for the contribution of the zone to each one of its flow knots [Itasca Consulting Group, 2013].

The need for hydromechanical analysis focuses on the direct effect of the deformability of the system on the fluid pressure and vice-versa. The hydraulic aperture is therefore a function of the mechanical aperture which is defined as the average distance between the joint walls. For equations 2.24 and 2.26 the hydraulic aperture is equal to its initial value plus the normal displacement of the fracture according to the following equation:

$$u_h = u_{h0} + f \Delta u_n \tag{2.27}$$

where u_{h0} is the initial hydraulic aperture (at zero stress or at the insitu stress conditions), Δu_m is the joint deformation and f is a factor reflecting the influence of the roughness on the tortuosity of the flow. The factor f in 3DEC calculations is taken equal to 1. The hydraulic aperture is bounded by two extreme values. A lower bound (u_{res}) below which the mechanical deformation does not affect the permeability of the discontinuity, and an upper bound (u_{max}) for calculation efficiency as the calculation time significantly increases for very large apertures. Both values have to be set by the user. Based on the above, the relation between the hydraulic aperture and the effective normal stress is illustrated in Figure 2.13.

3DEC provides different approaches towards the hydromechanical coupling. A complete coupling is adopted in our numerical modeling based on a simultaneous fluid flow/mechanical calculation. The solution in this case is performed by alternating frequently between mechanical and fluid calculations in order to account for the fluid pressure changes due to the solid deformation and the variation of the mechanical stresses and strains due to the fluid pressure. More specifically, the hydromechanical model in 3DEC is quasi-static meaning that the mechanical model is in equilibrium for the current distribution of the pore pressures. Therefore, for each flow timestep there is a number of mechanical timesteps executed in order to reach mechanical equilibrium and the physical time is then represented by the flow time.

Once the updated geometries are determined from the mechanical calculations, the new values can be defined for the apertures of all contacts. The calculation of the fluid pressure is done in the "flow knot" data structure. After the flow rates have been calculated for the flow zones, the flow knot pressures are updated taking into account the net flow into the know and the possible changes in flow knot volume due

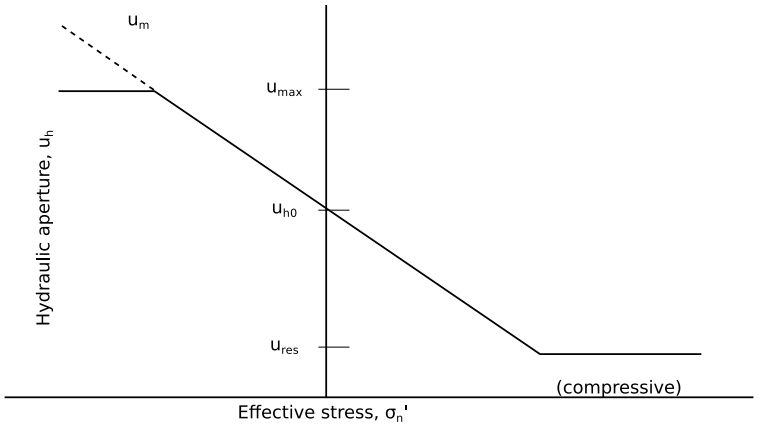

Figure 2.13: Idealized relation between hydraulic aperture and effective normal stress for a rock joint (after Itasca Consulting Group [2013]).

to surrounding blocks' motion. The new flow knot pressure is obtained according to:

$$p = p_0 + k_w Q \frac{\Delta t}{V} - K_w \frac{V - V_0}{\frac{V+V_0}{2}} \tag{2.28}$$

where p_0 is the flow knot pressure in the preceding timestep, K_w is the fluid bulk modulus, Q is the sum of the flow rates into the knot from all surrounding contacts and V and V_0 are the new and old flow knot volumes respectively.

It should be mentioned that when simulating transient fluid flow and for numerical stability reasons, the fully coupled hydromechanical algorithm can be practically applied only to short duration simulations.

2.2.2 General Methodology

The different aspects of the general methodology followed focus on i) the geometry of the model, ii) the constitutive model and the material properties, iii) the initial and boundary conditions, iv) the loading procedure and v) the analysis of the results.

Based on mesoscale field experiments carried out at the Tournemire site coupled hydromechanical calculations are attempted based on a 3D model with the characteristics of the Tournemire site. The calculations consist in realizing "injection experiments" that are able to enlighten some aspects of the stress-fluid pressure-permeability relation associated to injection induced fault reactivation.

Model geometry

Regarding the geometry of the developed models, the in-situ geology is taken into account for each injection test. The basic structures i.e. fractures or secondary faults involved in the given test are modeled as discontinuities in the 3DEC model. As a starting point and for simplification reasons, the structures to be modeled initially for the numerical calibration of each test are chosen by their orientation and their filling material. If the orientation of a fracture is favorable with respect to the stress field and if it is characterized as an open fracture with no calcification then it constitutes a strong candidate for reactivation. The injection borehole is not included in the models for the sake of simplicity. Nevertheless, the effect of the borehole is accounted for in order to directly compare the numerical results with the

experimental observations. This is achieved by defining a "damaged" area around the intersection of the borehole and the fractures. This area corresponds either to a set of initially failed sub-contacts or inferior material properties.

Initial and boundary conditions

Considering the initial and boundary conditions, these are selected according to the stress state and the in-situ pore pressure of the experimental site. However, the tests described in section 2.1.2 provide valuable information regarding the stress conditions under which the reactivation took place given the fluid pressure increase. Hence, the determination of the stress acting on each test location can be a parameter to calibrate.

Injection loading protocol

In terms of loading protocol, the injection can be controlled either in terms of fluid pressure or flow rate. This depends on the in-situ protocol that was followed for each test. In the present study, two different ways of performing the injection were defined:

- Point source injection (Figure 2.14): In this configuration the pressure or flow rate change is applied only on one point of the plane that is usually located at the center of the model. When modeling the field tests, this point corresponds to the intersection point between the injection borehole and the fracture plane. A radial fluid propagation is expected in this case if the plane is homogeneous while all the boundaries are considered permeable.
- Injection along a boundary: The pressure or the flow rate changes are applied along a boundary of the model, i.e. on a set of points. The fluid propagates along the fracture with a propagating fluid front that is perpendicular to the applied pressure gradient (the direction of the flow) as the lateral boundaries (parallel to the direction of the flow) are considered impermeable. This facilitates flow rate and permeability measurements for a given fracture by calculating the inlet and outlet flow rate that should converge as soon as a steady-state flow regime is reached.

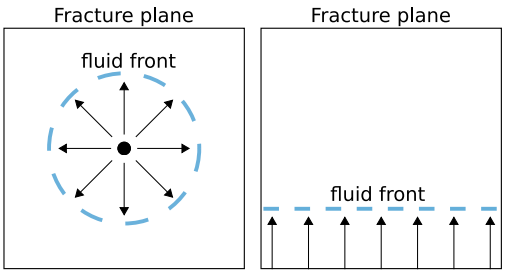

Figure 2.14: Point source injection (left), injection along a boundary (right).

During fluid propagation, flow in 3DEC can either occur in all flow planes of the model or within portions of the flow planes where the corresponding sub-contacts have failed. In the second option, the fluid propagation in the model is strongly associated to the fracture's failure. More specifically, the propagation of fluid presupposes the failure of the corresponding parts of the plane. For our models the second configuration is chosen ensuring a progressive failure of the fracture associated to the fluid pressure propagation, subsequent decrease of the effective stress and reactivation of the fracture plane.

Constitutive model and material properties

The constitutive models selected for the intact rock and the discontinuities have already been described in section 2.2.1. The material properties used such as the fault/fracture stiffness values, the static friction and the transmissivity are firstly estimated based on the field measurements, using the hydromechanical analyses in order to derive a best-fit set of parameters. These parameters are then used in the model in order to investigate the evolution of the fluid pressure, the discharge rate and the structure's displacements with time during the injection.

Interpretation and analysis

The specific field data that were used in the present modeling work concern the fluid pressure-, the flow rate-, and the displacement-versus-time measurements as captured by the pressure sensors and the probe displacement sensor anchors in the test interval. For the modeling of the in situ tests, fluid pressure and flow rate were monitored during the simulations at the injection point. The displacements evolution throughout the calculation was monitored in the model through the relative displacement of two points with coordinates that represented the position of the two anchors in the test interval. Matching of the model results with the field data is useful for calibrating the numerical model and understanding the mechanisms associated with the reactivation at the injection source as well as the processes that can occur in the far-field. Using that as a basis, different calculations were performed such as a sensitivity analysis so as to determine the dominant mechanisms influencing the observed response and investigate the key factors in the evolution of the fault permeability during reactivation.

Two different, more complex models were developed for the interpretation of Test 1 and Test 2. Modeling of Test 1 (West damage zone) aims at understanding the role of the pre-existing fracture network on the measure quantities (flow rate and displacements). In addition, it provides information on the relation between the orientation of the fractures and their reactivation potential under pressurization conditions revisiting the concept of optimally oriented faults. The role of the surrounding structures can be evaluated by comparing the model results with the field measurements in terms of pressure, flow rate and displacements. The objective of the modeling of Test 2 (host rock) was to investigate the links between the observed seismicity and permeability enhancement. In other words, the location of the seismic events were used in a static model in an attempt to estimate whether the observed seismicity was the result of a pressure diffusion process and effective stress variations in the fault zone far from the injection source. This required first the calibration of the injection parameters at the test interval similarly to Test 1 by observing the pressure and displacements evolution close to the injection point and comparing them to the experimental curves. The monitoring of the fluid and rupture propagation at the course if the injection simulation can then be compared to the location of the microseismic events.

Based on the observations from the in situ experiments two more "theoretical" cases were investigated setting up a simple small model. In the developed model, heterogeneous fault properties were used for the purpose of evaluating the effect of flow channeling in the rupture propagation and the permeability variation under a channeling flow regime. While for the two cases the geometry of the model was the same, different loading conditions were applied that included the point source injection and the injection along a boundary (Figure 2.14).

Chapter 3

Role of the in-situ stress and fractures' orientation on fault permeability

The in-situ Test 1 in the Tournemire fault zone, offers an opportunity for investigating the response of a secondary fault inside the damage zone of the main fault zone. Given the complex structural nature of the fault zone, an effort is made towards estimating the effect of the fractures' connectivity and orientation on the resulting permeability and mechanical response of the system. Hence the following study could correspond mostly to the hydro-mechanical response of a fracture network since the matrix is impermeable and the bulk permeability of the system will strongly depend on the connectivity and orientation of the interval fractures. In addition, based on the modeling observations, a second simpler model is considered for performing a sensitivity analysis. The second model is a plane strain model comprising only two intersecting fractures.

3.1 Modeling of the in-situ injection test in the fault damage zone

3.1.1 Single persistent fault model

A numerical model has been set up and calibrated in Guglielmi et al. [2015b] based on the experimental data of the evolution of flow rate and displacements with time (see also Figure 2.7). The geometry of the model together with the applied stresses is shown in Figure 3.1(left). The model consists of a 10 m cube cut by a persistent fault with the orientation of the secondary fault observed in the test interval. The six faces of the domain are submitted to the in-situ stress field according to Cornet [2000] and the initial pore pressure of the model is equal to 0.2 MPa. Table 3.1 shows the best-fit set of parameters that better reproduced the experimental observations in terms of fault movement and flow rate (Figure 3.1).

The injection borehole was not explicitly represented in the model. Instead, a borehole effect was accounted for by assigning a lower friction of 22° in a fault area of diameter 0.5 m centered around the injection point. This low static friction value was assigned to better match the model with the measurements at the beginning of the test. It was shown in Guglielmi et al. [2015b] that before 237 s, the measurements are dominated by near-field effects close to the borehole wall. The injection was simulated by imposing a step-rate fluid pressure loading at the center of the model (gridpoint 0, 0, 0) corresponding to the loading

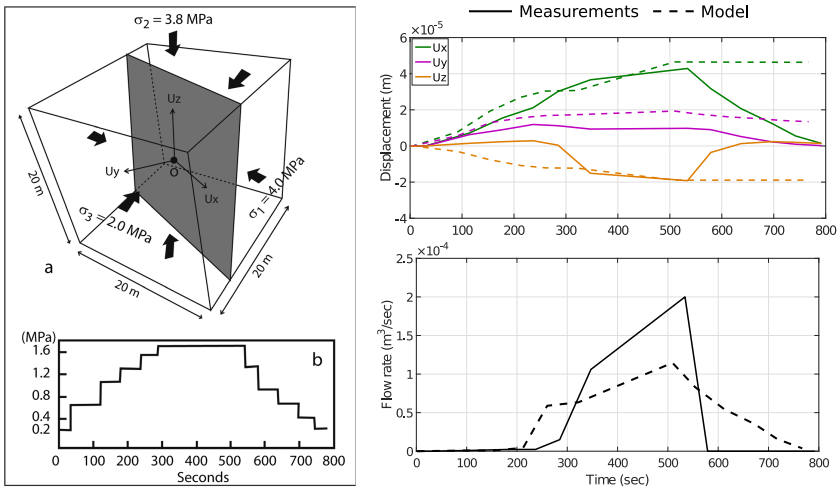

Figure 3.1: Left: Geometry of the single persistent fault model and the applied stresses. Right: Best-fit numerical solutions of fault hanging wall displacements (upper graphs) and flow rate (lower graphs) (modified from Guglielmi et al. [2015b]).

protocol applied during the field experiment (Figure 3.1 (left, b)). The point at the center of the model represented the intersection of the borehole test interval with the secondary fault. The intact rock was considered isotropic, elastic while the generalized Coulomb friction model was used to model the response of the fault as described in section 2.2.1. The properties values used in the model are summarized in Table 3.1.

Rock matrix properties		
Density	ρ	2500 kg/m^3
Bulk modulus	K	5.15 GPa
Shear modulus	G	3.94 GPa
Fault plane properties		
Normal stiffness	K_n	200 GPa/m
Shear stiffness	K_s	4 GPa/m
Friction angle	ϕ	35 $^\circ$
Cohesion	c	0
Dilation angle	ψ	5 $^\circ$
Hydraulic aperture at zero normal stress	u_{h0}	3×10^{-5} m
Fluid properties		
Bulk modulus	K_f	2 GPa
Density	ρ_f	1000 kg/m^3
Dynamic viscosity	μ	10^{-3} $Pa \times s$

Table 3.1: Best-fit model properties.

The flow rate in the model was calculated according to Equation 2.24 for a smooth parallel plate fracture. In the elastic range, the hydraulic aperture varied as a function of the effective normal stress [Detournay, 1980]:

$$u_{he} = u_{h0} + \frac{\Delta\sigma'_n}{K_n} \tag{3.1}$$

where $\Delta\sigma'_n$ is the variation of the effective normal stress and K_n is the fault's normal stiffness.

In the plastic range, the effect of dilation was also taken into account as the fault slips. Therefore, the hydraulic aperture in the plastic range varied as a function of the effective normal stress and as a function of the dilation induced by fault slip:

$$u_{hp} = u_{h0} + \frac{\Delta\sigma'_n}{K_n} + u_{hs} \tag{3.2}$$

Nevertheless, the hydraulic aperture recovered from the above relationship in the plastic range was not large enough to reproduce the increase in the flow rate because the latter was not associated with a normal component during fault slip. Hence, a relationship was considered:

$$u_{hs} = Bu_{he} \tag{3.3}$$

where B ($\sim$ 7) is evaluated as a function of the measured flow rate and pressure during the step rate experiment.

While the measurements corresponding to the increasing pressure steps of the test are in a reasonable agreement with the numerical results, the model is poorly representing the response during the unloading steps (after 500 s approximately). Indeed, there is a large amount of residual inelastic displacement that is not in agreement with the experimental observations where a significant part of the deformation appears to be reversible. In addition, the calculated flow rate from the model is progressively decreasing contrasting the measured one that sharply falls to zero as soon as the unloading takes place. Such discrepancies between the model and the measurements could be possibly attributed to more complex mechanisms in situ that consider the connectivity and interaction between the fractures intersected by the borehole interval or the more realistic fluid flow scenario where the roughness and surface characteristics of the fault could strongly diverge from the parallel plate flow model assumed in the numerical analysis [Guglielmi et al., 2015b].

3.1.2 Single finite size fault model

In a first attempt to explain the reversibility, the effect of the non-persistence of the secondary fault is considered in order to account for the possible effect of the surrounding medium's elasticity during the reactivation. Hence, a finite size fault is introduced in the model surrounded by an elastic medium. The secondary fault was found to be larger than 10 m (see Table 3.2). Therefore, the model domain was increased to 20 m in order to introduce a finite size disk with a diameter equal to 10 m (see Figure 3.2, left). In this way, the reactivated area should be comparable to the previous persistent fault model. The properties of the fault are identical to the persistent fault case.

Figure 3.2, right illustrates a vertical cross section at the center of the model domain with the fluid pressure distribution inside the fracture. Due to the finite size of the fracture, the propagation of the fluid is possible only within the disk as for the given injection test, the fluid pressure was not high enough to induce failure of the intact material and propagation of the preexisting fracture. In the persistent fault configuration, the fluid pressure distribution inside the fault (Figure 3.4(a)) shows that due to the permeable hydraulic boundaries, the high pressure value is only localized around the injection point without severe pressurization occurring inside the totality of the fault. On the other hand, the fluid pressure inside the total surface of the 10 m fault disk is equal to the high pressure imposed at the

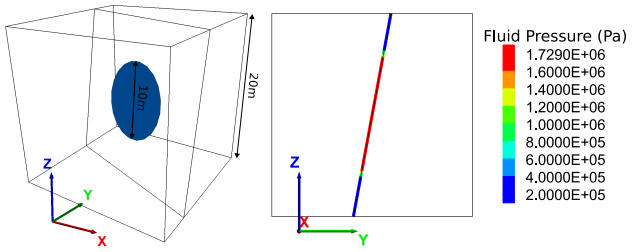

Figure 3.2: Geometry of single finite size fault model (left). The fault is characterized by a radius of 10 m in a 20 m model. Fluid pressure distribution along the fault for a vertical plane of view at the center of the model and for the highest pressure imposed (right).

injection point leading to a 10 m homogeneously pressurized zone.

A significant increase in the fault displacements and a decrease in the flow rate are observed for the pressurized finite plane (Figure 3.3). The high magnitude of the fault displacements is the result of the increased fluid pressure inside the total fault surface. Every single point inside the reactivated finite size fault is characterized by the same fluid pressure and therefore the same effective stress variation (decrease). This leads to a larger surface of the area experiencing the same slip that explains the increased calculated displacements. This mechanical response is certainly not in agreement with the experimental results implying that there was no severe pressurization over a large portion of the reactivated fault that appeared to be connected to permeable hydraulic boundaries preventing pressurization.

The calculated flow rate and consequently the permeability increase is very low pointing out once again the importance of the structure's hydraulic connectivity with permeable boundaries. Therefore, the assumption of an isolated finite size structure is not valid leading to the investigation of the response of a connected fracture network as described in the following section.

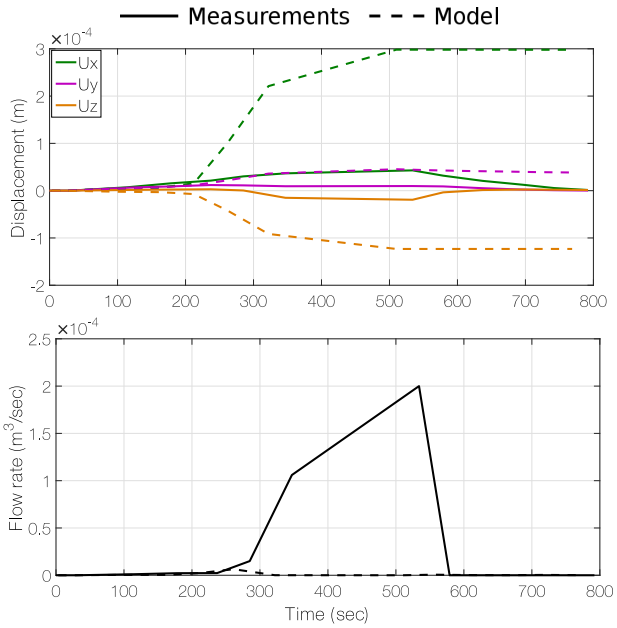

Figure 3.3: Displacements variation versus time (top), flow rate variation versus time (bottom) for the finite size fault.

3.1.3 Fracture interaction within the test interval

Hydro-mechanical coupled effects within one fracture depend not only on its hydro-mechanical properties, but also on the nature of the hydro-mechanical connections with other fractures, the orientation and magnitude of effective stresses applied to fracture walls, and general orientation (e.g. [Cappa et al., 2006]). In the following, the effect of the interaction of the pre-existing fractures is considered as another mechanism accompanying the reactivation that could enlighten some aspects of the observed hydromechanical response. Figure 2.6 shows the borehole geology for the Test 1. In total nine relatively "open" (not fully sealed with calcite) fractures were intersected by the borehole test interval characterized by different orientations and surface characteristics as described in Section 2.1.2. The fractures were grouped in 3 main families, the secondary fault, the sub-vertical (dip $> 20°$) and the sub-horizontal family (dip $< 20°$). While the majority of the fractures in the fault zone are dipping towards the West there was one fracture dipping towards the East (N50°-42°E) that was included in the sub-horizontal fracture family. Information regarding the size and orientation of the fractures in terms of dip direction and dip angle are summarized in Table 3.2.

Family	Dip Direction	Dip Angle	Size
Secondary fault	200	80	$>$ 10 m
Sub-vertical	200	46	$<$ 10, $>$ 2 m
	200	28	$<$ 10, $>$ 2 m
	183	27	$<$ 10, $>$ 2 m
	158	36	$<$ 10, $>$ 2 m
Sub-horizontal	50	42	$<$ 1 m
	145	20	$<$ 1 m
	178	8	$<$ 1 m
	163	12	$<$ 1 m

Table 3.2: Estimated orientation and size of the fractures intersected by the Test 1 interval.

Initially, a more complex model geometry is considered by including in the 10 m model domain all nine fractures (Figure 3.4, top(b)).

The model is based on the following assumptions:

- The totality of the fractures in the model is persistent ($>$ 10 m). Their real size is not accounted for and consequently a high connectivity is assumed since the fractures that are introduced are in reality much smaller than the secondary fault.

- All the fractures inside the model are characterized by the same material properties as the calibrated secondary fault in Section 3.1.1. This is a strong assumption since the majority of these fracture families are partially or fully sealed with calcite. This means that different hydro-mechanical properties are expected depending on the level of calcification.

- Similarly to the single fault model, the borehole is not explicitly represented but its effect is taken into account. The fractures' material around the injection point is characterized by a lower friction angle as mentioned in the previous section, due to the expected damage around the borehole injection.

The first two assumptions aim at considering an extreme case where the fractures are highly connected and equally potential fluid paths in terms of mechanical and hydraulic properties. As there is no injection

chamber representation, the pressurization of the intersected fractures is achieved by placing injection points where the pressure is controlled at each intersection point between borehole and fractures. Regarding the loading of the system, the pressure step-rate procedure is applied according to the experimental loading protocol. The displacements are recorded in two points representing the anchors of the probe and the resulting flow rate will be equal to the sum of the flow rates recorded for each fracture-borehole intersection point.

Apart from the model containing the totality of the interval's fractures, the contribution of each fracture family's orientation is also tested. More specifically, the secondary fault is modeled together with the sub-vertical fracture family in the first configuration (Figure 3.4, top(c)) and in the second the fault is modeled with the sub-horizontal fracture family (Figure 3.4, top(d)). As none of the models considered resulted in a reversible mechanical response at the onset of the fluid pressure decrease, the analysis below mainly focuses on the increasing pressure part of the test and on the role of the adjacent discontinuities in the rock mass.

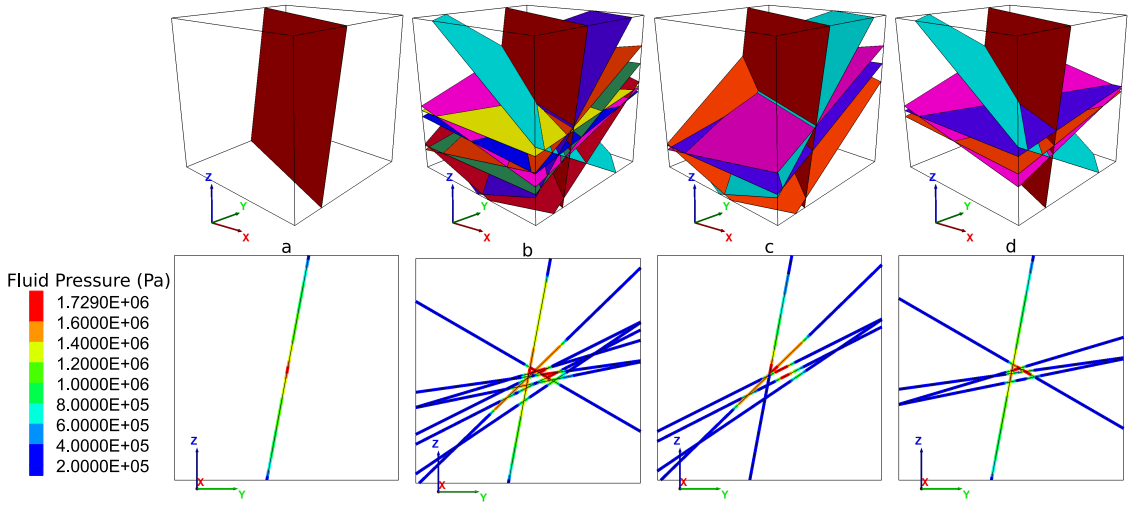

Figure 3.4: Model geometry and fluid pressure distribution shown along a vertical plane at the center of the model for $t = 537$ seconds corresponding to the end of the highest pressure test, for: (a) single secondary fault, (b) secondary fault with the sub-vertical and sub-horizontal families, (c) secondary fault with the sub-vertical family, (d) secondary fault with the sub-horizontal family.

When considering all the fractures intersected by the borehole interval, the fracture that was more affected by the fluid pressurization was the secondary fault (Figure 3.4, bottom(b)). The pressure appears to be higher for a larger radius inside the secondary fault comparing to the single persistent fault model. The next "most vertical" fracture of the model (deep purple fracture in Figure 3.4, top(b)) appears also to be reactivated for a smaller surface but characterized by a higher pressure. The rest of the fractures appear to be locally pressurized only at the injection point (point of intersection with the borehole) or at the intersection points with the pressurized fault but without any fluid propagation taking place within their planes. This is also confirmed by the flow rate values recovered for each fracture. The highest flow rate was calculated for the next "most vertical" fracture of the test that was evidently reactivated during the numerical simulation. For a number of fractures mainly from the sub-horizontal family, the flow rate was close to 0 at the end of the highest pressure step. So far, as the properties of the fractures considered are

identical, the effect of the orientation with respect to the stress field is pronounced. Keeping in mind that $\sigma_{min} = \sigma_y$ which is almost normal to the secondary fault, even for identical hydro-mechanical properties, the fractures characterized by a dip angle lower than $\sim 40^\circ$ will not be activated in the presence of more favorably oriented structures that are prone to slip under the strike-slip stress regime.

Comparing this fracture geometry configuration with the experimental data, the temporal evolution of the displacements calculated is not in agreement with the field measurements (Figure 3.5(a)). While the displacement in the x-direction is quite well represented, the displacement in the z and y-direction are overestimated. Especially the y-component of the displacement is more than two times higher than the measured one explaining also the larger pressurization area along the secondary fault in Figure 3.4(b). Given the number of the fractures included in the model, the material surrounding the pressurized fractures becomes more compliant. Additional fracture opening is then induced as the adjacent fractures are compressed or sheared if they are not conducting the fluid, accommodating part of the reactivated fractures' deformation [Cappa et al., 2006]. For the same reason, displacement in the z-direction is also overestimated as the majority of the fractures are located in the lower part of the model increasing the compliance in the z-direction. In terms of flow rate, an abrupt increase can be observed in Figure 3.5(b) for $t = 200$ seconds that remains almost constant until the unloading takes place. The increased flow rate is the result of the contribution of more than one fractures affected by the pressure increase in the model. Moreover, the additional opening because of the more compliant surrounding rock mass favors the flow rate increase. The decrease of the flow rate is occurring in the same way as the single persistent fault configuration. From analyzing the multi-fracture model, it can be concluded that the discrepancies observed in this first case between the model and the measurements imply that the majority of the pre-existing fracture families are much stiffer in-situ than what we assume in our model, or much smaller meaning that they do not affect in a significant way the properties of the surrounding rock mass during the test.

Eliminating the sub-horizontal fracture family from the model, fluid propagation is again dominantly occurring in the secondary fault and the next most vertical fracture (Figure 3.4, bottom(c)). Thereafter, the fluid propagation path is similar to the previous case except for the secondary fault plane for which the pressure distribution is concentrated in the upper part, above the intersection area with the sub-vertical fracture family. The displacements for this configuration are shown in Figure 3.5(c). The displacement variations versus the injection time are in a reasonable agreement with the experimental results for the increasing pressure path. The comparison of the mechanical response obtained indicates that the fractures of the sub-vertical family are contributing to the mechanical reactivation process and they are satisfyingly taken into account in the model. Nevertheless, the calculated flow rate (Figure 3.5(d)) is characterized by an abrupt increase similarly to the previous case indicating an injected volume of water higher than the one measured in-situ and than the previously modeled cases. This observation could possibly imply different hydraulic properties of the sub-vertical fractures attributed to their calcite filling favoring flow channeling effects and a lower resulting permeability of the fracture network. Indeed numerical studies on fracture network flow showed that even local heterogeneities along the interconnected fracture planes can significantly affect the bulk permeability of the network [Dreuzy et al., 2012]. If the direct effect of channeling cannot be taken into account in the model, equivalent hydraulic apertures could be also considered accounting for the fracture's surface roughness and contact areas [Witherspoon et al., 1980; Gentier et al., 1989; Tsang, 1992; Zhao & Brown, 1992; Zimmerman et al., 1992; Alvarez et al., 1995; Zimmerman & Bodvarsson, 1996; Oron & Berkowitz, 1998; Aydin, 2001; Méheust & Schmittbuhl, 2001] .

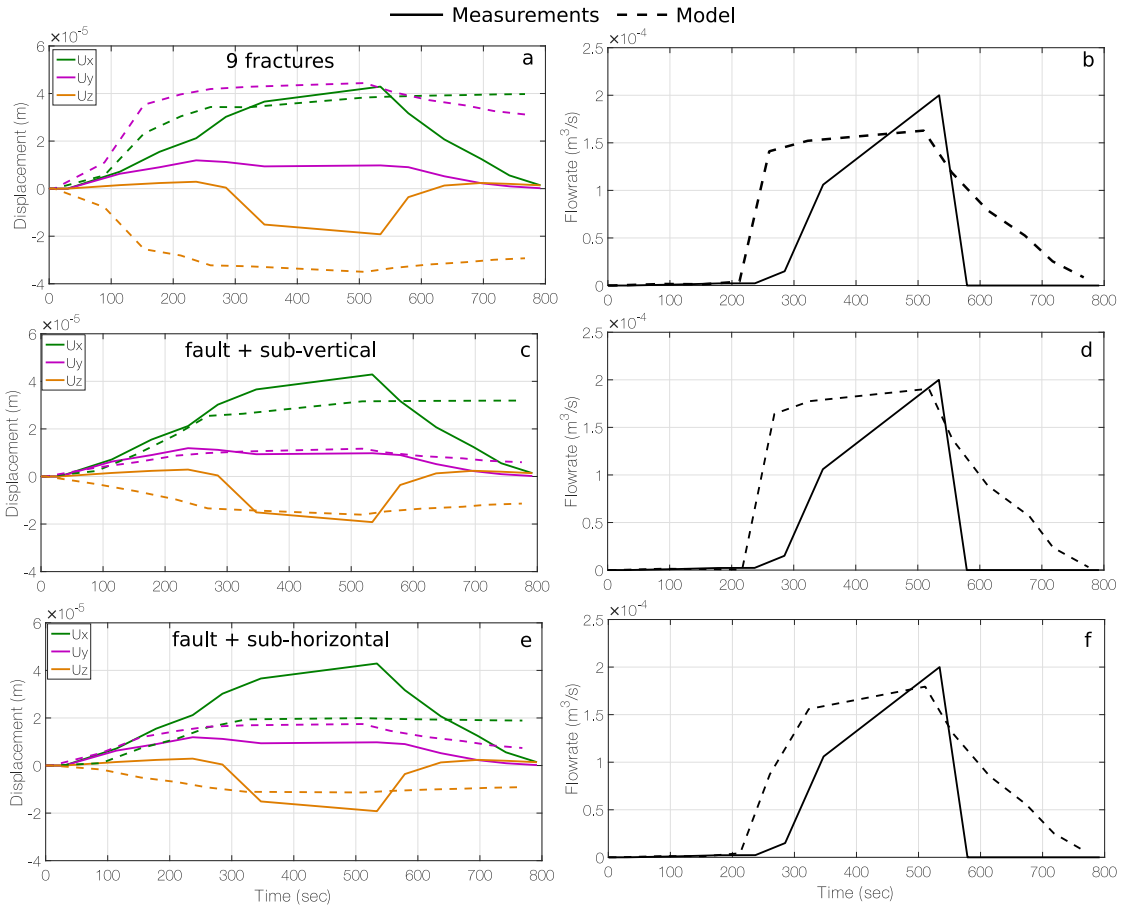

Figure 3.5: Displacement (top) and flow rate versus time for: 1st line: secondary fault with the sub-vertical and sub-horizontal families (9 fractures), 2nd line: secondary fault with the sub-vertical family, 3rd line: secondary fault with the sub-horizontal family.

For the last configuration tested where the sub-vertical fracture family was excluded from the model, the fluid pressure propagation appears to be very similar to the single fault case. The pressure gradient caused by the injection is mainly distributed in the secondary fault plane (Figure 3.4, bottom(d)). Local aperture variations at the borehole intersection with the fractures result in an increase in the calculated flow rate of the model (Figure 3.5(f)). Nevertheless, no further fluid propagation is taking place in the sub-horizontal fractures' plane. The sub-horizontal fractures are oriented almost perpendicularly to the vertical stress (whose value is close to the maximum stress) and for the given pressure value they are not reactivated. This implies that most of the sub-horizontal fractures stay hydraulically inactive throughout the injection test. In terms of mechanical response, there is a discrepancy between the calculated and the measured displacement in the x-direction as a result of the high contrast in the modeled fractures' orientation preventing the strong strike-slip movement measured in situ.

3.2 Fracture interaction generic model - Sensitivity study

Building on the observations from the complex multi-fracture model, a simpler model is set up with the purpose of investigating some key parameters and their impact on the fluid propagation path and on the

associated deformation of two intersecting fractures. The complexity of the models described above and the increased calculation time make it difficult for a sensitivity study to be performed. It was observed that the reactivation of the fractures in situ was sensitive to their orientation, properties and the stress field. In order to quantify the combined effect of these parameters, a study is presented in this section providing some insight into the mechanisms involved in fracture systems and restraining the first order parameters controlling the nature of the interaction. The potential for reactivation of a natural fracture intersected by a fluid–driven or a cohesive fracture is investigated. Such a configuration was chosen in order to represent more natural loading conditions. In a natural context, this plane corresponds to a fluid-driven fracture created by strong deep source overpressures, to an extensional vein fracture in a fault environment formed during pre-seismic stages [Sibson et al., 1988; Sibson, 1989; Cox, 1995; Sibson, 1996; Faleiros et al., 2014] or to preexisting fractures with varying degrees of cohesive and tensile strength as a result of chemical healing and vein filling [Fournier, 1996]. In all cases mentioned, the cohesion and tensile strength of the fracture are higher than the natural fracture's ones. Considering the fluid pressure increase associated to a fluid-driven fracture growth or cohesive fracture reactivation, we explore the interaction mechanisms between a propagating fracture and a natural fracture.

A simple three-dimensional model is set up figuring the two intersecting fractures. The main points that are addressed are:

- under which conditions of fracture's orientation and stress and for which hydraulic and mechanical properties, a natural fault or fracture is reactivated?
- what are the dominant activation mechanisms between permeability-controlled and shear-controlled mechanisms?

Thereafter, a sensitivity analysis is carried out in order to estimate the respective role of the following parameters on the natural fracture's reactivation: the maximum principal stress, the initial pore pressure of the formation, the hydro-mechanical properties of the natural discontinuity, the properties of the hydraulic fracture plane and the elastic properties of the surrounding intact material.

3.2.1 Model description

The model corresponds to a parallelepiped of 20 m $\times$ 10 m $\times$ 10 m cut by two intersecting fractures, respectively mentioned as the hydraulic fracture (black plane in Figure 3.6) and as the natural fracture (gray plane in Figure 3.6). The hydraulic fracture is favorably oriented, i.e. in the direction of the maximum stress, facilitating the propagation of fluid. The plane figuring the hydraulic fracture is introduced in the model as a pre-existing plane along which the hydraulic fracture is forced to propagate. Therefore, as the injection takes place, the hydraulic fracture is propagating along this plane presupposing the failure of the corresponding parts of the plane. Accordingly, the intact material is considered impermeable and the fluid is only propagating along the parts of the discontinuity planes that have failed in tension or shear mode.

The effect of the orientation of the natural fracture is investigated by rotating the natural fracture plane's dip. The dip angle rotation is measured from the horizontal, and it is varied from 0° to 80° with increments of 10° (Figure 3.6(c)). For a dip angle of 0°, the natural fracture is horizontal, thus perpendicular to the hydraulic fracture and to the vertical stress (σ_1). For a dip angle of 80° the fracture is

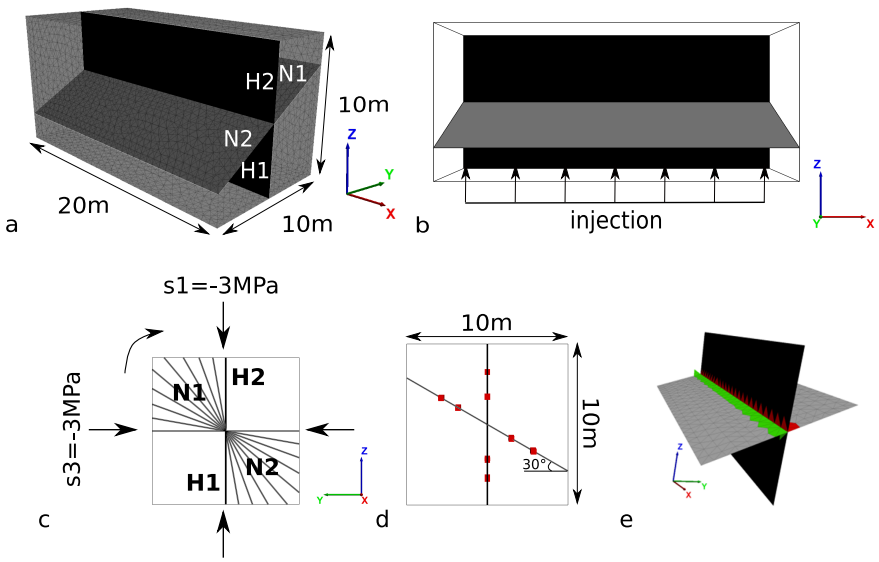

Figure 3.6: (a) Geometry of the numerical model, (b) application of injection pressure at the bottom of the hydraulic fracture plane, (c) stress field and rotation of the natural fracture dip from 0° (perpendicular to the hydraulic fracture) to 80° (almost parallel to the hydraulic fracture), (d) fluid pressure and displacement recording points (red squares) along the hydraulic and natural fractures, (e) flow zones (red and green) around the intersection for the calculation of the flow rate for each half-plane.

almost vertical, thus sub-parallel to the hydraulic fracture. The analysis is performed under plane strain conditions, meaning that only faults having poles within the σ_1-σ_3 plane are considered [Cox, 2010]. In this case, according to the Mohr-Coulomb criterion, the intermediate principal stress σ_2, the direction of which is parallel to the intersection line of the fractures, does not influence failure [Jaeger et al., 2009]. An initial pore pressure is applied inside the model and a vertical pore pressure gradient is applied from the bottom to the top model boundary to initiate the fluid propagation. The other boundaries are impermeable. The injection time is 15 seconds long, which corresponds to the time needed to reach a steady-state flow regime.

To simplify the analysis, the two planes of the model are both divided into half-planes (Figure 3.6(a)):

- The hydraulic fracture is divided into half-plane H1 below the intersection and half-plane H2 above the intersection with the natural fracture.
- Similarly, the natural fracture is divided into half-plane N1 on the left of the intersection and into half-plane N2 on the right of the intersection with the vertical hydraulic fracture.

Throughout the calculation and in order to capture the mechanical response of the natural fracture, the normal and shear displacement and the flow rate magnitudes are recorded for each half-plane (Figures 3.6(d) and 3.6(e)). In the hydraulic fracture, the flow rate is computed as a surface average for a group of zones along H1 half-plane just below the intersection with the natural fracture and for a group of zones along H2 half-plane just above the intersection with the natural fracture. In the natural fracture, the flow rate is calculated just after the intersection with the hydraulic fracture on both sides. This will provide the quantitative amount of fluid crossing or not the natural fracture.

3.2.2 Reference case

As a reference case, the stress field is considered isotropic with $\sigma_x = \sigma_y = \sigma_z = -3$ MPa and the dip angle of the natural fracture is 30°. The intact rock is modeled as a transversely isotropic shale material. The properties are taken from the well-documented Mont Terri shales (Bossart [2011] and Table 3.3). The bedding plane induced anisotropy is considered horizontal with the directions 1 and 3 being the directions parallel and normal to the bedding respectively. The properties of the natural fracture are in the range of values considered in the previous section in order to take into account properties that could well represent the reactivation of a natural fracture tested in situ.

Boundary conditions		
Stress field: $\sigma_x = \sigma_y = \sigma_z = -3 \times 10^6$ Pa		
Initial pore pressure: $pp_{ini} = 1.2 \times 10^6$ Pa		
Injection pressure: $p_{inj} = 4.5 \times 10^6$ Pa		
Rock matrix properties		
Density: $\rho = 2500 kg/m^3$		
Young's modulus parallel to bedding: $E_1 = E_2 = 7.2 \times 10^6$ Pa		
Young's modulus normal to bedding: $E_3 = 2.8 \times 10^9$ Pa		
Poisson's ratio parallel to bedding: $\nu_{12} = 0.24$		
Poisson's ratio normal to bedding: $\nu_{13} = \nu_{23} = 0.33$		
Shear modulus parallel to bedding: $G_{12} = 2.9 \times 10^9$ Pa		
Shear modulus normal to bedding: $G_{13} = G_{23} = 1.2 \times 10^9$ Pa		
Fractures properties		
	Hydraulic fracture	Natural fracture
Normal stiffness: K_n	200 GPa/m	200 GPa/m
Shear stiffness: K_s	4 GPa/m	4 GPa/m
Friction angle: ϕ	20°	20°
Cohesion: c	3×10^6 Pa	0
Tensile strength: σ_t	10^6 Pa	0
Hydraulic aperture: u_{h0}	1×10^{-4} m	1×10^{-4} m
Fluid properties		
Bulk modulus: $K_f = 2 \times 10^9$ Pa		
Density: $\rho_f = 1000 kg/m^3$		
Dynamic viscosity: $\mu = 10^{-3} Pa \times s$		

Table 3.3: Boundary conditions and material properties for the reference case (dip angle=30°).

The calculated time variations of fluid pressure, normal and shear displacements and flow rate in the four half-planes H1, H2, N1 and N2 are shown in Figure 3.7. The fluid pressures inside H1, N1 and N2 have reached approximately the injection pressure of 4.5 MPa imposed at the bottom of the fluid-driven fracture (see also Figure 3.8). No pressure variation occurred in H2 showing that the hydraulic fracture did not propagate above the intersection with the natural fracture. The flow rate in H1 and N1 shows a peak which is explained by the high hydraulic gradient as the fluid preferentially propagates from H1 to N1. Once a steady value is reached when the model boundary is reached at 1.3 seconds (Figure 3.8), the flow rate starts increasing in N2 until final stabilization. After 15 seconds of injection, all recorded signals have reached a steady state value, the fluid has propagated inside the fractures following a preferential flow path to connect with the model boundaries.

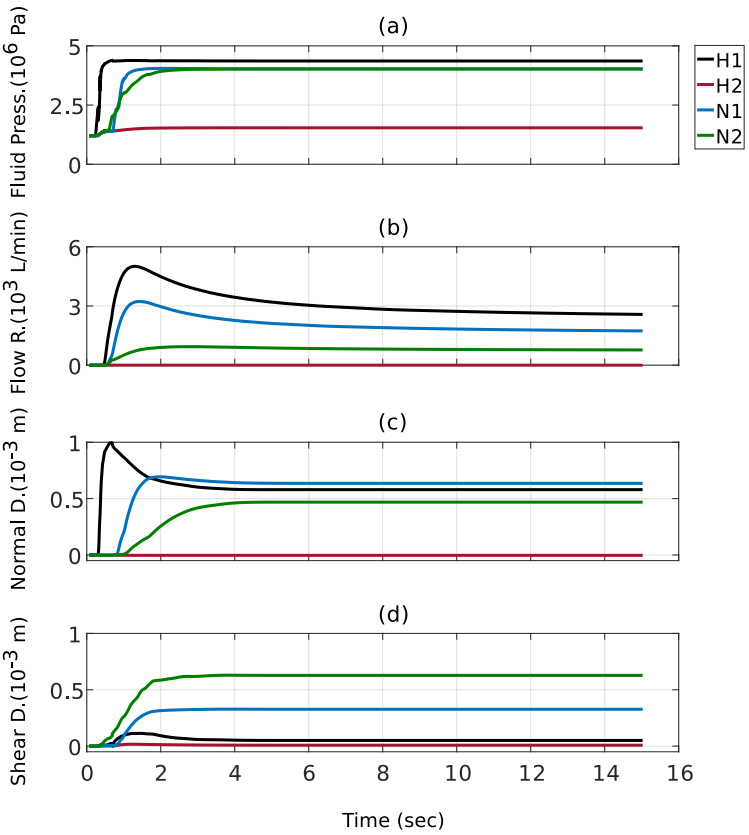

Figure 3.7: From top to bottom: (a) fracture fluid pressure, (b) flow rate, (c) normal displacement, (d) shear displacement versus time for the half-planes H1, H2, N1, N2.

The evolution of the mean stress (Equation 3.4 and Figure 3.8 left column) and of the second invariant of the deviatoric stress inside the model (Equation 3.5 and Figure 3.8 right column) are shown at different time steps in Figure 3.8. Fluid pressure in the fractures is superimposed to the stress contour maps. The negative mean stress values correspond to compressive stresses.

$$\sigma_m = \frac{1}{3}(\sigma_{11} + \sigma_{22} + \sigma_{33)} \tag{3.4}$$

$$J_2 = \frac{1}{6}[(\sigma_{11} - \sigma_{22})^2 + (\sigma_{22} - \sigma_{33})^2 + (\sigma_{11} - \sigma_{33})^2] + {\sigma_{12}}^2 \tag{3.5}$$

A hydraulic fracture interacting with a natural fracture can either cross it or stop due to the mechanical, or hydraulic or hydro-mechanical reactivation of the natural fracture. For 30° of dip orientation and for a homogeneous stress field, the hydraulic fracture does not cross the natural fracture. Accordingly, the calculated flow rate signals show that the flow rate of the half plane H2 (red line in Figure 3.7(b)) is null by the end of the calculation while the flow rate of the natural fracture's segments is increasing during the injection (blue and green lines in Figure 3.7(b)). Hence the natural fracture is hydraulically activated and the propagation of the hydraulic fracture becomes impossible ahead of the intersection. Both the normal and shear deformation of N1 and N2 half planes show opposite behaviors and significantly different values. There is a higher normal opening of N1 compared to N2, with final apertures 6 and 4 times higher than initial respectively in N1 and N2. Shear amplitude of N1 and N2 is opposite to normal amplitude

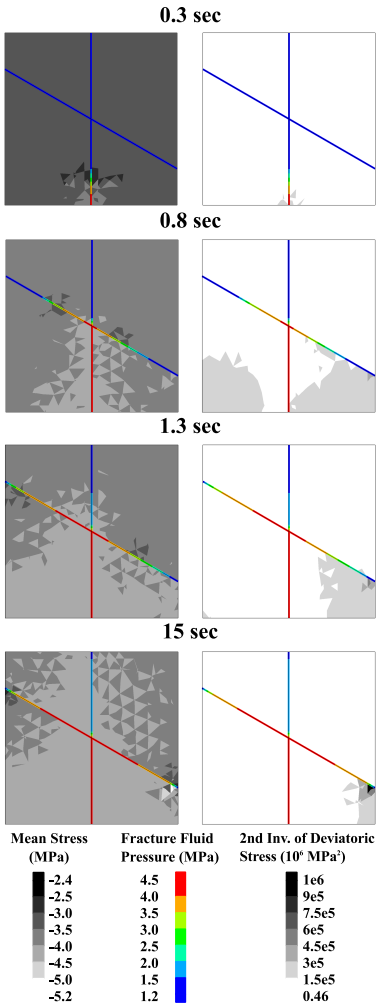

Figure 3.8: Evolution of the mean stress (left column), the second invariant of deviatoric stress (right column) and of the fracture fluid pressure at different injection times.

variations. N2 displays the smaller normal opening and the higher shear displacement. One can observe that shear displacement is also taking place in the H1 half-plane at earlier time steps of the injection even though the hydraulic fracture is supposed to grow under zero shear. Reminding at this point that the hydraulic fracture is growing along an imposed predefined plane and that the surrounding medium is not isotropic, we would expect some stress alterations as the pressure increases and the hydraulic fracture deforms. If the hydraulic fracture plane was allowed to deviate to a more favorable orientation imposed by the intact matrix anisotropy, it is possible that there would not be any shear displacement recorded along the plane.

In Figure 3.8, the evolution of the mean stress and of the second invariant of the deviatoric stress is illustrated for four different times during the simulation. As the fluid propagates and the hydraulic fracture plane dilates, the surrounding stress field is affected and the mean stress magnitude increases (Figure 3.8 on the left). This is a result of the increase of the fluid pressure inside the hydraulic fracture plane and the plane's subsequent deformation. As the plane deforms, the total minimum stress inside the rock matrix will become higher. Due to the Poisson's effect, an increase in the maximum and intermediate

stresses is also observed leading to an increase in the mean stress value. As the hydrofracture's tip approaches the intersection with the natural one (0.8 seconds in Figure 3.8), the increase in the mean stress magnitude is affecting a larger area of N2 compared to N1. This explains the delay in the fluid propagation inside N2, characterized by the delay in the fluid pressure variation and by the lower flow rate variation (Figures 3.7a and 3.7b). At $t = 0.8$ seconds and $t = 1.3$ seconds, there is an increase in the second invariant of the deviatoric stress close to the bottom corners of the model (Figure 3.8 on the right) affecting a surface area of N2 away from the intersection. This deviatoric stress increase originates from the hydraulic fracture propagation and from the induced total stress changes that will also affect the deformation of the intact surrounding material. Close to the bottom corners of the model, the intact material is deforming in shear contributing to the increase in the deviatoric component of the stress tensor. As a result, at 0.3, 0.8 and 1.3 seconds, N2 appears to deform in shear well before conducting the fluid.

3.2.3 Effect of natural fracture's orientation

Figure 3.9(a) shows that the flow rate in H2 never increases highlighting that the hydraulic fracture never crosses the natural fracture for all possible orientations of the natural fracture. The growth of the hydraulic fracture is stopped at the intersection with the natural fracture. The half-plane H2 is only exhibiting some negligible shear displacement (red line in Figure 3.9(c)) as a result of stress transfer mechanisms. As N1 dilates an increase and reorientation of the total stresses takes place in the block between N1 and H2. Due to the isotropic stress state acting on the fracture system, we can observe a symmetrical response in terms of flow rate, normal and shear displacement magnitudes of the half-plane N1 above and below a critical rotation angle approximately of 40°. N1 stays hydraulically active for all the natural fractures dip angles with a maximum value at the 40° dip angle, where the maximum shear displacement is also recorded for the same half-plane. The shear displacement of the half-plane N1 is increasing around 20°, which is coherent with the friction value of 20° assigned to the fracture.

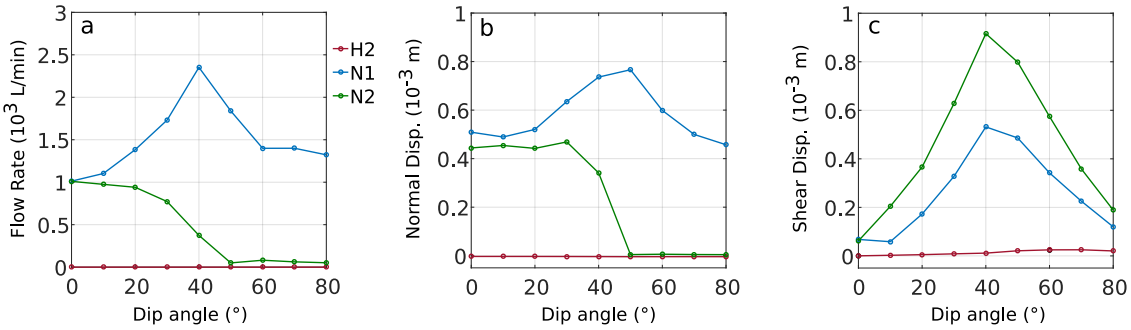

Figure 3.9: From left to right; (a) variation of the flow rate, (b) the normal displacement and (c) the shear displacement versus the dip angle of the natural fracture at the end of the simulation for half-planes H2, N1, N2.

On the other hand, the behavior of the half-plane N2 is dominated by the normal opening of the hydraulic fracture and by the consequent stress transfer. For higher dip angles and as the plane gets sub-parallel to the hydraulic fracture plane, N2 hydraulic activation becomes highly limited under the action of an increased normal stress. For all possible natural fracture orientations, N2 shear displacement (green line in Figure 3.9(c)) is higher than N1 (blue line in Figure 3.9(c)). As explained in the reference case,

stress transfer effects determine the response of N2 by promoting shear displacement along the part of the half-plane that is closer to the model boundaries (Figure 3.8, right column).

3.2.4 Effect of the initial loading and stress conditions

In order to estimate the effect of the stress field, the maximum stress (σ_1) and the pore pressure are varied considering four cases:

- A differential stress of 2 MPa (corresponding to an increase of σ_1 from 3 to 5 MPa)
- A differential stress of 20 MPa (corresponding to an increase of σ_1 from 3 to 23 MPa)
- An initial fracture pore pressure of 0.2 MPa
- An initial fracture pore pressure of 2 MPa

For an increase of 2 MPa of the differential stress, the flow rate is highly limited for N1 and N2 dip angles $\leq 60^\circ$ (green line in Figures 3.10(a), 3.10(d)). Above 60°, the hydraulic fracture growth is prohibiting the hydraulic activation of N2 (green line in Figure 3.10(d)). Therefore, it is only for angles $< 30^\circ$ between the hydraulic and the natural fracture that the total stress increase due to the hydraulic fracture propagation will affect the response of the natural fracture.

For a principal stress difference of 20 MPa, the natural fracture remains hydraulically inactive for all the dip angles orientation (green dashed curves in Figures 3.10(a) and 3.10(d)). The two segments of the natural fracture respond in the same mechanical way. It appears that for orientation angles of 30° to 70°, the natural fracture is undergoing a mechanical closure (negative values for the green dashed curves in Figures 3.10(b) and 3.10(e)) accompanied by a large slip (green dashed curves in Figures 3.10(c) and 3.10(f)).

For the same range of dip angles, the hydraulic fracture is not reaching the intersection with the natural fracture. This is shown in Figure 3.11 where the stress tensor components magnitudes inside the model can be seen together with the fluid pressure along the fracture for 20° (Figure 3.11 left) and 50° dip angle (Figure 3.11 right), for the area around the intersection. Under such a high differential stress and for critical fracture orientations (in this case $> 20^\circ$) the natural fracture is slipping well before the injection and propagation takes place. The stress field in the intact rock is reorganized with the minimum stress magnitude increasing significantly. Hence, a higher pressure is needed for the propagation of the hydraulic fracture.

Varying the initial pore pressure of the formation shows that no significant impact of the initial pore pressure value is observed (red and red dashed curves in Figure 3.10) while there is a strong effect of the applied stress. In cases of extreme stress difference the propagation of the HF can be stopped due to the slip of the natural fracture and to the subsequent increase of the minimum stress. For a non-hydrostatic stress field, the far-field stresses will determine the response of the system. For slightly higher differential stresses, the stress transfer effects will be of second order importance inside the model and it is only for very low angles between the natural fracture and the hydraulic fracture that the total stress changes will limit the natural fracture's reactivation ($< 30^\circ$). In the case of very high differential stresses, the natural fracture will be reactivated for a wide range of critical orientations even before the propagation of the

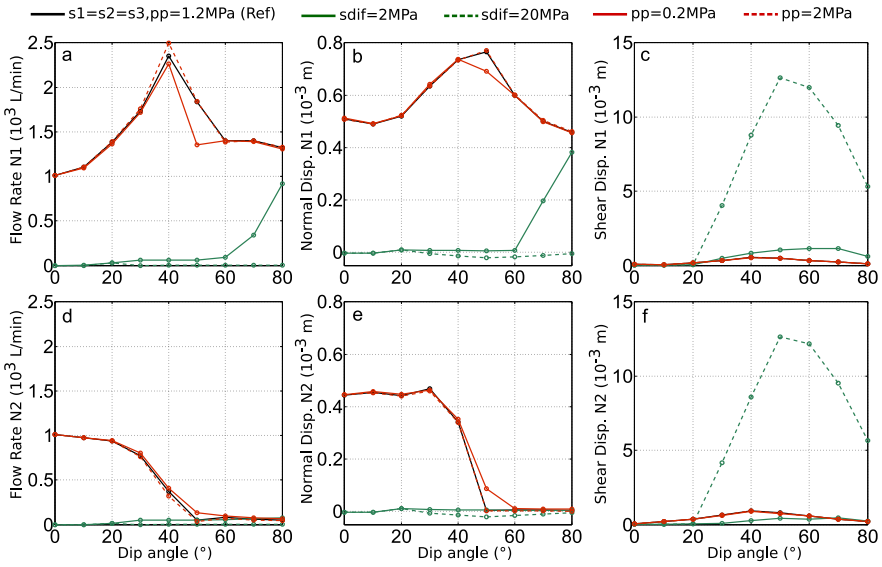

Figure 3.10: Variation of flow rate (left column), normal displacement (middle column) and shear displacement (right column) for N1 (top line) and N2 (bottom line) as a function of stress and initial pore pressure.

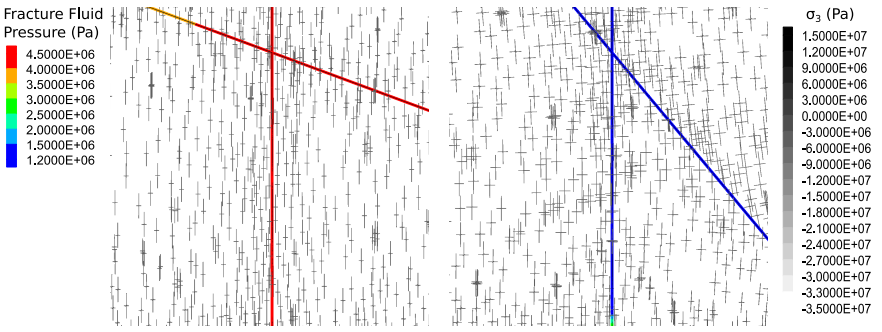

Figure 3.11: Stress tensor magnitudes inside the model and fluid pressure variation along the fracture for 20° (left) and 50°(right) natural fracture dip angle.

hydraulic fracture. Stress magnitude alterations that are promoted can affect significantly the propagation of the hydraulic fracture.

3.2.5 Effect of the material properties

Mechanical properties of the natural discontinuity

The elastic normal and shear stiffness of the natural fracture do not influence much the response of the fracture (Figure 3.12). For a 10 times lower shear stiffness, N1 appears more permeable (red curve in Figure 3.12a) and N2 less permeable for a dip angle of 40° to 60° (red curve in Figure 3.12d). The normal deformation of the half-planes follows more or less the flow rate evolution. Shear displacement in N1 is unchanged whereas shear displacement in N2 changes according to the assigned shear stiffness value. This points out the difference between the induced shear displacement of each half plane. More specifically, N1 shear displacement is the result of effective stress variation not dependent on the elastic properties of the natural fracture. On the other hand, above a critical angle, the shear displacement of N2 induced by

the fluid-driven fracture propagation is determined by the elastic properties of the fracture.

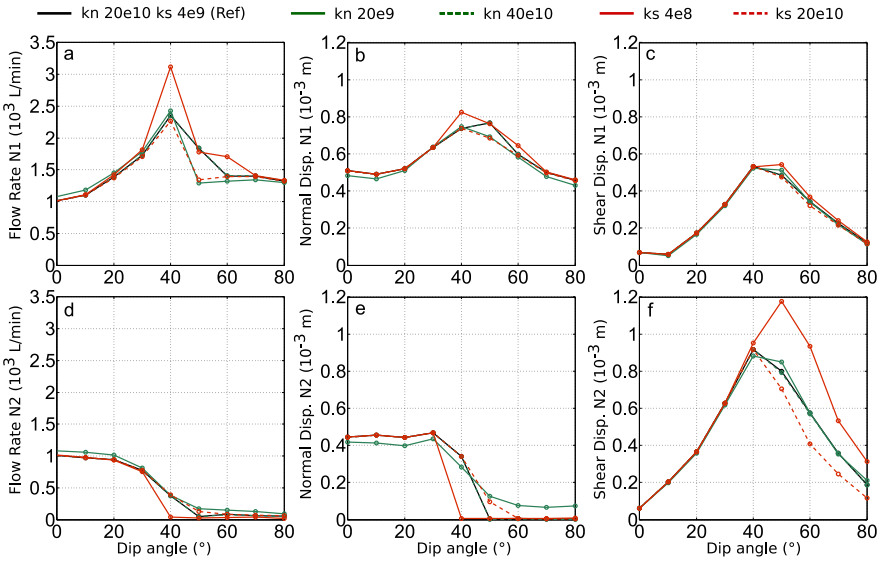

Figure 3.12: Variation of flow rate (left column), normal displacement (middle column) and shear displacement (right column) for N1 (top line) and N2 (bottom line) as a function of the elastic properties of the natural fracture.

The effect of friction variations on the shear displacement is limited as the model shows an almost identical to the reference case response, except for a very low friction angle $\leq 10^\circ$ (red curves in Figure 3.13). Below a friction angle of 10°, the half-planes are influenced in a different way. At 40° of orientation, N1 is more conductive than the reference case whereas N2 is not activated. The effect of the variation of the dilation angle on the hydro-mechanical response of N1 is negligible as by the end of the calculation, the normal opening of the fracture reaches its maximum possible value for all cases considered (Figures 3.13(b), 3.13(c)). The normal deformation of N2 is increased for higher dilation angles and higher dip angles (green dashed curve in Figure 3.13(e)), accompanied by a slightly enhanced resulting permeability (green dashed curve in Figure 3.13(d)).

Elastic properties of the intact material

In the reference case, the intact material of the model is considered as transversely isotropic, accounting for the anisotropy induced by the bedding planes. Two cases are examined with a Young's modulus $E = E_1$ and a Poisson's ratio $v = v_{12}$ (green curves in Figure 3.14) and $E = E_3$ and $v = v_{13} = v_{23}$ (blue curves in Figure 3.14). In addition, a bi-material model is considered as a third configuration where the natural fracture is a bi-material interface separating two media with different elastic properties (red curves in Figure 3.14). Above the natural fracture, the medium is characterized by $E = E_3$ and $v = v_{13} = v_{23}$ and below the fracture, the second medium is characterized by $E = E_1$ and $v = v_{12}$. When the intact material is isotropic and stiffer ($E = E_1$), the normal deformation and flow rate magnitudes are increased for both half-planes (green curves in Figures 3.14(a), 3.14(b), 3.14(d), 3.14(e)). On the other hand, the shear deformation appears limited (green curves in Figures 3.14(c), 3.14(f)). In the isotropic and softer intact

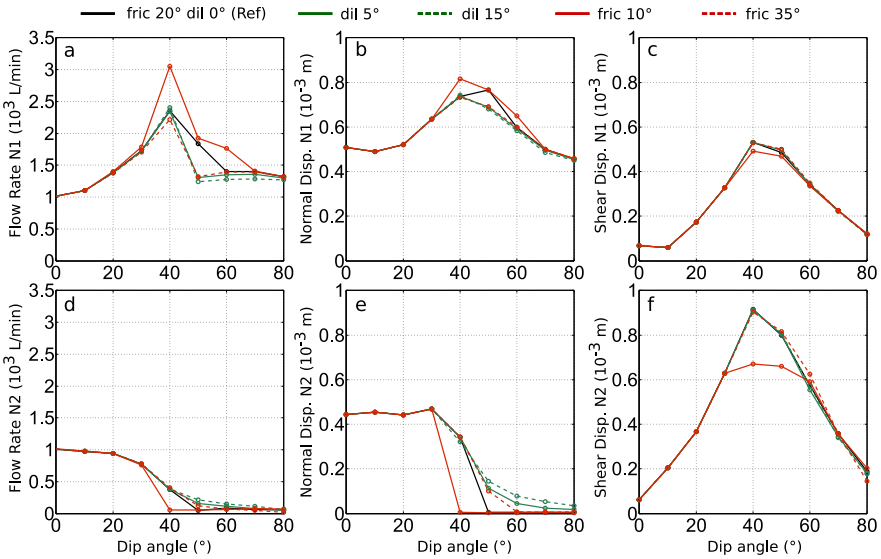

Figure 3.13: Variation of flow rate (left column), normal displacement (middle column) and shear displacement (right column) for N1 (top line) and N2 (bottom line) as a function of the strength properties of the natural fracture.

material case, the calculated flow rate and normal displacement are higher than the reference case (blue curves in Figures 3.14(a), 3.14(b), 3.14(d), 3.14(e)).

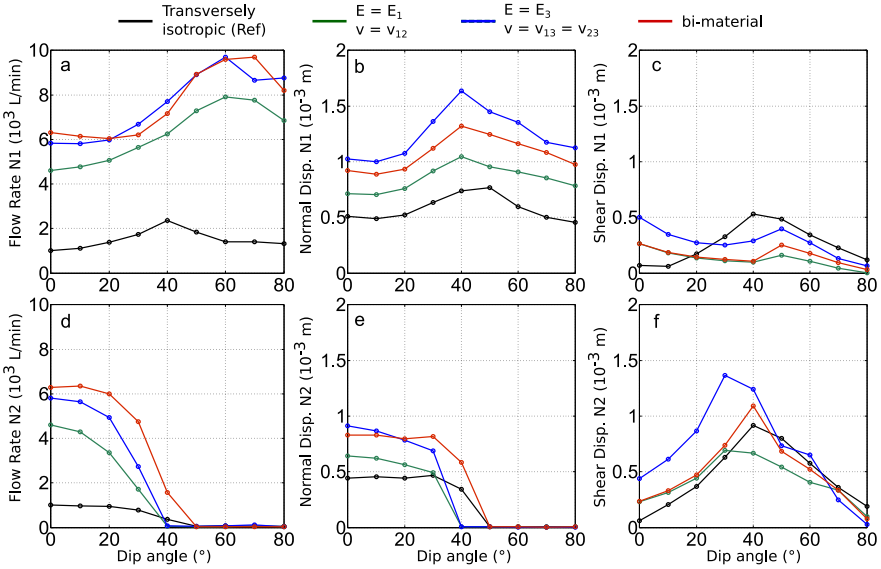

Figure 3.14: Variation of flow rate (left column), normal displacement (middle column) and shear displacement (right column) for N1 (top line) and N2 (bottom line) as a function of the elastic properties of the surrounding medium.

N1 shear deformation stays generally lower than the reference case in this configuration (blue curve in Figure 3.14(c)) whereas N2 shear deformation increases (blue curve in Figure 3.14(f)). Similar trends are observed for the bi-material model (red curves in Figure 3.14). It is shown that the flow rate calculated in the half-planes N1 and N2 is higher when the planes are surrounded by the isotropic material or

when a bi-material interface is considered (Figures 3.14(a), 3.14(d)). The volumetric strain increment of the surrounding intact material is shown in Figure 3.15 for a natural fracture orientation of 40° in all cases considered. The volumetric deformation of the transversely isotropic material (Figure 3.15(a)) appears to be the lowest among the cases studied. Thus, the material appears more compliant in the isotropic and the bi-material cases explaining the higher calculated magnitudes of flow rate and normal deformation of the half-plane N1. Considering the response of N2, it is again conditioned by the stress transfer due to the deformation of the hydraulic fracture. Nevertheless, depending on the elastic properties and the deformability of the medium the response of N2 could be less affected by the hydraulic fracture propagation. In the case of a more compliant medium, a larger part of the deformation will be accommodated by the intact material elastically deforming. Therefore the stress effect will be less pronounced and N2 will exhibit a higher normal deformation with a higher calculated flow rate for the isotropic and bi-material models.

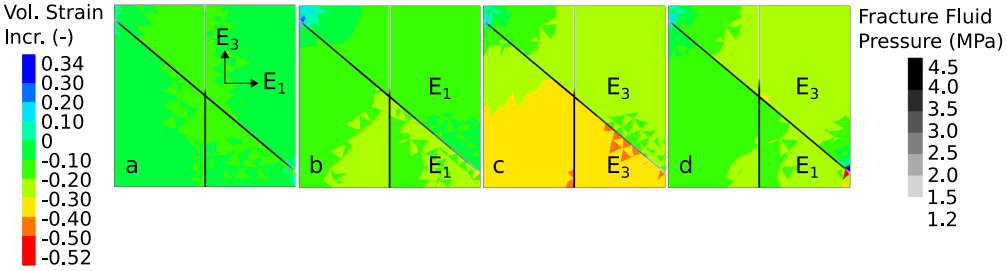

Figure 3.15: Volumetric strain increment and fracture fluid pressure variation for a) transversely isotropic material (reference), b) isotropic material with $E = E_1$ and $v = v_{12}$, c) isotropic material with $E = E_3$ and $v = v_{13} = v_{23}$, d) bi-material model with $E = E_1$ and $v = v_{12}$ below the natural fracture and $E = E_3$ and $v = v_{13} = v_{23}$ above the natural fracture.

N2 stays hydraulically active around 40° when elastic anisotropy is introduced either in the bi-layer model or in the transversely isotropic model (black and red curve in Figure 3.14(e)). For the half-plane N1, the curve showing the response of the fracture as a bi-material interface is always between the curves of the two isotropic material cases (red curves in Figures 3.14(a), 3.14(b), 3.14(c)). The shear displacement on N1 is higher for a transversely isotropic material than for an isotropic one. N2 is exhibiting higher shear displacement when a weaker Young's modulus characterizes the layer above the plane (blue and red curve in Figure 3.14(f)). For higher dip angles $> 40°$, the recorded magnitudes vary in the same range approximately.

Mechanical properties of the hydraulic fracture

In the reference case, under an isotropic stress state, the hydraulic fracture was characterized by similar-to-the-rock-matrix properties, demanding a higher fluid pressure for its propagation compared to the one needed to reactivate the natural fracture. If the hydraulic fracture is assigned the properties of the natural fracture, therefore the system is modeling two intersecting natural fractures without cementation or surface contact areas (Figure 3.16). The original natural fracture is behaving in almost the same way as the reference case pointing out the effect of the material anisotropy. If the material was isotropic, we would expect a fluid path from the half-plane H1 into the half-planes N1 and H2 since the stress field is homogeneous and the properties of the fractures are identical. However, under the effect of the

material anisotropy the fluid preferentially propagates inside the original natural fracture (N1) because H2 is perpendicular to the direction of higher Young's modulus.

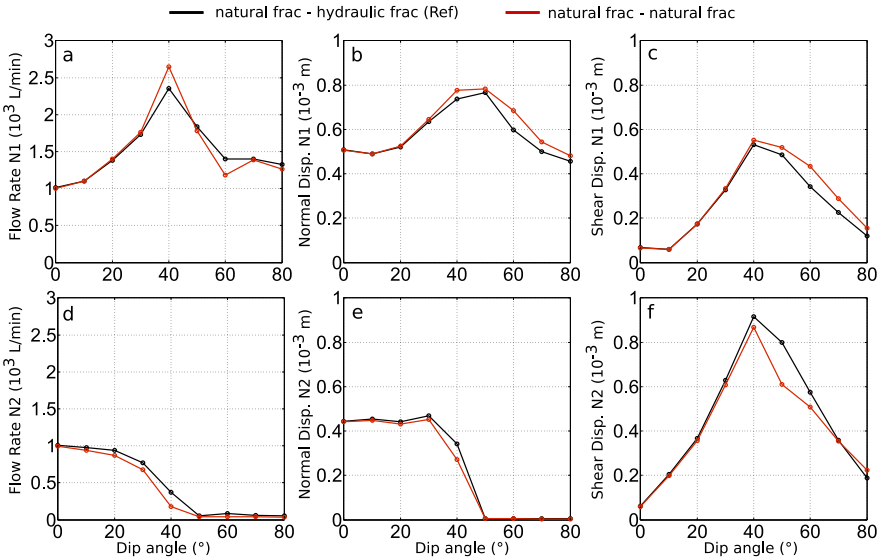

Figure 3.16: Variation of flow rate (left column), normal displacement (middle column) and shear displacement (right column) for N1 (top line) and N2 (bottom line) as a function of the strength properties of the hydraulic fracture (system of two intersecting natural fractures).

3.3 Discussion

In the model described in Section 3.1, the effect of fracture network geometry was considered. The properties of the fractures were identical and the inter-connectivity was assumed to be high since all fractures were persistent. Nevertheless, the fracture network was not found to be overall stimulated apart from a rather small number of fractures that conducted the fluid promoting flow channeling at the scale of the network. The effect of the stress field and of the orientation of the fractures was pointed out through the results obtained. Only a few fractures appeared to be hydraulically stimulated in the models, showing the strong dependency of fracture reactivation on its orientation with respect to the ambient stress field. Even if a high number of fractures were considered, the flow appeared to be always localized along critically stressed fractures which are prone to shear failure and dilatancy induced aperture increase (e.g. Min et al. [2004]). It was observed that for the present stress conditions, the fractures characterized by a dip angle lower than 40° cannot serve as potential fluid paths under a fluid pressure increase in the presence of more favorably oriented fractures.

Comparing with the experimental data, it was not possible to reproduce the observed reversibility of the displacements and the abrupt decrease of the flow rate with the models presented in this section. Modeling results for Test 1 reported in Rivet et al. [2016] succeeded to represent part of the displacements reversibility. Nevertheless, the geometrical configuration presented was a specific fracture representation that proved to best match the displacements evolution. In an effort to understand the mechanisms behind the in-situ response of the stimulated volume, fracture interaction could still be one dominant mechanism. However, reproducing in a numerical model a similar mechanism would require considering a large

number of different combinations and scenarios due to the uncertainty regarding the geometry of the network and the fractures' hydro-mechanical properties. Another possible mechanism that could explain the measured fault response is the channeling of the flow at the scale of a major fault or fracture. As hydraulic activation is observed at a fluid pressure which is well below the minimum principal stress, the scenario of a sub-critical permeability increase without fault mechanical instability can be considered. This scenario is further discussed in the next chapter (Chapter 4) where a model was set up to account for a channeling flow regime that could partly explain such behavior.

Apart from the pressure decreasing part of the test, the numerical study presented above can provide some information regarding the properties of the surrounding fractures. Discrepancies between the measured data and the model results, suggest that the fractures dipping $< 20^\circ$ are characterized by "stronger" mechanical properties than the ones assumed in the modeling. This might be attributed to the strong cementation present in the fault zone. Modeling of the fractures dipping $> 20^\circ$ showed reasonable agreement with the field data. This implies that this fracture family is characterized by properties closer to the properties of the secondary fault. However, the high calculated flow rate implies that even though the sub-vertical fractures could contribute to the response mechanically, their hydraulic activation is much more limited in situ. It is possible that these structures could be better considered as partially calcified, implying a channeling flow regime along their plane due to the presence of calcite patches and therefore heterogeneous properties. It was shown that only a few fractures dominate the reactivation which in turn can not be explained and described just by the critically stressed fault concept. The criticality of the fault is a necessary condition for its reactivation as shown above but it is not sufficient to explain and predict the variation of the fault permeability upon reactivation.

The sensitivity study performed with the model of two intersecting fractures showed the importance of three parameters, i.e. the stress field, the fracture's orientation with respect to the maximum stress and the intact rock's elastic properties. Based on the numerical results, we observe two distinct responses on the same natural fracture plane showing that even for a simple configuration, the mechanisms due to fracture interaction can be quite complex. A natural fracture cut by a fluid-induced or cemented fracture will respond differently on each one of its sides. The response depends on the orientation of the plane with respect to the maximum principal stress and on the angle between the natural and the hydraulic fracture.

The response of the half plane which is away from the HF (N1) is conditioned by the effective stress variations in the plane, which is in accordance with previous works focusing on the hydraulic-natural fracture interaction [Blanton et al., 1986; Warpinski et al., 1987; Zhou et al., 2008] and failure and fracture-controlled permeability enhancement in fault zones [Fournier, 1996; Cox, 2010]. Under an isotropic state of stress, and for a range of fracture and rock properties, the half-plane is activated for all possible orientations. When the stress field is isotropic the fluid absorbed by the NF induces a pressure decrease in the HF and when there is a high differential stress, shear failure along the NF favors an increase in σ_3 relative to σ_1 close to the HF tip which can stop the HF propagation. This result is complementary to other theoretical studies that showed that for high differential stresses and specific angles of approach (probably depending on the friction coefficient) the hydraulic fracture does not cross the natural fracture but is arrested instead by shear slippage with no opening and diverting of fluid of the natural fracture [Warpinski et al., 1987; Zhou et al., 2008; Liu et al., 2015]. For a moderate differential stress, resulting in a stress ratio $\frac{\sigma_1}{\sigma_3} = 2$ which is similar to the natural stress conditions of Test 1 ($\frac{\sigma_2}{\sigma_3} \approx \frac{\sigma_1}{\sigma_3} = 2$) described above, the half plane is reactivated for a dip angle $> 60^\circ$ meaning an angle $< 30^\circ$ with respect to σ_1. This

is representative of the response observed in the modeling results of the multi-fracture model of Test 1 in the previous section where only fractures characterized by an orientation $< 40°$ with respect to σ_2 (which is very close to σ_1) can act as potential fluid paths while the rest stay almost completely hydraulically inactive.

Considering the half plane the closest to the HF and an almost isotropic state of stress, the natural fracture will "easily" absorb the fluid for HF-NF angles $> 50°$. For a slight ~ 2 MPa differential stress, the natural fracture will only experience a purely mechanical shear activation for HF-NF angles $< 50°$. This kind of natural fracture response was not observed in the Test 1 multi-fracture model since the normal deformation of the reactivated planes was limited and part of the fractures formed an angle $\geq 50°$ with the reactivated planes. For higher differential stresses of ~ 20 MPa, shear is triggered on a larger zone affecting the two natural fracture's half planes.

Considering the well studied fracture interaction and microseismic monitoring during hydraulic fracturing operation for unconventional shale reservoirs, this contrasted shear behavior of the two half-planes shows that both "wet" and "dry" events can be potentially produced on the same stimulated natural fracture. The "dry" events are associated to the response of the plane that is closer to the fluid-driven fracture that exhibits shear deformation that is not related to fluid flowing into the fracture. This is a complementary result to previous works from [Nagel et al., 2013] that showed that stress transfer effects could trigger "dry" events on fractures not hydraulically connected to the propagating HF.

The hydraulic fracture in the models is strictly developing along a pre-defined plane. This can be considered as a strong assumption for newly created fractures since even if the crack would mainly grow along the direction of the maximum stress, direction changes are possible near the interfaces due to interactions between the sheared and dilated fracture branches [Jeffrey et al., 2009]. Under an isotropic stress field, a reorientation of the stress field is observed in the model at the tip of the hydraulic fracture on a very local scale and for early time steps (around 0.3 seconds) probably due to the anisotropic nature of the intact material. Indeed, at zero or low differential stresses, variations in material properties tend to become more important than stress orientation in controlling the direction of fracture propagation [Blanton et al., 1986]. Nevertheless, the assumption of a pre-defined plane of propagation or activation is not very strong if we consider that the fracture is a pre-existing plane characterized by a higher cohesion and tensile strength or high fraction of surface contact areas.

The sensitivity analysis results show that the mechanical properties of the natural fracture slightly influence the response of the HF-NF interactions while the bulk properties of the surrounding material have a significant impact mainly on the magnitudes of the flow rate and displacements of the natural fracture. Indeed, for a lower shear stiffness, an increase of the flow rate was observed for N1 and a decrease for N2 at a dip angle equal to $40°$. A friction angle of $10°$ lower than the reference case had the same effect as the shear stiffness on the flow rate of the two half-planes and finally the value of the initial aperture defining the value of the initial permeability will not influence the nature of interaction. When an anisotropy of the intact rock properties is considered or when the natural fracture is figured as the boundary between two materials of contrasted elastic properties, the flow rate and normal deformation tend to significantly vary while the shear displacement on the fracture plane remains more or less the same. Anisotropy of the mechanical elastic properties which is a common feature of shales and of many sedimentary rocks is known to influence the in-situ stress [Amadei et al., 1987]. We show that in the case of a HF propagating in a uniform and homogeneous horizontal anisotropic rock under an isotropic state of stresses, fluid preferentially propagates inside the natural fractures that are the most favorably

oriented with respect to the direction of elastic anisotropy characterized by the higher Young's modulus. Bi-material interfaces are often encountered in fault zones where slip surfaces develop at the boundary between high elasticity granular and intensely deformed cores and fractured damage zones. Our results are in good accordance with studies showing that contrasted bi-material properties favor changes in the compressive normal stress and promote slip on the interface between the two materials [Weertman, 1980; Cappa, 2011].

3.4 Summary

Summarizing, two models were presented in this chapter, the first one (Section 3.1) corresponded to the in-situ injection Test 1 and the second was set up in order to perform a parametric analysis regarding the factors influencing fracture interaction (Section 3.2). The first model was constructed with the purpose of estimating the effect of the fracture network geometry on the hydro-mechanical response observed during Test 1. While with the specific model it was not possible to reproduce the reversibility of the fault's displacements, useful information were provided. The significant role of stress and orientation was confirmed in both models showing that under an intermediate differential stress, fractures forming an angle $> 40^{\circ}$ with the maximum stress cannot be reactivated unless they are characterized by a very low coefficient of friction (e.g. Sibson et al. [1988]). Modeling of Test 1 gave an idea about the in-situ properties of the fracture families by comparing the numerical results with the experimental observations and by evaluating the respective role of each family. Finally, the sensitivity analysis performed with the simple two fractures model showed that contrasted responses can coexist on the same fracture plane depending on the orientation and size of the natural fracture and on the stress field with regard to the fluid-induced fracture propagation plane. More specifically, a de-coupling between the permeability and the shear displacement may occur along the natural fracture plane (mostly in the case of a homogeneous stress field). Indeed, if the NF orientation is close to the HF's one (less than 60° between the two planes) part of the NF will experience a high shear displacement and a limited permeability increase. This results show that the slip induced by effective stress variation within the fracture and the slip induced by total stress changes away from the fracture plane may coexist within the same stimulation volume. Characterizing the orientation and stress field are thus first order parameters to improve our understanding of fracture interaction. Nevertheless, the hydro-mechanical properties of the natural fracture have a minor effect on the response of the natural fracture compared to the influence of the elastic properties of the medium.

Chapter 4

Role of fault heterogeneities on rupture and fault permeability variation

In this chapter, a model is presented taking into account the heterogeneities of the fault resulting from asperities, infill material patches or rock bridges. At the scale of the fault structures these heterogeneities might result from the different fracture orientation as discussed in the previous chapter. Such heterogeneities are known to affect the hydro-mechanical response of a single structure or a fracture network. At the scale of a single fracture, the presence of contact areas and asperities will result in channeling of the flow if the fluid pressure is not high enough to cause the contacts to fail mechanically. In terms of hydraulic properties, this channeling process is enough to generate a fracture permeability that will be much higher than the intact rock's permeability. The fracture is therefore able to conduct the fluid at relatively high rates without exhibiting a major slip event as only a part of the plane is hydro-mechanically active. This process has been referred to as a subcritical permeability increase and has been observed in several cases (see section 1.3.2). Using a simple model, the effect of flow channeling on fault permeability is evaluated. In addition, channeling is discussed as a potential process that can promote migration of fluids along rather mechanically "inactive" faults. In this context, the controversial case of the South Eugene Island minibasin is also discussed based on the numerical results.

4.1 Subcritical permeability increase induced by channelling effects

As mentioned in Chapter 2, a number of tests were performed at the Tournemire fault zone in different locations (see also Figure 2.3). For all tests performed within the fault zone, a large increase in flow rate at constant pressure was observed after reaching a threshold pressure. Such threshold pressure value has also been observed for different types of rock, even stiff ones like granite [Cornet et al., 2003]. Analyzing the transmissivity-pressure relation for the Tournemire tests, the transmissivity exhibited a substantial increase (more than 100 mL/min) only above this pressure threshold which has been called the Fault Opening Pressure (FOP) (Henry et al. [2016], Chapter 3, Figure 4.1). Nevertheless, even below the FOP, the permeability values recovered for each test were found to be several orders of magnitude higher than the permeability of the shale formation (less than 10^{-19} m^2).

Mainly focusing on Test 1 described in the previous chapter (Chapter 3), it was observed in brief that

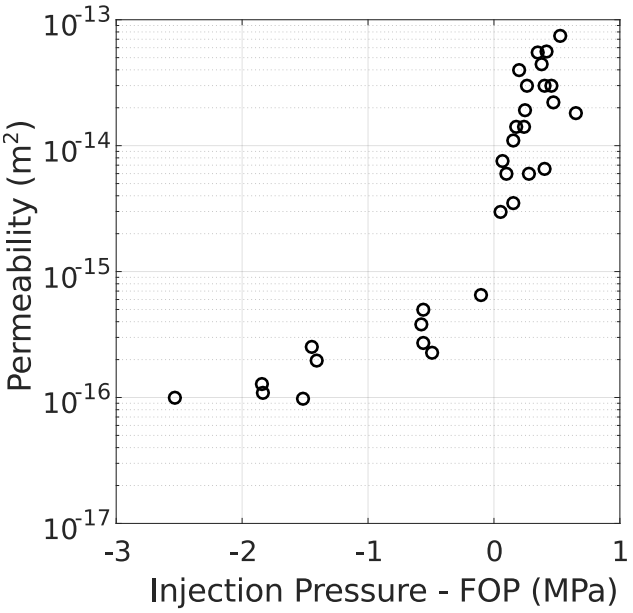

Figure 4.1: Permeability as a function of pressure in the injection borehole relative to the Fracture Opening Pressure (FOP) for all tests performed during the Tournemire tests. The FOP is defined for a resulting injection flow higher more than 100 mL/min.

(i) fracture opening (axial displacement) was always associated to shear displacement, (ii) the hydraulic opening, i.e. the large increase in the flow rate, occurred below the in-situ minimum stress, σ_3 and (iii) a significant part of the deformation associated with the hydraulic opening appeared to be associated with a low level of irreversible displacement, of a maximum order of a hundred of micrometers (see also Figure 2.7). Comparable observations were obtained from similar tests carried out at the Mont Terri Main fault zone affecting shale layers. During the tests, high leakage potential was induced by relatively low infra-millimeter slip movements with a low level of irreversibility [Henry et al., 2016]. This has also been observed in laboratory experiments on different rock types, like tuff for which the hydraulic properties of the fracture can change up to a factor of 3 under a shear displacement that is well below the millimeter [Ahola et al., 1996].

In addition to the hydro-mechanical measurements, geophysical anomalies [Rivet et al., 2016], seismic activity [De Barros et al., 2016] and leakage through boreholes and the tunnel EDZ several meters away from the injection location, showed that water flow was channeled.

Based on the results obtained from the field injection tests, a numerical model has been set up in order to better understand the hydro-mechanical conditions under which the flow rate and permeability increase dramatically depending on the fluid pressure while the mechanical response of the hydraulically loaded zones, exhibits a relatively minor irreversible strain response. Using the results of the model, the study carried out by Finkbeiner et al. [2001] is revisited concerning the Eugene Island case. More specifically, the possibility that the fluids are being transiently channeled along the fault plane through the propagation of fluid pulses is discussed. This could also be a complementary observation to the mechanical significance of the solitary pressure waves propagation [Rice, 1992; Henry, 2000; Revil & Cathles, 2002; Bourlange & Henry, 2007].

4.1.1 Numerical modeling

Model description

The model consists of a 2 m cube cut by a single sub-vertical fault oriented N171/86°W with a prescribed response that follows the Coulomb criterion for the reference configuration. The surrounding intact material is elastic and impermeable. Hence, flow only occurs along the fault plane and strictly along the parts of the plane that have failed either in shear or in tension. The stress field applied is in the range of the in-situ stress values measured from the Tournemire fault experiments. Similarly, the orientation of the fault plane is close to the main orientation of the Tournemire fault and the hydro-mechanical properties used have been calibrated based on the field experiments (Test 1 and Test 2). Previous modeling efforts of Test 1 assuming a single and homogeneous slipping plane could well reproduce data during the first steps of the pressurization associated to the hydraulic opening of the Tournermire tests [Guglielmi et al., 2015b], but they remain limited to explain the observed FOP associated to a low plastic response. The FOP concept associated to this limited mechanical response might be a consequence of the heterogeneous nature of the stimulated rock volume. Models considering fracture interactions might explain partly the limited irreversibility of the slip movement [Rivet et al., 2016] but they make reference to a complex and very specific spatial organization of the fracture set as discussed in Chapter 3. At the fracture scale, a possible explanation of this behavior is that the permeability depends directly on the flow rate [Candela et al., 2015; Jeanne et al., 2018]. However, the physical meaning of such a relationship requires further studies in order to be better understood. Taking into account the in-plane heterogeneities can also explain the observed FOP with the plane's permeability increase and limited slip motion while explaining explicitly the channeling process of the fluid [Cornet et al., 2003; Dick et al., 2016]. In the present model, heterogeneities along the fault plane have been considered in terms of mechanical properties in order to account for the presence of a roughness on the fracture plane. The model's geometry together with the applied stresses is presented in Figure 4.2(a).

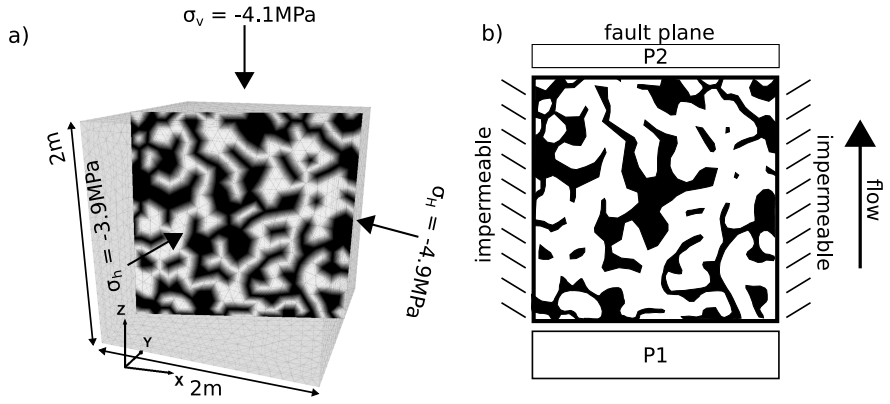

Figure 4.2: Geometry of the numerical model with the stress field applied and the distribution of the heterogeneities along the plane. The white areas represent low friction areas while the black areas represent the high friction areas. (b) Hydraulic pressure applied at the boundaries with P1 larger than P2.

The implementation of heterogeneities along the discontinuity is based on the fact that the fluid is only propagating in fault areas where the sub-contacts have failed either in tensile or shear mode. High friction areas correspond numerically to a percentage of the sub-contacts that will be statistically assigned

a higher friction value using a random function in 3DEC. In the case of 50% of higher friction areas, the function used is based on the probability of a random function to be above 0.7 while looping over the model's sub-contacts. Therefore, for each sub-contact the following test is performed:

- if $v > 0.7 \rightarrow$ high friction sub-contact
- if $v < 0.7 \rightarrow$ low friction sub-contact

where v is a variable returning a random number drawn from uniform distribution in the range [0, 1] and the number on the right of the condition depends on the desired percentage of high friction fault areas.

For comparison, four configurations have been selected. The first one considers a homogeneous plane with a constant friction angle of 15° that has been assigned on the overall fracture plane without any cohesion or tensile strength. Then, three other configurations have been considered. In the three other configurations, the heterogeneities, i.e. the asperities have been introduced along the fracture surface by selecting in a random manner different zones representing 50% of the total surface. In the second configuration, asperities have a friction of 40°, in the third one, the friction is still 40° but with added cohesion of 1 MPa and for the last configuration, a tensile strength of 1 MPa is added (see Table 4.1). The spatial distribution of these heterogeneities or asperities along the plane, is represented by the black zones in Figure 4.2(a),(b). Based on the assigned properties, the higher resistance zones can either represent frictional heterogeneities such as gouge patches, contact areas or calcified zones along the fault plane [Lefèvre et al., 2016]. Regarding the size distribution of the heterogeneities, one could use a power-law distribution but since the model covers a narrow range of scale a uniform distribution has been used, securing that the connectivity of the low friction parts (white zones) is high enough to allow the fluid to cross the medium through these low friction zones (Figure 4.2(b)).

Initially, in order to calculate the failure envelopes for the heterogeneous configurations, a fluid pressure is applied uniformly over the whole plane for different stress states. Increasing progressively the fluid pressure, mechanical instabilities appear leading ultimately to a general slipping process. The resulting failure envelopes are presented for the three different configurations in Figure 4.3.

The points selected for each specific case correspond to the effective stress value for which the totality of the plane fails under the given stress state. Lines connecting these different points were also drawn in Figure 4.3, in order to show the shape of the corresponding equivalent failure envelops. Then, the permeability measurements are performed as follows: after applying the in-situ stresses, a pore pressure is uniformly applied on the fracture plane. This pressure value corresponds to the fluid pressure for which the effective normal stress leads to the shear failure of the homogeneous configuration (P2 in Figure 4.2(b)), i.e. with a friction angle of 15° but not high enough to destabilize the plane in the presence of the heterogeneities. Then, an entrance and higher pressure P1 is applied at the bottom of the model resulting in an imposed hydraulic gradient as the exit pressure P2 is kept constant, i.e. corresponding to the initial and uniform fluid pressure while keeping the lateral boundaries impermeable. Then the flow rate at the bottom and at the top of the model are calculated once a steady state flow regime is reached. The applied entrance pressure values P1 cover a range between 3 MPa to 4.3 MPa. The equivalent permeability of the overall fracture is then estimated using the following equation [Min et al., 2004]:

$$k_{in} = k_{out} = \frac{Q\mu}{A}\frac{dx}{dP} \tag{4.1}$$

Boundary conditions		
Stress field: $\sigma_x = -4.9 \times 10^6$ Pa, $\sigma_y = -3.9 \times 10^6$ Pa, $\sigma_z = -4.1 \times 10^6$ Pa		
Initial pore pressure: $pp_{ini} = 0.2 \times 10^6$ Pa		
Rock matrix properties		
Density: $\rho = 2500 kg/m^3$		
Young's modulus parallel to bedding: $E_1 = E_2 = 8.5 \times 10^9$ Pa		
Young's modulus normal to bedding: $E_3 = 3.6 \times 10^9$ Pa		
Poisson's ratio parallel to bedding: $\nu_{12} = 0.33$		
Poisson's ratio normal to bedding: $\nu_{13} = \nu_{23} = 0.33$		
Shear modulus parallel to bedding: $G_{12} = 3.2 \times 10^9$ Pa		
Shear modulus normal to bedding: $G_{13} = G_{23} = 1.4 \times 10^9$ Pa		
Fault properties		
	Plane	**Heterogeneities (asperities)**
Normal stiffness: K_n	100 GPa/m	100 GPa/m
Shear stiffness: K_s	4 GPa/m	4 GPa/m
Friction angle: ϕ	15°	40°
Cohesion: c	0	10^6 Pa (in the case of cohesional and tensional heterogeneities)
Tensile strength: σ_t	0	10^6 Pa (in the case of tensional heterogeneities)
Hydraulic aperture: u_{h0}	3×10^{-5} m	3×10^{-5} m
Fluid properties		
Bulk modulus: $K_f = 2 \times 10^9$ Pa		
Density: $\rho_f = 1000 kg/m^3$		
Dynamic viscosity: $\mu = 10^{-3} Pa \times s$		

Table 4.1: Boundary conditions and material properties for the reference case (dip angle=30°).

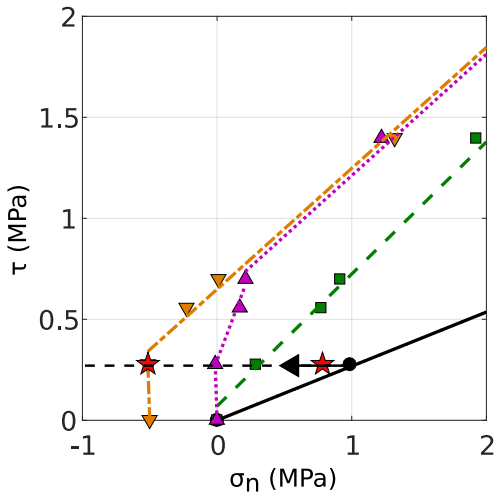

Figure 4.3: Equivalent failure envelopes for the fault plane: the black solid line corresponds to the homogeneous plane, the green dashed line to the case of higher friction heterogeneities, the purple dotted line to the case of higher friction, cohesion heterogeneities and the orange dash-dot line to the higher friction, cohesion, tensile strength heterogeneities. The black arrow indicates the direction of the evolution of the effective stress as the fluid pressure increases. The two red stars correspond to the two configurations presented in Figure 4.5 for the frictional case, i.e. the failure envelope corresponds to the green dashed line.

where Q is the flow rate calculated at the boundaries, A is the cross-sectional area of the inflow and outflow faces of the domain, μ is the dynamic viscosity of the fluid, P is the fluid pressure and x the general fluid flow direction (Figure 4.2(b)).

For the four different cases, the evolution of the permeability value, depending on the properties of the fracture plane, is followed by increasing the entrance fluid pressure P1 while keeping the same applied stress condition (dashed horizontal black line, starting from the black dot to the left, in Figure 4.3) and the same exit fluid pressure P2.

Results

The plot of the results obtained with the numerical model for the four different configurations are combined with the Tournemire in-situ tests results is presented in Figure 4.4. For the homogeneous fracture plane, with the increase of fluid pressure, the evolution of the resulting permeability follows a power law evolution (linear curve in the vertical log plot) with no clear FOP transition as observed in the experimental tests (black circles in Figure 4.4) since the displacement along the fault plane is irreversible as soon as the fluid propagates along the totality of the plane. In this case the hydraulic response, i.e. the increase of permeability is directly related to the slippage of the plane. Now, considering the heterogeneous fault plane cases, the evolution of the permeability exhibits a two-step evolution (colored disks in Figure 4.4) with a clear and sharp transition, corresponding to the FOP observed in the field tests.

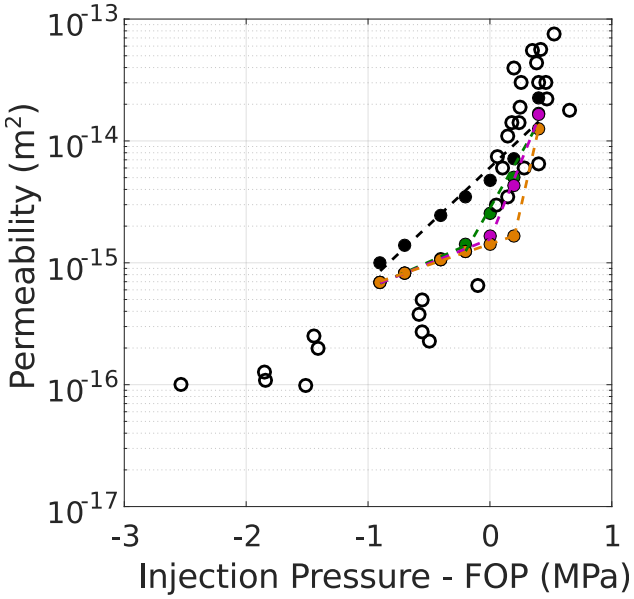

Figure 4.4: Permeability as a function of pressure in the injection borehole relative to the Fracture Opening Pressure (FOP) for (i) all tests performed during the Tournemire tests in black circles, (ii) the numerical tests for the uniform fault plane in black disks, (iii) the numerical tests for the heterogeneous fault plane with only frictional asperities in green disks, (iii) the numerical tests for the heterogeneous fault plane with frictional-cohesive asperities in purple disks and (iv) the numerical tests for the heterogeneous fault plane with frictional-cohesive-tensile strength asperities in orange disks.

Starting from the frictional-only asperities (green disks in Figure 4.4) going through the frictional-cohesive ones (purple disks) and to the frictional-cohesive-tensile strength rock bridges (orange disks), the

FOP value is shifted to higher fluid pressures. Then, from this FOP value, the permeability increases up to the one corresponding to a fully open fracture. At the FOP value, the fluid pressure does not trigger yet an overall mechanical instability of the fracture plane because the effective stress remains in the stable domain (see Figure 4.3), but a substantial increase of the permeability is already observed as the fluid is channeling between the heterogeneities (see Figure 4.5). The numerical model provides an evolution of the permeability which seems to be in good agreement with the Tournemire observations, as soon as the heterogeneities are taken into account. Their contribution can explain the existence of the sharp permeability change as soon as the fluid pressure reaches the FOP value. Below or around this value, the permeability is already increasing as the fluid can start channeling in the fault zone. It is above the FOP value that the overall fault surface starts to be mechanically active. For example, in the frictional case (green dashed linear failure envelop in Figure 4.3) for a fluid pressure resulting in an effective stress well below the shear failure (right star in Figure 4.3), the fluid is already channeling (Figure 4.5, left). As the fluid pressure increases, the effective stress reaches the failure limit which triggers the irreversible slip of the fracture plane and consequently the fluid propagates on the entire fault surface (Figure 4.5, right).

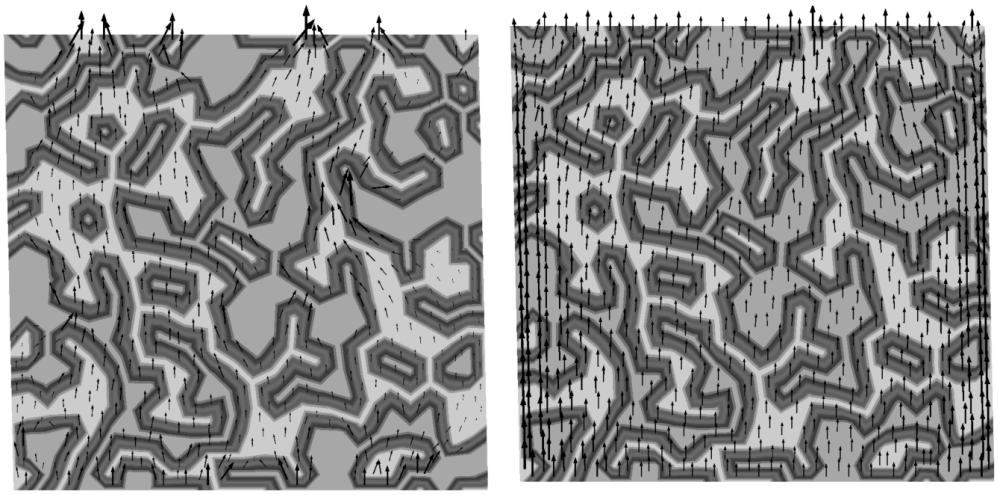

Figure 4.5: For the frictional case (green dashed failure envelope in Figure 4.3): (Left) below the FOP transition (right red star in Figure 4.3) as well as below the irreversible slip of the fracture plane, the fluid is channeling between the asperities and (right) well above the FOP and after the shear failure of the fracture plane (left red star in Figure 4.3), the fluid propagates and spreads all over the fracture zone. The fluid discharge rate is represented by arrows to show the local fluid flow direction and the asperities are represented by the darker grey zones.

Based on these results, it is now possible to propose a conceptual model which relates the fluid pressure to an apparent permeability depending on the in-situ stress state (Figure 4.6). For the sake of simplicity, the resulting conceptual model has been formulated using a linear Mohr-Coulomb criterion, knowing that for fractured shale, this is not representative of the non-linearity of their failure envelop [Amann et al., 2012; Barton, 2013; Bonnelye et al., 2017].

In the fault zone, the heterogeneities can be found at the scale of the fractures [Cornet et al., 2003; Dick et al., 2016] but also at the fracture network scale due to the size and orientation of the connected fracture sets [Dreuzy et al., 2012; De Dreuzy et al., 2013; Rivet et al., 2016]. Moreover, secondary connected faults can also play the role of hydro-mechanical heterogeneities at a larger scale. Considering the multiscale

nature of these heterogeneities, different ranges of permeability values could result from the interaction between the fluid pressure and the in-situ stress.

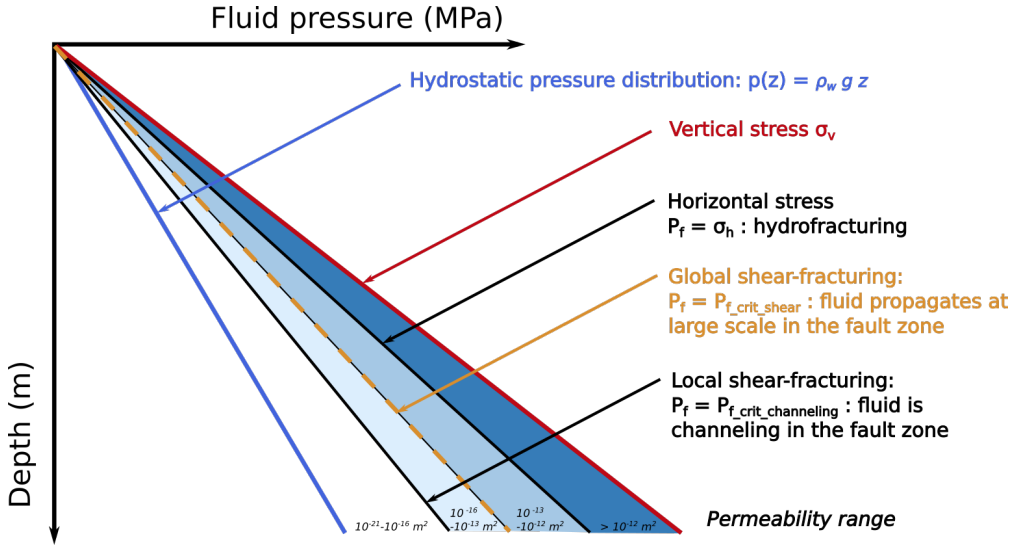

Figure 4.6: Conceptual model introducing critical fluid pressure for channeling ($P_{\texttt{f\_crit\_channeling}}$), which is a subcritical criterion involving only a hydraulic response without major irreversible strain of the fault zone.

Fluid pressure leading to channeling, i.e. P_f equals to $P_{\texttt{f\_crit\_channeling}}$ (see Figure 4.6) would correspond to permeability values ranging from 0.1 mD to 100 mD without triggering large scale slippage along the main fault. This sub-critical mechanical criterion would correspond to the FOP concept observed in the Tournemire experimental test and illustrated by our numerical model when fluid starts to channel in the presence of heterogeneities. As a first approximation, this would correspond to a sub-critical mechanical criterion with an equivalent friction angle of 15° (from our model), if expressed using a Mohr-Coulomb formalism. As the fluid pressure increases, the global shear failure would be reached (for a higher equivalent friction angle of 30° for shale), the resulting permeability would range from 100 mD to 1 D and above the hydrofracturing threshold, the equivalent permeability would be higher than 1 Darcy (Figure 4.6).

4.1.2 Subcritical permeability channeling effects on Eugene Island Fault leakage potential

Here, we propose to apply our model of subcritical permeability (Figure 4.6) related to channeling process in a fault zone to revisit the fluid migration observed in Eugene Island's block 330. In this area, two fault zones were studied in details: (i) a South dipping fault "A" (also called "Red fault") which is the major Northern structure bounding fault and (ii) a Northern dipping fault "F" which is an accommodation fault on the rollover anticline separating the field in two compartments (see Figure 4.7). Along the "A" fault, hydrocarbon is trapped in both upthrown and downthrown sides with a major part of the accumulation located in the downthrown side of the fault. The considered sandstone reservoirs here are identified as "OI" and "JD" (Grey bands in Figure 4.7) interbedded with shale layers (white zones). The "A fault" seemed to have experienced a maximum rate of slip between 1.8 and 1 My ago [Holland et al., 1990] but there is no evidence that it is still active and despite the huge amount of wells, none of them has

been reported as severely unstable due to shear stress. Oil was found in the "A" fault zone by several crossing wells and gas was observed in almost all the wells crossing this fault. Several wells were specially deepened across the faults in order to collect data and help in understanding the fluid flow mechanism along the faults. From the A20st well, information showed that the "A" fault is constituted by a wide and complex fault zone with probably a major plane ("A" fault) and several secondary fault planes altogether forming the "A" fault zone of 100 m width [Losh et al., 2002].

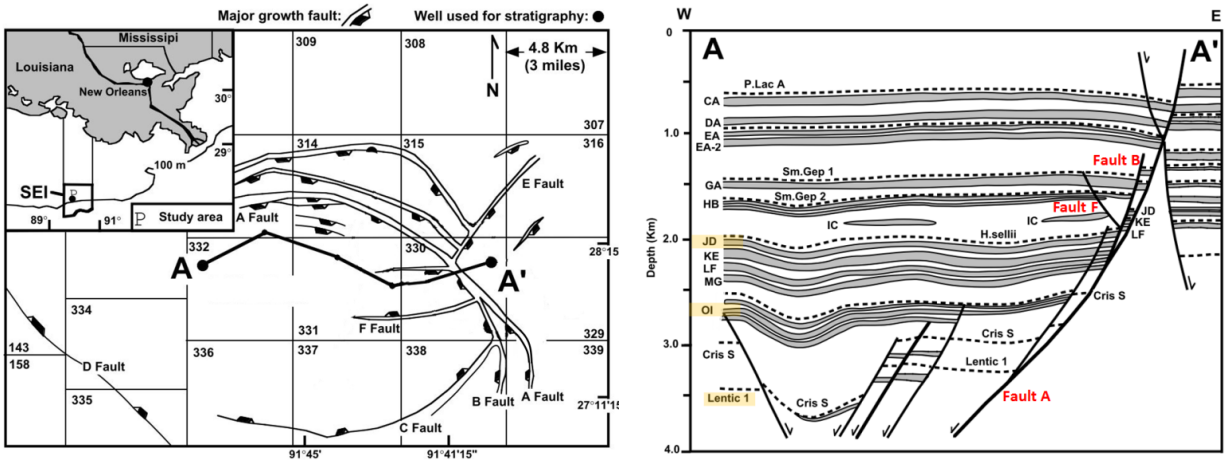

Figure 4.7: Location map of the block 330 is presented on the left. The cross section along A-A', is presented on the right (from Revil & Cathles [2002]).

The mineralogy of samples collected near the fault zone indicates that the amount of clay rock is ranging from 40 to 60%. The matrix permeability from laboratory measurements provides a low value about 100 nDarcy (10^{-19} m^2), in the absence of fractures. The indication of a fluid flow along the fault has been suspected based on a 10°C residual temperature anomaly observed in the fault zone. This could potentially be created by upward migration of warm fluid along the fault system. Moreover, seismic reflection imaging tends to confirm this scenario [Haney et al., 2005]. The pulse anomaly could correspond to a Darcean flow of about 300 m/year from 3 km deeper. The equivalent transient permeability should be of the order of 100 mDarcy (around 10^{-13} m^2). Noting also that the high presence of calcite precipitation in the fault zone is probably also related to a fluid activity within the fault zone. To explain the fluid migration process, two scenarios were debated. The first one proposed that the fluid migrates through different reservoirs involving the following mechanisms [Finkbeiner et al., 2001]:

- In the deepest parts highly over-pressurized, i.e. deep lentic sands, hydraulic fracturing or fault slipping occurs (dynamic mechanism),
- In the intermediate reservoirs, i.e. OI-1 reservoirs, the HC column is partly controlled by fault slipping (also dynamic mechanism),
- The pressure in the shallowest reservoirs, i.e. JD reservoirs, is below hydraulic fracturing and fault slipping thresholds (static mechanism).

The two last mechanisms are presented in Figure 4.8, left. Other authors (e.g. Haney et al. [2005]) also agree that in the deepest reservoirs (Lentic sands, see Figure 4.7), the fluid pressure should be between 92% and 96% of the overburden stress, leading to hydraulic fracturing.

Using the proposed conceptual model, the scenario presented by Finkbeiner et al. [2001] is revisited. The same friction angle values have been used, i.e. 15° for the sub-critical criterion triggering only channeling process of the fluid and 30° for the shear reaction of the fault zone. In order to compare in a direct manner the predictions provided by the conceptual model and the one proposed by Finkbeiner et al. [2001], both results are plotted in Figure 4.8. It can be seen that the over-pressurization of the reservoir OI-1A and OI-1E should not lead to shear failure anymore but to a channeling migration of the fluid below any overall mechanical instability, explaining why the wellbores can remain stable (Figure 4.8, right). This result is in good agreement with Losh's assessment[Losh et al., 2002], who did not expect shear failure. This channeling process could be driven by a permeability of 100 mD, compatible to equivalent transient permeability value noted previously [Haney et al., 2005]. The Upper JD sands are slightly over-pressured (Figure 4.8, upper colored JDA and JDB bars). The fluid pressures at the top of the reservoirs are below the critical pressure for both model and neither hydraulic nor shear fracturing nor even channeling should take place. HC column should be here limited by a spill point.

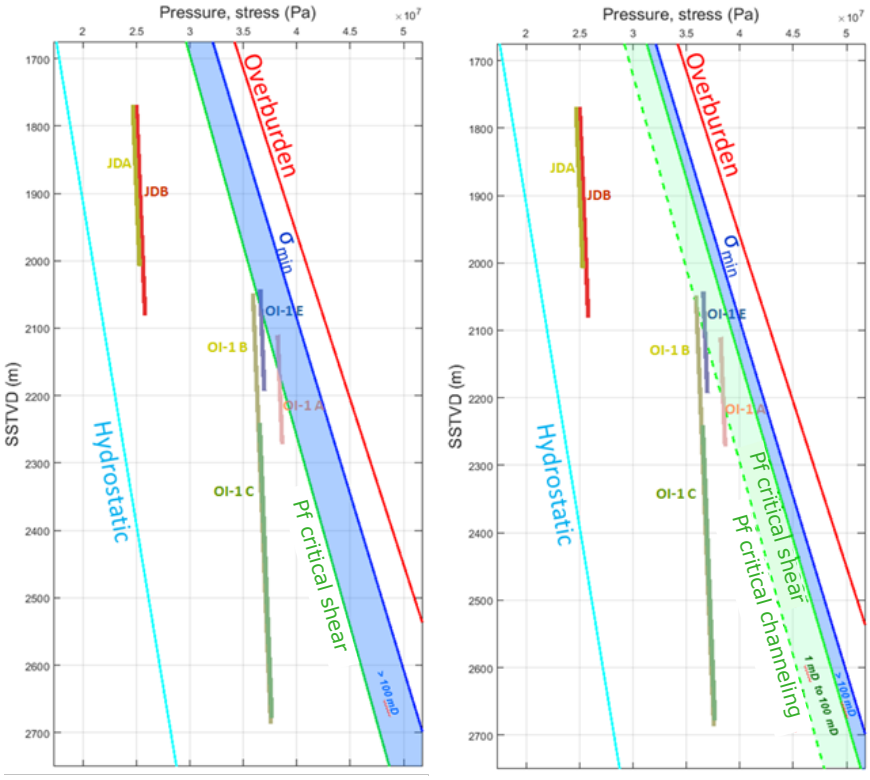

Figure 4.8: Pressure and stress state of the OI-1 and JD sands in minibasin fault blocks A. On the left the Finkbeiner et al. [2001] is presented. On the right, for the same stress states of the reservoirs OI-1 and JD but taking into account the critical fluid pressure above which channeling migration can be trigger while remaining in the stable mechanical domain of the fault zone.

Beyond this reservoir leakage scenario, the chemical signature of the fluid migrating along the fault seems different from the one obtained from the fluid collected inside the OI reservoirs. This could imply that fluid-pressure driven shear failure in the downthrown reservoir section probably has not occurred. Thus the fault could act as a "one-way valve" from deep accumulations to shallower reservoirs. In this

scenario, a cycle involving fluid pressure buildup, tectonic slip, fluid transport, and ultimately, draining of the fault has been proposed by Losh et al. [2002]. Based on the model, tectonic slips are not required since the fluid can channel along the fault without triggering any large mechanical instabilities.

Another fluid migration process which requires no mechanical activation has been proposed through the concept of "porosity wave" [Joshi & Appold, 2016]. The results show that gradual rates of pore fluid pressure generation typically caused by diagenesis are too slow for porosity waves to transport methane at kilometer per year rates. Instantaneous pore fluid pressure increases should be needed, which then could allow porosity waves to ascend 1 to 2 km at velocities over ten meters per year. Here again, the lack of earthquake events argues more in favor of a subcritical fluid migration channeling mechanism.

4.1.3 Discussion

Building on the presented results and application case study, the hydro-mechanical behavior of faults in low permeability formations requires considering three conditions: (i) A sealed fault condition, with permeability comparable to the formation. (ii) An intermediate conductivity, which may apply to fault subject to limited or localized shear dilatancy as the fluid pressure reaches a subcritical pressure leading to channeling mechanisms. A constant permeability may be assumed that will be a function of lithology and cementation. From our results as well as previous studies in fault zones this permeability is expected to be 2 to 4 orders of magnitude higher than the permeability of the formation (up to 100 mDarcy for shales). (iii) An open conduit condition that may apply to fault zones well above the FOP (Fracture Opening Pressure) leading to a plastic deformation of the fault zone. A power or exponential law could be assumed to represent the evolution of the permeability depending on the fluid pressure.

The critical fluid pressure leading to the channeling mechanism is a key parameter that will determine clay fault conduit behavior, even if the fault is considered as inactive (Jeanne et al., 2018). This has also been observed at the laboratory scale for fluid injection in a fault zone for different type of rocks, where the fluid was channeling at pressure much lower than the minimum value needed to trigger a mechanical instability [Nishiyama et al., 2014; Cuss & Harrington, 2016].

The model presented, could be also applied to the Barbados decollement zone where abundant evidence shows that episodic fluid migration occurs along low angle faults. The hydro-mechanical reactivation of such structures would require a very low friction coefficient close to 0.2 for the Barbados decollement zone [Henry, 2000]. Based on the model, it is therefore possible to consider that areas of very low friction are present along the zone which exhibit local failure and channel the fluid along the decollement. More field observations suggest the existence of these flow paths in inactive fault zones that transmit fluids rapidly over large distances [Fabryka-Martin et al., 1997; Fairley & Hinds, 2004; Campbell et al., 2003; Kluesner & Brothers, 2016] and some of them have been observed to line up with regularly spaced pockmarks on the seabed [Ligtenberg, 2005; Gay et al., 2007]. These observations highlight the importance of weak zones along the faults, as suggested in the present model.

4.2 Summary of the chapter

Summarizing, in this chapter a conceptual model was proposed based on a numerical model accounting for fault heterogeneities. Such a conceptual model can possibly explain hydro-mechanical observations made at the laboratory scale, the meso-scale and the basin scale. It was shown that the channeling of the

flow along a fault surface can result in a subcritical permeability increase that can be 4 orders of magnitude higher than the permeability of the intact rock allowing for considerable fluid migration to take place. The boundary between the channeling dominated regime and the full hydro-mechanical reactivation of the fault can be identified by the FOP as observed at the Tounemire injection tests. It was shown that such a hydraulic activity is not necessarily accompanied by large slip events along the fault but rather localized failures at the level of the low friction areas.

Chapter 5

Hydro-mechanical analysis of injection induced seismicity

Given the increasing concern about fluid injection induced seismicity related to anthropogenic activities, we explore in this chapter, the link between the induced seismicity and the hydraulic properties of a fault. This is done in the framework of a hydro-mechanical analysis. In the first part of the chapter (section 5.1), using the model described in Chapter 4, we investigate whether the fluid propagation regime is radial or channeled. This can lead to some conclusions regarding the evolution of the hydraulic properties and the induced seismicity along the fault/fracture plane. Assuming that a large part of the induced seismicity is related to effective stress variations, the location of seismic events could inform about the extent at which the fluid has propagated into the fault zone and therefore about the hydraulic properties of the fault as discussed in Chapter 1 (section 1.4). Here we figure the fault zone as a complex surface containing asperities with different frictional and hydraulic properties. The correspondence between the rupture events in the model and the resulting fault hydraulic diffusivity is investigated considering different fault orientations towards the stress field and surface characteristics.

In the second part of the chapter (section 5.2), we apply this concept to the analysis of the seismicity induced during one injection test conducted into the Tournemire fault zone. More specifically, the mechanisms behind the induced seismicity are discussed, whether it is the result of effective stress variations and diffusivity increase or stress transfer effects within the rock mass. Using a large scale model, we discuss the validity of using seismic events to track the pressure diffusion in an activated fault zone.

5.1 Channeling effects on hydraulic diffusivity and induced seismicity

The geometrical model developed in Chapter 4 is now used in order to examine the connection between rupture events and slip enhanced hydraulic diffusivity in the particular case of a heterogeneous fault surface. The triggering front concept [Shapiro et al., 2002] assumes that the microseismicity front follows the pressure diffusion law based on Equation 1.8 and it is discussed in section 1.4. Here we approximate that all the calculated ruptures are potentially seismic. For the purpose of this study, the scalar diffusivity

of the fault is calculated as:

$$D = \frac{T}{S} \tag{5.1}$$

where T (m^2/s) is the resulting transmissivity of the activated fault and S (-) is its corresponding storativity. In order to estimate the storativity of the fracture, the formulation by Rutqvist et al. [1998] is used:

$$S = \frac{\rho g}{f \kappa_n} \tag{5.2}$$

where f is the fracture surface characteristics factor accounting for deviations from the ideal conditions of flow along two parallel smooth plates and κ_n (Pa/m) is the hydraulic stiffness of the fracture defined as the inverse of the pressure dependency of the hydraulic aperture:

$$\kappa_n = -\frac{\partial \sigma_n'}{\partial u_h} = \alpha \frac{\partial P}{\partial u_h}, \sigma_n = constant \tag{5.3}$$

where α is the Biot's effective stress constant and σ_n (Pa) is the total normal stress.

In this analysis, the factor f is calculated according to Zimmerman et al. [1992]; Zimmerman [2012], by assuming that the heterogeneities along the plane are circular impermeable contacts:

$$f = \frac{1+c}{1-c} \tag{5.4}$$

where c is the fractional contact area of the fracture. The effect of introducing heterogeneities and therefore the variation of the factor f is being investigated on the hydraulic diffusivity of the fault. In order to account for the heterogeneities and the potential channeling effects, f is changing according to the level of in-plane heterogeneity, meaning the percentage of the heterogeneities along the plane. By introducing in a simple way the factor f, the higher or lower percentage of contacts is indirectly taken into account. In the model the contacts are represented as areas of higher fault friction. Flow channels are expected to drive the fluid to greater distances than the ones expected for a uniformly radial propagation around the injection source. Taking into account flow channeling and possible evacuation through a single point, the appropriate value of transmissivity has to be determined. The transmissivity value is used for calculating the diffusivity in Equation 1.8. The transmissivity is recovered in 3DEC during the calculations for each rupture event (Equation 2.25). After recovering the transmissivity values of all stimulated "points" along the reactivated fracture plane, it is possible to deduce a minimum transmissivity, an average transmissivity and a maximum transmissivity value. These three transmissivity values have been used subsequently for the calculation of three different diffusivity values (minimum, average and maximum). Reminding that the transmissivity in 3DEC is calculated as follows:

$$T = k \nabla x \tag{5.5}$$

where ∇x is a geometrical gradient accounting for the contribution of the zone to each one of its flow knots [Itasca Consulting Group, 2013] and

$$k = \frac{u_h^3}{12\nu} \tag{5.6}$$

where u_h is the hydraulic aperture and ν is the fluid viscosity.

The injection takes place at the center of the model as a point source injection that corresponds to the

intersection point between the injection borehole and the fault plane. The injection flow rate is imposed at a constant value of $2.7 \times 10^{-6}\ m^3/s$ for a duration of 20 seconds. The calculations performed were fully coupled taking into account the hydro-mechanical response of the model under a pressure increase induced by fluid injection. The effect of the fault orientation with respect to the maximum horizontal stress was first investigated (Figure 5.1(a)). The impact of frictional heterogeneities was then investigated by considering several configurations based on the percentage of the heterogeneity along the plane. The heterogeneity is expressed by the presence of "contacts" along the plane which are characterized by a higher friction angle. The eight different cases examined are the homogeneous case (0%), 20%, 30%, 40%, 50%, 60%, 70% and 80% of contacts. According to Equation 5.4, $f = 1$ for the homogeneous case ($c = 0$), $f = 1.5$ for 20% ($c = 0.2$), $f = 1.9$ for 30% ($c = 0.3$), $f = 2.3$ for 40% ($c = 0.4$), $f = 3$ for 50% ($c = 0.5$), $f = 4$ for 60% ($c = 0.6$), $f = 5.7$ for 70% ($c = 0.7$) and $f = 9$ for 80% ($c = 0.8$) of contacts. Depending on the percentage of contacts the propagation of the fluid will either be uniform or conditioned by channels growth through rupture of low friction contacts.

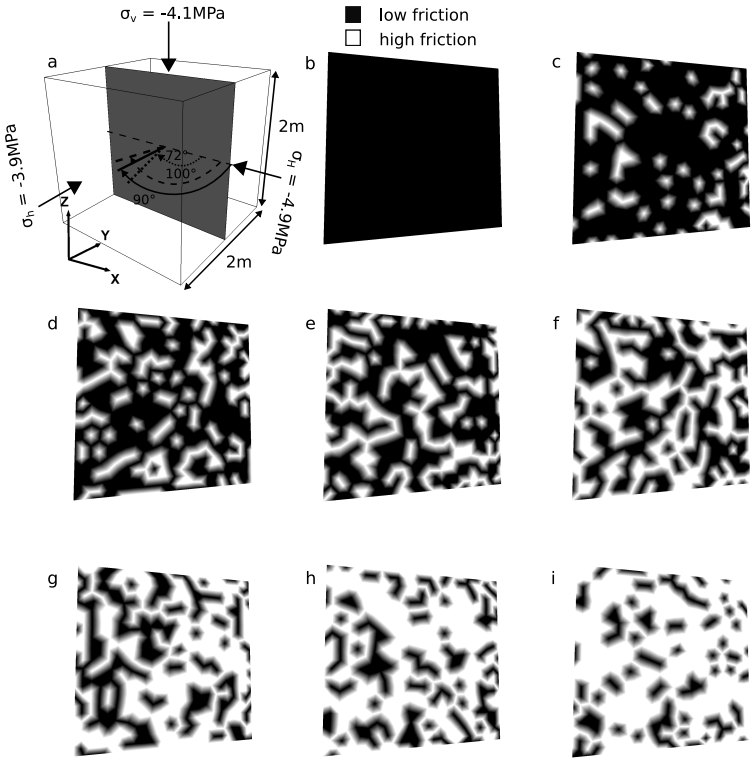

Figure 5.1: a) base case numerical model with the in situ stress field and the fault represented as a discontinuity separating two blocks, b) fault plane with homogeneous friction, c) with 20% of contacts, d) with 30% of contacts, e) with 40% of contacts, f) with 50% of contacts, g) with 60% of contacts, h) with 70% of contacts, i) with 80% of contacts.

5.1.1 Reference case-homogeneous aligned fault plane

The reference case consists of a homogeneous fault aligned with the axes of the principal stresses (see Figure 5.1(a). The material properties and boundary conditions of the model are identical to the model described in Chapter 4 (Table 4.1) with the only difference in the fault strength properties. The fault is

characterized by a single friction value equal to 20° without any cohesion or tensile strength. At 0 seconds a constant flow rate is imposed at the center of the model until 20 seconds when the calculation stops. During the hydro-mechanical calculations, the occurrence time, the distance from the injection point and the resulting transmissivity values are recorded for each sub-contact rupture as the fluid propagates.

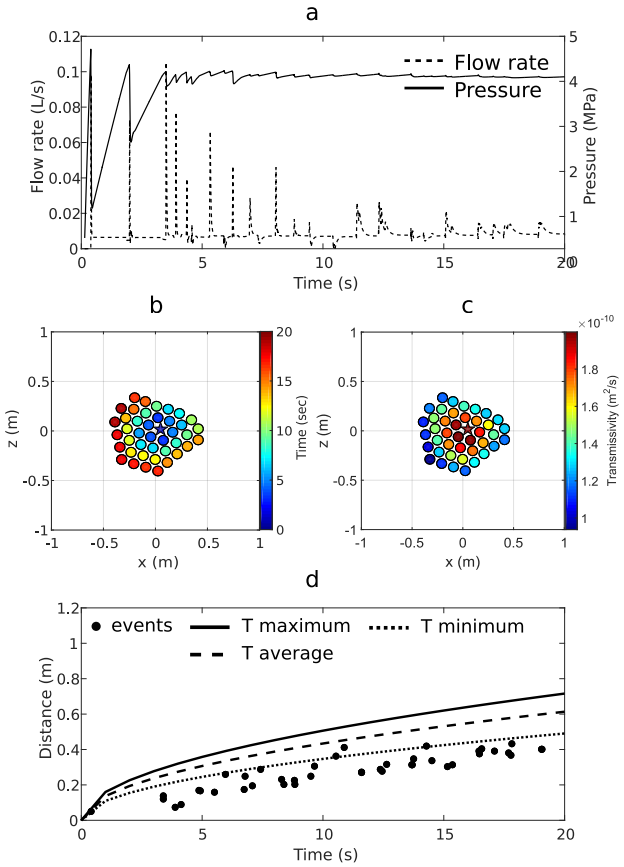

Figure 5.2: Reference case, the fault plane is aligned with the principal axes. a) Flow rate and pressure versus injection time recorded at the injection point throughout the calculation, b) occurrence time and coordinates of the rupture events, c) transmissivity values for each event, d) distance of the events from the injection point versus injection time and triggering front envelopes calculated using the maximum (solid line), the average (dashed line) and the minimum (dotted line) transmissivity value.

During the simulation, the pressure recorded at the injection point remains close to 4 MPa and represents the pressure at which rupture propagates in the fault under the specific stress conditions (Figure 5.2(a), solid line). The peaks observed on the flow rate curve and the drops on the pressure curve correspond to the successive ruptures occurring along the plane (Figure 5.2(a), dashed line). Figure 5.2(b) shows the coordinates of the rupture points in the plane of the fault with a color code that corresponds to the occurrence time of the rupture events. Given the orientation of the fault, there is no differential stress acting on the plane. Therefore, the fault is failing in tension. It can be observed that at the end of the injection the pressurized zone is a circle with the injection point (represented by a star in Figure 5.2(b)) at the center of the zone. In Figure 5.2(c), the maximum transmissivity values correspond to the rupture points close to the injection source while the minimum values correspond to the points at the outer boundaries of the pressurized zone where the fluid is evacuating in the part of the fracture characterized by a lower pressure. Figure 5.2(b) shows that the distance of the rupture events from the injection source

is increasing as a function of the injection time (r-t plot) because the fluid is propagating progressively and uniformly around the injection point with its propagation being preconditioned by the failure of the adjacent points. If we assume that the rupture events could potentially represent microseismic events, we make use of the triggering front concept. We calculate three transmissivity values, a maximum value that could well represent the measured transmissivity at the injection point, an average value and a minimum which corresponds to the resulting transmissivity of the points at the propagation front and therefore three diffusivity values since the fracture storativity is constant. According to Equation 1.8, the curves for the three triggering fronts that correspond to the three different diffusivities, envelop well the evolution of the events with the distance to the injection source. All three possible transmissivities seem to fit well the distance of the rupture events with the minimum value being the best fit. This is expected as the specific case satisfies the conditions of the triggering front concept according to which the medium is considered isotropic and weakly heterogeneous.

5.1.2 Effect of the orientation of the fault towards the maximum horizontal stress

Compared to the reference case where the principal horizontal stress is normal to the fault plane, we studied two cases with σ_h forming an angle of 72° and 100° with the normal to the fault plane. For both orientations tested, the properties along the fault are homogeneous with the same friction as the reference case. In the analyses that follow, the slip rate is also calculated based on the measured displacement in the direction of shear. The displacement is measured at two points, one on each side of the fault plane close to the injection point throughout the simulation. The slip rate is then calculated for every timestep Δt according to:

$$\dot{u} = \frac{\Delta u_s}{\Delta t} \tag{5.7}$$

Figure 5.3(a) shows the coordinates of the rupture events in the plane of the fault together with the time of the events occurrence for an angle of 72° between the normal of the fault and the maximum horizontal stress. The occurrence time of the events shows that the fluid and rupture front propagates towards a direction left downwards conditioned by the stress state and the strong dextral strike slip fault movement. Due to the presence of a differential stress, the fault is failing in shear mode. Rupture occurs first at points close to the injection source (see also Figure 5.3(c)). But there are some events occurring around the injection source at an advanced time after the injection has started, i.e. $t = 5$ and $t = 13$ seconds for example. The time periods when the fluid starts propagating towards another direction starting from a point close to the source are also characterized by an increased slip rate as shown in Figure 5.3(c), red line. The dependence of the fluid front propagation towards a preferential direction imposed by the slip direction is the result of the low flow rate controlled injection loading. The propagation is conditioned by the slip direction of the fault probably due to the development of slightly higher shear forces towards the slip direction which is determined by the orientation of the plane towards the principal stresses. For the same model configuration, after performing a pressure controlled injection resulting in a higher flow rate, the fluid propagation was uniformly radial pointing out the sensitivity of the propagation direction to the loading conditions. The maximum transmissivity values correspond to the events around the injection point while the minimum values correspond to the events at the propagation front (Figure 5.3(b)). The triggering front lines for the different transmissivity values appear to be very close as the fluid pressure inside the rupture zone is uniform. This results in similar aperture values of all points within

the pressurized zone and therefore similar transmissivity and diffusivity values. Given the impact of the differential stress on the fluid propagation, this case is deviating from the ideal conditions where the fluid would progressively propagate uniformly in all directions. This explains the fact that the majority of the events are located outside the domain limited by the triggering front surface.

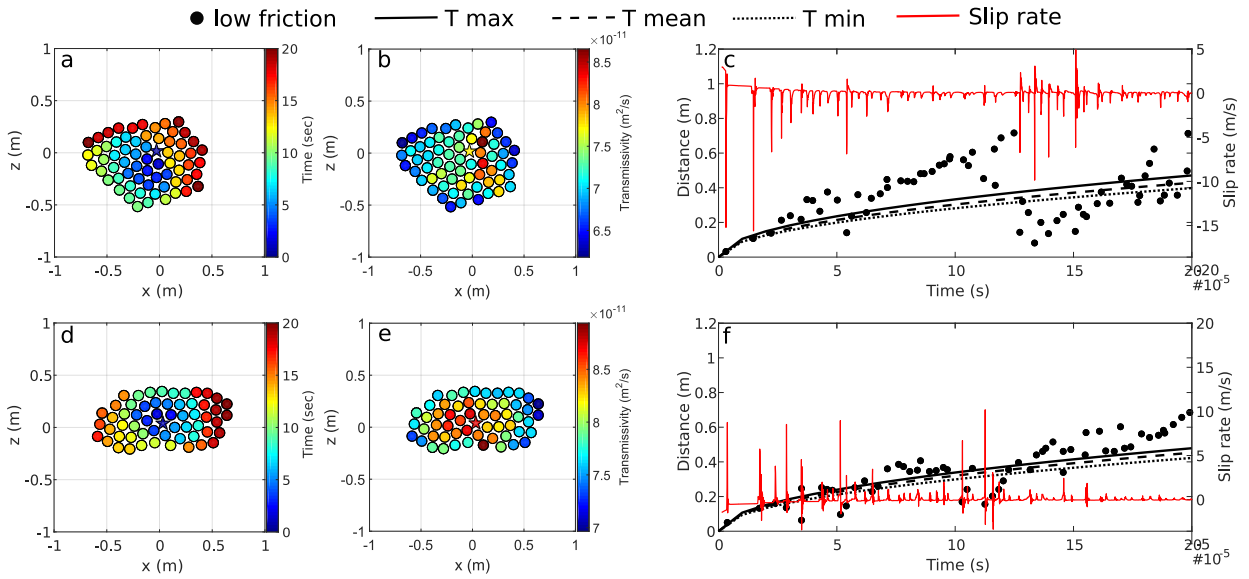

Figure 5.3: Fault plane orientation: a) occurrence time and coordinates b) transmissivity values c) distance of the events from the injection point versus injection time and triggering front envelopes for an angle of 72° between the normal of the fault and the maximum horizontal stress, d) occurrence time and coordinates e) transmissivity values f) distance of the events from the injection point versus injection time and triggering front envelopes for an angle of 100° between the normal of the fault and the maximum horizontal stress.

In the model where the normal to the fault and the maximum horizontal stress form an angle of 100°, the fault fails in shear mode as expected. We observe in this case that since the fault is sub-parallel to the maximum horizontal stress, the fluid propagation is more uniform comparing to the previous configuration (Figure 5.3(d)). Nevertheless, the pressurized zone is larger in the horizontal direction (x-direction) than in the vertical (z-direction). The propagation of the fluid is again conditioned by the imposed stresses and the left-lateral fault slip. The resulting transmissivity values are very close to the values observed in the previous case around $8.5 - to - 9 \times 10^{-11}\ m^2/s$ (Figure 5.3(e)). The fault diffusivity can be predicted from the distance of the rupture events up to $t = 13$ seconds approximately (Figure 5.3(f)). For $t > 13$ seconds the propagation appears to become conditioned by the slip direction of the fault. We can observe the same pattern as in the previous case regarding the sequence of the events, within a given radius from the injection source the points are not failing at the same time. The slip in this case (red line in Figure 5.3(f)) is of opposite sign compared to the previous case because of the opposite shear displacement of the fault.

5.1.3 Effect of the heterogeneous distribution of the Coulomb friction

The effect of a heterogeneous fault friction on the hydraulic diffusivity and on the localization of the rupture events is evaluated for the case where the normal vector to the fault and the maximum horizontal

stress form an angle of 72° (case 1 in section 5.1.2). As mentioned above, seven configurations were tested where the percentage of the contacts along the plane varied for 20%, 30%, 40%, 50%, 60%, 70% and 80% of frictional heterogeneities as shown in Figures 5.1(c)-to-(i). The high friction characterizing the contact areas is equal to 35° while the rest of the plane is assigned a friction value of 20°. No cohesion or tensile strength is assigned to the plane meaning that the heterogeneities are purely frictional. Figure 5.4 summarizes the occurrence time of the rupture events (Figure 5.4(a), (d), (g)), their transmissivity (Figure 5.4(b), (e), (h)) and the spatio-temporal plot (Figure 5.4(c), (f), (i)) for three of the tested cases, 20%, 60% and 80% of frictional heterogeneities. In all the figures the high friction points are represented by a square while the low friction points are represented by a circle.

For 20% of high friction heterogeneities, a similar pattern as for the homogeneous fault is observed. The high friction areas have not failed by the end of the injection (Figure 5.4(a)) as the fluid propagates preferentially through the low friction areas. However, the rupture surface is not exclusively conditioned by the stress field. The spatial distribution of the contact areas (see also Figure 5.1(c)) imposes a different fluid propagation path than the one observed in the homogeneous case. Nevertheless, the rupture points at the outer boundaries of the resulting pressurized and rupture zones are at a similar distance in all directions. In terms of transmissivity, the values are in the same range as in the homogeneous case (5.3(b)). For the fault storativity calculation a factor $f = 1.5$ is considered leading to a higher fault diffusivity than in the homogeneous case. The triggering front for a diffusivity deduced from the maximum transmissivity value (solid line in Figure 5.4(c)) which is close to the value at the injection point, is the best-fit upper bound with the other two curves being quite close.

While for low percentages of contacts ($< 40\%$) along the fault plane the response remains more or less close to the homogeneous case, increasing the percentage of contacts along the plane to a value close to 60%, leads to the creation of flow channels as observed in Figure 5.4(d). The majority of ruptures correspond to low friction areas while a few high friction areas fail at a later time when surrounded by low friction ruptures. As long as the connectivity between the low friction parts of the fault is high enough, the propagation of the fluid is almost exclusively taking place inside the channel propagating upwards and leftwards from the injection point (see also Figure 5.1(g)). The direction of fluid propagation is strongly conditioned by the distribution of the frictional heterogeneities. The stress field has a secondary impact. The transmissivity (Figure 5.4(e)) is lower than in the previous configurations because of the created flow channel which is evacuating the fluid from a very narrow area. It is worth noting that there is a larger contrast between the minimum and maximum transmissivity values. As channeling dominates fluid flow, the fluid pressure is not uniform within the reactivated part of the fault as high permeability boundaries (model boundaries) are met. This leads to a larger discrepancy between the aperture and consequently to a large discrepancy between transmissivities at the injection point, in a channel and at the model boundaries. The triggering front lines are therefore not close to each other (Figure 5.4(f)) and rupture events distance-versus-time does not match the lines whatever the factor f considered (the fractional area c in this case is 0.6 giving a factor f equal to 4). Indeed, most of the events are located above the triggering front lines.

For 80% of frictional heterogeneities along the fault, the flow direction is again dictated by the stress field (Figure 5.4(g)). Because of the presence of the small isolated low friction areas a pattern can be distinguished where "sharp" propagation is observed at the onset of the injection. At $t = 2.5$ seconds the rupture reaches fast a distance of 0.4 m because of an isolated channel (see also Figure 5.1(i)). The same

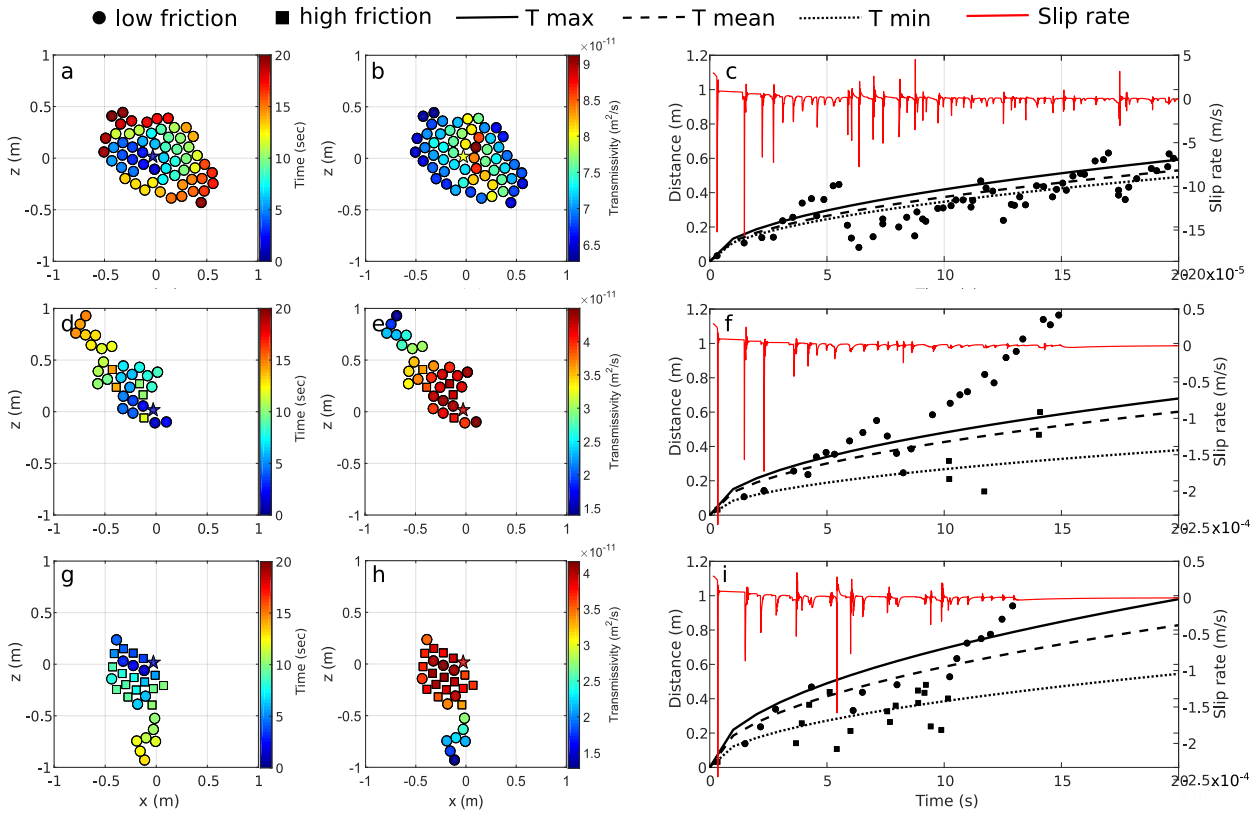

Figure 5.4: Heterogeneous distribution of the Coulomb friction: a) occurrence time and coordinates b) transmissivity values c) distance of the events from the injection point versus injection time and triggering front envelopes for 20% of frictional heterogeneities, d) occurrence time and coordinates, e) transmissivity values, f) distance of the events from the injection point versus injection time and triggering front envelopes for 60% of frictional heterogeneities, g) occurrence time and coordinates h) transmissivity values i) distance of the events from the injection point versus injection time and triggering front envelopes for 80% of frictional heterogeneities.

is observed for $t = 3.5$ and $t = 5$ seconds where high friction points fail in the vicinity of the pressurized low friction ones with the rupture propagating fast. At $t = 10$ seconds approximately, a low friction area is encountered towards the bottom of the model that leads the fluid to the model's boundaries. At this point the fluid propagation regime transitions from stress dominated to channel dominated and due to the fluid evacuation there is no more rupture taking place along the fault plane. The values of transmissivity shown in Figure 5.4(h) are similar to the ones recovered for the 60% case. The factor f is now equal to 9 for a fractional contact area $c = 0.8$. Due to the transmissivity variability of the reactivated part, the triggering front surfaces are not close to each other. The rupture events inside the channel leading to the model's boundaries are well above all of the surfaces because of the strong geometrical heterogeneity. The triggering front for a minimum diffusivity can hardly explain any low friction event and only includes some of the high friction events very close to the injection source. The mean and maximum diffusivity fronts are in good agreement with the spatio-temporal characteristics of the rupture events just before the distinctive flow channeling occurs.

In an effort to further distinguish between the different propagation regimes observed in the calculations, the cumulative number of events is shown for each heterogeneities percentage varying from 0% to

80% (Figure 5.5, left). While the injection time was 20 seconds, the first 14 seconds are shown in the plot as for some cases where channeling was observed, the fluid front reached the model boundaries and no further events occurred. There is an apparent trend regarding the number of the events which depends on the percentage of higher friction zones. The highest number of events occurs for a homogeneous fault plane ($f \sim 1$) while the lowest number occurs for 50%-60% of higher friction zones ($f \sim 4$). The results for the rest of the cases appear to lie between these two extreme cases for which the fitting curves are also shown in Figure 5.5 (black and red dashed lines). The difference in the number of events is the result of the propagation regime with the highest number occurring for f close to 1 (0%-20% of heterogeneities) where no channeling is taking place and the lowest number for a factor f around 4 (40%-60%) for which the propagation is almost entirely occurring in a reactivated channel. For the rest of the percentages tested, both stress and low friction areas geometry influence the fluid propagation resulting in an intermediate number of events. Based on this observation, it is possible to conclude that a threshold exists ($f \sim 4$) for which the connectivity of the low friction parts of the fault is high enough to allow flow and rupture to occur only along channels but it is low enough to allow radial propagation similar to the 0% case.

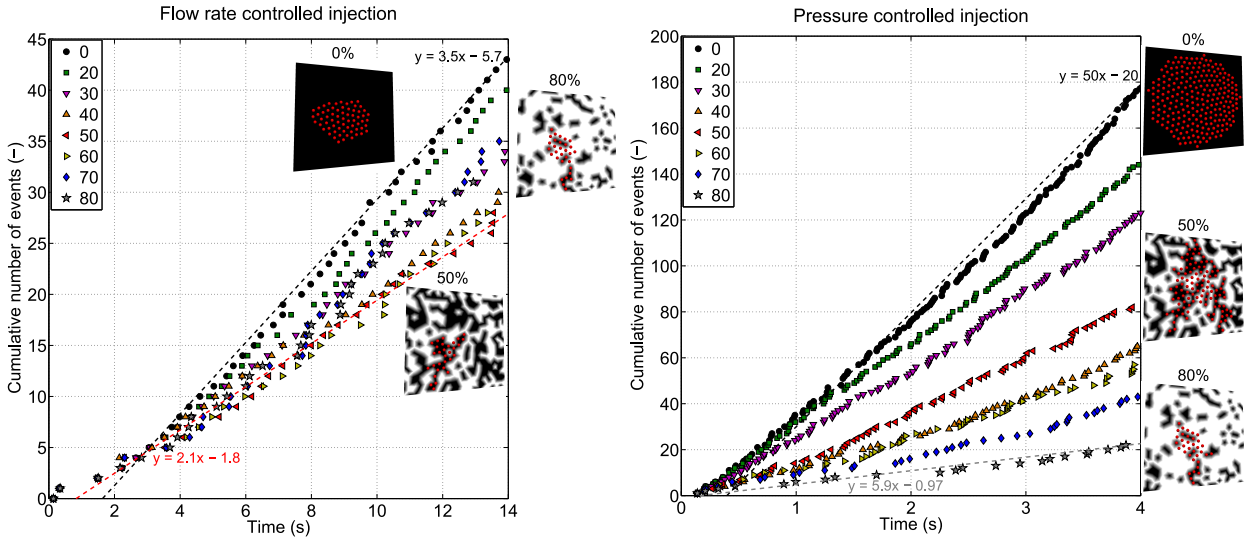

Figure 5.5: Cumulative number of events for a flow rate controlled injection (left) and a pressure controlled injection (right). Pressurized and rupture zones for 0%, 50% and 80% of heterogeneities for a flow rate and pressure controlled injection.

For all the cases tested, the fluid pressure at the injection point reached a value of approximately 3.9-4 MPa at the onset of the flow rate controlled injection. As mentioned above, a number of simulations were also performed by imposing a constant fluid pressure at the injection source equal to 3.9 MPa. Such loading results in a flow rate of about one order of magnitude higher, which consequently influences the propagation path. The events along the fault plane for 0%, 50% and 80% of contacts are shown in Figure 5.5, right. The largest number of events occurs for a homogeneous fault plane and it decreases almost proportionally to the increasing presence of high friction areas along the plane. In order to avoid boundary effects in the interpretation of the results, the cumulative number of events is shown for the first 4 seconds of the injection. After this time, the fluid front had reached the model boundaries for most of the cases. Comparing the two loading protocols, the resulting pressurized zone is larger for a pressure

controlled injection for almost all configurations. When a low flow rate is imposed, the fluid propagation becomes sensitive to the presence and the geometrical characteristics of the low friction patches while for an imposed fluid pressure, the propagation is driven by the effective stress variations along the plane and the heterogeneous strength of the fault zone.

5.1.4 Discussion

Considering different stress orientations on a vertical fault affected with heterogeneous hydro-mechanical properties, the spatio-temporal characteristics of rupture events triggered by pressure diffusion were explored. More specifically, we investigated how and how these characteristics can inform on emerging patterns of fault hydraulic diffusivity evolution before an eventual catastrophic rupture occurs (defined as a complete rupture of the fault plane).

- **Effect of fault orientation and channeling on fluid flow and rupture propagation regime**

A rather radial flow pattern is observed only in cases where the fault is aligned or slightly ($< 10°$) deviated from the principal stress and if the fault's frictional heterogeneity is lower than 20%. For all the other cases, an non radial flow develops in channels that grow by local Coulomb failure on low friction asperities. When $a > 10°$ oblique stress is acting on a fault plane with homogeneous friction properties the pressurized zone follows the strike of the slip vector because of the low flow rate imposed. This result is in good accordance with the experimental observations from Cuss et al. [2011] reporting that flow is predominantly occurring in the direction of shear for an initially planar fracture surface in shale material. Méheust & Schmittbuhl [2000] have pointed out the sensitivity of the hydraulic response of a rough fracture to the orientation of the applied pressure drop. In this case where the fault surface characteristics are considered homogeneous, it is shown that the stress orientation which conditions the direction of fault slip and shear stress concentration at the slip front, imposes an orientation to the pressurized area. Compared to the distance predicted from the radial uniform propagation of rupture, the calculated position of the fluid front can almost be twice further away.

Stanchits et al. [2011] performed fluid injection laboratory tests on dry porous sandstone during which the induced AE activity was monitored. It was suggested that the spatio-temporal migration of AE hypocenters may be used as a proxy to estimate permeability of samples that are critically stressed close to failure. In the present study, considering only the spatio-temporal characteristics of the events from the injection source would lead to an overestimation of the hydraulic properties of the fault and to an underestimation of the stimulated zone if the strong impact of the fault orientation under low flow rate conditions is not accounted for.

When an oblique stress of angle $> 10°$ is acting on a fault plane with $> 20\%$ friction heterogeneity, a statistical representation of the f factor is used to associate the percentage of the high friction areas to the total area. This allows studying fault diffusivity variations associated to the dynamic growth of flow channels within the fault plane. A critical $f \sim 2-4$ interval is identified for which channeling dominates the fluid flow while for $f < 2$ stress dominates the fluid flow. For $f > 5$, the propagation is influenced both by the stress and the isolated low friction channels. For a low value of flow rate imposed, the specific $f \sim 2-4$ (40%-60%) represents a strongly heterogeneity-dependent regime with the fluid flowing through larger aperture regions forming a set of higher permeability channels as observed in analogue laboratory experiments of flow viscous fingering related to high pressure air injection in granular media confined in Hele-Shaw cell [Eriksen et al., 2017]. This critical value of f is in agreement with the work by Tsang [1984]

who performed a numerical study using the electrical analog method to model the variation of fracture aperture by electrical resistances and concluded that for a fractional contact area higher than 35%, flow tortuosity significantly affects fluid flow.

- **Relationship between hydraulic diffusivity and events spatio-temporal characteristics**

When flow channeling occurs in the fault zone, there is a significant discrepancy between the distance and occurrence time of the rupture events and the calculated diffusivity of the fault. The result is that only very few events are located below the triggering front surfaces calculated from the maximum and average transmissivity. This is certainly because the Darcy law used in the model poorly represents flow in channels that would require a more adequate flow law considering a tube transmissivity accounting for the flow tortuosity. Nevertheless, considering the factor f a reasonable correspondence is observed between the rupture events characteristics and the hydraulic properties of the fault after reactivation. Thus, fitting a parabolic-like envelope to the cloud of the events, can provide with an estimate of the hydraulic diffusivity of the uniformly reactivated zone as stated by Shapiro et al. [2002] but does not inform on the diffusivity variations related to the initial emergence of channels which might be crucial in the detection of fault leakage and in monitoring the nucleation of potential "catastrophic" earthquakes.

Successions of rupture sequences were observed, associated to the complex growth of the rupture patch within the fault plane. At the onset of the injection, rupture initiates when the injection pressure exceeds the Coulomb stress, producing a high slip rate event followed by decreasing slip rate events as the pressure decreases while the rupture propagates away from the injection point. After a given time, new rupture sequences trigger for different reasons, (i) after a flow patch growth change in direction, (ii) when a new flow channel develops from an existing one or (iii) when shear stress concentration effects trigger un-failed high friction contacts inside a pressurized patch that does not grow anymore. The two factors that favor "late" ruptures are fault-stress obliquity and a friction critical heterogeneity of the fault plane characterized by a factor f close to 3. If in the simple model, we assume that only high slip rate events figure stick-slip failures following Lockner et al. [1982], these factors also appear as the most favorable to produce seismicity.

- **Effect of the loading conditions on the fluid flow and rupture propagation regime**

The cumulative number of events as a function of time strongly depends on the propagation regime and the presence of contacts along the fault plane. For both loading protocols, the number of events is the largest for a homogeneous fault plane since the seismic activity associated to the reactivation of a fault with a low coefficient of static friction is expected to be characterized by a large number of seismic events of lower magnitude [Jeanne et al., 2017b]. Consequently, for a constant fluid pressure injection (Figure 5.5, right), the number of the events decreases as the percentage of contacts and higher strength areas increases in the plane.

For a lower flow rate the dependency of the flow path on the contacts spatial arrangement was observed. Unlike the higher flow rate injection, no direct relationship was observed between the number of events and the percentage of contacts. The lowest slope of the cumulative number of events versus time curve corresponded to the channeling regime due to the percolation effect that implies a critical threshold distinguishing different responses. Based on the discrepancy in the response observed between the different loading protocols, useful information can be deduced. With the injected fluid volume being a crucial operational parameter in a number of industrial applications associated with induced seismicity

(e.g. McGarr [2014]), we observe that for a higher flow rate, there will be more induced rupture events with the size and shape of the pressurized zone depending on the effective stress variation while for a lower flow rate the number of events is lower and the propagation path can become extremely complex and absolutely dependent on the connectivity of lower strength channels.

5.2 Field injection test at the Tournemire host rock (Test 2)

Motivated from the induced microseismicity observed during the injection test in the Tournemire host rock, a hydro-mechanical model was built in order to better understand the process by which structures within the fault zone can be potentially reactivated from a pressurization occurring several meters away. Keeping in mind the objective of the study, it was necessary to split the modeling procedure in two parts. The first part was focused on the injection source location and aimed at the understanding of the physics and mechanisms involved during the pressurization of the interval. More specifically, based on the fluid pressure and displacement data measured in-situ, a model was created that was able to reproduce well enough the observed response. As it has been already mentioned in Chapter 2, during the test the last cycle was assumed to correspond to the reactivation of a structure under the influence of the natural stress field away from the borehole stress perturbation zone. For this reason, the last cycle was modeled and more specifically the high pressure duration for which a possible reactivation of a pre-existing fracture was maintained and the majority of the microseismic events occurred at a distance of 3.5-to-15 m away approximately (Figures 2.9 and 2.10). The hydro-mechanical calculation at the injection source gave an estimation of the injection parameters, the stress conditions, the size of the reactivation meaning the size of the pressurized area and the rupture patch.

After understanding the injection source mechanisms, a second plane was introduced in the model that represents the main fault direction and corresponds to the boundary between the East damage zone and the intact rock. It was possible then to investigate whether and how rupture and potentially seismicity can migrate from the injection source to the fault zone provided that the fractures are hydraulically connected.

5.2.1 Modeling at the injection source

Even if Test 2 was performed in a relatively intact borehole interval, there were a few fractures intersected by the interval from which the most favorable to conduct the flow are shown in Figure 2.8. It was therefore assumed that in the presence of natural fractures, the pressurization of the interval would not lead to the creation of a new fracture, i.e. a hydraulic fracture. Modeling at the injection source consisted of two distinct stages. Initially, in order to simplify the analysis, a single fracture model was considered to determine the stress conditions of the test (section 5.2.1). The fracture considered was the N161-42°W fracture (red plane in Figure 2.8) that was the closest to the anchors of the borehole extensometer. In the second stage (section 5.2.1), the effect of all the interval fractures was investigated. Five different models were compared in terms of displacement and pressure as described below.

Stress determination

The model is firstly calibrated by defining the stress field and the material properties that can explain the temporal curves obtained from the field experiment. The fracture N161-42°W was considered and the

first tests consisted in investigating the response of the plane under the stress field determined by Cornet [2000] and validated by the Test 1 in the West damage zone (Chapter 3).

Accounting for the possible hydro-mechanical interaction with the fault plane, it was necessary to consider a larger model that would include also the assumed intersection between the interval fractures and the fault plane. Thereafter, the model corresponds to a cube of 35 m and the injection took place at the intersection points of the plane with the borehole. The displacements were monitored at two gridpoints representing the positions of the sensors in-situ, located above the tested fractures. The same injection protocol was applied according to which a constant flow rate of 2.7×10^{-5} m^3 was imposed at all injection points. Provided the size of the model and the distance between the two sensors ($\sim$ 0.4 m) a finer mesh had to be considered around the two gridpoints were the displacements were monitored during the calculation that gradually increased with the distance from the recording points and the center of the model. In this model, the intact rock was considered to be transversely isotropic in order to take into account the anisotropy induced by the bedding. The fracture's response followed the generalized Coulomb friction law. The initial formation pore pressure was set equal to 0.2 MPa as the one measured in-situ. Initially, the same stress field was applied in the model as in the Test 1 case [Cornet, 2000] where the measured fault movement was found to be in agreement with the stress conditions. The highest fluid pressure attained during the injection cycle modeled was equal to $\sim$ 4.2 MPa and the fracture propagation pressure was equal to 3.9 MPa. Under these stress conditions, the fluid pressure during the simulation was much lower than the one measured, 2 MPa lower approximately and the calculated displacements much higher. It was shown that the stress magnitude had to be increased in order to better reproduce the experimental observations in terms of maximum fluid pressure and displacement magnitudes. The principal stress magnitudes were estimated to be:

σ_1	σ_2	σ_3
-4.9 MPa	-4.1 MPa	-3.9 MPa
N188°	N72°	N98°

Table 5.1: Estimated magnitude and direction of the principal stresses for Test 2.

After satisfyingly reproducing the maximum pressure and the displacement order of magnitude, the direction of the displacements was then compared to the experimental data. The slip vector measured was analyzed taking into account the position of the sensors that were placed above the fractures in the interval. Therefore, the sensors did not directly measure the movement of the fractures located below in terms of strike-slip and dip movement. While the principal stress magnitudes were increased, the principal stress directions resulted to a movement along the plane that was characterized as normal slip with a left-lateral slip component as it had been also observed in Test 1. However, such a movement was not in agreement with the displacement signals that mostly showed a normal slip with a right-lateral component along the fractures. With the purpose of reproducing the measured slip vector, the horizontal stresses were rotated by 27° clockwise. The rotation angle was determined by combining the slip tendency analysis with the 3DEC solutions on models including a single N161-42°W fracture, a single N174-65°W fracture or a model with both. The angle of the slip vector with respect to the strike of the fractures was then compared to the one measured. Figure 5.6 shows a schematic view of the resulting slip vector for the stress tensor estimated for Test 1 (dashed red arrow) and the slip vector for the rotated horizontal stresses (solid red arrow) for the fracture N161-42°W that corresponded to the slip vector measured during the last cycle of the test. The orientations of the stress tensor are shown in Table 5.1.

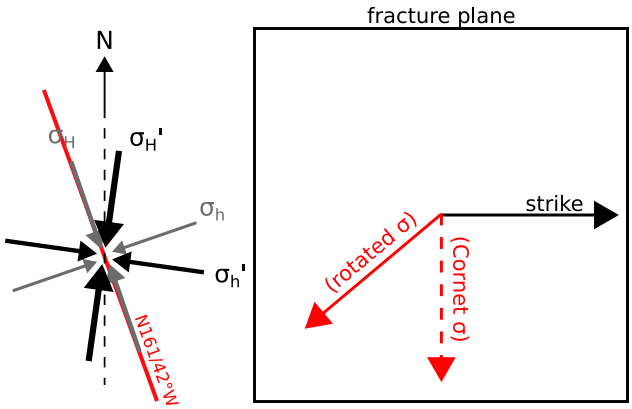

Figure 5.6: (Left): Rotated horizontal stresses 27° clockwise (σ'), and the N161-42°W fracture's strike line. (Right): Slip vector projected on the N161-42°W fracture resulting from the stress tensor as estimated by [Cornet, 2000] and Test 1 and for the rotated stress field (measured slip vector).

Effect of the interval fractures on the hydro-mechanical response

Since more fractures were present in the interval, a study was carried out in order to estimate the effect of the structures on the displacements and pressure evolution during the test. Initially, the N161-42°W fracture is considered together with the fracture N174-65°W (second red plane in Figure 2.8). Then, another model is created that includes the N161-42°W and the bedding plane located above the sensors oriented N166-10°W (green plane above the sensors in Figure 2.8). The results of the models are analyzed in terms of displacements and fluid pressure for the duration of the last cycle of Test 2 and compared to the field measurements. It is therefore possible to evaluate whether the consideration of more than one fractures influences the hydro-mechanical response.

- Single N161-42°W fracture model (case 1)

The single N161-42°W fracture model consists of a cube of 35 m cut by the persistent fracture. Since the injection borehole is not explicitly represented in the model, for a radius of 1 m around the injection point, an area is defined that is already damaged at the onset of the injection. In this way, the damage zone around the borehole is taken into account and a potentially already reactivated fracture part due to the preceding cycles. The injection takes place at a point-source that represents the intersection of the fracture with the borehole. The stress field as estimated above is applied at the faces of the model and an initial pore pressure equal to 0.2 MPa which is the formation in-situ pore pressure is also applied in the model. The flow rate imposed at the injection point is equal to $2.7 \times 10^{-5}\ m^3/s$ derived from the volume of water injected during 1000 seconds of the last cycle. In the presence of more fractures within the test interval (cases described below), the injection takes place at all points where the borehole intersects the fractures. The fluid pressure is monitored at the injection point(s) while the displacements are recovered as the relative displacement of two gridpoints representing the anchors. Considering the distance of the anchors in-situ that is 0.48 m and in order to well represent their position, it was necessary to create a much finer mesh around the injection point. Therefore, the mesh size gradually increased from the center of the model towards the boundaries starting from a side of the tetrahedral zones equal to 0.3 m reaching 1.2 m closer to the boundaries. The initial conditions and the material properties of the single or two-fracture model are summarized in Table 5.2. It is noted that a cohesion value of 0.5 MPa is assigned to

the fracture N161-42°W in order to approximate the maximum pressure at the beginning of the pumping cycle. This cohesion value can be justified by the presence of calcite in the Tournemire fault and fractures.

Boundary conditions		
Stress field: $\sigma_x = -4.9 \times 10^6$ Pa, $\sigma_y = -3.9 \times 10^6$ Pa, $\sigma_z = -4.1 \times 10^6$ Pa		
Initial pore pressure: $pp_{ini} = 0.2 \times 10^6$ Pa		
Rock matrix properties		
Density: $\rho = 2500 kg/m^3$		
Young's modulus parallel to bedding: $E_1 = E_2 = 8.5 \times 10^9$ Pa		
Young's modulus normal to bedding: $E_3 = 3.6 \times 10^9$ Pa		
Poisson's ratio parallel to bedding: $\nu_{12} = 0.33$		
Poisson's ratio normal to bedding: $\nu_{13} = \nu_{23} = 0.33$		
Shear modulus parallel to bedding: $G_{12} = 3.2 \times 10^9$ Pa		
Shear modulus normal to bedding: $G_{13} = G_{23} = 1.4 \times 10^9$ Pa		
Fractures properties		
	N161-42°W	**N174-65°W, N166-10°W**
Normal stiffness: K_n	100 GPa/m	100 GPa/m
Shear stiffness: K_s	4 GPa/m	4 GPa/m
Friction angle: ϕ	20°	20°
Cohesion: c	0.5×10^6 Pa	0
Tensile strength: σ_t	0	0
Hydraulic aperture: u_{h0}	3×10^{-5} m	3×10^{-5} m
Fluid properties		
Bulk modulus: $K_f = 2 \times 10^9$ Pa		
Density: $\rho_f = 1000 kg/m^3$		
Dynamic viscosity: $\mu = 10^{-3} Pa \times s$		

Table 5.2: Boundary conditions and material properties for the models at the injection location.

The single N161-42°W fracture model is shown in Figure 5.7(a) along with the displacement and pressure evolution (Figure 5.7(b)). The anchors location above the fracture is also shown in Figure 5.8(a) in black and the injection point in blue along the fracture plane. The injection point is the intersection of the borehole axis with the fracture. The properties of the fracture are shown in Table 5.2. The maximum pressure during the calculation is equal to 4.25 MPa (dashed line) and the maximum pressure measured in-situ is 4.2 MPa (solid line) showing a good agreement between the two values. The fluid pressure in both numerical and experimental data slightly decreases throughout the injection reaching a value of 3.9 MPa that corresponds to the fracture propagation pressure. Figure 5.7 shows the fluid pressure distribution at the end of the calculation ($t = 1000$ seconds) within the fracture. It is observed that the propagation is not occurring uniformly around the injection point but mostly upwards and towards the North (negative x) which is explained by the strong right-lateral movement. Under flow rate controlled loading conditions, it is expected that the propagation is not uniformly radial as discussed in Chapter 4. In terms of mechanical response, the displacement in the z-direction is slightly underestimated while the horizontal y-displacements is slightly overestimated (Figure 5.7(c)). The x-displacement is in good agreement with the experimental measurements. It is noted that at the onset of the injection the z-displacement direction is towards the negative z-axis probably due to numerical effects. Soon after the beginning of the injection the direction changes following the direction of the z-displacement captured in-situ. The pressurized and rupture zone is about 15 m in diameter with a maximum distance of 10 m

from the injection point. Keeping in mind that the exact reproduction of the measurements is not the main objective of the study, it is obvious that the stress field applied and the orientation of the fracture can satisfyingly represent the in-situ reactivation conditions where the fracture is assumed to have exhibited a normal slip with a right-lateral slip component.

- Single N174-65°W fracture model (case 2)

In the second model, the fracture N174-65°W is modeled (Figure 5.7(d)). Taking into account the geology of the interval, the N174-65°W fracture is further away from the measuring points in the injection chamber ($\sim$ 0.71 m) comparing to the position of the N161-42°W fracture ($\sim$ 0.36 m) (Figure 5.8(a), (b)). The pressure increase is in this case affecting larger area of the fracture (Figure 5.7(e)) without any pressure build-up occurring. This is attributed to the fracture being more optimally oriented with respect to the stress field and to the zero cohesion value assigned. As a result, the fluid pressure within the fracture was about 3.89 MPa, lower than the maximum pressure value recorded in-situ (Figure 5.7(f)). In terms of displacement, the calculated magnitudes in all direction were much lower than the ones measured in-situ showing that the movement of the N174-65°W, if it was reactivated, could not be directly captured by the anchors in-situ.

- Single N166-10°W fracture model (case 3)

The bedding plane located above the anchors in the interval was then modeled as shown in Figure 5.7(g) and Figure 5.8(c). The distance of the bedding plane from the upper anchor is approximately 0.56 m (Figure 5.8(c)), larger than the N161-42°W fracture's distance from the lower anchor but smaller than N174-65°W fracture's distance from the lower anchor. The fluid pressure distribution within the bedding plane appears to be uniform with the pressurized zone being larger than the N161-42°W fracture and smaller than the N174-65°W fracture (Figure 5.7(h)). The reason for which the bedding plane is reactivated for a larger area than the N161-42°W fracture is that even if it is unfavorably oriented, it characterized by zero cohesion unlike the fracture. The maximum pressure during the calculation was equal to 4.36 MPa, higher than the measured maximum fluid pressure (Figure 5.7(i)). The calculated fluid pressure remains higher than the measured for the whole duration of the injection. The calculated displacements remain very low with respect to the measurements (Figure 5.7(i)). Accounting for the orientation of the bedding plane, it is expected that the movement would be limited in terms of normal and shear displacement but also if the position of the plane is considered, its limited movement will result in an even more limited displacement captured by the anchors.

- N161-42°W and N174-6°W fractures model (case 4)

In order to investigate how the fractures in the interval interact, two additional models were tested that included the N161-42°W fracture together with the N174-65°W fracture (first model) and together with the bedding plane (second model). The two models are shown in Figure 5.7(k), (n). The material properties and initial conditions are the same as for the single fracture models (Table 5.2). Under the same stress conditions, in a model comprising the fractures N161-42°W and N174-6°W, the propagation is mainly occurring along the N174-65°W fracture that is more favorably oriented with respect to the stress field (Figure 5.7(l)). Similarly to what was discussed in Chapter 3, both fractures can be reactivated considering only their orientation with respect to σ_2. Nonetheless, in the presence of the N174-65°W

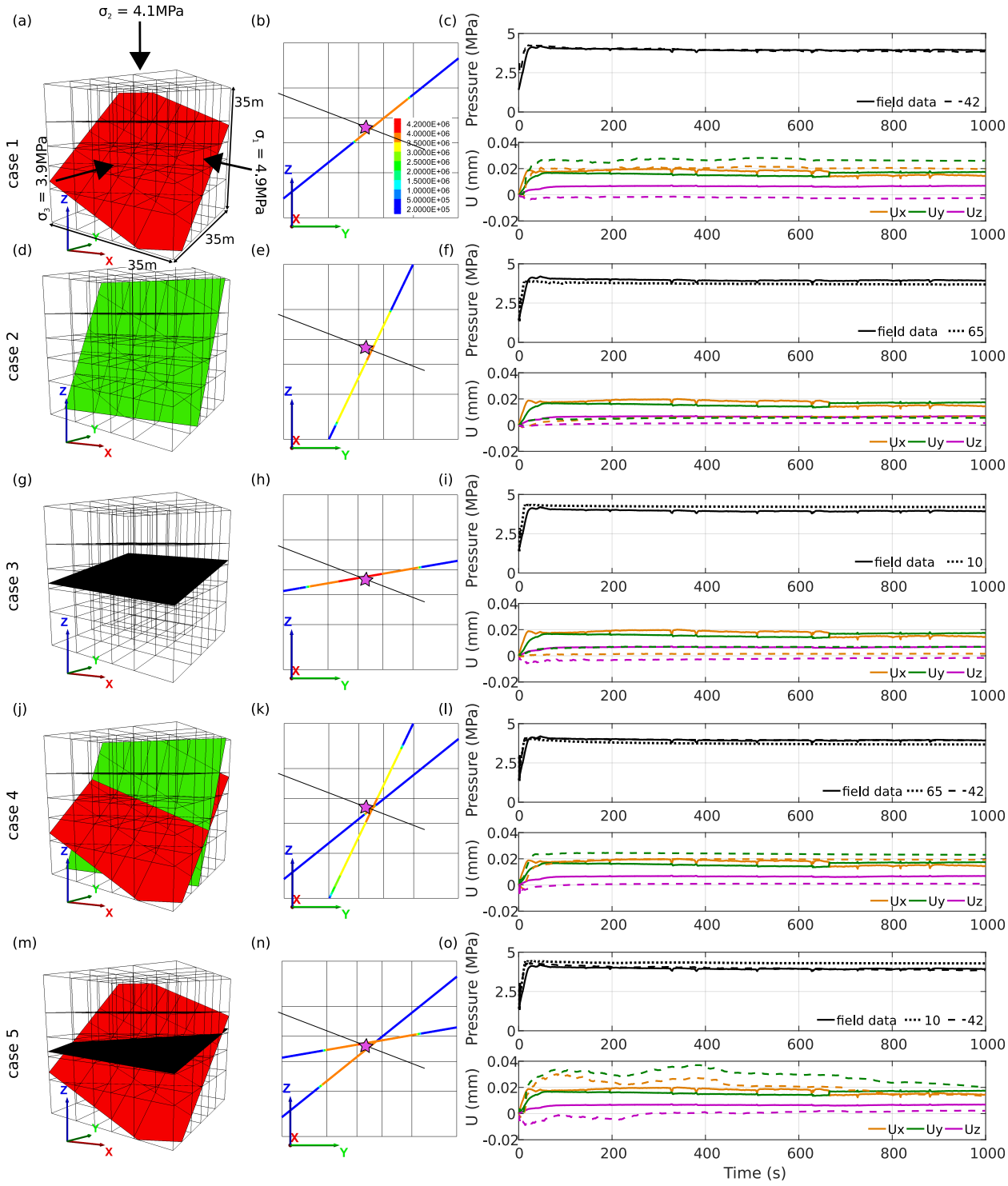

Figure 5.7: Left: model, middle: fluid pressure distribution along the fracture(s) in the z-y plane for $t = 1000$ seconds, right: fluid pressure and displacement variation versus time of the injection for the different configurations studied.

cohesionless fracture, the fluid preferentially propagates along this plane. The fluid pressure in the N161-42°W fracture reached a maximum value of 4.1 MPa and in the N174-65°W fracture 4.0 MPa (Figure

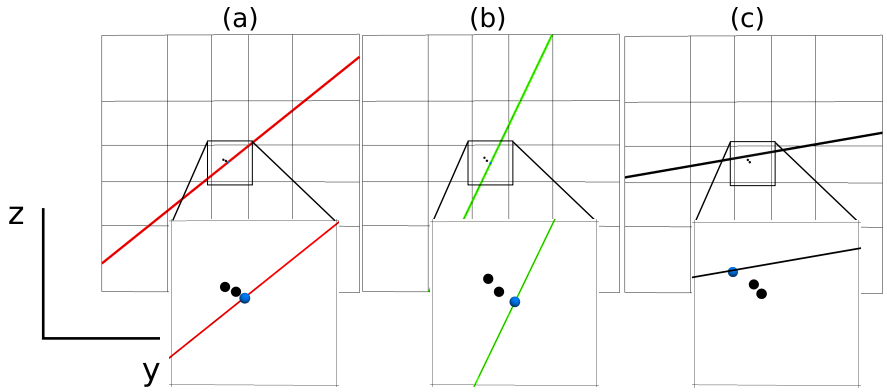

Figure 5.8: z-y view of the model with the zoomed in area (5 m $\times$ 5 m) around the anchors location for (a) N161-42°W fracture, (b) N174-65°W fracture and (c) N166-10°W fracture.

5.7(m)). Both fluid pressures recorded are in reasonable agreement with the field pressure measurement. The displacement monitoring points indicated very good correspondence between the model and field displacements and quite similar to the single N161-42°W fracture model (Figure 5.7(m)). It is therefore shown that the anchors in the model captured the displacement associated to the pressurization at the injection point of the N161-42°W fracture. The movement of the N174-65°W was not directly captured once again but it is possible that it was reactivated together with the other fracture.

- N161-42°W and N166-10°W fractures model (case 5)

In the last model, the bedding plane along with the fracture N161-42°W are modeled. The reactivation takes place in both planes, at both sides of the intersection for the bedding plane and only below the intersection for the N161-42°W (Figure 5.7(o)). Despite the non optimal orientation of the bedding plane, it is conducting the flow since it is characterized by a zero cohesion in contrast with the fracture N161-42°W. This configuration shows a competition of the fractures properties and their orientation. The fluid pressure within the bedding plane reached the value of 4.4 MPa and 4.3 MPa inside the N161-42°W fracture as shown in Figure 5.7(p). The temporal variation of the displacements for this last model shows an overestimation of the horizontal displacements (Figure 5.7(p)). Interestingly, changes of direction are observed throughout the calculation approximately at 200 and 400 seconds for all displacement components. This observation could be the result of the position of the fractures with respect to the anchors. The two fractures included in the model are located outside of the anchors system, one above and one below close to the anchors. The movement of the two fractures can significantly influence the signal showing movement direction changes recorded by the anchors but not actually occurring along the reactivated planes complicating the interpretation. The increase in the displacements and the higher fluid pressure developed in the bedding plane suggest that its reactivation probably did not occur in the way it has been modeled here as it would require a slightly higher fluid pressure. Nonetheless, the 4.4 MPa value reached during the injection in the presence of the bedding plane, approximates the maximum pressure during the first cycle of Test 2 (see Figure 2.9) suggesting that the bedding plane's reactivation should not be excluded.

In terms of pressure, for all the configurations tested, the single N161-42°W fracture model gave the best approximation. Nevertheless, it was shown that the pressure within the fracture N161-42°W slightly changed in the presence of adjacent fractures as the recording points for each fracture were very close in

the model. It was lower in the N161-42°W, N174-65°W fractures model where the fluid was easily absorbed by the more optimally oriented fracture and it was higher in the N161-42°W, N166-10°W fractures model where higher fluid pressure was developed inside the bedding plane due to its misorientation. It should be noted that under such conditions fluid pressure will not necessarily increase uniformly in the interval but it can vary locally depending on the orientation and properties of the intersected fractures. The measured displacements in-situ were better reproduced with the consideration of the N161-42°W fracture either in a single fracture model or together with the N174-65°W fracture. Thereafter, during the last cycle of the injection test in the host rock, the N161-42°W fracture must have been reactivated without excluding the reactivation of the adjacent fractures that must have been reactivated without the anchors being able to capture their real movement magnitude. The comparison of the displacements for the N161-42°W fracture (case 1), the N161-42°W, N174-65°W fractures model (case 4) and the N161-42°W, N166-10°W model (case 5) presented above did not show important differences in terms of displacement direction and magnitude implying that the stress tensor primarily determines the measured movement during the test. The interval geology and fractures interaction plays a secondary role for the interpretation of the experimental observations. Based on the above, either configuration considering the N161-42°W fracture can satisfyingly explain the measurements at the injection source. Nonetheless, keeping in mind that the main purpose of this study is to associate the injection reactivation with the observed seismicity, the fractures that would intersect a sub-vertical fault plane at a higher elevation are selected for the following analysis. Consequently, the fracture N161-42°W and the bedding plane are considered in the models presented below excluding for simplification reasons the N174-65°W fracture that was most probably reactivated during the injection.

5.2.2 Modeling of the injection induced fault reactivation-relation with induced seismicity

Once the injection parameters have been defined at the test location, in a second time and in an effort to explain the microseismicity observed farther away from the injection point, a sub-vertical plane is considered in the model with an orientation that corresponds to the main Tournemire fault orientation (N171-86°W). This modeling study aims at investigating of the mechanism behind the induced seismicity. By performing a hydro-mechanical analysis of the field injection, the possibility of hydraulically connected structures and seismicity resulting from pressure perturbation is examined. The scenario that predicts the hydraulic connection of the involved structures is based on a conceptual geometry of the investigated area shown in Figure 5.9, left. The main idea is that the planes that are potentially reactivated during the injection are hydraulically connected with the fault plane located 5 m away approximately along the borehole. It is assumed that the fracture and the bedding plane are sufficiently long in order to intersect and cross the fault plane. The seismic events as it has been already mentioned are mainly located at the upper and southern part of the investigation area, or the fault plane in the study. Thereafter, the planes that would intersect the fault plane at a higher elevation were considered, i.e. the planes with a lower dip angle with respect to the horizontal. This means that the N174-65°W fracture that mainly conducted the flow in the models presented above, is not included in the models presented below. Initially, two models are investigated according to the number of planes reactivated at the injection source. In the first model, both the N161-42°W fracture and the bedding plane are included along with the fault plane. In the second configuration, the bedding plane is eliminated from the model. The two models are shown in Figure 5.9,

together with the conceptual connection in-situ between the considered structures (left). With the purpose of making the distinction between the planes involved, the N161-42°W fracture plane reactivated during the injection is called "injection plane", N166-10°W is the bedding plane and the plane representing the fault is called "fault plane". The fault plane is considered homogeneous with properties identical to the bedding plane properties shown in Table 5.2. Reminding that the injection takes place at the intersection points of the borehole with the planes and the borehole intersects the fault plane 5 m away as shown in Figure 5.9.

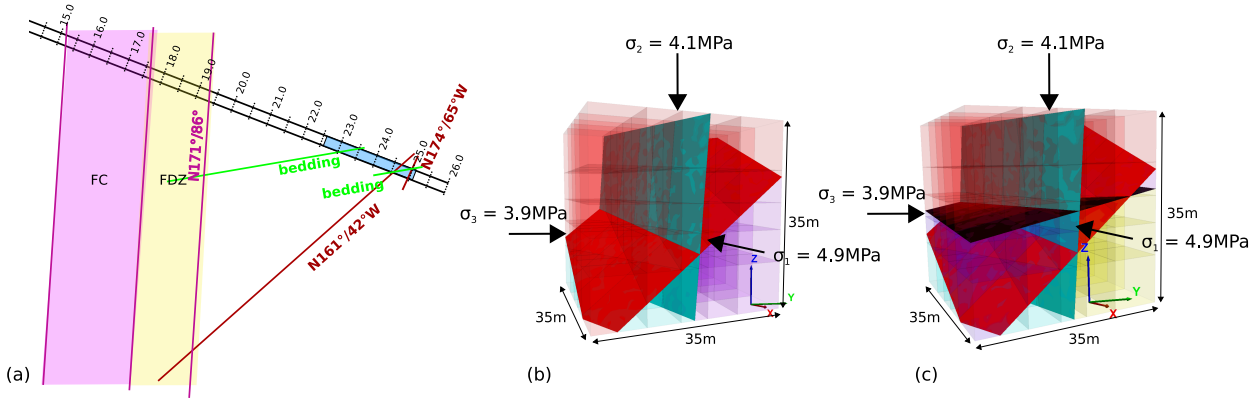

Figure 5.9: (a) Conceptual model showing the intersection of the injection planes with the fault planes. (b) Single injection plane (N161-42°W) and fault plane model. (c) Two injection planes (N161-42°W and N166-10°W) and fault plane model.

N161-42°W fracture, bedding plane and fault plane

Relying on the geometrical aspect of the problem, a first attempt towards understanding the induced seismicity during Test 2 consists of a model with 3 planes, the N161-42°W fracture, the bedding plane and the fault plane as shown in Figure 5.9(c). The fluid propagates inside both planes of the injection interval and at $t = 30$ seconds it starts propagating inside the fault plane at the intersection with the bedding plane. Figure 5.10(a), (b) shows different views of the rupture events for the 3 planes model and the microseismic events recorded in the field. In the presence of the injection plane and the bedding plane intersecting the fault plane, the latter is reactivated for a large surface characterized by a diameter of 25 m. The boundaries of the pressurized zone are at the location of the field microseismic events the closer to the injection source. A propagation tendency towards the bottom of the model is observed even if there are rupture events at higher elevations due to the presence of the reactivated bedding plane. Throughout the injection, the fluid within the injection and bedding planes are not crossing the fault plane but instead flow and rupture propagation is mainly occurring along the fault plane. This is in agreement with the observations discussed in the previous chapters regarding the orientation of the planes also evidenced by the interval fractures interaction of the previous section (Section 5.2.1). The inclined fractures are subjected to a higher normal stress compared to the fault plane.

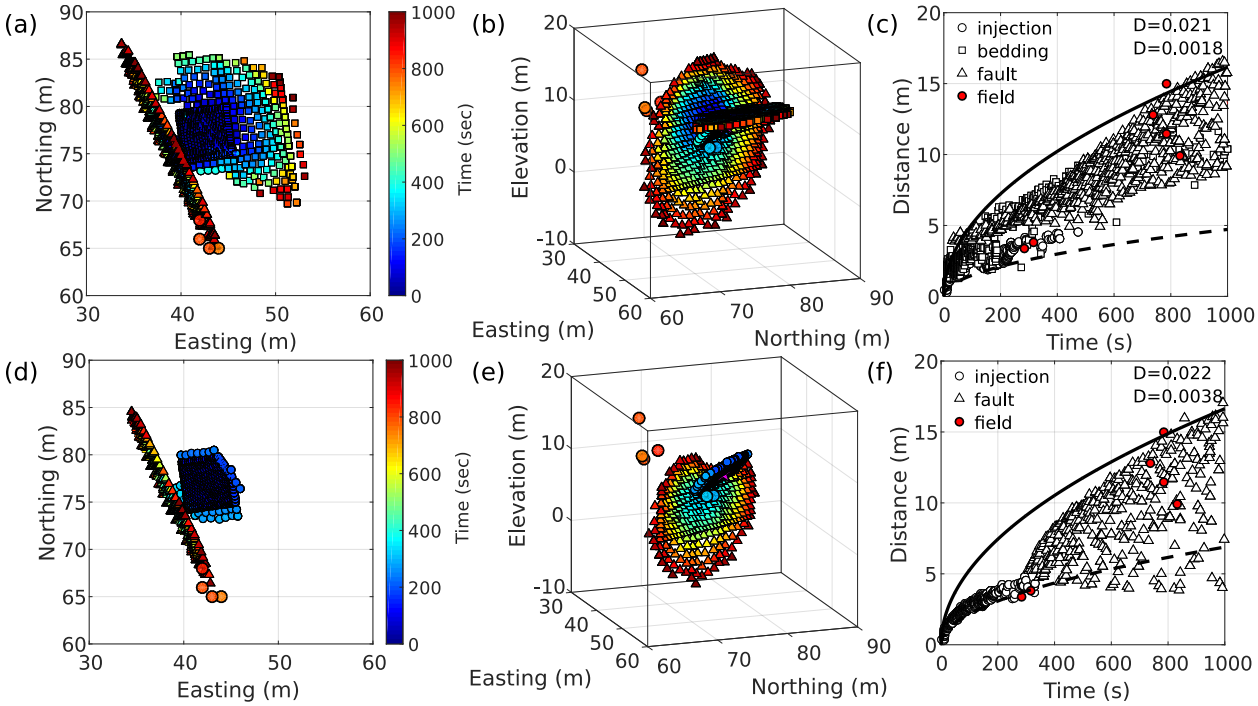

Figure 5.10: (Left) Map view, (middle) view from the East and (right) Distance of the rupture (model) and microseismic (field) events from the injection point as a function of time (r-t plot) for 3 planes model (top) and 2 planes model (bottom). The disks represent the injection plane events, the squares the bedding plane events, the triangles the fault plane events and the field microseismic events are disks characterized by a thicker line (red disks in r-t plots) The triggering front lines correspond to the maximum and minimum diffusivity of the injection plane.

N161-42°W fracture and fault plane

In a second model, the bedding plane is eliminated and a single injection plane is considered that intersects the fault plane at a lower elevation than the bedding plane. Figure 5.10(d),(e) shows different views of the test domain where the rupture events were recorded during the calculation along with the location of the microseismic events recorded in-situ. At the injection plane, the rupture events of the model are within a radius of 5 m around the injection that develops quite uniformly. The pressurized zone is then migrating inside the fault plane at $t = 307$ seconds when the first recorded rupture event occurs. As the injection continues, fluid propagation is mainly occurring along the fault plane with no more rupture events recorded for the injection plane.

In the fault plane the fluid preferentially propagates downwards towards the bottom boundary of the model (Figure 5.10(d),(e)). This is reminiscent of the behavior observed in the Chapter 4 and more specifically in Section 5.1.2 where the obliqueness of the fault resulted in a propagation front towards the direction of slip under flow rate controlled loading conditions. Comparing with the location of the events recorded in-situ, the model events are partitioning downwards showing clearly that there is no agreement in terms of location. The larger distance from the injection point in the model is approximately 16 m similar to the maximum distance of field events but not in the same direction. The size of the reactivated zone is smaller compared to the previous case. However, even if this configuration is not in agreement with the in-situ location of the microseismic activity recorded during the test, it is shown that rupture can

occur at a distance of 15 m away from the injection by reactivating a fault plane through pressure diffusion and effective stress decrease mechanisms.

- **Effect of fault heterogeneities**

So far, the fault plane was considered homogeneous in terms of hydro-mechanical properties. Based on the study in Chapter 4 and Section 5.1.3, it was shown that channeling can significantly affect the hydraulic properties evolution and the form of the events cloud in the model. More specifically, the reactivation of a structure is highly conditioned by the surface characteristics and by the presence of material heterogeneities along the plane. Depending on the connectivity of the less resistant areas, flow channeling can occur and the fluid front can travel farther away in the presence of low friction zones as described in the previous chapter. In an attempt to examine how channeling can affect fluid propagation and rupture in a complex configuration based on experimental observations, different scenarios are tested. In the following, the fault plane is considered heterogeneous by introducing a statistical variability of the friction with a "homogeneous" or not distribution. The different configurations tested are shown in Figure 5.11 as a view from the East (y axis). The N161-42°W fracture is not shown for clarity reasons but the trace of the plane, or the intersection line can be seen on the fault plane. The homogeneous fault plane is shown in Figure 5.11(a) for which the static friction is equal to 20°. The higher friction zones are characterized by a static friction value equal to 35° while the rest of the strength properties, elastic properties and hydraulic aperture are identical to the original fault plane's properties.

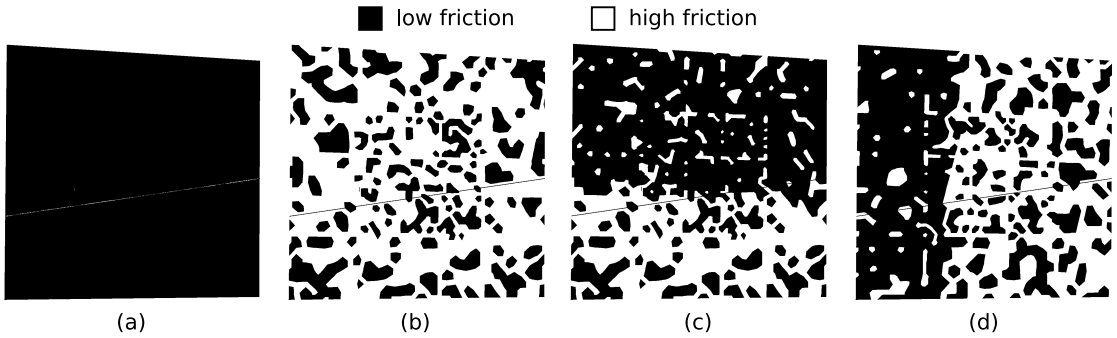

Figure 5.11: Cases considered for the sensitivity analysis. (a) Homogeneous fault plane, fault plane with (b) 80% of high friction areas, (c) 20% in the upper part and 80% in the lower part, (d) 20% in the southern (left) part and 80% in the northern (right) part.

"Homogeneously" distributed mechanical heterogeneities

A homogeneous distribution of contacts is considered for the first configuration of the sensitivity study shown in Figure 5.11(b). The frictional heterogeneities take up 80% of the fault's total surface resulting in a fractional area $c = 0.8$. Figure 5.12, upper line, shows the location comparison of the model rupture events and the microseismic events. The activated zone of the fault is again located at the lower part of the plane as for 80% of contacts, the flow regime is influenced by the stress field and slip direction. Reminding that due to the large size of the model and the small distance of the anchors, a part of the model encasing the injection location on the fracture N161-42°W and the two monitoring points for the displacements had to be finely meshed (0.3 m side of each zone), as such a mesh size would not be possible or practical for the whole model volume. It is understood that the implementation of heterogeneities strongly depends

on the size of the mesh as the heterogeneous properties are assigned to the sub-contacts of the plane. For a smaller mesh, the high/low friction areas (depending on the dominant friction value) will be smaller while for a larger mesh they will be larger. This is also evident in Figure 5.11(b) where the size of the low friction areas gradually increases from the center of the plane towards the boundaries. As a result, the response of the plane closer to the center tends to be similar to the homogeneous case since there are no low friction channels of large size that can significantly influence the propagation regime. It can be seen that such channels are encountered around 700-800 seconds towards the bottom the model. Here again, the location of the field events could not be approximated with the rupture cloud of this configuration.

Different heterogeneities distribution in the upper and lower fault plane

The next configuration tested consists of a fault plane characterized by 20% of heterogeneities along the upper part and 80% along the lower part (Figure 5.11(c)). The fault plane is therefore characterized by an overall lower friction above the intersection with the injection plane and an overall higher friction below. Since fluid propagation in the model is directly linked to the failure of the sub-contacts, the largest surface affected by the fluid pressure is located above the intersection with the injection plane, as the dominant friction is lower (Figure 5.12, middle line). Nonetheless, the seismic events are still outside or at the limits of the pressurized area predicted by the model. It is obvious that such a configuration approximates better the location of the events as a result of pressure diffusion within the fault plane. However, the friction distribution implies that the presence of heterogeneities in the form of contact areas or calcite patches is stronger in the lower part of the plane, an assumption that cannot be directly associated to field observations.

Different heterogeneities distribution in the southern and northern fault plane

Accordingly to the Southern and upwards location of the majority of the events occurring during the last cycle, the fault plane in the third configuration is vertically divided in two domains (5.11(d)). In the left part of the plane, 20% of contacts are present, while on the right 80%. For the two last configurations, the idea was to facilitate fluid propagation and effective stress variation towards the direction of the observed seismicity. The pressurized and rupture zone along the fault plane is again migrating towards the bottom of the model with a number of events above the intersection with the injection plane but well below the field events (Figure 5.12, lower line). Channeling is more pronounced in this configuration for $t = 600$ seconds approximately where at least three distinct channels can be observed towards the bottom of the model. The maximum distance of the events from the injection point was almost 20 m due to the creation of the flow channels as illustrated also in the r-t plot in Figure 5.12, bottom line. This configuration, like the second case too, is a strong assumption as it is arbitrarily considered that the fault is weaker towards the South and upwards.

5.2.3 Discussion

The experimental observations regarding the seismic activity within the fault zone combined with the numerical study performed offers an opportunity to explore the possible mechanisms responsible for the induced seismicity. These mechanisms behind natural or induced seismicity normally include pressure diffusion processes and associated effective stress variations [Shapiro et al., 2002; Parotidis et al., 2003; Miller et al., 2004; Cappa et al., 2009; Shelly et al., 2015] or poroelastic stress transfer and aseismic de-

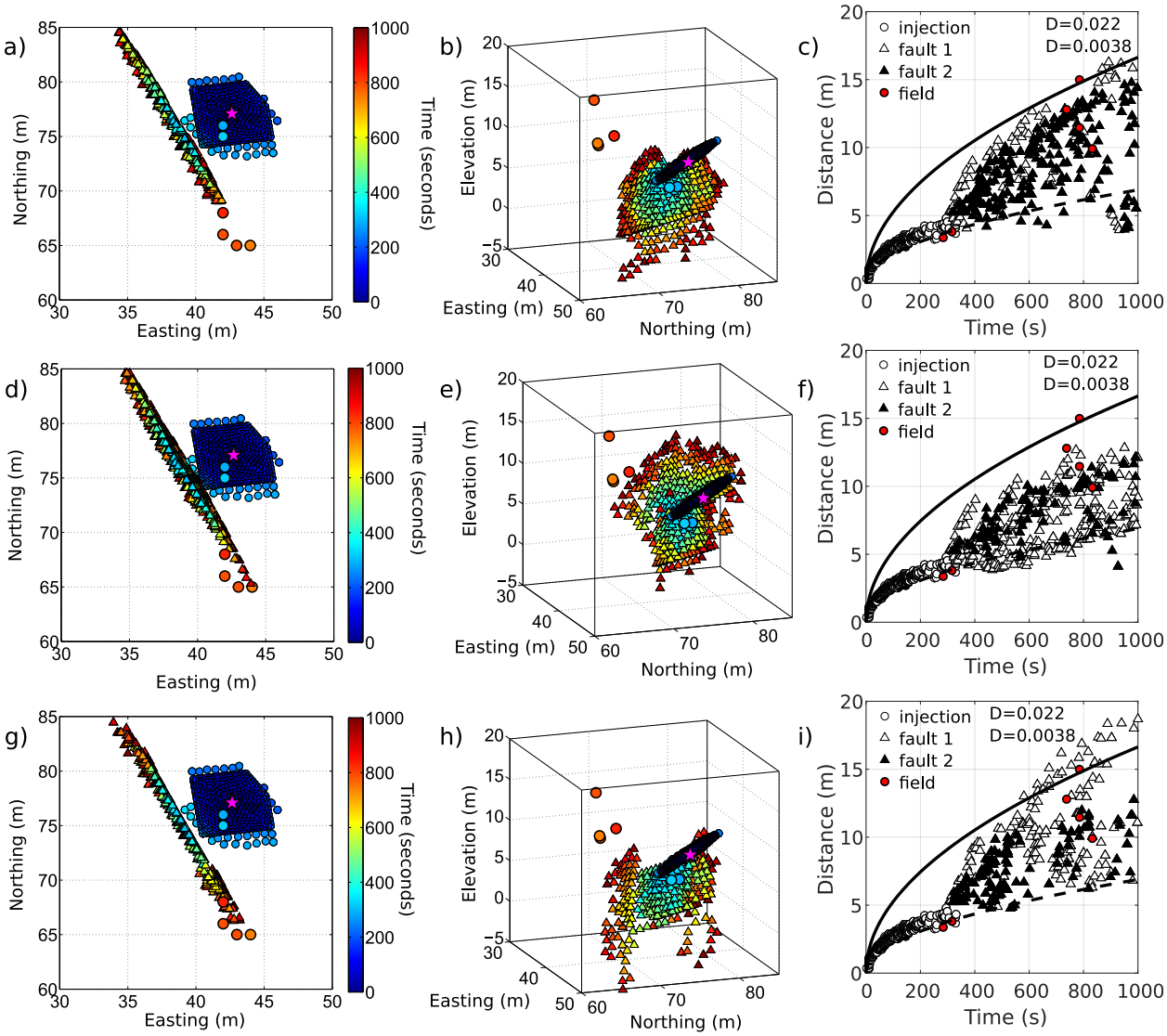

Figure 5.12: (Left) Map view, (middle) view from the East and (right) Distance of the rupture (model) and microseismic (field) events from the injection point as a function of time (r-t plot) for 3 planes model (top) and 2 planes model (bottom). In the r-t plot, the disks represent the injection plane events, the hollow triangles the low friction fault plane events, the solid triangles the high friction events and the field microseismic events are the disks characterized by a thicker line (red disks in r-t plots) The triggering front lines correspond to the maximum and minimum diffusivity of the injection plane.

formations [Scotti & Cornet, 1994; Bourouis & Bernard, 2007; Wei et al., 2015; Goebel et al., 2017]. The interpretation of fluid induced seismicity in a natural or industrial context is not straightforward since it will always incorporate both mechanisms [Hainzl & Ogata, 2005].

Fluid diffusion induced seismicity

The effective stress concept dictates that fluid pressure diffusion within the formation and the consequent decrease in the effective stress causes critically oriented structures to fail seismically [Healy et al., 1968]. Therefore, fluid pressure propagates accordingly to the diffusion equation and seismicity is directly related

to the diffusivity of the formation [Shapiro et al., 2002; Shapiro & Dinske, 2009]. The triggering front concept as discussed in section 5.1 was applied to the model cases described in section 5.2.2 in order to observe whether there is a link between the hydraulic properties of the reactivated structures, the associated rupture and in-situ seismicity.

- Hydraulic diffusivity of the structures

Starting from the tested models, the triggering front lines were calculated for all different cases using the recovered maximum and minimum transmissivity values for the injection plane, N161-42°W (Equation 1.8) that in all cases appears to be similarly reactivated. The spatio-temporal characteristics of the rupture events and the triggering front lines in distance-versus-time (r-t) plots are shown in Figure 5.10(c), (f) and 5.12(c), (f), (i). The minimum and maximum diffusivity values were 0.0038 and 0.02 m^2/s respectively with the exception of the 3 planes model, for which the minimum diffusivity was 0.0018 m^2/s. Focusing on the rupture events produced during the injection simulations, the spatio-temporal characteristics seem to be well enveloped by the two triggering front lines with the maximum diffusivity defining the upper limit and the minimum diffusivity the lower limit. The triggering front line calculated based on the minimum diffusivity seems to provide a lower limit to the majority of the events along both planes for most of the configurations considered. The maximum diffusivity appears to better envelope the events occurring along the fault plane and not necessarily during the reactivation of the injection plane. It should be noted that the distance from the injection in all cases is assumed to be the distance of the events from the injection point on the N161-42°W fracture.

For the N161-42°W fracture and fault plane model case (without the bedding plane), in an effort to precisely fit the triggering front lines according to the events' characteristics, the diffusivity should increase at $t = 307$ seconds when the fluid starts propagating inside the fault zone. This pattern is not as evident in the N161-42°W fracture, bedding plane and fault plane case where the interaction of 3 planes results in a much more "diffusive" pattern without clear transition from one plane to the other (Figure 5.10(c)). It is obvious that without the bedding plane, once the inclined fracture becomes hydraulically connected with the fault plane, no further rupture is occurring along the injection plane. Taking into account the orientation of the N161-42°W fracture and the fault plane, under constant fluid pressure conditions the increase in diffusivity is justified in the sense that the fluid propagates initially along a plane of lower permeability due to the orientation with respect to the stress field and then meets an optimally oriented plane where it can diffuse at larger distances easily "opening" the plane. Nonetheless, under flow rate controlled conditions, which is the case in this study, the fluid pressure inside the planes significantly varies depending on the orientation. Consequently, the fluid pressure inside the injection and the fault plane is 4.2 MPa and 3.3 MPa respectively. The high fluid pressure in the N161-42°W fracture ($\sim$ 4.2 MPa) results in a highly pressurized zone around the injection point that produces local aperture increases and consequently higher local transmissivity. On the contrary, the ability of the fault plane to conduct the flow results in a more rapid pressure diffusion without pressure build up and consequently a larger reactivated zone that is however characterized by lower apertures and a diffusivity around 4 times lower than that of the injection plane. Hence, using the fault diffusivity for calculating the triggering front line would not describe the cloud of the events. Through this analysis, the difficulty in applying the triggering front concept on hydraulically connected and interacting structures is pointed out as the interaction of fractures of different orientation under fluid pressurization conditions induces a strong heterogeneity and as a result the rupture events' spatio-temporal characteristics cannot be directly related to the hydraulic

properties of each plane. However, it is shown that the hydraulic properties around the injection point are able to better represent the conditions under which both the injection plane and the fault are affected by the injection.

- Location of the microseismic events

The seismic events recorded in-situ are also better explained considering the diffusivity of the injection plane. More specifically, assuming that the seismicity front followed the pressure diffusion front, the first two events around 300 seconds would be described by a diffusivity approximately equal to 0.0038 m^2/s while the events at 800 seconds and at a distance of 10-to-15 m would correspond to a diffusivity of 0.02 m^2/s. Nevertheless, such seismic behavior observed at 800 seconds where the events are scattered in space and clustered in time is rather associated to a mechanism of stress perturbation through failure than fluid diffusion [Duboeuf et al., 2017]. The events at 300 seconds located at 3.5 m from the injection point are potentially related to effective stress variations close to the source.

For all the cases studied, there were only two where the fluid and rupture (strictly coupled in the model) approximated the location of the seismic events. Only in these two cases it was possible to associate seismicity with a fluid diffusion process. It should be noted that in nearly all cases, the rupture events along the fault reached a distance of 15 m away from the injection point, similar to the distance of the farthest microseismic event but towards a different direction. The activity was mainly concentrated towards the South and above of the injection location. These two "best-fit" cases were the N161-42°W fracture, bedding plane and fault plane model and the configuration where the fluid is horizontally divided in a low (upper) and high (lower) friction area. Therefore, the two possibilities observed in this study where the fluid can propagate upwards and towards the South and potentially result in seismicity along the plane are that the bedding plane is hydraulically active during the injection cycle or that the fault is characterized by lower strength properties above the intersection with the injection plane favoring propagation upwards where the the failure criterion is satisfied for lower fluid pressure values.

The first scenario that includes the bedding plane requires that the bedding plane is hydraulically connected with the fault plane and that it is at least hydraulically activated. The first point can be considered valid since the bedding plane is a structure that is strongly present in the Tournemire shale responsible for the elastic and strength anisotropy. The reactivation of the bedding plane needs 0.2 MPa higher fluid pressure than the one measured during the last cycle of Test 2 and equal to 4.2 MPa. A fluid pressure of 4.4 MPa corresponds to the maximum pressure observed during the first cycle and generally during Test 2 and might as well correspond to shear activation of the bedding plane [De Barros et al., 2016]. It is possible that the mechanical activation of the bedding plane occurred during the first cycle and re-occurred during the last cycle without reaching the same pressure values because of the first reactivation. Therefore, the assumption of a bedding plane hydraulically connecting the injection location with the fault plane could be viewed as a possible explanation for the observed seismicity that in this case would be attributed to fluid flow within the fault plane and effective stress variations.

The second scenario is based on the assumption that the fault is "weaker" in terms of frictional strength above the intersection with the injection plane. This "forces" the fluid to preferentially propagate upwards. While the pressurized zone is close to some of the events occurring upwards, such a distribution of frictional properties along the fault plane cannot be evidenced from field observations. This scenario of pressure diffusion induced seismicity consists of a particular case that cannot be directly and properly justified so far. Thus, in the absence of the bedding plane, the hydro-mechanical reactivation of the N161-42°W fracture and its hydraulic connection with the fault plane is more unlikely to provide the triggering

of rupture and potential seismicity on the upper part of the fault plane. The effect of the heterogeneities along the fault could not be directly evaluated in the sense of distinct flow channels creation, because of the mesh size variation in the model. This led to the results of two out of three cases being quite similar to the homogeneous plane configuration. Flow channels along the plane could explain the occurrence of events clustered in time and at a certain distance from the injection point. For example the 80% case of section 5.1 showed high friction rupture events clustering in time for $t = 3, 5, 10$ seconds approximately (see Figure 5.4(l)). Nevertheless, the scale dependency of such a response should be carefully taken into account.

Stress perturbation associated to aseismic slip

The general direction tendency of the fault plane reactivation was downwards except for the two case analyzed above as the fluid under the given stress conditions propagates in the opposite direction of the migrating seismicity. Even in the two "best-fit" cases, it was shown that although rupture can occur close to the seismic events location, the events always stay at the limits of this pressurized zone. This implies that in-situ it was probably the combination of fluid pressure diffusion and aseismic slip that determined the seismic signature. This is in agreement with recent studies emphasizing the significance of the fluid driven aseismic deformations and their effect on the induced seismicity [Bourouis & Bernard, 2007; Guglielmi et al., 2015a; Cornet, 2016; Duboeuf et al., 2017]. Moreover, Guglielmi et al. [2015a] concluded that micro-earthquakes occur off the pressurized zone and more specifically when the size of the slip zone becomes larger than the pressurized zone. While the events at 300 seconds can be attributed to fluid flow given the size of reactivation in the model, the events clustering at 800 seconds might as well be characterized as "dry" events occurring at the boundaries of the pressurized zone as the indirect effect of aseismic slip within the pressurized zone. This preconditions that the seismic front will be ahead of the pressure front. McClure & Horne [2011] proposed a mechanism that does not involve dry events but predicts that friction weakening allows slip and permeability enhancement to advance ahead of the pressure front. However in this case fluid is required for friction weakening to occur. Such behaviors cannot be directly predicted in the models used in this study since fluid pressure propagation and rupture are tightly coupled along the same plane.

In the analysis by De Barros et al. [2016] regarding the seismicity recorded during the Tournemire experiments, it was concluded that the seismicity distribution was more likely to be localized outside or at the extremities of the pressurized area linked to stress perturbations and to the internal properties of the fault architecture, the seismicity therefore being a secondary, indirect effect of fluid flow. The direct decoupling of fluid pressure and seismicity implies also a decoupling between permeability and seismicity that has been observed during fluid injection tests [De Barros et al., 2016; Duboeuf et al., 2017]. The results in both campaigns suggest that there is a lack of seismicity in high permeability test intervals due to lower fluid pressure development. Seismicity was mostly associated to higher fluid pressures in zones with low bulk permeability. The fault plane assumed to be the plane where seismicity took place is a high permeability structure taking into account only its orientation towards the stress field. Upon fluid pressurization, such a plane would offer a rate-strengthening behavior deforming aseismically considering that the friction is homogeneous along the plane. Therefore, the events would be explained by some areas along the plane experiencing weakening during deformation [Guglielmi et al., 2015a] provided frictional heterogeneity is present. Furthermore, accounting for the Tournemire fault architecture, the plane used in the model to represent the fault corresponds in-situ to the boundary between the East Damage zone

and the host rock. The East damage zone is characterized by fractures striking N150-180 and dipping 30-60°W (Family 1). This orientation is in good agreement with the source mechanisms estimated by De Barros et al. [2016] for the events who concluded that the seismicity during the experimental tests resulted from stress transfer effects that are more intense in the East part of the fault. These structures present in the East damage zone are calcite-filled and characterized by a lower permeability comparing to the sub-vertical fault plane. It is therefore possible that the events occurred along these adjacent or intersecting with the fault plane fractures as a response to the fluid pressure increase and large aseismic deformation of the fault plane. This is also supported by the mineralogical signature of the structures that favors unstable failure [Niemeijer & Spiers, 2005].

Based on the aforementioned, the links between the fluid pressure diffusion and seismicity are not straightforward in the study presented. It can be concluded that most probably the seismicity was not a direct effect of fluid presence along the seismic patches. Even though different mechanisms of unstable slip cannot be investigated in the model, useful information can be deduced regarding the potential position of the pressurized zone and its correspondence with the events location recorded in-situ.

5.3 Summary of the chapter

The model described in section 5.1 showed that the plane orientation as well as the heterogeneous distribution of the frictional properties affect the rupture propagation regime along a plane. The rupture propagation regime is also influenced by the applied loading conditions as distinctive behaviors were underlined for a flow rate and a pressure controlled injection. For a constant low flow rate controlled injection, we observed that the flow is radial and uniform only for a homogeneous fault plane almost aligned with the principal stress axes. For the rest of the configurations tested, the flow was either affected by the obliquity and slip direction of the plane (0%-30% of contacts), by the spatial arrangement of low friction areas (40%-60%) or by both (70%-80%). The triggering front concept was used by correcting the storativity equation with a factor f that reflects the percentage of the high friction areas to the total area. We found that for approximately radial flow patterns, the hydraulic diffusivity of the fault is in good agreement with the distance and occurrence time of the events. Where strong channeling was observed, it was not possible to correlate the hydraulic properties and the distance of the events. Finally, considering in our model the events characterized by higher slip rates as possible stick-slip failures, we observed that "late" ruptures initiating at a direction different from the one imposed by the slip movement or the low friction channel could favor potential seismicity.

In the second part of the chapter, modeling of the Test 2 in the Tournemire host rock was presented. Initially, a numerical model was developed focusing on the injection source location. Through the first analysis, the injection parameters were calibrated that include the stress field active at the time of the reactivation, the structures that were reactivated, their orientation and properties. It was shown that in order to reproduce the fluid pressure magnitude and the slip direction measured during the last cycle of Test 2, it was necessary to rotate and increase the magnitude of the horizontal stress components. The horizontal stresses were rotated by 28° clockwise while σ_H, σ_v, σ_h were increased by 0.9, 1.8 and 0.2 MPa respectively. This implies that the stress tensor is different on each side of the fault if the stress tensor determined by Cornet [2000] and validated by Test 1 (modeled in Chapter 3) is taken into account. The response of the fractures intersected by the interval was investigated showing that the anchors most probably captured the displacements along the N161-42°W fracture. The bedding plane and the N174-

65°W fracture were also likely to have been reactivated. Integrating the results of these ”injection location” models it was shown that the stress field is the main factor determining the movement captured by the anchors as the movement direction of all three planes tested was similar.

Then, an attempt was made towards investigating through a coupled hydro-mechanical model the processes associated to the induced seismicity of the test. Different configurations were tested showing that only two of them resulted in a pressurized zone nearing the location of the events recorded in-situ. The first one considered the modeling of the N161-42°W fracture and the bedding plane together with the fault plane and in the second one it was assumed that the fault zone was characterized by lower friction properties in the upper part facilitating the upwards fluid movement closer to the events. In both cases, the events were located at or close to the extremities of the fluid pressure perturbation zone. For the rest of the cases the pressurized and rupture zones were developed below the intersection with the injection plane far from the events' location. The above observations suggest that seismicity cannot be directly associated to a pressure diffusion process and effective stress decrease but rather to the aseismic fluid induced deformation close to the events promoting stress transfer effects. This conclusion is in agreement with recent studies and the interpretation of the microseismicity during or after field injection at the meso-scale and the reservoir scale.

Conclusions and Perspectives

In the present thesis, an attempt was made towards defining the links between fault permeability and fault hydro-mechanical reactivation based on experimental data and field observations. To that end, three-dimensional fully coupled hydro-mechanical analyses were performed using the Discrete Element Method and more specifically the Distinct Element Code, 3DEC. The specific method and tool were chosen in order to capture the hydro-mechanical processes occurring at the scale of a single discontinuity and at the scale of fracture networks that in most cases tend to control fluid flow and deformation in fractured rock masses.

Chapter 1 provided an overview of the problem and of the basic concepts and recent developments in the field of fault reactivation related issues. The description of the experimental site and the conducted field tests that were used as a basis for the numerical analysis were described in the second chapter (Chapter 2) together with the numerical tool selected and the general methodology followed.

Chapter 3 was focused on the role of the fault-related structures orientation, interaction and the applied stress field. Three "multi-fracture" configurations assuming high fracture connectivity were presented that emphasized the combined effect of orientation and stress conditions on the bulk permeability of the fault damage zone. Only two or three fractures were reactivated during the test and for given fluid pressure values promoting channeling of the flow along optimally oriented fractures. Under such loading conditions, fractures forming an angle $> 50°$ with the maximum principal stress remain hydraulically inactive not contributing actively to the hydro-mechanical response of the system. After confirming the significance of the stress and of the fracture orientation, the model used for the sensitivity analysis also demonstrated that natural fracture reactivation is also controlled by the deformation (opening in this case) of adjacent fractures. It was concluded from this study that two distinct responses co-exist along the same fracture plane depending on the vicinity to the mode I fracture. The natural fracture is experiencing shear displacement and permeability increase associated to effective stress variations but also the segment close to the mode I fracture is hydraulically inactive and experiences shear displacement as the result of stress transfer effects. Such an observation shows that the hydraulic and mechanical reactivation along a fracture do not necessarily coincide. Under isotropic stress conditions, the fracture material properties had a minor effect on the natural fracture reactivation while the intact material properties affected mainly the flow rate and displacement magnitudes but not the general trends.

In a simple single fault model presented in Chapter 4, the fault heterogeneities were taken into account in the form of frictional heterogeneities statistically distributed along the plane. This approach allowed to partly explain observations suggesting that notable permeability increase and therefore fluid migration can occur well below the critical threshold for shear reactivation or hydraulic fracturing. Based on the model results, there is a fluid pressure range for which the permeability of the fault increases without being accompanied by large slip events along the whole plane, attributed to the presence of weaker zones characterized by lower friction that channel the fluid and prevent pressure buildup. Distinct thresholds

were then defined according to the fluid pressure and its relation to the minimum stress as well as to the critical Coulomb stress. The conceptual model proposed was then applied to the Eugene Island case showing that flow channeling can be one possible mechanism explaining the upwards migration of the fluid along the fault in the lack of large slip events. In a more general context, flow channeling can occur along the fault plane or in the fracture network as a result of optimally or not oriented fractures as observed in Chapter 3. Acknowledging the role of fault heterogeneities on the induced seismicity in the form of seismic and aseismic patches, using the same model, the relation between the pressure diffusion induced seismicity and hydraulic diffusivity of the fault plane was investigated. For a homogeneous fault plane, the impact of the slip direction as imposed by the stress field was displayed since the fluid tends to propagate towards the same direction under flow rate loading conditions. Introducing different percentages of frictional heterogeneities along the plane ranging from 0% to 80%, revealed different fluid and rupture propagation patterns from radial (0-20%) to strongly channeled flow (40-60%) or a combination of both (70-80%). Assuming that the model rupture events were microseismic events, an effort was made to explore whether the spatio-temporal characteristics of the events were in good agreement with the hydraulic diffusivity of the plane calculated during the simulations. Applying the triggering front concept on the case of a reactivated heterogeneous fracture showed that flow regimes that are strongly characterized by channeling patterns cannot be used to correlate the events cloud with the hydraulic diffusivity of the plane as the events tend to cluster in time along a created channel. For the rest of the cases, using a factor accounting for the heterogeneities percentage can improve the results.

In the fluid induced seismicity context, Test 2 was studied in Chapter 5 and more specifically the last cycle of the test during which the majority of the events occurred. In the first part of the chapter the injection parameters were calibrated including the stress field under which the reactivation took place, the structures that were reactivated, their orientation and properties. The calibration of the test and the comparison to Test 1 showed that different stress conditions are active on each side of the fault studied. After calibrating the injection parameters, we used the quasi-static fully coupled hydro-mechanical model in order to study the potential origins of the migrated seismicity. The fluid front approximated the location of the events only in two configurations implying that the recorded seismicity was more likely to be the result of aseismic deformation and stress transfer effects rather than fluid diffusion process.

Integrating the results presented in all chapters, several conclusions can be drawn keeping in mind the objectives of this work. The different cases studied based on different motivations clearly display the primary role of the in-situ stress conditions and the necessity to properly assess the magnitudes and orientation of the principal stresses. It was made obvious that estimating the stress field characteristics of the area of interest is a necessary component giving information about the structures that are most likely to be reactivated, the expected slip direction, the fluid pressure thresholds and the fluid propagation path. It is natural that there exists a combined effect of the stress field and the structural properties of the fault zone that will determine in the first place the nature of the reactivation. This is in agreement with the concept of critically stressed faults or fractures already existing in the literature. Nevertheless, even though it was shown that the criticality of a structure is a necessary condition for a permeability increase to take place, this condition alone is not able to describe the mechanisms leading to the permeability increase and quantify the enhancement. We have shown that the fluid pressure and fault heterogeneous properties are also first order factors that can help describe and quantify the permeability evolution. The fault-valve model dictates that at given overpressures, the effective normal stress acting on the most favorably oriented fault plane becomes sufficiently low, promoting fault slip and significant permeability

enhancement allowing for fluids to migrate in the direction of the hydraulic gradient. This is followed by a re-strengthening of the fault via different processes until the next overpressure episode occurs. This kind of model as well as the pressure waves propagation mechanism proposed in the literature assume that the permeability enhancement is accompanied by a slip event along the fault. However, field studies show that fluid migration can occur along rather mechanically inactive faults. Considering the Coulomb friction law, it was demonstrated in this study that two fluid pressure thresholds can be defined that essentially decouple the global hydraulic and mechanical component of the fault. Therefore, after restraining the stress and geological conditions, the fault permeability can be classified according to the fluid pressure level. The two thresholds are namely the critical pressure for local shear and flow channeling ($P_{\texttt{f\_crit\_channeling}}$) and the critical pressure for global shear and fluid flow along the plane ($P_{\texttt{f\_crit\_shear}}$). Below $P_{\texttt{f\_crit\_channeling}}$ fault permeability can be assumed equivalent to the intact rock's permeability (1 nD-0.1 mD). Above the $P_{\texttt{f\_crit\_channeling}}$ and below the $P_{\texttt{f\_crit\_shear}}$ the permeability can increase up to 100 mD without the occurrence of large slip events but only localized failures imposed by the heterogeneities of the fault. At $P_{\texttt{f\_crit\_shear}}$ the permeability could range between 100 mD and 1 D. Further increase of the fluid pressure approximates the minimum principal stress value and hydraulic fracturing is the dominant mechanism accompanied by a large permeability enhancement. Such fault response described can be reproduced in a simple model by accounting for the fault's heterogeneities and can conceptually, for the moment, explain field observations at different scales since it is obvious that channeling can occur at the scale of the fracture network as shown in Chapter 3. The same permeability trend is to be expected inside the damage zone where a larger number of fractures can become hydraulically active as the pressure increases.

Apart from predicting the permeability evolution of a fault zone, our results have implications in the research field of fluid induced seismicity. Presupposing that seismicity is a direct effect of fluid flow and effective stress variation, information on the permeability of critical structures can help estimate the spatio-temporal characteristics of the events and vice-versa. However, recent studies tend to consider the induced seismicity as an indirect fluid flow effect resulting mostly from the fluid induced aseismic deformation. Considering the field injection Test 2 and the migrated seismicity, we showed that in the framework of a quasi-static hydro-mechanical analysis combined with field experimental data, it is possible to gain some insight into the geomechanical processes that led to the events occurrence at specific locations. These processes are once again controlled by the stress field, the architecture and geology of the investigation area, the fluid pressure, the loading conditions and the heterogeneities that include material property variations and structures orientation variation.

Overall, the work presented provides useful insight in fault reactivation processes in the framework of the "Fluids and Faults" project and the Tournemire mesoscale experiments. While the results analyzed in this study have contributed to the interpretation and understanding of field observations, there are certainly some aspects that can be improved or complemented. The fault behavior during the numerical analyses is described using the generalized Coulomb friction law. While such a fault constitutive behavior provides satisfying results, a natural extension would be the implementation of a more complex fault mechanical response including a strain softening frictional law commonly used in fault hydromechanical modeling [Cappa & Rutqvist, 2011b; Rutqvist et al., 2013, 2015]. Such a law takes into account the mechanism of progressive damage under shear with the shear strength (basically the friction) decreasing as a function of the plastic displacement. Using 3DEC, the already implemented "continuously yielding joint model" can be selected in order to reproduce a fault response in an alternative way and simulate a sudden slip event. These considerations can potentially improve the quality of the results and give better

explanations to physical phenomena occurring during fault reactivation.

As far as the fault heterogeneous properties are concerned, it was shown that their consideration is mesh-dependent and is certainly a function of the size of the model and problem. Therefore, in order to further strengthen the conceptual model proposed, it will be necessary to come up with a scaling parameter and suitably account for the fault heterogeneities at different scales (e.g. Dreuzy et al. [2012]).

Regarding the fluid flow option considered and used in 3DEC, there was a strict coupling between fluid propagation and rupture occurring along the plane. Such a configuration assumes that the fault or fracture plane is initially closed and it is reactivated due to the progressive fluid and pressure propagation. While this approach is somewhat realistic, it limited our interpretations and prevented us from further analyzing possible de-coupling mechanisms taking place as shown in the fractures interaction case and the induced seismicity of Test 2 where rupture is strictly the result of pressure diffusion in our model. Furthermore, the use of 3DEC hydro-mechanical analysis is based on the assumption that deformation and fluid flow are mainly or exclusively controlled by the presence of distinct structures. The intact material's response is simplified to an elastic or transversely isotropic constitutive law without any possibility to conduct the flow. While, from our point of view, pre-existing fractures tend to focus the hydro-mechanical phenomena as shown by the interpretation of the experimental results, the consideration of matrix plasticity and fluid flow by new options implemented in 3DEC would be of great interest. In addition, the use of continuum based softwares would offer different possibilities and combined with our discrete element approach provide complementary results and physical explanations to some points that were potentially missed out.

Considering the general objective of this work, a natural extension of the presented approach would be the modeling of the rest of the Tests performed in-situ in the context of the "Fluids and Faults" project, i.e. Test 3 in the East damage zone, Test 4 targeting the fault core and the single packer tests 5 and 6. It would be then possible to extract information regarding the reactivation mechanism at each fault compartment determined by the geology, the stress field, the fluid pressure threshold and the mineralogy. Even in the case of a relatively small scale fault, such as the Tournemire fault zone, significant differences were observed regarding the hydro-mechanical response and permeability evolution between each compartment tested.

Another interesting idea enhancing the observations and the understanding of the permeability evolution of faults in clayrocks would be the comparison of the experimental data and numerical results with similar injection experiments at the same scale. For example the injection tests at the Mont Terri URL provide a good case of comparison due to the similarity of the host rock hydro-mechanical properties and to the identical test protocol applied during the tests [Guglielmi et al., 2016; Jeanne et al., 2018]. More comparisons can be made with the field tests at the Low Noise Underground Laboratory (LSBB) targeting geological structures in a fault damage zone in limestone [Duboeuf et al., 2017]. Limestone is known to be a high porosity rock unlike shale, potentially offering dissimilar response in terms of structures reactivation and fluid flow. Furthermore, the subcritical fluid flow concept and the conceptual model proposed could be tested against mesoscale experimental results but also against other case studies and data sets such as the Barbados accretionary prism fluid flow [Fisher & Zwart, 1997; Screaton et al., 2000; Henry, 2000].

Taking into account fault juxtaposition and sequence of rock types in a sedimentary basin, the elements mentioned above are fundamental in order to gain the appropriate information for upscaling the results of the compartmental tests and define a permeability constitutive law applicable to a larger scale

model potentially integrated in basin scale modeling. Considering for example Figure 5.13, synthesizing information based on in-situ tests and literature, it would be interesting to construct ”small” models corresponding to different juxtapositions at various depths along the fault according to the numbered ”windows” of Figure 5.13.

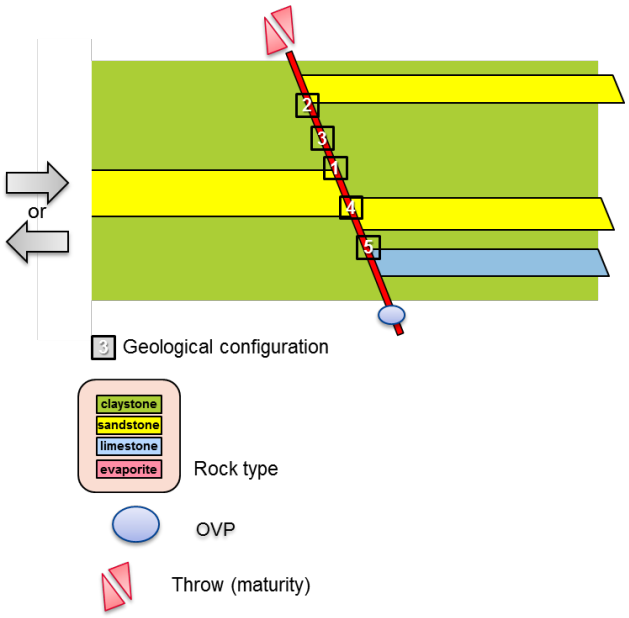

Figure 5.13: Representation of the fault zone and reservoir system. The numbered windows correspond to specific cases that can be

From each window a permeability law can be deduced as a function of lithology, depth, stress and pressure that will be later implemented in a larger model with the fault represented as a single entity with varying properties. Nevertheless, modeling of a large scale site extending several kilometers would be most probably impractical in terms of calculation time using the Distinct Element code 3DEC, provided that for the calculations presented in this work with models ranging from 10 to 35 m the simulation time is far from negligible. Continuum based approaches appear to be more suitable with the condition that dominant structures can be appropriately modeled.

Concluding, in order to properly address currently urgent research matters of importance in industrial applications but also fluid flow systems and natural or induced seismicity, we have shown that a minimum knowledge of the tightly interacting parameters broached is fundamental even though recovering such information is often associated to a high degree of uncertainty. The advancements in the in-situ monitoring techniques and systems and the continuously increasing capacities of numerical softwares can certainly provide with satisfying solutions and results. Nonetheless, a lot of questions remain yet to be answered due to the high complexity of fault systems and the multi-disciplinary approach required in order to evaluate fault hydro-mechanical reactivation related risks.

Bibliography

Ahola, M. P., Mohanty, S., & Makurat, A., 1996. Coupled mechanical shear and hydraulic flow behavior of natural rock joints, in *Developments in geotechnical engineering*, vol. 79, pp. 393–423, Elsevier.

Alvarez, T. A., Cording, E. J., Mikhail, R. A., et al., 1995. Hydromechanical behavior of rock joints: a re-interpretation of published experiments, in *The 35th US Symposium on Rock Mechanics (USRMS)*, American Rock Mechanics Association.

Amadei, B., Savage, W., & Swolfs, H., 1987. Gravitational stresses in anisotropic rock masses, in *International Journal of Rock Mechanics and Mining Sciences & Geomechanics Abstracts*, vol. 24, pp. 5–14, Elsevier.

Amann, F., Kaiser, P., & Button, E. A., 2012. Experimental study of brittle behavior of clay shale in rapid triaxial compression, *Rock mechanics and rock engineering*, **45**(1), 21–33.

Amann, F., Gischig, V., Evans, K., Doetsch, J., Jalali, R., Valley, B., Krietsch, H., Dutler, N., Villiger, L., Brixel, B., et al., 2018. The seismo-hydromechanical behavior during deep geothermal reservoir stimulations: open questions tackled in a decameter-scale in situ stimulation experiment, *Solid Earth*, **9**(1), 115.

Auradou, H., Drazer, G., Boschan, A., Hulin, J.-P., & Koplik, J., 2006. Flow channeling in a single fracture induced by shear displacement, *Geothermics*, **35**(5), 576–588.

Aydin, A., 2001. Fracture void structure: implications for flow, transport and deformation, *Environmental Geology*, **40**(6), 672–677.

Bailly, D., Matray, J.-M., & Ababou, R., 2014. Temporal behavior of a ventilated claystone at the tournemire url: Cross-spectral analyses focused on daily harmonics, *Engineering Geology*, **183**, 137–158.

Balsamo, F., Storti, F., Salvini, F., Silva, A., & Lima, C., 2010. Structural and petrophysical evolution of extensional fault zones in low-porosity, poorly lithified sandstones of the barreiras formation, ne brazil, *Journal of Structural Geology*, **32**(11), 1806–1826.

Barton, C. A., Zoback, M. D., & Moos, D., 1995. Fluid flow along potentially active faults in crystalline rock, *Geology*, **23**(8), 683–686.

Barton, C. A., Hickman, S., Morin, R. H., Zoback, M. D., Finkbeiner, T., Sass, J., & Benoit, D., 1997. Fracture permeability and its relationship to in-situ stress in the dixie valley, nevada, geothermal reservoir.

Barton, N., 2013. Shear strength criteria for rock, rock joints, rockfill and rock masses: Problems and some solutions, *Journal of Rock Mechanics and Geotechnical Engineering*, **5**(4), 249–261.

Barton, N., Bandis, S., & Bakhtar, K., 1985. Strength, deformation and conductivity coupling of rock joints, in *International Journal of Rock Mechanics and Mining Sciences & Geomechanics Abstracts*, vol. 22, pp. 121–140, Elsevier.

Berkowitz, B., 2002. Characterizing flow and transport in fractured geological media: A review, *Advances in water resources*, **25**(8), 861–884.

Bésuelle, P. & Rudnicki, J. W., 2004. Localization: shear bands and compaction bands, *INTERNATIONAL GEOPHYSICS SERIES.*, **89**, 219–322.

Biot, M. A., 1962. Mechanics of deformation and acoustic propagation in porous media, *Journal of applied physics*, **33**(4), 1482–1498.

Blanton, T. L. et al., 1986. Propagation of hydraulically and dynamically induced fractures in naturally fractured reservoirs, in *SPE unconventional gas technology symposium*, Society of Petroleum Engineers.

Boisson, J.-Y., Bertrand, L., Heitz, J.-F., & Golvan, Y., 2001. In situ and laboratory investigations of fluid flow through an argillaceous formation at different scales of space and time, tournemire tunnel, southern france, *Hydrogeology Journal*, **9**(1), 108–123.

Bonnelye, A., Schubnel, A., David, C., Henry, P., Guglielmi, Y., Gout, C., Fauchille, A.-L., & Dick, P., 2017. Strength anisotropy of shales deformed under uppermost crustal conditions, *Journal of Geophysical Research: Solid Earth*, **122**(1), 110–129.

Bossart, P., 2011. Characteristics of the opalinus clay at mont terri, *Mont Terri Project, Wabern Switzerland*.

Bourlange, S. & Henry, P., 2007. Numerical model of fluid pressure solitary wave propagation along the décollement of an accretionary wedge: application to the nankai wedge, *Geofluids*, **7**(3), 323–334.

Bourouis, S. & Bernard, P., 2007. Evidence for coupled seismic and aseismic fault slip during water injection in the geothermal site of soultz (france), and implications for seismogenic transients, *Geophysical Journal International*, **169**(2), 723–732.

Brace, W. & Byerlee, J., 1966. Stick-slip as a mechanism for earthquakes, *Science*, **153**(3739), 990–992.

Byerlee, J., 1978. Friction of rocks, *Pure and applied Geophysics*, **116**(4), 615–626.

Byerlee, J., 1990. Friction, overpressure and fault normal compression, *Geophysical Research Letters*, **17**(12), 2109–2112.

Caine, J. S., Evans, J. P., & Forster, C. B., 1996. Fault zone architecture and permeability structure, *Geology*, **24**(11), 1025–1028.

Campbell, K., Wolfsberg, A., Fabryka-Martin, J., & Sweetkind, D., 2003. Chlorine-36 data at yucca mountain: statistical tests of conceptual models for unsaturated-zone flow, *Journal of contaminant hydrology*, **62**, 43–61.

Candela, T., Brodsky, E. E., Marone, C., & Elsworth, D., 2015. Flow rate dictates permeability enhancement during fluid pressure oscillations in laboratory experiments, *Journal of Geophysical Research: Solid Earth*, **120**(4), 2037–2055.

Cappa, F., 2009. Modelling fluid transfer and slip in a fault zone when integrating heterogeneous hydromechanical characteristics in its internal structure, *Geophysical Journal International*, **178**(3), 1357–1362.

Cappa, F., 2011. Influence of hydromechanical heterogeneities of fault zones on earthquake ruptures, *Geophysical Journal International*, **185**(2), 1049–1058.

Cappa, F. & Rutqvist, J., 2011a. Impact of co2 geological sequestration on the nucleation of earthquakes, *Geophysical Research Letters*, **38**(17).

Cappa, F. & Rutqvist, J., 2011b. Modeling of coupled deformation and permeability evolution during fault reactivation induced by deep underground injection of co 2, *International Journal of Greenhouse Gas Control*, **5**(2), 336–346.

Cappa, F., Guglielmi, Y., Fénart, P., Merrien-Soukatchoff, V., & Thoraval, A., 2005. Hydromechanical interactions in a fractured carbonate reservoir inferred from hydraulic and mechanical measurements, *International Journal of Rock Mechanics and Mining Sciences*, **42**(2), 287–306.

Cappa, F., Guglielmi, Y., Rutqvist, J., Tsang, C.-F., & Thoraval, A., 2006. Hydromechanical modelling of pulse tests that measure fluid pressure and fracture normal displacement at the coaraze laboratory site, france, *International Journal of Rock Mechanics and Mining Sciences*, **43**(7), 1062–1082.

Cappa, F., Guglielmi, Y., Rutqvist, J., Tsang, C.-F., & Thoraval, A., 2008. Estimation of fracture flow parameters through numerical analysis of hydromechanical pressure pulses, *Water resources research*, **44**(11).

Cappa, F., Rutqvist, J., & Yamamoto, K., 2009. Modeling crustal deformation and rupture processes related to upwelling of deep co2-rich fluids during the 1965–1967 matsushiro earthquake swarm in japan, *Journal of Geophysical Research: Solid Earth*, **114**(B10).

Chuprakov, D., Melchaeva, O., & Prioul, R., 2014. Injection-sensitive mechanics of hydraulic fracture interaction with discontinuities, *Rock mechanics and rock engineering*, **47**(5), 1625–1640.

Cooper, A. K., Twichell, D. C., & Hart, P., 1999. *A seismic-reflection investigation of gas hydrates and sea-floor features of the upper continental slope of the Garden Banks and Green Canyon regions, northern Gulf of Mexico: Report for cruise G1-99-GM (99002)*.

Cornet, F., 2000. Détermination du champ de contrainte au voisinage du laboratoire souterrain de tournemire, *Rapport du Laboratoire de Mécanique des Roches, Département de Sismologie, Institut de Physique du Globe de Paris, Rapport N98N33/0073*.

Cornet, F., Helm, J., Poitrenaud, H., & Etchecopar, A., 1997. Seismic and aseismic slips induced by large-scale fluid injections, *Pure and applied geophysics*, **150**(3-4), 563–583.

Cornet, F., Li, L., Hulin, J.-P., Ippolito, I., & Kurowski, P., 2003. The hydromechanical behaviour of a fracture: an in situ experimental case study, *International Journal of Rock Mechanics and Mining Sciences*, **40**(7-8), 1257–1270.

Cornet, F. H., 2016. Seismic and aseismic motions generated by fluid injections, *Geomechanics for Energy and the Environment*, **5**, 42–54.

Cox, S., 2010. The application of failure mode diagrams for exploring the roles of fluid pressure and stress states in controlling styles of fracture-controlled permeability enhancement in faults and shear zones, *Geofluids*, **10**(1-2), 217–233.

Cox, S. F., 1995. Faulting processes at high fluid pressures: an example of fault valve behavior from the wattle gully fault, victoria, australia, *Journ al of Geophysical Research: Solid Earth*, **100**(B7), 12841–12859.

Cundall, P. A., 1980. Udec-a generalised distinct element program for modelling jointed rock., Tech. rep., CUNDALL (PETER) ASSOCIATES VIRGINIA WATER (ENGLAND).

Cundall, P. A., 1988. Formulation of a three-dimensional distinct element model—part i. a scheme to detect and represent contacts in a system composed of many polyhedral blocks, in *International Journal of Rock Mechanics and Mining Sciences & Geomechanics Abstracts*, vol. 25, pp. 107–116, Elsevier.

Cundall, P. A. & Hart, R. D., 1985. Development of generalized 2-d and 3-d distinct element programs for modeling jointed rock, Tech. rep., ITASCA CONSULTING GROUP INC MINNEAPOLISMN.

Cundall, P. A. & Strack, O. D., 1979. A discrete numerical model for granular assemblies, *geotechnique*, **29**(1), 47–65.

Cuss, R. J. & Harrington, J. F., 2016. An experimental study of the potential for fault reactivation during changes in gas and pore-water pressure, *International Journal of Greenhouse Gas Control*, **53**, 41–55.

Cuss, R. J., Milodowski, A., & Harrington, J. F., 2011. Fracture transmissivity as a function of normal and shear stress: first results in opalinus clay, *Physics and Chemistry of the Earth, Parts A/B/C*, **36**(17), 1960–1971.

Damjanac, B. & Cundall, P., 2016. Application of distinct element methods to simulation of hydraulic fracturing in naturally fractured reservoirs, *Computers and Geotechnics*, **71**, 283–294.

Daneshy, A. A., 2016. Mechanics of natural fracture activation by hydraulic fracturing, *HFJ*, **3**(3).

David, C., Wong, T.-F., Zhu, W., & Zhang, J., 1994. Laboratory measurement of compaction-induced permeability change in porous rocks: Implications for the generation and maintenance of pore pressure excess in the crust, *Pure and Applied Geophysics*, **143**(1-3), 425–456.

David, C., Dautriat, J., Sarout, J., Delle Piane, C., Menéndez, B., Macault, R., & Bertauld, D., 2015. Mechanical instability induced by water weakening in laboratory fluid injection tests, *Journal of Geophysical Research: Solid Earth*, **120**(6), 4171–4188.

Davies, R., Foulger, G., Bindley, A., & Styles, P., 2013. Induced seismicity and hydraulic fracturing for the recovery of hydrocarbons, *Marine and Petroleum Geology*, **45**, 171–185.

De Barros, L., Daniel, G., Guglielmi, Y., Rivet, D., Caron, H., Payre, X., Bergery, G., Henry, P., Castilla, R., Dick, P., et al., 2016. Fault structure, stress, or pressure control of the seismicity in shale? insights from a controlled experiment of fluid-induced fault reactivation, *Journal of Geophysical Research: Solid Earth*, **121**(6), 4506–4522.

De Dreuzy, J.-R., Pichot, G., Poirriez, B., & Erhel, J., 2013. Synthetic benchmark for modeling flow in 3d fractured media, *Computers & Geosciences*, **50**, 59–71.

Detournay, E., 1980. Hydraulic conductivity of closed rock fracture: An experimental and analytical study., in *Can Rock Mech Symp Proc 13th, Underground Rock Eng, The HR Rice Mem Symp*, CIM.

Dick, P., Wittebroodt, C., Courbet, C., Sammaljärvi, J., Estève, I., Matray, J.-M., Siitari-Kauppi, M., Voutilainen, M., & Dauzères, A., 2016. The internal architecture and permeability structures of faults in shale formations, in *The Clay Minerals Society Workshop Lectures Series*, vol. 21, pp. 227–242.

Dong, J.-J., Hsu, J.-Y., Wu, W.-J., Shimamoto, T., Hung, J.-H., Yeh, E.-C., Wu, Y.-H., & Sone, H., 2010. Stress-dependence of the permeability and porosity of sandstone and shale from tcdp hole-a, *International Journal of Rock Mechanics and Mining Sciences*, **47**(7), 1141–1157.

Dreuzy, J.-R., Méheust, Y., & Pichot, G., 2012. Influence of fracture scale heterogeneity on the flow properties of three-dimensional discrete fracture networks (dfn), *Journal of Geophysical Research: Solid Earth*, **117**(B11).

Duboeuf, L., De Barros, L., Cappa, F., Guglielmi, Y., Deschamps, A., & Seguy, S., 2017. Aseismic motions drive a sparse seismicity during fluid injections into a fractured zone in a carbonate reservoir, *Journal of Geophysical Research: Solid Earth*, **122**(10), 8285–8304.

Ellsworth, W. L., 2013. Injection-induced earthquakes, *Science*, **341**(6142), 1225942.

Eriksen, F. K., Toussaint, R., Turquet, A. L., Måløy, K. J., & Flekkøy, E. G., 2017. Pneumatic fractures in confined granular media, *Physical Review E*, **95**(6), 062901.

Fabryka-Martin, J., Flint, A., Sweetkind, D., Wolfsberg, A., Levy, S., Roemer, G., Roach, J., Wolfsberg, L., & Duff, M., 1997. Evaluation of flow and transport models of yucca mountain, based on chlorine-36 studies for fy97, *YMP Milestone Rep SP2224M3, Los Alamos National Laboratory, Los Alamos, New Mexico*.

Fairley, J. P. & Hinds, J. J., 2004. Rapid transport pathways for geothermal fluids in an active great basin fault zone, *Geology*, **32**(9), 825–828.

Faleiros, A. M., da Cruz Campanha, G. A., Faleiros, F. M., & da Silveira Bello, R. M., 2014. Fluid regimes, fault-valve behavior and formation of gold-quartz veins—the morro do ouro mine, ribeira belt, brazil, *Ore Geology Reviews*, **56**, 442–456.

Faulkner, D., Jackson, C., Lunn, R., Schlische, R., Shipton, Z., Wibberley, C., & Withjack, M., 2010. A review of recent developments concerning the structure, mechanics and fluid flow properties of fault zones, *Journal of Structural Geology*, **32**(11), 1557–1575.

Finkbeiner, T., Zoback, M., Flemings, P., & Stump, B., 2001. Stress, pore pressure, and dynamically constrained hydrocarbon columns in the south eugene island 330 field, northern gulf of mexico, *AAPG bulletin*, **85**(6), 1007–1031.

Fisher, A. T. & Zwart, G., 1997. 15. packer experiments along the décollement of the barbados accretionary complex: Measurements of in situ permeability1.

Fournier, R. O., 1996. Compressive and tensile failure at high fluid pressure where preexisting fractures have cohesive strength, with application to the san andreas fault, *Journal of Geophysical Research: Solid Earth*, **101**(B11), 25499–25509.

Fu, W., Ames, B. C., Bunger, A. P., & Savitski, A. A., 2016. Impact of partially cemented and non-persistent natural fractures on hydraulic fracture propagation, *Rock Mechanics and Rock Engineering*, **49**(11), 4519–4526.

Gale, J. F., Laubach, S. E., Olson, J. E., Eichhubl, P., & Fall, A., 2014. Natural fractures in shale: A review and new observations, *AAPG bulletin*, **98**(11), 2165–2216.

Gay, A., Lopez, M., Berndt, C., & Seranne, M., 2007. Geological controls on focused fluid flow associated with seafloor seeps in the lower congo basin, *Marine Geology*, **244**(1-4), 68–92.

Gentier, S., Billaux, D., & Van Vliet, L., 1989. Laboratory testing of the voids of a fracture, *Rock mechanics and rock engineering*, **22**(2), 149–157.

Gentier, S., Lamontagne, E., Archambault, G., & Riss, J., 1997. Anisotropy of flow in a fracture undergoing shear and its relationship to the direction of shearing and injection pressure, *International Journal of Rock Mechanics and Mining Sciences*, **34**(3-4), 94–e1.

Gentier, S., Riss, J., Archambault, G., Flamand, R., & Hopkins, D., 2000. Influence of fracture geometry on shear behavior, *International Journal of Rock Mechanics and Mining Sciences*, **37**(1), 161–174.

Goebel, T., Weingarten, M., Chen, X., Haffener, J., & Brodsky, E., 2017. The 2016 mw5. 1 fairview, oklahoma earthquakes: Evidence for long-range poroelastic triggering at¿ 40 km from fluid disposal wells, *Earth and Planetary Science Letters*, **472**, 50–61.

Grasselli, G., Lisjak, A., Mahabadi, O. K., & Tatone, B. S., 2015. Influence of pre-existing discontinuities and bedding planes on hydraulic fracturing initiation, *European Journal of Environmental and Civil Engineering*, **19**(5), 580–597.

Gu, H., Weng, X., Lund, J. B., Mack, M. G., Ganguly, U., Suarez-Rivera, R., et al., 2012. Hydraulic fracture crossing natural fracture at nonorthogonal angles: a criterion and its validation, *SPE Production & Operations*, **27**(01), 20–26.

Guglielmi, Y., Cappa, F., & Amitrano, D., 2008. High-definition analysis of fluid-induced seismicity related to the mesoscale hydromechanical properties of a fault zone, *Geophysical Research Letters*, **35**(6).

Guglielmi, Y., Cappa, F., Lançon, H., Janowczyk, J. B., Rutqvist, J., Tsang, C.-F., & Wang, J., 2013. Isrm suggested method for step-rate injection method for fracture in-situ properties (simfip): Using a 3-components borehole deformation sensor, in *The ISRM Suggested Methods for Rock Characterization, Testing and Monitoring: 2007-2014*, pp. 179–186, Springer.

Guglielmi, Y., Cappa, F., Avouac, J.-P., Henry, P., & Elsworth, D., 2015a. Seismicity triggered by fluid injection–induced aseismic slip, *Science*, **348**(6240), 1224–1226.

Guglielmi, Y., Elsworth, D., Cappa, F., Henry, P., Gout, C., Dick, P., & Durand, J., 2015b. In situ observations on the coupling between hydraulic diffusivity and displacements during fault reactivation in shales, *Journal of Geophysical Research: Solid Earth*, **120**(11), 7729–7748.

Guglielmi, Y., Birkholzer, J., Rutqvist, J., Jeanne, P., & Nussbaum, C., 2016. Can fault leakage occur before or without reactivation? results from an in situ fault reactivation experiment at mont terri, in *13th International Conference on Greenhouse Gas Control Technologies*, pp. 14–18.

Gutierrez, M., Øino, L., & Nygård, R., 2000. Stress-dependent permeability of a de-mineralised fracture in shale, *Marine and Petroleum Geology*, **17**(8), 895–907.

Hainzl, S. & Ogata, Y., 2005. Detecting fluid signals in seismicity data through statistical earthquake modeling, *Journal of Geophysical Research: Solid Earth*, **110**(B5).

Haney, M. M., Snieder, R., Sheiman, J., & Losh, S., 2005. Geophysics: A moving fluid pulse in a fault zone, *Nature*, **437**(7055), 46.

Hantschel, T. & Kauerauf, A. I., 2009. Pore pressure, compaction and tectonics, in *Fundamentals of Basin and Petroleum Systems Modeling*, pp. 31–101, Springer.

Hart, B., Flemings, P., & Deshpande, A., 1995. Porosity and pressure: Role of compaction disequilibrium in the development of geopressures in a gulf coast pleistocene basin, *Geology*, **23**(1), 45–48.

Hart, R., Cundall, P., & Lemos, J., 1988. Formulation of a three-dimensional distinct element model—part ii. mechanical calculations for motion and interaction of a system composed of many polyhedral blocks, in *International Journal of Rock Mechanics and Mining Sciences & Geomechanics Abstracts*, vol. 25, pp. 117–125, Elsevier.

Healy, J., Rubey, W., Griggs, D., & Raleigh, C., 1968. The denver earthquakes, *Science*, **161**(3848), 1301–1310.

Henry, P., 2000. Fluid flow at the toe of the barbados accretionary wedge constrained by thermal, chemical, and hydrogeologic observations and models, *Journal of Geophysical Research: Solid Earth*, **105**(B11), 25855–25872.

Henry, P., Guglielmi, Y., Morereau, A., Seguy, S., Castilla, R., Nussbaum, C., Dick, P., Durand, J., Jaeggi, D., Donze, F., et al., 2016. Permeability-fluid pressure-stress relationship in fault zones in shales, in *AGU Fall Meeting Abstracts*.

Holland, D. S., Leedy, J. B., & Lammlein, D. R., 1990. Eugene island block 330 field–usa offshore louisiana.

Hooker, J., Laubach, S., Gomez, L., Marrett, R., Eichhubl, P., Diaz-Tushman, K., & Pinzon, E., 2011. Fracture size, frequency, and strain in the cambrian eriboll formation sandstones, nw scotland, *Scottish Journal of Geology*, **47**(1), 45–56.

Hubbert, M. K. & Rubey, W. W., 1959. Role of fluid pressure in mechanics of overthrust faulting i. mechanics of fluid-filled porous solids and its application to overthrust faulting, *Geological Society of America Bulletin*, **70**(2), 115–166.

Itasca Consulting Group, I., 2011. *FLAC3D V5.0, fast Lagrangian analysis of continua in 3 dimensions, user's guide*, Itasca, Minneapolis, Minn.

Itasca Consulting Group, I., 2013. *3DEC 3-Dimensional Distinct Element Code*, Itasca, Minneapolis, Minn.

Jaeger, J. C., Cook, N. G., & Zimmerman, R., 2009. *Fundamentals of rock mechanics*, John Wiley & Sons.

Jeanne, P., Guglielmi, Y., Cappa, F., Rinaldi, A. P., & Rutqvist, J., 2014. The effects of lateral property variations on fault-zone reactivation by fluid pressurization: application to co 2 pressurization effects within major and undetected fault zones, *Journal of Structural Geology*, **62**, 97–108.

Jeanne, P., Guglielmi, Y., Rutqvist, J., Nussbaum, C., & Birkholzer, J., 2017a. Field characterization of elastic properties across a fault zone reactivated by fluid injection, *Journal of Geophysical Research: Solid Earth*, **122**(8), 6583–6598.

Jeanne, P., Rutqvist, J., Foxall, W., Rinaldi, A. P., Wainwright, H. M., Zhou, Q., Birkholzer, J., & Layland-Bachmann, C., 2017b. Effects of the distribution and evolution of the coefficient of friction along a fault on the assessment of the seismic activity associated with a hypothetical industrial-scale geologic co 2 sequestration operation, *International Journal of Greenhouse Gas Control*, **66**, 254–263.

Jeanne, P., yes, Y., Rutqvist, J., Nussbaum, C., & Birkholzer, J., 2018. Permeability variations associated with fault reactivation in a claystone formation investigated by field experiments and numerical simulations, *Journal of Geophysical Research: Solid Earth*.

Jeffrey, R. G., Zhang, X., Thiercelin, M. J., et al., 2009. Hydraulic fracture offsetting in naturally fractures reservoirs: Quantifying a long-recognized process, in *SPE hydraulic fracturing technology conference*, Society of Petroleum Engineers.

Jiang, S., 2012. Clay minerals from the perspective of oil and gas exploration, in *Clay Minerals in Nature-Their Characterization, Modification and Application*, InTech.

Jonas, E. C., 1977. *Diagenesis of sandstone and shale: application to exploration for hydrocarbons*, Department of Geological Sciences, the University of Texas at Austin.

Jones, R. M. & Hillis, R. R., 2003. An integrated, quantitative approach to assessing fault-seal risk, *AAPG bulletin*, **87**(3), 507–524.

Joshi, A. & Appold, M. S., 2016. Potential of porosity waves for methane transport in the eugene island field of the gulf of mexico basin, *Marine and Petroleum Geology*, **75**, 1–13.

Keranen, K. M., Weingarten, M., Abers, G. A., Bekins, B. A., & Ge, S., 2014. Sharp increase in central oklahoma seismicity since 2008 induced by massive wastewater injection, *Science*, **345**(6195), 448–451.

Khazaei, C., Hazzard, J., & Chalaturnyk, R., 2016. Discrete element modeling of stick-slip instability and induced microseismicity, *Pure and Applied Geophysics*, **173**(3), 775–794.

Khoei, A., Vahab, M., & Hirmand, M., 2016. Modeling the interaction between fluid-driven fracture and natural fault using an enriched-fem technique, *International Journal of Fracture*, **197**(1), 1–24.

Kluesner, J. W. & Brothers, D. S., 2016. Seismic attribute detection of faults and fluid pathways within an active strike-slip shear zone: New insights from high-resolution 3d p-cable™ seismic data along the hosgri fault, offshore california, *Interpretation*, **4**(1), SB131–SB148.

Kwon, O., Kronenberg, A. K., Gangi, A. F., Johnson, B., & Herbert, B. E., 2004. Permeability of illite-bearing shale: 1. anisotropy and effects of clay content and loading, *Journal of Geophysical Research: Solid Earth*, **109**(B10).

Lefèvre, M., 2016. *Propriétés structurales, pétro-physiques et circulations de fluides au sein d'une zone de failles dans les argiles*, Ph.D. thesis, Université d'Aix-Marseille.

Lefèvre, M., Guglielmi, Y., Henry, P., Dick, P., & Gout, C., 2016. Calcite veins as an indicator of fracture dilatancy and connectivity during strike-slip faulting in toarcian shale (tournemire tunnel, southern france), *Journal of Structural Geology*, **83**, 73–84.

Ligtenberg, J., 2005. Detection of fluid migration pathways in seismic data: implications for fault seal analysis, *Basin Research*, **17**(1), 141–153.

Lin, W., Yamamoto, K., Ito, H., Masago, H., & Kawamura, Y., 2008. Estimation of minimum principal stress from an extended leak-off test onboard the chikyu drilling vessel and suggestions for future test procedures, *Scientific drilling*, **6**, 43–47.

Lindsay, N., Murphy, F., Walsh, J., & Watterson, J., 1993. Outcrop studies of shale smears on fault surface, *The geological modelling of hydrocarbon reservoirs and outcrop analogues*, pp. 113–123.

Liu, Y., Xiu, N., Ding, Y., Wang, X., Lu, Y., Dou, J., Yan, Y., & Liang, T., 2015. Analysis of multi-factor coupling effect on hydraulic fracture network in shale reservoirs, *Natural Gas Industry B*, **2**(2), 162–166.

Lockner, D., 1993. The role of acoustic emission in the study of rock fracture, in *International Journal of Rock Mechanics and Mining Sciences & Geomechanics Abstracts*, vol. 30, pp. 883–899, Elsevier.

Lockner, D. A. & Byerlee, J. D., 1993. How geometrical constraints contribute to the weakness of mature faults, *Nature*, **363**(6426), 250–252.

Lockner, D. A., Okubo, P. G., & Dieterich, J. H., 1982. Containment of stick-slip failures on a simulated fault by pore fluid injection, *Geophysical Research Letters*, **9**(8), 801–804.

Losh, S. & Haney, M., 2006. Episodic fluid flow in an aseismic overpressured growth fault, northern gulf of mexico, *Earthquakes: Radiated energy and the physics of faulting*, pp. 199–205.

Losh, S., Walter, L., Meulbroek, P., Martini, A., Cathles, L., & Whelan, J., 2002. Reservoir fluids and their migration into the south eugene island block 330 reservoirs, offshore louisiana, *AAPG bulletin*, **86**(8).

Matray, J. M., Savoye, S., & Cabrera, J., 2007. Desaturation and structure relationships around drifts excavated in the well-compacted tournemire's argillite (aveyron, france), *Engineering Geology*, **90**(1), 1–16.

Matsuki, K., Kimura, Y., Sakaguchi, K., Kizaki, A., & Giwelli, A., 2010. Effect of shear displacement on the hydraulic conductivity of a fracture, *International Journal of Rock Mechanics and Mining Sciences*, **47**(3), 436–449.

Maxwell, S. C., Cipolla, C. L., et al., 2011. What does microseismicity tell us about hydraulic fracturing?, in *SPE Annual Technical Conference and Exhibition*, Society of Petroleum Engineers.

Mazzoldi, A., Rinaldi, A. P., Borgia, A., & Rutqvist, J., 2012. Induced seismicity within geological carbon sequestration projects: maximum earthquake magnitude and leakage potential from undetected faults, *International Journal of Greenhouse Gas Control*, **10**, 434–442.

McClure, M. W. & Horne, R. N., 2011. Investigation of injection-induced seismicity using a coupled fluid flow and rate/state friction model, *Geophysics*, **76**(6), WC181–WC198.

McGarr, A., 2014. Maximum magnitude earthquakes induced by fluid injection, *Journal of Geophysical Research: solid earth*, **119**(2), 1008–1019.

McGarr, A., Bekins, B., Burkardt, N., Dewey, J., Earle, P., Ellsworth, W., Ge, S., Hickman, S., Holland, A., Majer, E., et al., 2015. Coping with earthquakes induced by fluid injection, *Science*, **347**(6224), 830–831.

Méheust, Y. & Schmittbuhl, J., 2000. Flow enhancement of a rough fracture, *Geophysical Research Letters*, **27**(18), 2989–2992.

Méheust, Y. & Schmittbuhl, J., 2001. Geometrical heterogeneities and permeability anisotropy of rough fractures, *Journal of Geophysical Research: Solid Earth*, **106**(B2), 2089–2102.

Mildren, S. D., Hillis, R. R., Kivior, T., & Kaldi, J. G., 2004. Integrated seal assessment and geologic risk with application to the skua field, timor sea, australia, in *Timor Sea Petroleum Geoscience. Proceedings of the Timor Sea Symposium, Darwin, Australia. Northern Territory Geological Survey, Special Publications*, vol. 1, pp. 275–294, Citeseer.

Miller, S. A., Collettini, C., Chiaraluce, L., Cocco, M., Barchi, M., & Kaus, B. J., 2004. Aftershocks driven by a high-pressure co2 source at depth, *Nature*, **427**(6976), 724–727.

Min, K.-B., Rutqvist, J., Tsang, C.-F., & Jing, L., 2004. Stress-dependent permeability of fractured rock masses: a numerical study, *International Journal of Rock Mechanics and Mining Sciences*, **41**(7), 1191–1210.

Morrow, C., Shi, L., & Byerlee, J., 1984. Permeability of fault gouge under confining pressure and shear stress, *Journal of Geophysical Research: Solid Earth*, **89**(B5), 3193–3200.

Nagel, N., Sanchez-Nagel, M., Zhang, F., Garcia, X., & Lee, B., 2013. Coupled numerical evaluations of the geomechanical interactions between a hydraulic fracture stimulation and a natural fracture system in shale formations, *Rock mechanics and rock engineering*, **46**(3), 581–609.

Neuzil, C., 1994. How permeable are clays and shales?, *Water resources research*, **30**(2), 145–150.

Niemeijer, A. & Spiers, C., 2005. Influence of phyllosilicates on fault strength in the brittle-ductile transition: Insights from rock analogue experiments, *Geological Society, London, Special Publications*, **245**(1), 303–327.

Nishiyama, S., Ohnishi, Y., Ito, H., & Yano, T., 2014. Mechanical and hydraulic behavior of a rock fracture under shear deformation, *Earth, planets and space*, **66**(1), 108.

Nur, A. & Booker, J. R., 1972. Aftershocks caused by pore fluid flow?, *Science*, **175**(4024), 885–887.

Olsson, R. & Barton, N., 2001. An improved model for hydromechanical coupling during shearing of rock joints, *International Journal of Rock Mechanics and Mining Sciences*, **38**(3), 317–329.

Oron, A. P. & Berkowitz, B., 1998. Flow in rock fractures: The local cubic law assumption reexamined, *Water Resources Research*, **34**(11), 2811–2825.

Papachristos, E., 2017. *A 3D hydro-mechanical discrete element model for hydraulic fracturing in naturally fractured rock*, Ph.D. thesis, Université Grenoble Alpes.

Parotidis, M., Rothert, E., & Shapiro, S., 2003. Pore-pressure diffusion: A possible triggering mechanism for the earthquake swarms 2000 in vogtland/nw-bohemia, central europe, *Geophysical Research Letters*, **30**(20).

Person, M., Raffensperger, J. P., Ge, S., & Garven, G., 1996. Basin-scale hydrogeologic modeling, *Reviews of Geophysics*, **34**(1), 61–87.

Preisig, G., Eberhardt, E., Gischig, V., Roche, V., Baan, M., Valley, B., Kaiser, P., Duff, D., & Lowther, R., 2015. Development of connected permeability in massive crystalline rocks through hydraulic fracture propagation and shearing accompanying fluid injection, *Geofluids*, **15**(1-2), 321–337.

Pruess, K., Oldenburg, C., & Moridis, G., 2011. Tough2 user's guide, version 2.1, lbnl-43134 (revised), *Lawrence Berkeley National Laboratory, Berkeley, CA*.

Raaen, A., Horsrud, P., Kjørholt, H., & Økland, D., 2006. Improved routine estimation of the minimum horizontal stress component from extended leak-off tests, *International Journal of Rock Mechanics and Mining Sciences*, **43**(1), 37–48.

Rejeb, A. & Cabrera, J., 2006. Time-dependent evolution of the excavation damaged zone in the argillaceous tournemire site, in *The GeoProc international conference on coupled THMC processes in geosystems: fundamentals, modelling, experiments and applications (invited lecture)*, pp. 22–25.

Revil, A. & Cathles, L., 2002. Fluid transport by solitary waves along growing faults: A field example from the south eugene island basin, gulf of mexico, *Earth and Planetary Science Letters*, **202**(2), 321–335.

Riahi, A. & Damjanac, B., 2013. Numerical study of interaction between hydraulic fracture and discrete fracture network, in *Effective and Sustainable Hydraulic Fracturing*, InTech.

Rice, J. R., 1992. Fault stress states, pore pressure distributions, and the weakness of the san andreas fault, *International Geophysics*, **51**, 475–503.

Rivet, D., De Barros, L., Guglielmi, Y., Cappa, F., Castilla, R., & Henry, P., 2016. Seismic velocity changes associated with aseismic deformations of a fault stimulated by fluid injection, *Geophysical Research Letters*, **43**(18), 9563–9572.

Rutledge, J. T. & Phillips, W. S., 2003. Hydraulic stimulation of natural fractures as revealed by induced microearthquakes, carthage cotton valley gas field, east texas, *Geophysics*, **68**(2), 441–452.

Rutqvist, J., 2011. Status of the tough-flac simulator and recent applications related to coupled fluid flow and crustal deformations, *Computers & Geosciences*, **37**(6), 739–750.

Rutqvist, J., Noorishad, J., Tsang, C.-F., & Stephansson, O., 1998. Determination of fracture storativity in hard rocks using high-pressure injection testing, *Water Resources Research*, **34**(10), 2551–2560.

Rutqvist, J., Tsang, C.-F., & Stephansson, O., 2000. Uncertainty in the maximum principal stress estimated from hydraulic fracturing measurements due to the presence of the induced fracture, *International Journal of Rock Mechanics and Mining Sciences*, **37**(1-2), 107–120.

Rutqvist, J., Wu, Y.-S., Tsang, C.-F., & Bodvarsson, G., 2002. A modeling approach for analysis of coupled multiphase fluid flow, heat transfer, and deformation in fractured porous rock, *International Journal of Rock Mechanics and Mining Sciences*, **39**(4), 429–442.

Rutqvist, J., Rinaldi, A. P., Cappa, F., & Moridis, G. J., 2013. Modeling of fault reactivation and induced seismicity during hydraulic fracturing of shale-gas reservoirs, *Journal of Petroleum Science and Engineering*, **107**, 31–44.

Rutqvist, J., Rinaldi, A. P., Cappa, F., & Moridis, G. J., 2015. Modeling of fault activation and seismicity by injection directly into a fault zone associated with hydraulic fracturing of shale-gas reservoirs, *Journal of Petroleum Science and Engineering*, **127**, 377–386.

Rutqvist, J., Rinaldi, A. P., Cappa, F., Jeanne, P., Mazzoldi, A., Urpi, L., Guglielmi, Y., & Vilarrasa, V., 2016. Fault activation and induced seismicity in geological carbon storage–lessons learned from recent modeling studies, *Journal of Rock Mechanics and Geotechnical Engineering*, **8**(6), 789–804.

Scotti, O. & Cornet, F., 1994. In situ evidence for fluid-induced aseismic slip events along fault zones, in *International journal of rock mechanics and mining sciences & geomechanics abstracts*, vol. 31, pp. 347–358, Elsevier.

Screaton, E., Carson, B., Davis, E., & Becker, K., 2000. Permeability of a decollement zone: Results from a two-well experiment in the barbados accretionary complex, *Journal of Geophysical Research: Solid Earth*, **105**(B9), 21403–21410.

Screaton, E. J., Carson, B., & Lennon, G. P., 1995. Hydrogeologic properties of a thrust fault within the oregon accretionary prism, *Journal of Geophysical Research: Solid Earth*, **100**(B10), 20025–20035.

Seyedi, D. M., Vu, M.-N., & Pouya, A., 2015. A two-scale hydromechanical model for fault zones accounting for their heterogeneous structure, *Computers and Geotechnics*, **68**, 8–16.

Shapiro, S. & Dinske, C., 2009. Fluid-induced seismicity: Pressure diffusion and hydraulic fracturing, *Geophysical Prospecting*, **57**(2), 301–310.

Shapiro, S. A., Rothert, E., Rath, V., & Rindschwentner, J., 2002. Characterization of fluid transport properties of reservoirs using induced microseismicity, *Geophysics*, **67**(1), 212–220.

Shapiro, S. A., Rentsch, S., & Rothert, E., 2005. Characterization of hydraulic properties of rocks using probability of fluid-induced microearthquakes, *Geophysics*, **70**(2), F27–F33.

Shelly, D. R., Taira, T., Prejean, S. G., Hill, D. P., & Dreger, D. S., 2015. Fluid-faulting interactions: Fracture-mesh and fault-valve behavior in the february 2014 mammoth mountain, california, earthquake swarm, *Geophysical Research Letters*, **42**(14), 5803–5812.

Shi, Y. & Wang, C.-Y., 1986. Pore pressure generation in sedimentary basins: overloading versus aquathermal, *Journal of Geophysical Research: Solid Earth*, **91**(B2), 2153–2162.

Shukla, R., Ranjith, P., Haque, A., & Choi, X., 2010. A review of studies on co 2 sequestration and caprock integrity, *Fuel*, **89**(10), 2651–2664.

Sibson, R. H., 1989. Earthquake faulting as a structural process, *Journal of Structural Geology*, **11**(1-2), 1–14.

Sibson, R. H., 1990. Conditions for fault-valve behaviour, *Geological Society, London, Special Publications*, **54**(1), 15–28.

Sibson, R. H., 1992. Fault-valve behavior and the hydrostatic-lithostatic fluid pressure interface, *Earth-Science Reviews*, **32**(1-2), 141–144.

Sibson, R. H., 1996. Structural permeability of fluid-driven fault-fracture meshes, *Journal of Structural Geology*, **18**(8), 1031–1042.

Sibson, R. H., Robert, F., & Poulsen, K. H., 1988. High-angle reverse faults, fluid-pressure cycling, and mesothermal gold-quartz deposits, *Geology*, **16**(6), 551–555.

Sorkhabi, R. & Tsuji, Y., 2005. The place of faults in petroleum traps.

Stanchits, S., Mayr, S., Shapiro, S., & Dresen, G., 2011. Fracturing of porous rock induced by fluid injection, *Tectonophysics*, **503**(1), 129–145.

Townend, J. & Zoback, M. D., 2000. How faulting keeps the crust strong, *Geology*, **28**(5), 399–402.

Tremosa, J., Arcos, D., Matray, J., Bensenouci, F., Gaucher, E. C., Tournassat, C., & Hadi, J., 2012. Geochemical characterization and modelling of the toarcian/domerian porewater at the tournemire underground research laboratory, *Applied geochemistry*, **27**(7), 1417–1431.

Tsang, Y., 1984. The effect of tortuosity on fluid flow through a single fracture, *Water Resources Research*, **20**(9), 1209–1215.

Tsang, Y., 1992. Usage of "equivalent apertures" for rock fractures as derived from hydraulic and tracer tests, *Water Resources Research*, **28**(5), 1451–1455.

Van Der Baan, M., Eaton, D., & Dusseault, M., 2013. Microseismic monitoring developments in hydraulic fracture stimulation, in *Effective and sustainable hydraulic fracturing*, Intech.

van der Elst, N. J., Savage, H. M., Keranen, K. M., & Abers, G. A., 2013. Enhanced remote earthquake triggering at fluid-injection sites in the midwestern united states, *Science*, **341**(6142), 164–167.

Vavryčuk, V., 2014. Earthquake mechanisms and stress field, *Encyclopedia of earthquake engineering*, pp. 1–21.

Warpinski, N., Teufel, L., et al., 1987. Influence of geologic discontinuities on hydraulic fracture propagation (includes associated papers 17011 and 17074), *Journal of Petroleum Technology*, **39**(02), 209–220.

Warpinski, N. R., Du, J., Zimmer, U., et al., 2012. Measurements of hydraulic-fracture-induced seismicity in gas shales, *SPE Production & Operations*, **27**(03), 240–252.

Weber, K., Mandl, G., Pilaar, W., Lehner, B., Precious, R., et al., 1978. The role of faults in hydrocarbon migration and trapping in nigerian growth fault structures, in *Offshore Technology Conference*, Offshore Technology Conference.

Weertman, J., 1980. Unstable slippage across a fault that separates elastic media of different elastic constants, *Journal of Geophysical Research: Solid Earth*, **85**(B3), 1455–1461.

Wei, S., Avouac, J.-P., Hudnut, K. W., Donnellan, A., Parker, J. W., Graves, R. W., Helmberger, D., Fielding, E., Liu, Z., Cappa, F., et al., 2015. The 2012 brawley swarm triggered by injection-induced aseismic slip, *Earth and Planetary Science Letters*, **422**, 115–125.

Wiprut, D. & Zoback, M. D., 2000. Fault reactivation and fluid flow along a previously dormant normal fault in the northern north sea, *Geology*, **28**(7), 595–598.

Witherspoon, P. A., Wang, J. S., Iwai, K., & Gale, J. E., 1980. Validity of cubic law for fluid flow in a deformable rock fracture, *Water resources research*, **16**(6), 1016–1024.

Yaghoubi, A. & Zoback, M., 2012. Hydraulic fracturing modeling using a discrete fracture network in the barnett shale, in *American Geophysical Union, Fall Meeting*.

Yew, C. H. & Weng, X., 2014. *Mechanics of hydraulic fracturing*, Gulf Professional Publishing.

Yielding, G., Freeman, B., & Needham, D. T., 1997. Quantitative fault seal prediction, *AAPG bulletin*, **81**(6), 897–917.

Zhang, X. & Sanderson, D. J., 1996. Effects of stress on the two-dimensional permeability tensor of natural fracture networks, *Geophysical Journal International*, **125**(3), 912–924.

Zhao, J. & Brown, E., 1992. Hydro-thermo-mechanical properties of joints in the carnmenellis granite, *Quarterly Journal of Engineering Geology and Hydrogeology*, **25**(4), 279–290.

Zhao, X., Young, R., et al., 2009. Numerical simulation of seismicity induced by hydraulic fracturing in naturally fractured reservoirs, in *SPE Annual Technical Conference and Exhibition*, Society of Petroleum Engineers.

Zhou, J., Chen, M., Jin, Y., & Zhang, G.-q., 2008. Analysis of fracture propagation behavior and fracture geometry using a tri-axial fracturing system in naturally fractured reservoirs, *International Journal of Rock Mechanics and Mining Sciences*, **45**(7), 1143–1152.

Zimmerman, R. W., 2012. The history and role of the cubic law for fluid flow in fractured rocks, *Proceedings of the Session H071 Dynamics of Fluids and Transport in Fractured Porous Media, San Francisco, CA, USA*, pp. 3–7.

Zimmerman, R. W. & Bodvarsson, G. S., 1996. Hydraulic conductivity of rock fractures, *Transport in porous media*, **23**(1), 1–30.

Zimmerman, R. W., Chen, D.-W., & Cook, N. G., 1992. The effect of contact area on the permeability of fractures, *Journal of Hydrology*, **139**(1-4), 79–96.

Zoback, M. D. & Harjes, H.-P., 1997. Injection-induced earthquakes and crustal stress at 9 km depth at the ktb deep drilling site, germany, *Journal of Geophysical Research: Solid Earth*, **102**(B8), 18477–18491.